On the Verge

Mechanics in the Limit of Vanishing Strength and Stiffness

Jan Maarten van Doorn

Propositions

1. Network topology is irrelevant for fatigue in colloidal gels.
   (this thesis)

2. Wave propagation micromechanics of soft solids is a solution to the regular misuse of other microrheology methods that rely on heavy assumptions.
   (this thesis)

3. Considering the second law of thermodynamics, a truly circular economy is an illusion.

4. Letting artificial intelligence into our homes is no more harmful then taking cats in.

5. Irrational fears for nuclear energy stand in the way of resolving climate change in the short term.

6. When optimizing experiments, good enough is often best.

7. Instead of a computer recipe, the term algorithm nowadays refers to a computer program we do not understand.

Propositions belonging to the thesis, entitled

'On the verge; Mechanics in the limit of vanishing strength and stiffness'

Jan Maarten van Doorn

Wageningen, 8 November 2019

On the verge

Mechanics in the limit of vanishing strength and stiffness

Jan Maarten van Doorn

Thesis committee

Promotor
prof. Dr J. van der Gucht
Professor of Physical Chemistry and Soft Matter
Wageningen University and Research

Promotor
prof. Dr J. Sprakel
Personal chair, Physical Chemistry and Soft Matter
Wageningen University and Research

Other members
prof. Dr B.M. Mulder, FOM Institute AMOLF
prof. Dr R. Dullens, Oxford University, United Kingdom
prof. Dr S.C.G. Leeuwenburgh, Radboud University Medical Center, Nijmegen
Dr H.B. Eral, TU Delft

This research was conducted under the auspices of the Graduate School VLAG (Advanced studies in Food Technology, Agrobiotechnology, Nutrition and Health Sciences).

On the verge

Mechanics in the limit of vanishing strength and stiffness

Jan Maarten van Doorn

Thesis
Submitted in fulfillment of the requirements for the degree of doctor
at Wageningen University
by the authority of the Rector Magnificus,
prof. Dr A.P.J. Mol,
in the presence of the
Thesis Committee appointed by the Academic Board
to be defended in public
on Friday 8 November, 2019
at 4 p.m. in the Aula.

Jan Maarten van Doorn
On the verge— Mechanics in the limit of vanishing strength and stiffness
257 pages

PhD thesis, Wageningen University, Wageningen, The Netherlands (2019)
with references, with summary in English.

ISBN: 978-94-6395-032-9
DOI: https://doi.org/10.18174/495806

Contents

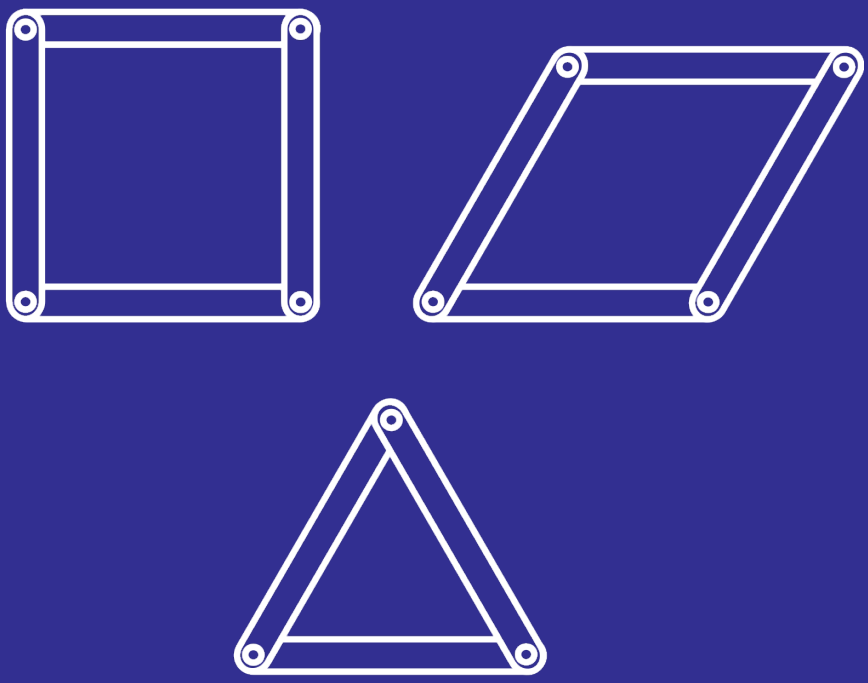

CHAPTER 1

Introduction

The discovery and use of new materials has shaped progress in the development of human societies, from the stone, bronze and iron ages of the distant past, to our current society in which information technology is driven by advances in semiconductor applications and in which plastics and synthetic polymers are essential to our daily life. [1, 2]. For many applications, from large buildings to soft implants, mechanical characteristics are central when deciding what material to use and can be classified with two parameters: strength and stiffness[1]. When designing a bridge we want a strong and stiff material like steel, however when eating ice cream we prefer something soft and a crunchy - easy to break - cone[3, 4, 5].

In most cases stiffness and strength are positively correlated: Stiff materials are in general stronger and soft materials tend to break earlier[Fig. 1.1][1]. However many biological materials do not follow this correlation, for example skin has a relatively low stiffness but is incredibly strong[6, 7]. These remarkable and often non-linear mechanics are the result of a complex interplay of cell components that exists in a delicate balance of enthalpic and entropic forces [8, 9, 10]. While a low *stiffness*, connectivity and rigidity are useful properties in nature, as this enables regulatory systems to achieve large changes in material property with small external cues, it also implies that the materials are on the verge of becoming unstable. However this highly dynamic environment is critical for biological systems to maintain their ro-

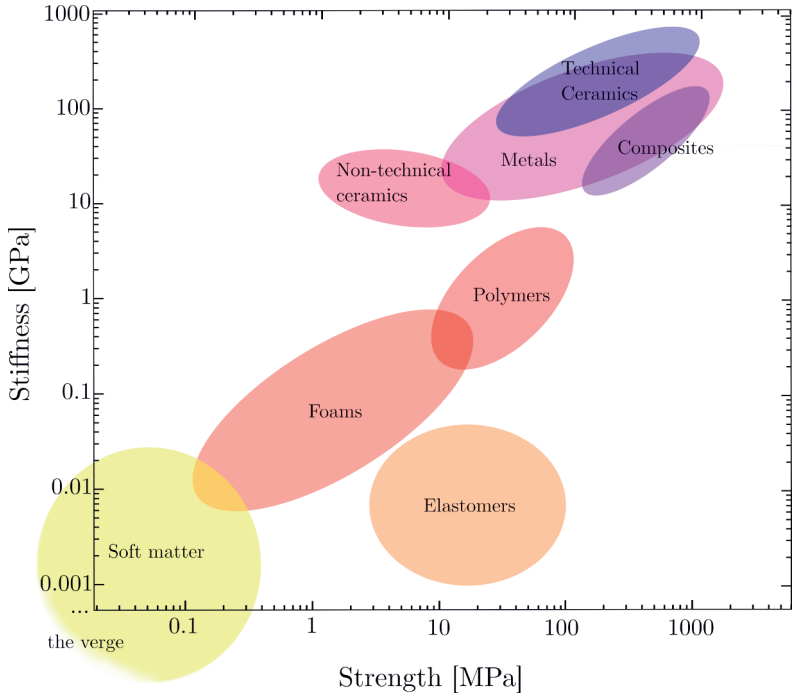

Figure 1.1: Ashby plot of common engineering materials. Strong materials are usually stiff and weak materials are generally soft. The range of soft matter is indicated by the yellow circle and extends beyond the lower limits of this graph.

bustness and adaptivity[11, 12, 13]. The relevance of solids close to a mechanical tipping point is not exclusive to nature; in the shaping of solid metals, one often works very close to their melting point, where the rigidity can become very small and entropy begins to govern [14, 13, 15]. These systems share many features with the biological systems such as a highly dynamic environment and an important role for entropy[16, 17]. In fact the entropic fluctuations in these solids are so large, they dominate and completely alter the nature of the solid itself[16].

Strength describes the resilience of a material to failure under the action of a mechanical stress. In the limit of decreasing strength we find extremely

weak materials that approach the point at which only the smallest stress will cause mechanical failure[18]. Mechanical failure comes in many different forms; a material can break in a brittle manner as glass or in a more ductile manner like bubble gum and many forms in between[19]. Both for solids with very low rigidity or strength, mechanical instability is around the corner. Even thermal fluctuations can drive these systems over the edge. This changes the physics these systems obey, deviating from the framework of linear elasticity, being very sensitive to local effects and non-affinity. Yet despite their importance both in the synthetic and biological world, much remains unknown about their properties and how these emerge from the details of the microscopic material structure. [20, 21].

The aim of this thesis is to establish the link between structure, dynamics and mechanics in the limit of hyperweak and hypersoft materials. For hypersoft materials we focus on reversible mechanics and attempt to link structure and dynamics to resulting mechanics. For hyperweak materials we aim to link structure to failure mechanics via dynamics. Finally for materials that are both hyperweak and hypersoft we directly link their structure to the resulting failure mechanics. To achieve all these links we use established experimental and numerical techniques. When these do not suffice we develop new techniques, analysis methods and materials to get as close to the verge as possible.

Reversible mechanics: Stiffness

The common operational definition of a solid is a material which has a finite resistance to shear deformations. In other words, a solid has a finite rigidity. A formal physical measure for rigidity or stiffness is the shear modulus μ which quantifies the resistance to shear deformation [Fig. 1.2 (a)][22]. The shear modulus is defined as the ratio between the shear stress $\sigma = \frac{F}{A}$ and the shear strain $\gamma = \frac{\Delta x}{l_0}$.

$$\mu = \frac{\sigma}{\gamma} \tag{1.1}$$

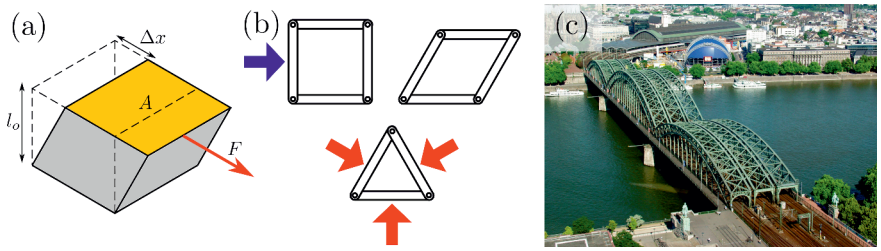

Figure 1.2: (a) A cube under shear deformation. (b) A triangle is an example of a structural rigid shape. A square is isostatic; it is only one bond away from being rigid. (c) The Hohenzollern bridge in Cologne. The diagonal connections make this bridge rigid which allows heavy trains to cross the Rhine river daily. ©Raimond Spekking / CC BY-SA 4.0 (via Wikimedia Commons)

If a material has a finite shear modulus it is considered a solid. Not every microstructure provides a material with rigidity; a minimal number of bonds has to be arranged in the correct configuration. A triangle resists shear deformation and therefore is a rigid arrangement of bonds[Fig. 1.2 (b)]. By contrast, a square is not rigid as opposite sides are free to move [Fig. 1.2 (b)]. Placing an extra diagonal bond prevents this movement and makes the structure rigid. This not only works on the microscopic level in materials but also for macroscopic structures such as bridges where diagonal steel beams ensure a solid construction that allows safe crossing[Fig. 1.2 (c)].

For triangles and squares it is easy to see whether they are rigid but for large disordered systems this becomes much more challenging. For this reason a mathematical theory has been developed by Maxwell. This theory provides a structural criterion for the minimal number of bonds N_b required for rigidity in dimension d based on the number of nodes N_n[23].

$$N_b > d(N_n - 2) \tag{1.2}$$

Systems that satisfy this condition can be rigid. Systems that have only one bond above this threshold, e.g. $N_b = d(N_n - 2) + 1$, are called marginal as removing one bond would make them collapse. The rigidity criterion is

independent of the system size which means that even in very large marginal systems the removal of a single bond in a rigid system will make it collapse. The point just after collapse, $N_b = d(N_n - 2)$, is called the isostatic point and systems or regions that have a number of bonds below this point are called floppy. Whereas Maxwell's criterion assumes rigid beams and hinging joints, many joints in real-life materials resist bending. This bending contributes to the overall rigidity and may cause overall rigidity at a lower number of bonds than prescibed by Maxwell's criterion.

However, containing the minimal number of bonds as described by Maxwell's criterion does not guarantee that the entire system is rigid[24]. When a marginal system has redundant bonds in one part it will not have enough bonds elsewhere. This highlights that also the distribution of bonds is important in maintaining rigidity. This is studied by percolation theory [25]. As more and more bonds are added to a system rigid and floppy regions emerge. When the rigid regions connect and span the entire network the rigidity percolation threshold is reached. In this case the rigidity has percolated the system. Similar to the Maxwell criterion the percolation threshold is critical as only one bond is required to form a generally rigid system. For bonds on a triangular lattice it has been shown that percolation occurs when 66% of the bonds are placed[26].

Many biological fiber networks are marginal and near the percolation threshold and thus on the verge of collapse [27, 28]. These materials however derive rigidity from the bending resistance of their fiber components as well. This is not included by the percolation theory or by Maxwell's criterion and is studied intensively as bending resistance results in complex mechanical responses[29, 30, 31].

Energy and length scales in soft materials

The rigidity criterion and the percolation threshold are structural only and describe whether the Hohenzollern bridge or a gelatin pudding is rigid. How-

ever , they do not tell us *how* rigid a material or structure is. To understand why soft materials are soft, we have to define energy and lengths scales as can be shown with dimensional analysis

$$\mu \propto \frac{k_B T}{a^3} \tag{1.3}$$

Thermal fluctuations play a large role in soft materials which results in a typical energy scale of $k_B T \approx 4 \cdot 10^{-21}$ J for soft materials[32]. The structural components of soft materials have typical dimensions of 10^{-9} to 10^{-6} m. For example, in a hydrogel, such as gelatin, mesh sizes are typically in the order of tens of nanometers[33]. According to equation 1.3 this corresponds to a shear modulus of around 4kPa which is in the same order of magnitude of what is found in experiments[34]. This demonstrates that the stiffness is largely defined by the density of bonds. In chapter 2 we study extremely soft materials that consist of colloidal particles with dimensions of micrometers. From the same dimensional analysis, we find that these solids have moduli of only milliPascals and below, one milion times softer than a gelatin pudding; a clear example of a material in which rigidity begins to vanish.

Fiber networks

Most biological materials such as the cytoskeleton and cell walls and processed materials as paper and fabrics derive their rigidity from fiber networks. These fibers often consist of celulose, collagen, fibrin, actin filaments and microtubules[Fig.1.3(a-c)]. Microtubules are part of the cytoskeleton and are a pinnacle of a biological system that is on the verge of collapse. Microtubules constantly grow, collapse and reform, allowing cells to constantly adapt their shape to a changing environment[35, 36]. From a mechanical point of view fiber networks are prototypical examples of disordered materials where resistance to bending plays an important role. For these systems the classic Maxwell criterion does not hold and these networks are often rigid below the isostatic point as defined by equation 1.2 because of the bending rigid-

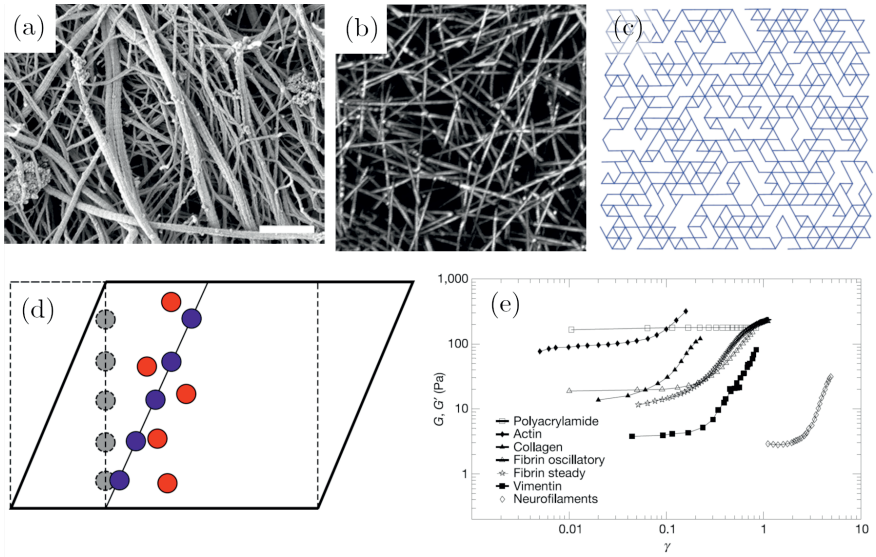

Figure 1.3: (a) A SEM image of collagen fibers in hip cartilage, adapted from[39]. (b) A Confocal image of fibrin fibers in a blood cloth[40](Copyright (2005) National Academy of Sciences.). (c) A model fiber network on a triangular lattice, adapted by permission from Springer Nature, Nature Physics [13], copyright 2011. (d) For purely affine deformation (blue) all points follow the global deformation whereas non-affine deformation (red) deviates from the global deformation. (e) Shear moduli as function of strain for different biological fibers, many fiber networks show a non-linear dependency, adapted by permission from Springer Nature, Nature [9], copyright 2005.

ity of the fibers[13, 29, 30, 31]. Fibers and the mesh size of fiber networks are usually large enough to study with electron and confocal microscopy. This makes them one of the few marginal systems for which internal dynamics can be studied both with simulations and experiments[27, 37, 38]. The complex interplay of stretching, bending and structural disorder gives fiber networks highly nonlinear but reversible mechanical properties[Fig.1.3(e)][9, 41]. As these systems approach the marginal regime this nonlinear behaviour is more and more pronounced[13]. This is often associated with non-affinities

that emerge under mechanical deformation[Fig.1.3(d)][42, 43, 44]. Non-affine deformations are those in which individual components in the network e.g. the fibers do not follow the general deformation that is imposed on the material or network as a whole. These local non-affine deformations can have a significant impact on the mechanical behaviour of the network as a whole[45]. Therefore fiber networks are extremely difficult to model as the individual behavior of each fiber has to be taken into account[46]. The further we approach the rigidity threshold the more these non affine deformations dominate and the more difficult modeling becomes[13]. In chapter 9 we study fiber networks near the rigidity threshold and attempt to predict mechanical behavior based exclusively on the structure and topology of the network with a machine learning approach.

Jammed solids and the glass transition

Another class of marginal solids are jammed solids[15, 47]. Jamming occurs when the volume fraction of particles is high enough that particles confine each other[Fig. 1.4(a)][48]. This results in a force-bearing network that can resist shear deformation in the system which can therefore be considered a solid[Fig.1.4(b)][49, 50, 51, 52]. Jammed systems are disordered and have many structural characteristics of a fluid and the question why, despite this structure, they exhibit solid-like behaviour is one of the central themes in soft matter science. The term jamming is in principle defined for athermal systems however it shows many similarities with the glass transition for thermal systems[Fig. 1.4(c)][53, 54, 55].

For atomic materials a glass is formed by cooling a liquid so rapidly that the atoms have no time to nucleate in a crystal, resulting in a dynamically arrested structure, which has solid-like features but which retains a liquid-like order. [57, 58]. Macroscopically the glass transition is associated with a strongly increased viscosity due to rapidly slowing down of microscopic dynamics[59]. In a variety of molecular or polymeric glass formers, the tran-

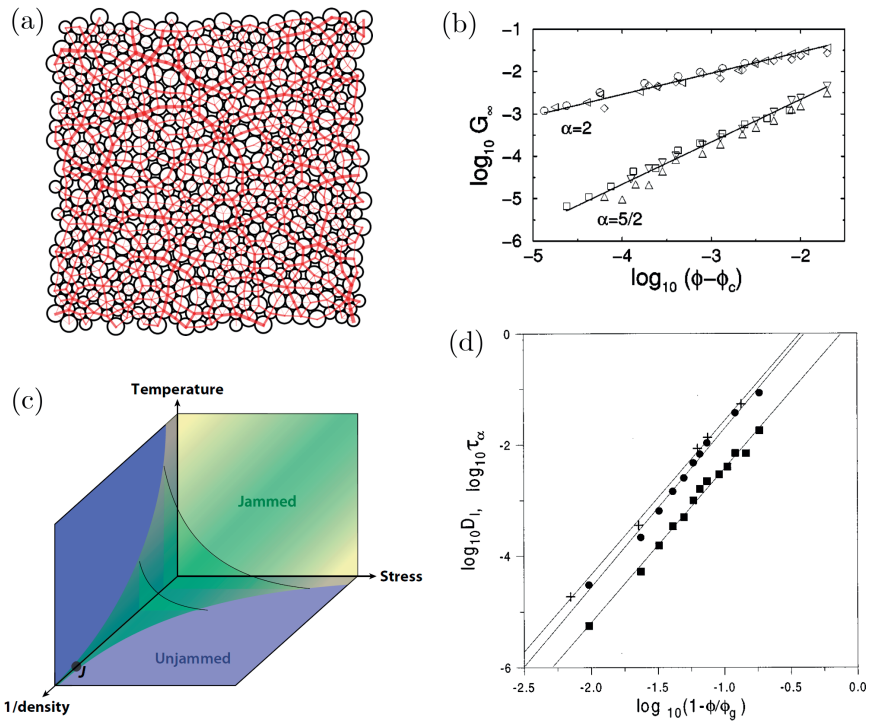

Figure 1.4: (a) A two-dimensional packing of a bidisperse mixture of disks, the resulting force-bearing network is shown in red, adapted with permission from[24]. (b) An emerging shear modulus just after the jamming transition, reprinted with permission from [47], copyright 2003 by the American Physical Society. (c) The jamming phase-diagram proposed by Liu *et al.*, increased temperature and applied stress will move the jamming point to higher volume fractions, adapted with permission from [15]. (d) Increasing relaxation times hallmark the glass transition, reprinted with permission from [56], copyright 1998 by the American Physical Society.

sition from freely flowing fluid to solid-like glass is induced by lowering the temperature. Colloidal systems show an equivalent change in properties upon increasing the particle volume fraction ϕ, which plays the role of an effective inverse temperature in this case[60, 61, 62]. When these systems approach a volume fraction $\phi_g \approx 0.58$ dynamics start to slow down and

viscosity rises rapidly[Fig. 1.4(d)]. Above ϕ_g increasing the volume fraction by a small amount leads to a viscosity increase of orders of magnitude[63, 56]. Similarly to jammed systems, glasses resist shear deformation, which gives them a finite shear modulus[64]. These similarities lead to the question whether the glass transition and the jamming transition are separate phenomena[54].

Jammed systems at their isostatic point, or glasses close to their transition point, often exhibit the features of marginality; very small changes in the control parameter lead to very large changes in material properties[24]. Combined with their disordered nature this marginality makes jammed systems and their force bearing networks very similar to the fiber networks discussed earlier. In fact porous materials such as fiber networks show force networks that are similar to granular systems[65]. Because glasses generally contain much smaller particles that are influenced by thermal fluctuations, different behaviour from jammed systems will only occur in regimes where thermal fluctuations can be dominant; the ultra weak limit. Therefore, to elucidate the distinction between jamming and the glass transition, colloidal systems extremely close to the critical volume fraction need to be studied. Similar to fiber networks, non-affine deformations dominate in this regime, making modeling extremely challenging[66]. Experimentally studying these systems is also difficult as current methods do not have the resolution to accurately measure such low elastic moduli and thermal fluctuations may mask any signal of rigidity. In chapter 2 we open up a new way to get past the thermal fluctuations and mechanically characterize extremely soft solids near the glass transition.

Composite soft materials

Composite materials are a class of materials with unique mechanical properties that consist of a combination of traditional materials[67]. Among these materials are for example glass- or carbon fiber reinforced plastics, reinforced

concrete and Glare, a composite of fused layers of glass and aluminum[68, 69, 70]. These materials often have an enhanced mechanical stiffness that is larger than the sum of the stiffness of the individual components. Reinforced concreted for example derives this synergistic enhanced stiffness to the fact that in reinforced concrete the steel supports all extensional stress and the concrete supports all compressional stress. As concrete would easily fracture under large extensional stress and a steel wire network would easily buckle under compressional stress the composite ensures the individual components are loaded such that they support the type of load for which they are the strongest, leading to overall enhanced stiffness[69]. Most real-world soft materials are composite materials. Foodstuffs and cosmetics often consist of vast ranges of different ingredients that have complex interactions to give a product unique properties[74]. Also skin consists of multiple, intertwined, networks of various protein fibers[6, 10]. Inspired by this example, several model hybrid polymer networks have been developed experimentally[Fig. 1.5(a)]These materials show, similar to reinforced concrete, significant mechanical enhancement of sometimes orders of magnitude[Fig.1.5(b)][72, 75]. However in contrast to reinforced concrete, these materials have a vastly different microstructure and a much larger contribution of entropic forces and non-affine deformations which will make the underlying mechanics greatly different for soft materials[76, 77, 78, 79, 80]. In chapter 4 we present an *in silico* model for studying the mechanisms underlying this mechanical enhancement in dilute fiber networks. We find different mechanisms for different mechanical regimes and critical behavior when transitioning form one regime to the other, which introduces a new verge of hyperstiffness.

As polymer networks have mesh sizes of several nanometers, studying these microscopic mechanisms *experimentally* is extremely difficult. To overcome this barrier and to study the mechanical interactions between the fibers of each component, the mesh and fiber size have to be enlarged. This could be achieved by studying hybrid colloidal gels[Fig. 1.5(c)][73]. These are net-

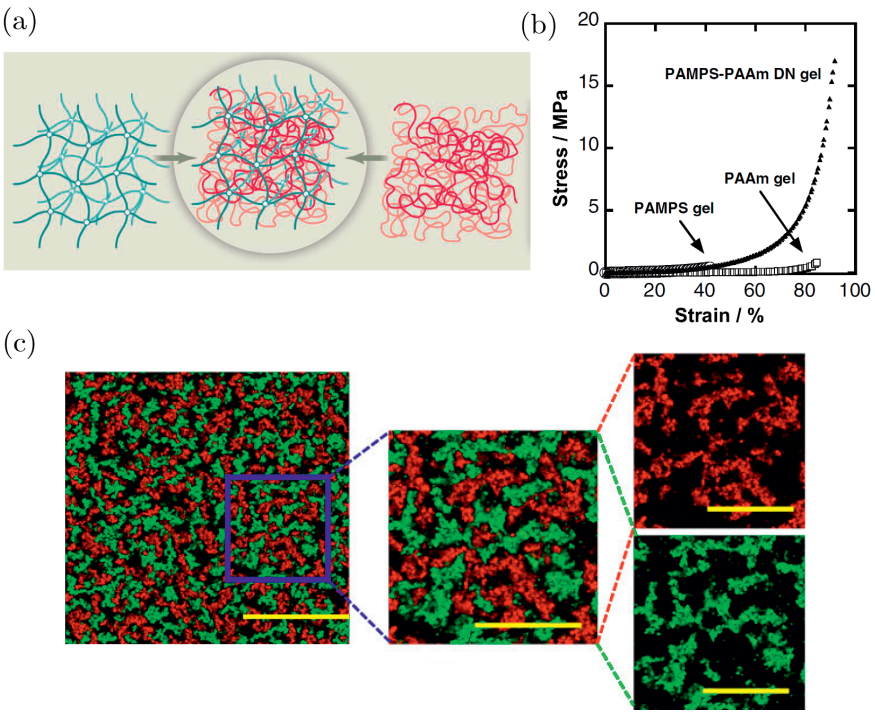

Figure 1.5: (a) Schematic of a double polymer network. The blue network is chemically cross-linked whereas the red network is entangled only. From [71]. Reprinted with permission from AAAS. (b) The stiffness of a double networks is greatly increased with respect to their individual components, reprinted with permission from[72]. (c) Confocal image of a hybrid colloidal gel that is assembled with highly specific DNA interactions[73].

works of colloidal particles with a highly specific interaction. This interaction is generally difficult to achieve and has only successfully been demonstrated by using DNA[81, 82]. In Chapter 5 we take the first steps towards a facile assembly of such a hybrid colloidal network by bringing highly versatile azide click chemistry for easy surface modification to tunable polymeric particles[83].

Table 1.1: Overview of common bonds in soft materials[32]

Type	**Bond Energy, ΔE**
Covalent	3 $\cdot 10^2$ k_BT
Ionic	1-3 $\cdot 10^2$ k_BT
Van der Waals interaction	3-10 k_BT
Hydrogen bonds	20 k_BT
Hydrophobic interactions	1-5 k_BT
Depletion interaction	1-20 k_BT

Non-linear irreversible mechanics: Strength

In the previous section we have only considered reversible mechanics; after deforming a material it behaves and looks exactly the same as before deformation. However we experience daily that is often not the case: yogurt is not the same after scooping some out of the jar for breakfast, after tearing a wrap from a candy bar it does not automatically glue itself back together and after crushing a soda can it does not inflate itself back. When a material is deformed too much, it does not return to its original shape. This is called plastic deformation and is characterized by energy dissipation, e.g. the rupture of bonds and a permanent shape change[84]. These irreversible transformations are often referred to as nonlinear mechanics. However to avoid confusion with the reversible nonlinear mechanics of marginal fiber networks we will use the term irreversible mechanics in this section.

Molecular materials are held together by interactions on the molecular scale such as covalent and ionic bonds, van der waals interactions and hydrophobic interactions[32][Table 1.1]. Many of these bonds have a fundamental origin. Covalent bonds result from the sharing electrons between atoms to complete their electron shells. Ionic and hydrogen bonds result from fundamental electrostatic interactions and van der waals interactions are induced

by the dipoles of the interacting molecules. In addition to these interactions many emergent or entropic forces such as the hydrophobic interaction exist.

Hydrophobic interactions play a crucial role in biological and non-biological systems at the molecular scale[85]. Water molecules on a hydrophobic-hydrophilic interface have less degrees of freedom than water molecules in bulk. This causes a decrease of entropy and an overall increase of free energy near a hydrophobic-hydrophilic interface. Reducing this interface would reduce the number of restricted water molecules and therefore reduce the overall free energy in the system. When applying this to two large hydrophobic molecules it is favorable for these molecules to stay close to reduce the total hydrophobic-hydrophilic interface in the system. This leads to an effective interaction between the hydrophobic molecules, that is crucial in for example protein folding, maintaining membrane integrity and micelle formation[86, 87].

Molecular interactions also manifest themselves on the larger colloidal scale. Van der Waals interactions induce colloidal particle attraction on a short range whereas equally charged particles repel each other on a longer range. These interactions can be tuned with salt concentration in the suspending liquid and are, together with the van der Waals interactions, described by the DLVO theory[88, 89]. Also entropic forces can be observed on the colloidal scale [90]. Here polymer molecules induce an effective interaction between colloidal particles. On the solid-liquid interface of the particles, in the depletion zone, polymers have less degrees of freedom than in bulk. Minimizing the depletion zone by making the depletion zones of multiple particles overlap reduces the amount of restricted polymers and decreases the overall free energy. More examples of entropic forces include the elastic behavior of a polymer chain and, more controversially, gravity has been proposed to be an entropic force as well[91, 92]. Entropic forces are crucial to soft matter systems, which makes soft materials fundamentally different from classical materials such as metals and concrete where enthalpy dominates[93].

All bonds between colloids and molecules can break. Without mechanical force this occurs depending on the binding energy ΔE and the magnitude of the thermal fluctuations. The entropic bonds often found in soft materials are weak and highly reversible with bonding energies that do not exceed several $k_B T$. This highlights the importance of entropy and thermal fluctuations that make bond-dissociation a relevant procces, which can cause irreversible change. Even without external mechanical stimuli this leads to complex mechanics[94, 95, 96]. The bond dissociation rate does not solely depend on the binding energy but also on bonding geometry, such as the valency Z of the bond; dissociating multiple bonds together is exponentially slower as $\tau_B \propto e^{Z \cdot \Delta E / k_B T}$. This makes the internal dynamics for ultra weak materials intimately lined to their structure and, especially for heterogeneous materials, highly complex. In chapter 6 we elucidate this intimate relation and show that these complex dynamics can be predicted based exclusively on structural information.

Mechanical failure

In extreme cases, a material under strain will not only deform permanently but it will also fracture[97]. Here, at a critical fracture stress, a solid is separated in two or more pieces and loses a significant part of its load bearing capability. A material can fail in a brittle or ductile fashion[Fig. 1.6(a,b)][19]. Brittle fracture happens almost instantly with no plastic deformation preempting the failure, much like window glass. Ductile fracture is a much slower process that is characterized with the material plastically deforming before ultimately fracturing, much like stretching bubble gum. Whether a material fractures in a brittle or ductile manner is governed by how much elastic energy can be dissipated in the material itself rather than forming new surface area. The creation of new surface area is often preferred in brittle materials with low internal dynamics where strong bonds such as covalent and ionic bonds are broken and not easily reformed. When bonds are softer

or more delocalized like metallic bonds, plastic deformation is more likely to dissipate mechanical energy before ultimate failure resulting in a ductile fracture process[Fig. 1.6(d)]. The extreme limit where all energy is dissipated through plastic deformation is called yielding. Here the solid flows like a liquid during the failure process until the internal bonds are restored upon stress relief[Fig.1.6(c)]. The critical stress at which we observe yielding is called the yield stress. In soft materials the full spectrum of mechanical failure can be found, from brittle fracture in hydrogels, ductile fracture in rubbers and yielding in jammed emulsions like mayonnaise[98, 99, 100, 101].

The process of fracture is governed by crack nucleation. In a similar way as occurs for rain drop nucleation in a cloud, crack nucleation is facilitated by the existence of nucleation sites, or defects, in the material structure[103]. This makes fracture and the critical fracture stress greatly dependent on the structure of the material and extremely complex in disordered materials[104]. Once a crack has nucleated it propagates with a crack tip. In this tip bonds are actually broken and dynamics are highly non-linear. For materials that approach the rigidity transition this region expands up to a point where a major part of the material can be considered the crack tip with accompanying non-linearities[105]. This makes fracture in soft materials extremely complex and highly unpredictable. In chapter 9 we investigate how machine learning methods can assist in predicting fracture and identify structural parameters that govern fracture in these weak disordered materials.

Even when materials are deformed below their critical fracture stress but repeatedly, they can still build up damage that ultimately lead to mechanical failure[Fig. 1.6][19]. This is a phenomenon known as mechanical fatigue and in practice is the most ubiquitous threat to material lifetime. For metals and concrete this process has been studied intensively as the lifespan of most buildings depends on the integrity of these materials[106, 107]. As a result the fatigue mechanisms for concrete and metals are quite well known. Upon repeated deformation, microcracks, often invisible to the naked eye,

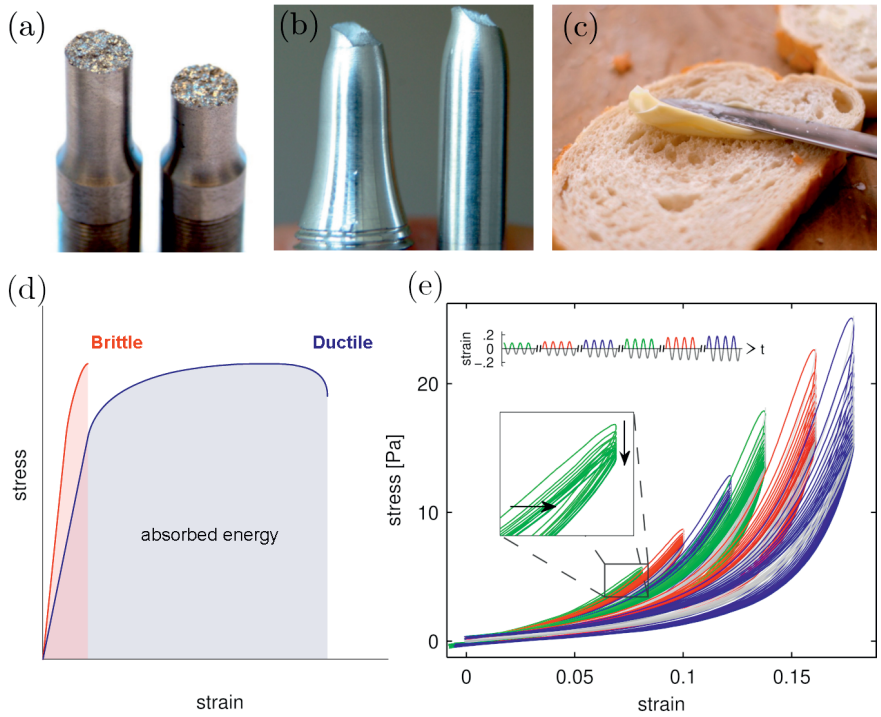

Figure 1.6: (a) Example of brittle fracture as a result of extensional strain. ©Sigmund419 / CC BY-SA 3.0 (via Wikimedia Commons) (b) Ductile failure of an aluminum rod. Plastic deformation preempting the failure caused thinning at the fracture location, a neck. ©Sigmund419 / CC BY-SA 3.0 (via Wikimedia Commons)(c) Spreading of butter is entirely plastic and therefore a typical example of yielding. (d) Stress- strain curves for brittle and ductile failure. ©Amgreen / CC BY-SA 3.0 (via Wikimedia Commons) (e) Collagen fiber networks progressively weaken when strain cycles are applied repeatedly[102].

accumulate and progressively weaken the material up to the point that the critical fracture stress is lowered and catastrophic failure is inevitable. For soft materials fatigue is much less understood. Fiber networks are known to progressively weaken as well, however muscles tend to strengthen when using them often[Fig. 1.6][102, 108]. As soft materials are much more dy-

namic and have a highly heterogeneous structure, fatigue mechanisms can be extremely complex. In chapter 7 we study fatigue mechanisms in weak and disordered solids and show how progressive weakening is related to highly localized dynamics.

Kinetically arrested solids

Whereas ordered solids generally derive their solidity from a thermodynamic equilibrium, many disordered materials derive their stability from a mere mechanical equilibrium[113, 114, 57]. This mechanical equilibrium arises from a kinetic arrest on the way to thermodynamic equilibrium[112]. A prototypical example of these kinetically arrested solids are colloidal gels[18]. These are rigid networks of mesoscopic strands of attractive colloidal particles[115, 116]. When inter-particle attraction and volume fraction are sufficiently high these particles cluster and eventually form a sample spanning cluster[Fig. 1.7 (a-d)][117]. This cluster is above the isostatic limit which provides rigidity and mechanical equilibrium. In order to reach the thermodynamic equilibrium state and minimize the free energy in the system the system would have to progress to an attractive crystalline sample. However during the aggregation of the particles, induced by the attractive interactions, the system not only crossed the colloidal glass transition line, but simultaneously forms a percolated network structure. The combination of these two effects leads to a kinetically-arrested solid-like material in which a complex network microstructure provides rigidity. For soft materials that are closer to the verge of collapse, where interactions are much weaker and thermal fluctuations more dominant, kinetically arrested systems still have residual dynamics[118, 95, 119, 95]. These dynamics give colloidal gels the unique property that irreversible deformations towards the equilibrium state already occur at the smallest strains and sometimes even without external stimuli[120]. This makes them exemplaric for materials with vanishing strength.

Kinetically trapped colloidal gels can generally be reached via two mech-

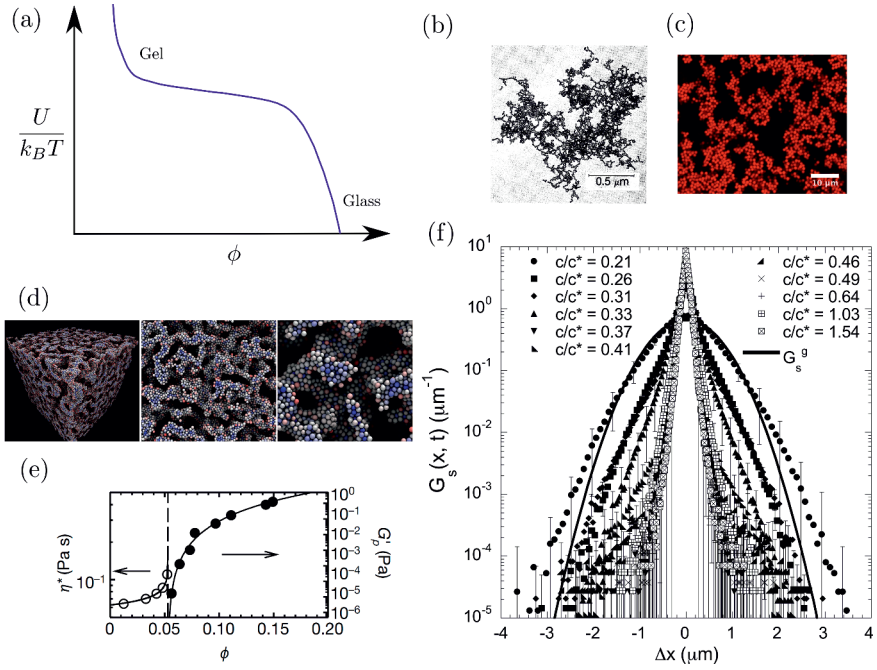

Figure 1.7: (a) Schematic gelation diagram, if volume fraction ϕ and attraction U are high enough a colloidal gel will form. For low attraction strength but at high volume fraction the system will enter a glassy state. (b) Electron micrograph of aggrated gold nanoparticles, a prototypical example of a hard colloidal gel, reprinted with permission from [109], copyright 1984 by the American Physical Society. (c) Confocal image of a colloidal depletion gel, an example of a soft colloidal gel. Reprinted with permission from [110]. Copyright 2014, The Society of Rheology. (d) Simulation snapshot of a soft colloidal gel. Reprinted with permission from [111]. Copyright 2014, The Society of Rheology. (e) Similar to the glass transition the viscosity of the bulk rises preempting gelation and an elastic modulus emerges after gelation, adapted by permission from Springer Nature, Nature [112], copyright 2001. (f) Van Hove functions for soft colloidal gels with different depletant concentrations. As attraction strength increases the van Hove function becomes more and more non-Gaussian highlighting strong heterogeneous dynamics, reprinted with permission from [95], copyright 2006 by the American Physical Society.

anisms: (i) Diffusion Limited Cluster Aggregation (DLCA) or (ii) spinodal decomposition. Depending on the strength of the inter-particle attraction these routes lead to strong or soft colloidal gels respectively[109]. When inter-particle attraction is so strong that particles are improbable to escape once aggregated, particles bind irreversibly upon collision and clusters are rapidly formed without rearrangement[121]. These clusters also aggregate upon collision ultimately leading to a fractal sample spanning network[Fig. 1.7(b)]. Because particles in these strong colloidal gels have little opportunity to rearrange, strands in these gels remain thin and highly branched[122]. When inter-particle attraction is weak enough to allow for rearrangements during the aggregation process, an entirely different mechanism preludes the kinetic arrest[18]. This mechanism is called spinodal decomposition and originates from the theory for phase separation where concentration fluctuations of each phase rapidly grow until one domain for each phase remains[123]. Soft colloidal gels gel by demixing in a particle-rich and a solvent-rich phase. When the particle rich phase becomes large enough to form a rigid and sample spanning network, kinetic entrapment is reached and demixing is rapidly slowed down. As during the growth of the particle rich clusters the particles can still rearrange, a state closer to the equilibrium state can be reached. This process causes the strands in soft colloidal gels to be much thicker than for gels formed with DLCA[Fig. 1.7(c,d)][110]. Especially colloidal gels formed by spinodal decomposition are extremely weak and soft and are on the verge according to the two criteria defined earlier. These gels are so weak that thermal fluctuations are sufficient to push the system out of mechanical equilibrium and further towards the thermodynamic equilibrium in a process that is known as aging[96]. In extreme cases ageing builds up sufficient internal tension to make the entire gel collapse[20, 21].

Similar to the colloidal glass transition, the dynamics in colloidal gels rapidly slow down upon reaching the percolation threshold. Also a shear modulus rapidly arises after this point[Fig. 1.7 (e)]. This makes the colloidal

gel transition related to the colloidal glass transition, as colloidal glasses and colloidal gels can both be regarded as kinetically arrested solids[124]. There are however some distinct differences. Unlike for the glass transition, the structure of a colloidal gel is different from that of a liquid structure. The structure for colloidal gels are network-like and show a clear load bearing network which makes it in theory possible to define the gel transition from structural data, whereas in colloidal glasses such a network can only be derived from the dynamics[125]. Both colloidal glasses and colloidal gels exhibit heterogeneous dynamics[Fig. 1.7 (f)]. For colloidal gels these heterogeneous dynamics have a much larger range than for colloidal glasses; particles can be completely stuck and hardly move or particles can be unbound and freely diffusing[126]. In chapter 6 we account for this great range and link these to the inherent heterogeneous structure of colloidal gels.

Colloidal gels often do not immediately collapse upon external deformation. This is a phenomenon know as delayed yielding and has been attributed to the brittle rupture of the mesoscopic strands of particles[127, 128]. Under an external strain, the bond-life time is decreased exponentially, $\tau_B \propto e^{-F\cdot\delta/k_BT}$ where δ is a microscopic lengscale. At sufficient external stress, bonds are broken faster than they can reform which ultimately leads to a broken strand and brittle fracture of the network as a whole. This picture however overlooks the inherent dynamics and plasticity occurring in colloidal gels, even at rest. In chapter 7 we show that these processes do play an role important role in the mechanical failure of colloidal gels in fatigue.

Outline

The aim of this thesis is to explore the mechanics of hypersoft and hyperweak systems in terms of their underlying strcuture and dynamics. Here we provide a short summary for each chapter and explain how they contribute to the general aim of the thesis.

In chapter 2 we study mechanical wave propagation in ultra soft solids. Mechanical waves are intimately linked to the mechanical properties of their medium. We show how these waves can be generated and detected despite abundant thermal fluctuations. Furthermore we develop an analytical theory that allows us to interpret these waves in terms of mechanical properties, directly linking the dynamics to the mechanics in these materials.

In chapter 3 we give a technical overview of the optical tweezers instrument used for generation and detection of the waves in chapter 2. Furthermore we present a calibration method that allows for a more constant force generation.

In chapter 4 we explore the different mechanical regimes of composite fiber networks. We show how mechanical enhancement arises by suppressing non affine deformations in a dilute fiber network with a secondary elastic network.

In chapter 5 we present a synthesis method for simple surface modification of particles. The synthesis allows for precise control of the surface concentration of the attached molecules and paves the way for hybrid colloidal networks that can provide experimental access to the mechanisms studied in chapter 4.

In chapter 6 we study the dynamics of hyperweak colloidal gels. We show how these heterogeneous dynamics are intimately coupled to the heterogeneous structure. Furthermore we provide a transition state theory that is capable of predicting the dynamics, based solely on structural input which directly links the structure to dynamic in hyperweak solids.

In chapter 7 we apply the results of chapter 6 to hyperweak solids under repeated external strain. We show how a new mechanism of plastic deformation weakens the mesoscopic strands gradually, leading to weakening and mechanical failure. This mechanism provides the link of dynamics in hyperweak materials to their corresponding failure mechanics.

In chapter 8 we describe the synthesis of a new experimental system that

allows for studying the effect of mechanical surface properties on the resulting dynamics and mechanics. We show that increasing the grating density on the particle surface leads to rotational hindrance and mechanical stiffening.

In chapter 9 we explore how machine learning methods can be applied to predict failure in dilute and disordered fiber networks. We also show how structural parameters crucial to the failure process can be identified and aid our understanding of fracture in dilute networks. This chapter provides a direct link of structure to the resulting fracture mechanics in hyperweak solids

In the last chapter, the general discussion, we look back on our findings and discuss how our findings can be placed in a more general context. Furthermore we provide an outlook on how our results can be used to provide more links that can lead to a more integral understanding of hypersoft and hyperweak solids.

Bibliography

[1] Michael F Ashby. *Materials selection in mechanical design*. Butterworth-Heinemann, 2004.

[2] Rolf E Hummel. *Understanding materials science: history, properties, applications*. Springer Science & Business Media, 2004.

[3] P Sherman. The texture of ice cream 3. rheological properties of mix and melted ice cream. *Journal of Food Science*, 31(5):707–716, 1966.

[4] A Baltsavias, A Jurgens, and T van Vliet. Fracture properties of short-dough biscuits: Effect of composition. *Journal of Cereal Science*, 29(3):235–244, 1999.

[5] Wai-Fah Chen and Lian Duan. *Bridge engineering handbook*. CRC press, 1999.

[6] Wen Yang, Vincent R Sherman, Bernd Gludovatz, Eric Schaible, Polite Stewart, Robert O Ritchie, and Marc A Meyers. On the tear resistance of skin. *Nature communications*, 6:6649, 2015.

[7] Peter Fratzl, Klaus Misof, Ivo Zizak, Gert Rapp, Heinz Amenitsch, and Sigrid Bernstorff. Fibrillar structure and mechanical properties of collagen. *Journal of Structural Biology*, 122(1):119–122, 1998.

[8] Erwin Schrödinger. *What is life?: With mind and matter and autobiographical sketches*. Cambridge University Press, 1992.

[9] Cornelis Storm, Jennifer J Pastore, Fred C MacKintosh, Tom C Lubensky, and Paul A Janmey. Nonlinear elasticity in biological gels. *Nature*, 435(7039):191, 2005.

[10] M. L. Gardel, F. Nakamura, J. Hartwig, J. C. Crocker, T. P. Stossel, and D. A. Weitz. Stress-dependent elasticity of composite actin networks as a model for cell behavior. *Phys. Rev. Lett.*, 96:088102, Mar 2006.

[11] Gareth E. Jones. Cellular signaling in macrophage migration and chemotaxis. *Journal of Leukocyte Biology*, 68(5):593–602, 2000.

[12] Daniel A Fletcher and R Dyche Mullins. Cell mechanics and the cytoskeleton. *Nature*, 463(7280):485, 2010.

[13] Chase P Broedersz, Xiaoming Mao, Tom C Lubensky, and Frederick C MacKintosh. Criticality and isostaticity in fibre networks. *Nature Physics*, 7(12):983, 2011.

[14] Peter Haasen and B. L. Mordike. *Physical Metallurgy*. Cambridge University Press, 3 edition, 1996.

[15] Andrea J. Liu and Sidney R. Nagel. The jamming transition and the marginally jammed solid. *Annual Review of Condensed Matter Physics*, 1(1):347–369, 2010.

[16] Joris Sprakel, Alessio Zaccone, Frans Spaepen, Peter Schall, and David A. Weitz. Direct observation of entropic stabilization of bcc crystals near melting. *Phys. Rev. Lett.*, 118:088003, Feb 2017.

[17] M. Dennison, M. Sheinman, C. Storm, and F. C. MacKintosh. Fluctuation-stabilized marginal networks and anomalous entropic elasticity. *Phys. Rev. Lett.*, 111:095503, Aug 2013.

[18] Peter J Lu, Emanuela Zaccarelli, Fabio Ciulla, Andrew B Schofield, Francesco Sciortino, and David A Weitz. Gelation of particles with short-range attraction. *Nature*, 453(7194):499, 2008.

[19] Flake C Campbell. *Fatigue and fracture: understanding the basics*. ASM International, 2012.

[20] S. Manley, J. M. Skotheim, L. Mahadevan, and D. A. Weitz. Gravitational collapse of colloidal gels. *Phys. Rev. Lett.*, 94:218302, Jun 2005.

[21] Poornima Padmanabhan and Roseanna Zia. Gravitational collapse of colloidal gels: non-equilibrium phase separation driven by osmotic pressure. *Soft Matter*, 14:3265–3287, 2018.

[22] LD Landau and EM Lifshitz. Theory of elasticity. 1986. *Course of theoretical physics*, 1986.

[23] J. Clerk Maxwell F.R.S. Xlv. on reciprocal figures and diagrams of forces. *The London, Edinburgh, and Dublin Philosophical Magazine and Journal of Science*, 27(182):250–261, 1864.

[24] TC Lubensky, CL Kane, Xiaoming Mao, Anton Souslov, and Kai Sun. Phonons and elasticity in critically coordinated lattices. *Reports on Progress in Physics*, 78(7):073901, 2015.

[25] M. F. Thorpe. *Rigidity Percolation*, pages 55–61. Springer US, Boston, MA, 1985.

[26] D. J. Jacobs and M. F. Thorpe. Generic rigidity percolation: The pebble game. *Phys. Rev. Lett.*, 75:4051–4054, Nov 1995.

[27] A Sharma, AJ Licup, KA Jansen, R Rens, M Sheinman, GH Koenderink, and FC MacKintosh. Strain-controlled criticality governs the nonlinear mechanics of fibre networks. *Nature Physics*, 12(6):584, 2016.

[28] AR Bausch and K Kroy. A bottom-up approach to cell mechanics. *Nature physics*, 2(4):231, 2006.

[29] Jan Wilhelm and Erwin Frey. Elasticity of stiff polymer networks. *Phys. Rev. Lett.*, 91:108103, Sep 2003.

[30] David A. Head, Alex J. Levine, and F. C. MacKintosh. Deformation of cross-linked semiflexible polymer networks. *Phys. Rev. Lett.*, 91:108102, Sep 2003.

[31] D. A. Head, A. J. Levine, and F. C. MacKintosh. Distinct regimes of elastic response and deformation modes of cross-linked cytoskeletal and semiflexible polymer networks. *Phys. Rev. E*, 68:061907, Dec 2003.

[32] Richard AL Jones. *Soft condensed matter*, volume 6. Oxford University Press, 2002.

[33] Florent Carn, François Boué, Madeleine Djabourov, Nathalie Steunou, Thibaud Coradin, Jacques Livage, Sébastien Floquet, Emmanuel Cadot, and Eric Buhler. Biopolymer folding driven nanoparticle reorganization in bio-nanocomposites. *Soft Matter*, 8:2930–2944, 02 2012.

[34] P.M Gilsenan and S.B Ross-Murphy. Rheological characterisation of gelatins from mammalian and marine sources. *Food Hydrocolloids*, 14(3):191–195, 2000.

[35] Richard C. Weisenberg. Microtubule formation in vitro in solutions containing low calcium concentrations. *Science*, 177(4054):1104–1105, 1972.

[36] Tim Mitchison and Marc Kirschner. Dynamic instability of microtubule growth. *nature*, 312(5991):237, 1984.

[37] Federica Burla, Justin Tauber, Simone Dussi, Jasper van der Gucht, and Gijsje H Koenderink. Stress management in composite biopolymer networks. *Nature Physics*, page 1, 2019.

[38] Albert James Licup, Stefan Münster, Abhinav Sharma, Michael Sheinman, Louise M. Jawerth, Ben Fabry, David A. Weitz, and Fred C. MacKintosh. Stress controls the mechanics of collagen networks. *Proceedings of the National Academy of Sciences*, 112(31):9573–9578, 2015.

[39] Riccardo Gottardi, Uwe Hansen, Roberto Raiteri, Marko Loparic, Marcel Düggelin, Daniel Mathys, Niklaus F. Friederich, Peter Bruckner, and Martin Stolz. Supramolecular organization of collagen fibrils in healthy and osteoarthritic human knee and hip joint cartilage. *PLOS ONE*, 11(10):1–13, 10 2016.

[40] Jean-Philippe Collet, Henry Shuman, Robert E. Ledger, Seungtaek Lee, and John W. Weisel. The elasticity of an individual fibrin fiber in a clot. *Proceedings of the National Academy of Sciences*, 102(26):9133–9137, 2005.

[41] M. L. Gardel, J. H. Shin, F. C. MacKintosh, L. Mahadevan, P. Matsudaira, and D. A. Weitz. Elastic behavior of cross-linked and bundled actin networks. *Science*, 304(5675):1301–1305, 2004.

[42] Qi Wen, Anindita Basu, Paul A. Janmey, and Arjun G. Yodh. Non-affine deformations in polymer hydrogels. *Soft Matter*, 8:8039–8049, 2012.

[43] Claus Heussinger and Erwin Frey. Floppy modes and nonaffine deformations in random fiber networks. *Phys. Rev. Lett.*, 97:105501, Sep 2006.

[44] H. Hatami-Marbini and R. C. Picu. Scaling of nonaffine deformation in random semiflexible fiber networks. *Phys. Rev. E*, 77:062103, Jun 2008.

[45] P. R. Onck, T. Koeman, T. van Dillen, and E. van der Giessen. Alternative explanation of stiffening in cross-linked semiflexible networks. *Phys. Rev. Lett.*, 95:178102, Oct 2005.

[46] C. P. Broedersz and F. C. MacKintosh. Modeling semiflexible polymer networks. *Rev. Mod. Phys.*, 86:995–1036, Jul 2014.

[47] Corey S. O'Hern, Leonardo E. Silbert, Andrea J. Liu, and Sidney R. Nagel. Jamming at zero temperature and zero applied stress: The epitome of disorder. *Phys. Rev. E*, 68:011306, Jul 2003.

[48] T. S. Majmudar, M. Sperl, S. Luding, and R. P. Behringer. Jamming transition in granular systems. *Phys. Rev. Lett.*, 98:058001, Jan 2007.

[49] Nicolas Brodu, Joshua A Dijksman, and Robert P Behringer. Spanning the scales of granular materials through microscopic force imaging. *Nature communications*, 6:6361, 2015.

[50] M. E. Cates, J. P. Wittmer, J.-P. Bouchaud, and P. Claudin. Jamming, force chains, and fragile matter. *Phys. Rev. Lett.*, 81:1841–1844, Aug 1998.

[51] Wouter G. Ellenbroek, Ellák Somfai, Martin van Hecke, and Wim van Saarloos. Critical scaling in linear response of frictionless granular packings near jamming. *Phys. Rev. Lett.*, 97:258001, Dec 2006.

[52] Roberto Arévalo, Iker Zuriguel, and Diego Maza. Topology of the force network in the jamming transition of an isotropically compressed granular packing. *Phys. Rev. E*, 81:041302, Apr 2010.

[53] Andrea J Liu and Sidney R Nagel. Nonlinear dynamics: Jamming is not just cool any more. *Nature*, 396(6706):21, 1998.

[54] Romain Mari, Florent Krzakala, and Jorge Kurchan. Jamming versus glass transitions. *Phys. Rev. Lett.*, 103:025701, Jul 2009.

[55] Zexin Zhang, Ning Xu, Daniel TN Chen, Peter Yunker, Ahmed M Alsayed, Kevin B Aptowicz, Piotr Habdas, Andrea J Liu, Sidney R Nagel, and Arjun G Yodh. Thermal vestige of the zero-temperature jamming transition. *Nature*, 459(7244):230, 2009.

[56] W. van Megen, T. C. Mortensen, S. R. Williams, and J. Müller. Measurement of the self-intermediate scattering function of suspensions of hard spherical particles near the glass transition. *Phys. Rev. E*, 58:6073–6085, Nov 1998.

[57] C. A. Angell, K. L. Ngai, G. B. McKenna, P. F. McMillan, and S. W. Martin. Relaxation in glassforming liquids and amorphous solids. *Journal of Applied Physics*, 88(6):3113–3157, 2000.

[58] C Austen Angell. Formation of glasses from liquids and biopolymers. *Science*, 267(5206):1924–1935, 1995.

[59] R. Busch, E. Bakke, and W.L. Johnson. Viscosity of the supercooled liquid and relaxation at the glass transition of the zr46.75ti8.25cu7.5ni10be27.5 bulk metallic glass forming alloy. *Acta Materialia*, 46(13):4725–4732, 1998.

[60] Gary L Hunter and Eric R Weeks. The physics of the colloidal glass transition. *Reports on Progress in Physics*, 75(6):066501, may 2012.

[61] Peter N Pusey and W Van Megen. Phase behaviour of concentrated suspensions of nearly hard colloidal spheres. *Nature*, 320(6060):340, 1986.

[62] PN Pusey, E Zaccarelli, C Valeriani, E Sanz, Wilson CK Poon, and Michael E Cates. Hard spheres: crystallization and glass formation. *Philosophical Transactions of the Royal Society A: Mathematical, Physical and Engineering Sciences*, 367(1909):4993–5011, 2009.

[63] Zhengdong Cheng, Jixiang Zhu, Paul M Chaikin, See-Eng Phan, and William B Russel. Nature of the divergence in low shear viscosity of colloidal hard-sphere dispersions. *Physical Review E*, 65(4):041405, 2002.

[64] T. G. Mason and D. A. Weitz. Linear viscoelasticity of colloidal hard sphere suspensions near the glass transition. *Phys. Rev. Lett.*, 75:2770–2773, Oct 1995.

[65] Hadrien Laubie, Farhang Radjai, Roland Pellenq, and Franz-Josef Ulm. Stress transmission and failure in disordered porous media. *Phys. Rev. Lett.*, 119:075501, Aug 2017.

[66] V. Chikkadi and P. Schall. Nonaffine measures of particle displacements in sheared colloidal glasses. *Phys. Rev. E*, 85:031402, Mar 2012.

[67] Robert M Jones. *Mechanics of composite materials*. CRC press, 2014.

[68] Jean-Marie Berthelot. Transverse cracking and delamination in cross-ply glass-fiber and carbon-fiber reinforced plastic laminates: static and fatigue loading. *Applied Mechanics Reviews*, 56(1):111–147, 2003.

[69] James Grierson MacGregor, James K Wight, Susanto Teng, and Paulus Irawan. *Reinforced concrete: Mechanics and design*, volume 3. Prentice Hall Upper Saddle River, NJ, 1997.

[70] Laurens Boudewijn Vogelesang and Gerardus Hubertus Joannes Joseph Roebroeks. Laminate of metal sheets and continuous glass filaments-reinforced synthetic material.

[71] Jian Ping Gong. Materials both tough and soft. *Science*, 344(6180):161–162, 2014.

[72] J.P. Gong, Y. Katsuyama, T. Kurokawa, and Y. Osada. Double-network hydrogels with extremely high mechanical strength. *Advanced Materials*, 15(14):1155–1158, 2003.

[73] Francesco Varrato, Lorenzo Di Michele, Maxim Belushkin, Nicolas Dorsaz, Simon H Nathan, Erika Eiser, and Giuseppe Foffi. Arrested demixing opens route to bigels. *Proceedings of the National Academy of Sciences*, 109(47):19155–19160, 2012.

[74] Peter Fischer and Erich J. Windhab. Rheology of food materials. *Current Opinion in Colloid & Interface Science*, 16(1):36–40, 2011.

[75] Wolf H. Rombouts, Marcel Giesbers, Jan van Lent, Frits A. de Wolf, and Jasper van der Gucht. Synergistic stiffening in double-fiber networks. *Biomacromolecules*, 15(4):1233–1239, 2014. PMID: 24580533.

[76] A. S. Shahsavari and R. C. Picu. Exceptional stiffening in composite fiber networks. *Phys. Rev. E*, 92:012401, Jul 2015.

[77] E. M. Huisman, C. Heussinger, C. Storm, and G. T. Barkema. Semiflexible filamentous composites. *Phys. Rev. Lett.*, 105:118101, Sep 2010.

[78] Mo Bai, Andrew R. Missel, William S. Klug, and Alex J. Levine. The mechanics and affine–nonaffine transition in polydisperse semiflexible networks. *Soft Matter*, 7:907–914, 2011.

[79] L. Zhang, S. P. Lake, V. H. Barocas, M. S. Shephard, and R. C. Picu. Cross-linked fiber network embedded in an elastic matrix. *Soft Matter*, 9:6398–6405, 2013.

[80] Moumita Das and F. C. MacKintosh. Mechanics of soft composites of rods in elastic gels. *Phys. Rev. E*, 84:061906, Dec 2011.

[81] Lorenzo Di Michele, Francesco Varrato, Jurij Kotar, Simon H Nathan, Giuseppe Foffi, and Erika Eiser. Multistep kinetic self-assembly of dna-coated colloids. *Nature communications*, 4:2007, 2013.

[82] Lorenzo Di Michele, D Fiocco, F Varrato, Srikanth Sastry, Erika Eiser, and Giuseppe Foffi. Aggregation dynamics, structure, and mechanical properties of bigels. *Soft matter*, 10(20):3633–3648, 2014.

[83] Himabindu Nandivada, Xuwei Jiang, and Joerg Lahann. Click chemistry: versatility and control in the hands of materials scientists. *Advanced Materials*, 19(17):2197–2208, 2007.

[84] Jacob Lubliner. *Plasticity theory*. Courier Corporation, 2008.

[85] David Chandler. Interfaces and the driving force of hydrophobic assembly. *Nature*, 437(7059):640, 2005.

[86] C NICK Pace, BRET A Shirley, M McNutt, and K Gajiwala. Forces contributing to the conformational stability of proteins. *The FASEB journal*, 10(1):75–83, 1996.

[87] Charles Tanford. *The hydrophobic effect: formation of micelles and biological membranes 2d ed*. J. Wiley., 1980.

[88] Evert Johannes Willem Verwey. Theory of the stability of lyophobic colloids. *The Journal of Physical Chemistry*, 51(3):631–636, 1947.

[89] B Derjaguin and L Landau. Theory of the stability of strongly charged lyophobic sols and of the adhesion of strongly charged particles in solutions of electrolytes. *Progress in Surface Science*, 43(1):30–59, 1993.

[90] Henk NW Lekkerkerker and Remco Tuinier. *Colloids and the depletion interaction*, volume 833. Springer, 2011.

[91] Richard M Neumann. The entropy of a single gaussian macromolecule in a noninteracting solvent. *The Journal of Chemical Physics*, 66(2):870–871, 1977.

[92] Erik Verlinde. On the origin of gravity and the laws of newton. *Journal of High Energy Physics*, 2011(4):29, Apr 2011.

[93] Philip L Taylor and Jason Tabachnik. Entropic forces—making the connection between mechanics and thermodynamics in an exactly soluble model. *European Journal of Physics*, 34(3):729–736, apr 2013.

[94] Nicholas B Tito, Costantino Creton, Cornelis Storm, and Wouter G Ellenbroek. Harnessing entropy to enhance toughness in reversibly crosslinked polymer networks. *Soft matter*, 15(10):2190–2203, 2019.

[95] Clare J. Dibble, Michael Kogan, and Michael J. Solomon. Structure and dynamics of colloidal depletion gels: Coincidence of transitions and heterogeneity. *Phys. Rev. E*, 74:041403, Oct 2006.

[96] Maria L Kilfoil, Eugene E Pashkovski, James A Masters, and DA Weitz. Dynamics of weakly aggregated colloidal particles. *Philosophical Transactions of the Royal Society of London. Series A: Mathematical, Physical and Engineering Sciences*, 361(1805):753–766, 2003.

[97] Leonardo Da Vinci. I libri di meccanica, reconstructed from the original notes by arturo uccelli. *Kraus Reprint, Nendeln, Liechtenstein*, 1972.

[98] Wei-Chun Lin, Wei Fan, Alba Marcellan, Dominique Hourdet, and Costantino Creton. Large strain and fracture properties of poly (dimethylacrylamide)/silica hybrid hydrogels. *Macromolecules*, 43(5):2554–2563, 2010.

[99] Costantino Creton and Matteo Ciccotti. Fracture and adhesion of soft materials: a review. *Reports on Progress in Physics*, 79(4):046601, 2016.

[100] L Ma and GV Barbosa-Cánovas. Rheological characterization of mayonnaise. part ii: Flow and viscoelastic properties at different oil and xanthan gum concentrations. *Journal of Food Engineering*, 25(3):409–425, 1995.

[101] A Van der Wal and RJ Gaymans. Polypropylene–rubber blends: 5. deformation mechanism during fracture. *Polymer*, 40(22):6067–6075, 1999.

[102] Stefan Münster, Louise M Jawerth, Beverly A Leslie, Jeffrey I Weitz, Ben Fabry, and David A Weitz. Strain history dependence of the nonlinear stress response of fibrin and collagen networks. *Proceedings of the National Academy of Sciences*, 110(30):12197–12202, 2013.

[103] Alan Arnold Griffith and Geoffrey Ingram Taylor. Vi. the phenomena of rupture and flow in solids. *Philosophical Transactions of the Royal Society of London. Series A, Containing Papers of a Mathematical or Physical Character*, 221(582-593):163–198, 1921.

[104] Leyou Zhang, D. Zeb Rocklin, Leonard M. Sander, and Xiaoming Mao. Fiber networks below the isostatic point: Fracture without stress concentration. *Phys. Rev. Materials*, 1:052602, Oct 2017.

[105] Michelle M. Driscoll, Bryan Gin-ge Chen, Thomas H. Beuman, Stephan Ulrich, Sidney R. Nagel, and Vincenzo Vitelli. The role of rigidity in controlling material failure. *Proceedings of the National Academy of Sciences*, 113(39):10813–10817, 2016.

[106] MK Lee and BIG Barr. An overview of the fatigue behaviour of plain and fibre reinforced concrete. *Cement and Concrete Composites*, 26(4):299–305, 2004.

[107] Mirko Klesnil and P Lukác. *Fatigue of metallic materials*, volume 71. Elsevier, 1992.

[108] Maria A Fiatarone, Elizabeth C Marks, Nancy D Ryan, Carol N Meredith, Lewis A Lipsitz, and William J Evans. High-intensity strength training in nonagenarians: effects on skeletal muscle. *Jama*, 263(22):3029–3034, 1990.

[109] D. A. Weitz and M. Oliveria. Fractal structures formed by kinetic aggregation of aqueous gold colloids. *Phys. Rev. Lett.*, 52:1433–1436, Apr 1984.

[110] Lilian C Hsiao, Michael J Solomon, Kathryn A Whitaker, and Eric M Furst. A model colloidal gel for coordinated measurements of force, structure, and rheology. *Journal of Rheology*, 58(5):1485–1504, 2014.

[111] Roseanna N. Zia, Benjamin J. Landrum, and William B. Russel. A micro-mechanical study of coarsening and rheology of colloidal gels: Cage building, cage hopping, and smoluchowski's ratchet. *Journal of Rheology*, 58(5):1121–1157, 2014.

[112] Veronique Trappe, V Prasad, Luca Cipelletti, PN Segre, and DAVID A Weitz. Jamming phase diagram for attractive particles. *Nature*, 411(6839):772, 2001.

[113] Max Born. Thermodynamics of crystals and melting. *The Journal of Chemical Physics*, 7(8):591–603, 1939.

[114] Max Born and Kun Huang. *Dynamical theory of crystal lattices*. Clarendon press, 1954.

[115] Emanuela Zaccarelli. Colloidal gels: equilibrium and non-equilibrium routes. *Journal of Physics: Condensed Matter*, 19(32):323101, 2007.

[116] Veronique Trappe and Peter Sandkühler. Colloidal gels—low-density disordered solid-like states. *Current opinion in colloid & interface science*, 8(6):494–500, 2004.

[117] AD Dinsmore and DA Weitz. Direct imaging of three-dimensional structure and topology of colloidal gels. *Journal of Physics: Condensed Matter*, 14(33):7581, 2002.

[118] A. H. Krall and D. A. Weitz. Internal dynamics and elasticity of fractal colloidal gels. *Phys. Rev. Lett.*, 80:778–781, Jan 1998.

[119] Y. Gao and M. L. Kilfoil. Direct imaging of dynamical heterogeneities near the colloid-gel transition. *Phys. Rev. Lett.*, 99:078301, Aug 2007.

[120] Luca Cipelletti, S. Manley, R. C. Ball, and D. A. Weitz. Universal aging features in the restructuring of fractal colloidal gels. *Phys. Rev. Lett.*, 84:2275–2278, Mar 2000.

[121] MY Lin, H_M Lindsay, DA Weitz, RC Ball, R Klein, and P Meakin. Universality in colloid aggregation. *Nature*, 339(6223):360, 1989.

[122] TA Witten Jr and Leonard M Sander. Diffusion-limited aggregation, a kinetic critical phenomenon. *Physical review letters*, 47(19):1400, 1981.

[123] John W Cahn. Phase separation by spinodal decomposition in isotropic systems. *The Journal of Chemical Physics*, 42(1):93–99, 1965.

[124] P. N. Segrè, V. Prasad, A. B. Schofield, and D. A. Weitz. Glasslike kinetic arrest at the colloidal-gelation transition. *Phys. Rev. Lett.*, 86:6042–6045, Jun 2001.

[125] Ruben Higler, Johannes Krausser, Jasper Van Der Gucht, Alessio Zaccone, and Joris Sprakel. Linking slow dynamics and microscopic connectivity in dense suspensions of charged colloids. *Soft matter*, 14(5):780–788, 2018.

[126] Antonio M. Puertas, Matthias Fuchs, and Michael E. Cates. Comparative simulation study of colloidal gels and glasses. *Phys. Rev. Lett.*, 88:098301, Feb 2002.

[127] Joris Sprakel, Stefan B Lindström, Thomas E Kodger, and David A Weitz. Stress enhancement in the delayed yielding of colloidal gels. *Physical review letters*, 106(24):248303, 2011.

[128] Stefan B Lindström, Thomas E Kodger, Joris Sprakel, and David A Weitz. Structures, stresses, and fluctuations in the delayed failure of colloidal gels. *Soft Matter*, 8(13):3657–3664, 2012.

Part I

Stiffness

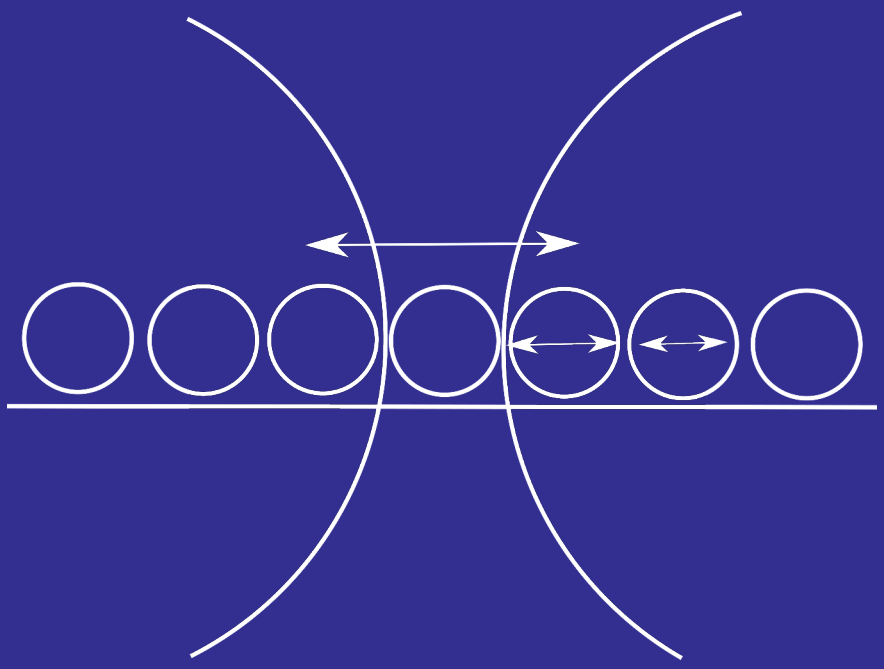

CHAPTER 2

Elastic wave propagation in ultrasoft overdamped solids

The propagation of elastic waves in soft materials plays a crucial role in the spatio-temporal transmission of mechanical signals, e.g. in biological mechanotransduction[15, 16] or in the failure of marginal solids[24, 10, 5, 9]. At high Reynolds numbers $Re \gg 1$, inertia dominates and wave propagation can be readily observed[6, 12, 19]. However, mechanical cues in soft and biological materials often occur at low Re [7], where waves are overdamped. Not only have low Re waves been difficult to observe in experiments, their theoretical description remains incomplete. In this paper, we present direct measurements of low Re waves propagating in ordered and disordered soft solids, generated by an oscillating point force induced by an optical trap. We derive an analytical theory for low Re wave propagation, which is in excellent agreement with the experiments. Our results present both a new method to characterize wave propagation in soft solids and a theoretical framework to understand how localized mechanical signals can provoke a remote and delayed response.

This chapter was submitted as:

J.M. van Doorn, R. Higler, R. Fokkink, R. Wegh,A. Zaccone, J. Sprakel and J. van der Gucht: *Infrasonic wave propagation in ultrasoft solids at low Reynolds numbers*

The spatiotemporal response to mechanical perturbations is one of the key factors that determines the fate of soft materials[4, 11]. For example, in marginally-stable systems, such as jammed packings or fiber networks, a stress at the right position can cause total loss of rigidity[24, 10, 5, 9]. Also in living cells, the propagation of mechanical signals through soft structures is crucial in mechanotransduction[15, 16], and controls, for example, cell differentiation[8]. Elastic wave propagation is a prototypic example of how a localised mechanical signal can spread in space and time, and is intimately linked to the mechanical properties of the medium[2]. However, it is governed by more complex mechanisms than the simple sum of elastic and viscous responses [23]. The complex viscoelastic response of soft materials becomes particularly apparent upon mechanical excitation at Deborah numbers $De = \omega\tau \approx 1$, where ω is the excitation frequency and τ the intrinsic relaxation time of the solid[22]. Excitation at these low frequencies also implies low Reynolds numbers where viscous attenuation of the wave signal is strong and their detection challenging. Moreover, in ultrasoft solids the relative amplitudes of thermal fluctuations are large, thus further obscuring accurate wave detection in experiments. In this Letter we show how Fourier filtering can reveal even very weak propagating elastic waves at extremely low Reynolds numbers, $Re \sim 10^{-6}$, in ultrasoft solids, formed from crystals and glasses of colloids in two dimensions. We create a localized oscillatory perturbation within these solids with an optical tweezer and use video microscopy and frequency-domain filtering to quantify the spatiotemporal strain response. On the basis of an overdamped equation of motion, which is in excellent quantitative agreement with our experimental results, this enables a full characterization of the linear mechanics of even very weak elastic solids.

We prepare two-dimensional hexagonal crystals by sedimenting monodisperse silica particles with diameter $d = 6.25\,\mu$m suspended in an aqueous solution. This yields dense crystals with long-ranged hexagonal order at a

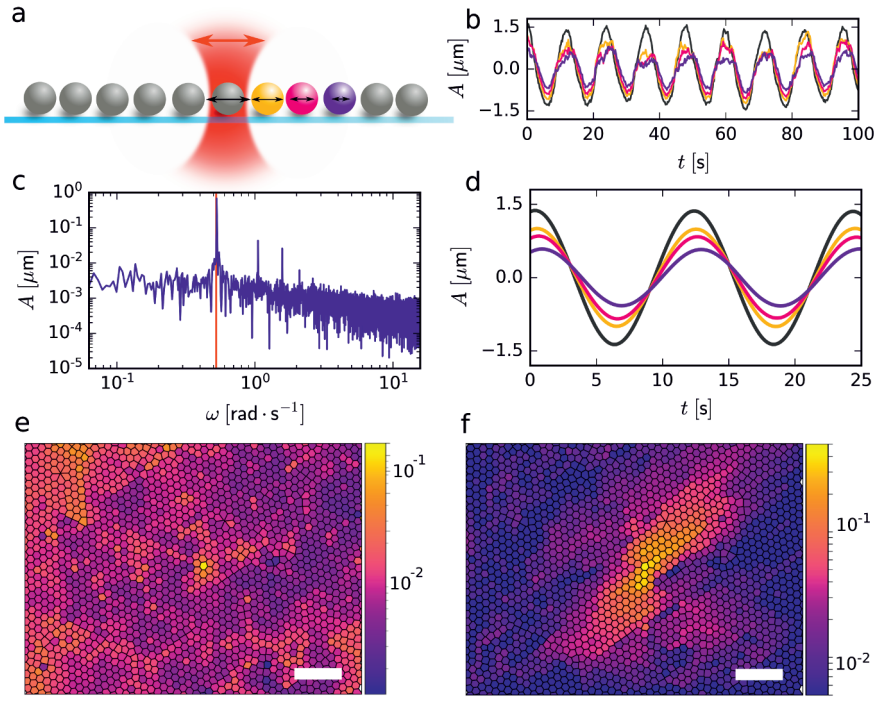

Figure 2.1: (a) Schematic overview of our experiment. (b) Raw experimental particle trajectories in the direction of the driven particle (grey), colors correspond to the particles in (a). (c) Amplitude spectrum of the driven particle, the red line corresponds to the driving frequency. (d) Trajectories of (b) after line filtering. (e) Unfiltered root-mean-square displacement and (f) Fourier-filtered amplitude map of particles in a crystal excited at 3.1 rad/s; the color scale in (e) and (f) represents the amplitude in μm, scale bars represent 40μm.

packing fraction of 0.89 (Appendix E). To create a propagating mechanical wave, we trap a single particle of the crystal in an optical trap and force it into an in-plane oscillatory motion with an amplitude of 2.5 μm (Fig.2.1a). We vary the frequency of this motion between 0.05 and 10 rad/s, corresponding to $2 < De < 2 \cdot 10^2$ and $Re \approx 3{\cdot}10^{-6}$ and confirm that this mechanical excitation is well within the linear regime (Appendix B, D).

The oscillating particle creates a mechanical wave that propagates through the surrounding material. This sets up a net ballistic displacement of the particles adjacent to the oscillating bead. However, the signal of interest is convoluted with the inherent Brownian motion of these microscopic colloids. Especially far away from the trapped colloid, where the elastic signal is attenuated, it may drown in the Brownian noise (Fig.2.1b,e). Upon filtering the positional trajectory of each particle in the frequency domain at the driving frequency (Fig.2.1c), even small displacements due to the propagating wave become apparent (Fig.2.1 d). To ensure statistical reliability of these data, we set-up a real-time distributed particle tracking algorithm that allows us to collect data during 20 000 – 35 000 frames, which is equivalent to 50–500 oscillation cycles. While the unfiltered mean-square displacement of the particles shows no apparent signature of the perturbation, except at the forced particle (Fig.2.1 e), the Fourier-filtered amplitude map clearly shows a propagating mechanical wave with an amplitude that decays steeply with increasing distance from the trapped bead (Fig.2.1 f) and a phase shift that gradually increases with distance (Fig.2.1 d).

To explain these results we assume that the colloidal crystal can be treated as a two-dimensional continuous elastic material. We write an equation of motion for the displacement field $\vec{u}$ in the solid [18] to which we add a dissipative term to account for the damping fluid and an oscillating point force $\vec{f}(t) = \vec{f_0} \cdot e^{i\omega t}$ that represents the perturbation:

$$\rho \frac{\partial^2 \vec{u}}{\partial t^2} + \gamma \frac{\partial \vec{u}}{\partial t} = \vec{f}(t) + \frac{E}{2(1+\nu)} \vec{\nabla}^2 \vec{u} + \frac{E}{2(1-\nu)} \vec{\nabla}(\vec{\nabla} \cdot \vec{u}) \qquad (2.1)$$

Here the first term describes the inertial forces with ρ the density of the 2D material. The second term represents the viscous damping due to the solvent with γ the drag coefficient per unit area, which we determine experimentally to be $\gamma = 2.9 \cdot 10^3$ Ns/m^3 (Appendix D). The last two terms correspond to the Navier-Cauchy equation that describes the elastic forces within the 2D solid with E the 2D elastic modulus and ν the Poisson ratio.

Since our experiments are performed at low Reynolds number, the inertial term is negligible, resulting in overdamped mechanics. Solving the equation of motion for this case yields the displacement field in the form $\vec{u} = \boldsymbol{\alpha} \cdot \vec{f}$ with $\boldsymbol{\alpha}$ the complex response function, which has components $\alpha_{\parallel}$ and $\alpha_{\perp}$ that describe the components of the displacement field parallel and perpendicular to the applied force, respectively. In polar coordinates, with r the distance from the point where the force is applied and $\theta = 0$ corresponding to the direction of the force, this becomes (see Appendix A for full details):

$$\alpha_{\parallel}(r,\theta) = \frac{1-\nu^2}{4\pi E}\left(K_0\Big(\frac{r\sqrt{i}}{\zeta}\Big) + \lambda^2 K_0\Big(\frac{r\sqrt{i}}{\lambda\zeta}\Big) + \cos(2\theta)\left[K_2\Big(\frac{r\sqrt{i}}{\zeta}\Big) - \lambda^2 K_2\Big(\frac{r\sqrt{i}}{\lambda\zeta}\Big)\right]\right) \quad (2.2)$$

and

$$\alpha_{\perp}(r,\theta) = \frac{1-\nu^2}{4\pi E}\sin(2\theta)\left[K_2\Big(\frac{r\sqrt{i}}{\zeta}\Big)) - \lambda^2 K_2\Big(\frac{r\sqrt{i}}{\lambda\zeta}\Big)\right] \quad (2.3)$$

where K_0 and K_2 denote modified Bessel functions of the second kind, $\zeta = (\omega\gamma(1-\nu^2)/E)^{-\frac{1}{2}}$ is a characteristic attenuation length of the displacement amplitude, and $\lambda = \sqrt{2/(1-\nu)}$ is a parameter that depends only on the Poisson ratio and diverges for $\nu \to 1$ which is the maximum Poisson ratio in 2D. The amplitude and the phase of the displacement fields are obtained as the magnitude and the argument, respectively, of the complex response functions.

To compare our experimental results with this prediction, we decompose the measured displacement amplitudes into their parallel and perpendicular components (Fig. 2.2a and e). This results in distinct lobed patterns for these two components that can be observed in all of our experiments. Our theoretical prediction produces identical patterns that are in excellent agreement, indicating that wave propagation in these colloidal crystals can indeed be described by treating the material as a continuous 2D elastic solid (Fig. 2.2b and

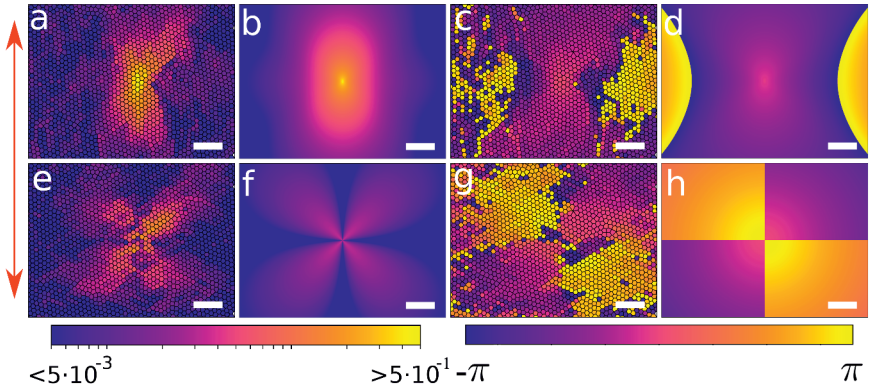

Figure 2.2: (a) Experimental amplitude map of the parallel displacement. (b) Parallel displacement amplitude predicted by our model. (c) Experimental phase shift for the parallel displacement. (d) Phase shift of parallel displacement predicted by our model.(e) Experimental map of perpendicular displacement. (f) Perpendicular displacement amplitude predicted by our model. (g) Experimental phase shift for the perpendicular displacement.(h) Phase shift of perpendicular displacement predicted by our model. Amplitudes and phases have units micron and radians respectively, scalebars represent 40μm, the red arrow indicates the oscillation direction.

f). The parallel component of the displacement response propagates preferentially along the excitation axis and shows a distinct asymmetry in the attenuation length along the two primary axes. The perpendicular displacement shows a four-lobed pattern, with maximum displacements at an angle of 45° with respect to the excitation direction. Also in the phase maps (Fig.2.2c,d), we observe patterns that are in excellent agreement with the theoretical prediction (Fig.2.2g,h).

We can now use our theoretical analysis to interpret the experimental results in terms of the linear elasticity of the solid. For this, we consider the parallel displacement component in the direction of the excitation, $\theta = 0$. An asymptotic expansion of Equation 2.2 for relatively large distances from

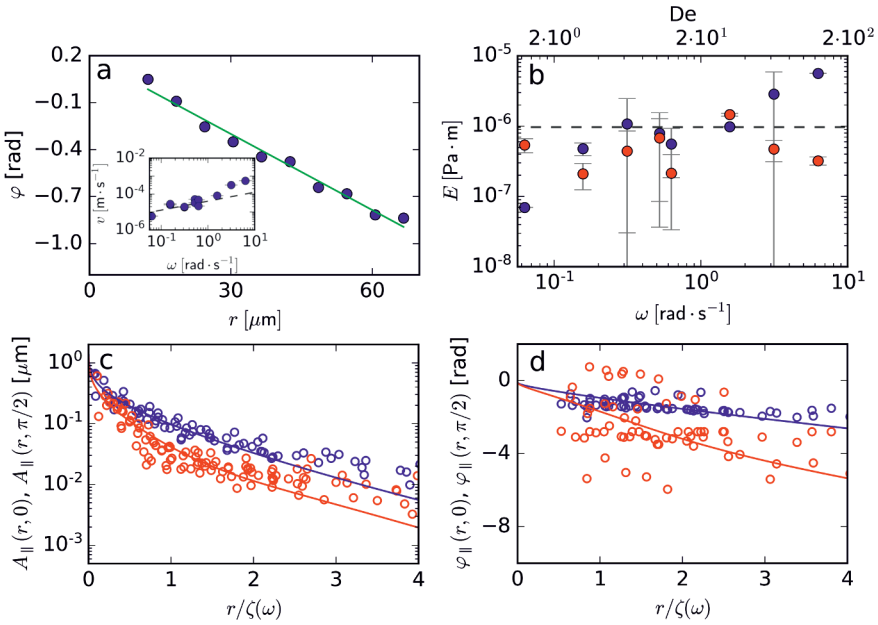

Figure 2.3: (a) Bin-averaged phase of the parallel displacement in the direction of the excitation for $\omega = 0.52$ rad/s . Inset shows the phase velocity versus probed frequency; dashed line depicts slope $\frac{1}{2}$, errorbars depict a 95% confidence interval. (b) Elastic modulus as a function of frequency, obtained from the phase (blue) and amplitude (blue) of the parallel displacement components; errorbars depict a 95% confidence interval and dashed line indicates affine prediction. (c) Superposition of parallel displacement amplitude for different frequencies along $\theta = 0$ (blue) and $\theta = \pi/2$ (red) versus normalized distance. (d) Superposition of parallel displacement phase for different frequencies along $\theta = 0$ (blue) and $\theta = \pi/2$ (red) versus normalized distance. Lines in c and d represent the theoretical predictions.

the perturbation $r > \zeta$ (see Appendix A) leads to a phase lag in the far field

$$\phi_\parallel(r,0) \approx -\frac{\pi}{8} - \frac{r}{\zeta\sqrt{2}} \tag{2.4}$$

and an amplitude

$$A_\parallel(r,0) \sim r^{-1/2} e^{-r/\zeta\sqrt{2}} \tag{2.5}$$

According to Equation 2.4, the phase varies linearly with r along $\theta = 0$, which

is indeed what we find experimentally (Fig. 2.3a). This means that the wave propagates at a constant velocity in the direction of the excitation, with a phase velocity $v_{\parallel} = |\omega(d\phi_{\parallel}/dr)^{-1}| \approx \omega\zeta\sqrt{2} = \sqrt{2E\omega/\gamma(1-\nu)^2}$. As shown in the inset of Fig. 2.3a, the phase velocity increases approximately as $v_{\parallel} \sim \sqrt{\omega}$ for low frequencies, which indicates that the elastic modulus and the Poisson ratio do not depend on the frequency in this regime. Using Equations 2.4 and 2.5 we can determine the characteristic length ζ as a function of frequency in two independent ways. Taking a value of the Poisson ratio $\nu = 0.5$ (see below), we can then estimate the elastic modulus of the colloidal crystal. Both the phase and amplitude data give moduli in the range $E \approx 10^{-6}$ N/m (Fig. 2.3b). These values for E may be compared with a simple estimate obtained by approximating the colloidal crystal as a hexagonal lattice of harmonic springs, for which $E = 2k/\sqrt{3}$ with k the spring constant of a particle pair [3]. We estimate k by analyzing the thermal bond length fluctuations (Appendix C) and find $E \approx 1 \cdot 10^{-6}$ N/m in very good agreement with the experimental values (dashed line in Fig. 2.3b).

We note that our method is limited at higher frequencies by the decrease in the attenuation length with increasing frequency. Once the characteristic length ζ becomes of the order of the particle size, discretization effects hinder the accurate determination of the wave propagation. This gives a limiting frequency $\omega_{max} \approx E/\gamma d^2 \approx 10$ rad/s.

The linear elasticity of a two-dimensional solid is described by two independent mechanical parameters, the elastic modulus and the Poisson ratio. While the modulus only affects the absolute magnitude of the response function and the characteristic length scale ζ, the shape of the spatial pattern is uniquely determined by the Poisson ratio, as expressed by the parameter λ in Equation 2.2 (SI Fig. 26). It should therefore be possible to superimpose the measured displacement data obtained at different frequencies by normalizing the distance r by the characteristic length ζ. Figure 2.3c and d show such a collapse for the amplitude and the phase, respectively, of the parallel displace-

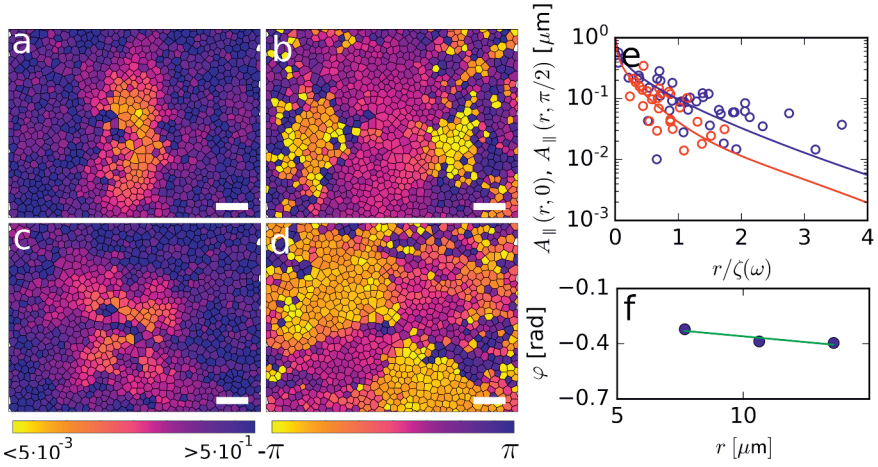

Figure 2.4: Experimental maps of (a) parallel displacement amplitude, (b) parallel displacement phase, (c) perpendicular displacement amplitude, and (d) perpendicular displacement phase of 2D colloidal glasses excited at $\omega = 0.52$ rad/s. Amplitudes and phases have units micron and radians respectively, scalebars represent 20μm. (e) Superposition of parallel displacement amplitude of colloidal glasses for different frequencies along $\theta = 0$ (blue) and $\theta = \pi/2$ (red) versus normalized distance, together with theoretical prediction. (g) Bin-averaged phase-distance plot to determine phase velocity for $\omega = 0.52$ rad/s in the parallel direction.

ment components in the direction of the excitation ($\theta = 0$) and perpendicular to it ($\theta = \pi/2$). We fit these curves to equation 2.2, using $\lambda = \sqrt{2/(1-\nu)}$ as the only fit parameter, giving a value for the Poisson ratio $\nu = 0.5$, comparable to values expected for crystalline solids in two dimensions [13, 21]. It should be noted, however, that the profiles do not depend very sensitively on ν, so that our determination of the Poisson ratio is not very precise. As a final consistency check, we use the measured Youngs modulus and Poission ratio to predict the absolute values of the response functions, which now provide a reasonable quantitative match with the experimental results [Fig. 2.2 a-i]. This highlights that our theoretical description captures the main phenomena in a quantitative fashion.

Finally, to emphasize that our approach is not exclusive to ordered, crystalline, solids, we repeat the experiments described above for a disordered colloidal glass that lacks long-ranged order[26, 14]. We prepare monolayers of a bi-disperse mixture (d=6.25 and 3.75 μm) of silica spheres by sedimentation. We confirm the absence of structural order from the liquid-like shape of the pair-correlation function and structure factor, while the particle dynamics are strongly arrested and caged as evidenced from their mean-squared displacement in the absence of external mechanical excitation (Appendix F). Despite the very different microstructure, we find that the displacement amplitude and phase patterns are very similar to those observed for the crystals (Fig.2.4 a-d). The same analysis (Fig. 2.4e,f) as for the crystals gives a Poisson ratio on the order of 0.5 and an elastic modulus on the order of $2 \cdot 10^{-7}$ N/m for the glasses. This is roughly a factor of three lower than for the crystals, which we attribute to non-affine softening due to the amorphous nature of glass[27]. This highlights that the observation of mechanical waves at low Re open up the way for mechanical characterization of both ordered and disordered ultra-weak solids where conventional approaches fail. From Fig. 2.4a-d it is also clear that the wave patterns are noisier for the glasses than for the crystals, which is probably due to their inhomogeneous structure, and therefore also inhomogeneous mechanical properties. This clearly shows how elastic wave propagation is affected by the structure of the medium. We note that this is not yet captured by the theory, which assumes a homogeneous elasticity.

Traditionally, microrheology is the method of choice to characterize the visco-elasticity of very weak elastic materials whose moduli are below the detection limit of conventional macroscopic rheometers. In microrheology, the visco-elastic features of the material are extracted from the motion of either actively-driven or thermally-excited (passive) tracer particles embedded in the material [20, 17]. This analysis is based on the assumption that the generalized Stokes-Einstein relation holds, which is only the case when

the characteristic length scale of the material is much smaller than the probe particles. In particular for very inhomogeneous soft solids, this condition is often not met. As our approach is not bound by these limitations, the study of mechanical wave propagation at low Re provides experimental access to the mechanical properties of extremely weak and strongly heterogeneous systems, such as marginal solids close to a mechanical critical point [25, 5].

In this paper we have shown how propagating elastic waves can be generated and detected at low Re in ultrasoft solids, both ordered and disordered. Moreover, we have proposed an analytical model to describe and interpret the wave propagation, which is in excellent quantitative agreement with our experimental results. On the basis of this theory, a measurement of the wave's phase velocity and decay length gives access to the full linear elasticity of the material, giving values in excellent agreement with lattice theory predictions. In principle, our approach can be extended to probe the mechanics of ultrasoft three-dimensional materials such a biopolymer networks, where the Fourier-filtered elastic displacements can be obtained e.g. by embedding tracer particles in the material or by using digital image correlation approaches. This could open the way to characterize how localised mechanical signals acting on biological structures give rise to the complex spatio-temporal response that underlies mechanical communication in living organisms and on the role of local structures on the response of marginal networks.

Materials and Methods

We use a home-built optical tweezers setup equipped with a high-power 1064 nm laser and a water-immersion objective (Nikon, CFI Plan Apo IR SR 60X WI, NA=1.27). Oscillation of the optical trap is achieved by beam steering with Acoustic Optical Deflectors (AODs). The intensity of the deflected beam deviates with position and therefore influences the trapping force. We mea-

sure this effect and correct for it by modulating the intensity of the beam that is transmitted through the AODs. A full description of this calibration together with an in-depth overview of our optical setup can be found in chapter 3. We prepare our 2D colloidal solids by sedimenting monodisperse silica particles (microParticles GmbH) with $d = 6.25\mu$m and $d = 3.75\mu$m dispersed in a 10 mM TAPS buffer at pH = 8.5. After equilibrating the samples for 48h for crystals and 96h for glasses we start an experiment by trapping the particle in the center of the field of view. We apply an oscillating point force by oscillating the trapped bead with the optical trap. The resulting response of the surrounding material is quantified by imaging the colloidal solid with bright-field microscopy and recovering the particle trajectories using established routines. We measure with a frame rate of 5 Hz for at least 20 000 frames. We locate particles in real-time during the experiment to improve data size manageability. To this end, we combine existing locating algorithms with a distributed messaging protocol ZMQ[1]. This approach enables to distribute the computational load of particle locating over several computers, enabling real-time acquisition of the experimental particle positions in time[15, 16, 8].

Appendix A: Theory

We apply a point deformation to a 2D material with a force $\vec{f}(t) = \vec{f_0} \cdot e^{i\omega t}$ which gives the equation of motion

$$\rho \frac{\partial^2 \vec{u}}{\partial t^2} + \underbrace{\gamma \frac{\partial \vec{u}}{\partial t}}_{\text{Viscous drag}} = \vec{f} + \overbrace{\mu \vec{\nabla}^2 \vec{u} + (\lambda + \mu)\vec{\nabla}(\vec{\nabla} \cdot \vec{u})}^{\text{Navier-Cauchy}} \tag{2.6}$$

with γ the friction coefficient per unit volume and μ, λ the 2D Lamé coefficients

$$\mu = \frac{E}{2(1+\nu)} \tag{2.7}$$

and

$$\lambda = \frac{\nu E}{(1+\nu)(1-2\nu)} = \frac{2\nu\mu}{1-\nu} \tag{2.8}$$

where E and ν are the 2D Youngs modulus and the Poisson ratio, respectively. Equation 2.6 yields a solution for the resulting displacement $\vec{u}(t) = \vec{u} \cdot e^{i\omega t}$ with $\vec{u}$ complex if there is a phase-shift with respect to the imposed force $\vec{f}(t)$. Fourier transforming the time-dependend part of equation 2.6 gives

$$-\rho\omega^2 \vec{u} + i\omega\gamma\vec{u} = \mu\nabla^2\vec{u} + (\lambda+\mu)\nabla(\nabla \cdot \vec{u}) + f_0 \tag{2.9}$$

or

$$\mu\nabla^2\vec{u} + (\lambda+\mu)\nabla(\nabla \cdot \vec{u}) + f_0 + A\vec{u} = 0 \tag{2.10}$$

with $A = \rho\omega^2 - i\omega\gamma$. Writing in components gives

$$\Big[\mu\Big[\frac{\partial^2 u_x}{\partial x^2} + \frac{\partial^2 u_x}{\partial y^2}\Big] + (\lambda+\mu)\frac{\partial}{\partial x}\Big[\frac{\partial u_x}{\partial x} + \frac{\partial u_y}{\partial y}\Big]\Big] + Au_x + f_{x0} = 0 \tag{2.11}$$

and

$$\Big[\mu\Big[\frac{\partial^2 u_y}{\partial x^2} + \frac{\partial^2 u_y}{\partial y^2}\Big] + (\lambda+\mu)\frac{\partial}{\partial y}\Big[\frac{\partial u_x}{\partial x} + \frac{\partial u_y}{\partial y}\Big]\Big] + Au_y + f_{y0} = 0 \tag{2.12}$$

Fourier transforming the spatially dependent part yields

$$\mu[-k_x^2\tilde{u}_x - k_y^2\tilde{u}_x] + (\lambda+\mu)[-k_x^2\tilde{u}_x - k_xk_y\tilde{u}_y] + A\tilde{u_x} + \tilde{f_{x0}} = 0 \tag{2.13}$$

and

$$\mu[-k_x^2\tilde{u}_y - k_y^2\tilde{u}_y] + (\lambda+\mu)[-k_xk_y\tilde{u}_x - k_y^2\tilde{u}_y] + A\tilde{u_y} + \tilde{f_{y0}} = 0 \quad (2.14)$$

Assuming overdamped mechanics $A = \rho\omega^2 - i\omega\gamma \approx -i\omega\gamma$ and rewriting gives

$$\mu\Big[\vec{k}^2\tilde{u}_x + \frac{1+\nu}{1-\nu}k_x^2\tilde{u}_x + \frac{i\omega\gamma}{\mu}\tilde{u}_x + \frac{1+\nu}{1-\nu}k_xk_y\tilde{u}_y\Big] = f_x \quad (2.15)$$

and

$$\mu\Big[\vec{k}^2\tilde{u}_y + \frac{1+\nu}{1-\nu}k_x^2\tilde{u}_y + \frac{i\omega\gamma}{\mu}\tilde{u}_y + \frac{1+\nu}{1-\nu}k_xk_y\tilde{u}_x\Big] = f_y \quad (2.16)$$

which corresponds to

$$\vec{f} = \mu\begin{pmatrix} \vec{k}^2 + \frac{1+\nu}{1-\nu}k_x^2 + \frac{i\omega\gamma}{\mu} & k_xk_y\frac{1+\nu}{1-\nu} \\ k_xk_y\frac{1+\nu}{1-\nu} & \vec{k}^2 + \frac{1+\nu}{1-\nu}k_y^2 + \frac{i\omega\gamma}{\mu}\end{pmatrix}\tilde{\vec{u}} \quad (2.17)$$

Inverting gives

$$\tilde{\vec{u}} = \frac{1}{\mu(\vec{k}^2 + \frac{i\omega\gamma}{\mu})(\frac{2}{1-v}\vec{k}^2 + \frac{i\omega\gamma}{\mu})}\begin{pmatrix} \vec{k}^2 + \frac{1+\nu}{1-\nu}k_y^2 + \frac{i\omega\gamma}{\mu} & -k_xk_y\frac{1+\nu}{1-\nu} \\ -k_xk_y\frac{1+\nu}{1-\nu} & \vec{k}^2 + \frac{1+\nu}{1-\nu}k_x^2 + \frac{i\omega\gamma}{\mu}\end{pmatrix}\vec{f} \quad (2.18)$$

which has the form $\tilde{\vec{u}} = \tilde{\alpha}\vec{f}\delta(\vec{r})$. The complex response function α is obtained as the inverse Fourier transform and has a perpendicular component

$$\alpha_\perp = \mathcal{F}^{-1}\Big[-\frac{1}{\mu}\frac{1+\nu}{2}\frac{k_xk_y}{(k^2 + \frac{i\omega\gamma}{\mu})(k^2 + \frac{i\omega\gamma}{\mu}\cdot\frac{1-\nu}{2})}\Big] \quad (2.19)$$

and a parallel component

$$\alpha_\parallel = \frac{1}{\mu}\mathcal{F}^{-1}\Big[\frac{1}{\frac{2}{1-\nu}\cdot k^2 + \frac{i\omega\gamma}{\mu}} + \frac{\frac{1+\nu}{1-\nu}\cdot k_y^2}{(k^2 + \frac{i\omega\gamma}{\mu})(\frac{2}{1-\nu}k^2 + \frac{i\omega\gamma}{\mu})}\Big] \quad (2.20)$$

where $\mathcal{F}^{-1}$ indicates the inverse Fourier transform,

$$\mathcal{F}^{-1}\Big[\tilde{X}(\vec{k})\Big] = \frac{1}{(2\pi)^2}\int_{-\infty}^{\infty}\int_{-\infty}^{\infty}\tilde{X}e^{i\vec{k}\cdot\vec{r}}\mathrm{d}k_x\mathrm{d}k_y \quad (2.21)$$

The integrals can be evaluated by transforming to polar coordinates, which leads to

$$\alpha_{\parallel}(r,\theta) = \frac{1-\nu^2}{4\pi E}\left(K_0\Big(\frac{r\sqrt{i}}{\zeta}\Big) + \lambda^2 K_0\Big(\frac{r\sqrt{i}}{\lambda\zeta}\Big) + \cos(2\theta)\left[K_2\Big(\frac{r\sqrt{i}}{\zeta}\Big) - \lambda^2 K_2\Big(\frac{r\sqrt{i}}{\lambda\zeta}\Big)\right]\right) \quad (2.22)$$

and

$$\alpha_{\perp}(r,\theta) = \frac{1-\nu^2}{4\pi E}\sin(2\theta)\left[K_2\Big(\frac{r\sqrt{i}}{\zeta}\Big)) - \lambda^2 K_2\Big(\frac{r\sqrt{i}}{\lambda\zeta}\Big)\right] \quad (2.23)$$

(equations 2 and 3 in the main text). Here K_0 and K_2 denote modified Bessel functions of the second kind, $\zeta = (\omega\gamma(1-\nu^2)/E)^{-\frac{1}{2}}$ is a characteristic attenuation length of the displacement amplitude, and $\lambda = \sqrt{2/(1-\nu)}$ is a parameter that depends only on the Poisson ratio.

For the parallel displacement in the direction $\theta = 0$ we find from Equation 2.22

$$\alpha_{\parallel}(r,0) = \frac{1-\nu^2}{4\pi E}\left(K_0\Big(\frac{r\sqrt{i}}{\zeta}\Big) + K_2\Big(\frac{r\sqrt{i}}{\zeta}\Big)\right) \quad (2.24)$$

For large $r \gg \zeta$ this can be expanded by using the approximation $K_n(z) \approx \sqrt{\frac{\pi}{2z}}e^{-z}$. In our case z has the form $a\sqrt{i}$, with $a = r/\zeta$, so for $a \gg 1$

$$K_n(a\sqrt{i}) \approx \sqrt{\frac{\pi}{2a}} \cdot i^{-\frac{1}{4}} \cdot e^{-a\sqrt{i}} \quad (2.25)$$

With $i^{\frac{1}{4}} = e^{-\frac{\pi i}{8}}$ and $\sqrt{i} = e^{i\pi/4} = (1+i)/\sqrt{2}$ we obtain

$$K_n(a\sqrt{i}) \approx \sqrt{\frac{\pi}{2a}} \cdot e^{-\frac{\pi i}{8} - \frac{1}{\sqrt{2}}\cdot a\cdot(1+i)} = \sqrt{\frac{\pi}{2a}} \cdot e^{-\frac{a}{\sqrt{2}} - i(\frac{\pi}{8} + \frac{a}{\sqrt{2}})} \quad (2.26)$$

so that

$$\alpha_{\parallel}(r,0) \approx \frac{1-\nu^2}{2\sqrt{2\pi}E}\sqrt{\frac{\zeta}{r}} \cdot \exp\left(-\frac{r}{\sqrt{2}\zeta} - i(\frac{\pi}{8} + \frac{r}{\sqrt{2}\zeta})\right) \quad (2.27)$$

and

$$\phi_{\parallel}(r,0) = \mathrm{Arg}\left(\alpha_{\parallel}(r,0)\right) \approx -\frac{\pi}{8} - \frac{r}{\zeta\sqrt{2}} \tag{2.28}$$

and

$$A_{\parallel}(r,0) = \left|\alpha_{\parallel}(r,0)\right| \sim r^{-1/2} e^{-r/\zeta\sqrt{2}} \tag{2.29}$$

Appendix B: Plasticity analysis

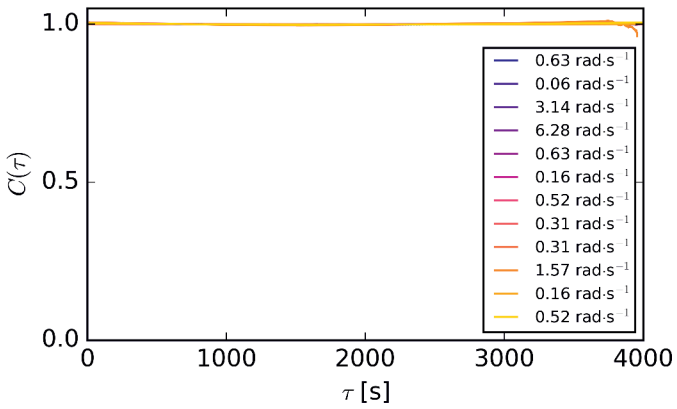

Figure 2.5: Plasticity analysis for all measured frequencies. $C(\tau)$ remains 1.0 during experimental timescales which indicates that no irreversible rearrangements are occurring and we are measuring in the linear elastic regime.

Mechanical excitation with a too large amplitude could lead to irreversible rearrangements of the colloids within the monolayers. In this case we are no longer measuring in the linear regime. To ensure that linear elasticity applies during all our experiments, we test for irreversible rearrangements by calculating the autocorrelation of the particles equilibrium position $r_{eq}(t) = r(t) - \langle r(t)\rangle_t$:

$$C(\tau) = \frac{\langle r_{eq}(t+\tau)\cdot r_{eq}(t)\rangle}{\langle r_{eq}(t)\rangle^2} \tag{2.30}$$

We find hardly any decorrelation which confirms that no irreversible rearrangements occur and we are performing our experiments in the linear elastic limit (Fig. 2.5).

Appendix C: Spring constant determination

To make a prediction for the appropriate moduli of our samples based on a simple lattice model, we estimate the inter-particle spring constant. For this we make a histogram of inter-particle distance fluctuations $R_{ij}(t) = |\vec{r}_i(t) - \vec{r}_j(t)|$ (Fig 2.6). We normalize the histogram and apply a Boltzmann distribution $U(x) = -k_B T \log(F(x))$,with U the potential of mean force in [J] and $F(x)$ the frequency of the histogram, to obtain a measure for the inter particle potential of mean force (Fig. 2.7). While the potential of mean force is not symmetric around the minimum, we extract the linear spring constant by considering only the region around the minimum, where we fit a harmonic potential $U(x) - U_{min} = \frac{1}{2}\kappa x^2$, with κ representing the effective spring constant and sole adjustable parameter (Fig. 2.8). We repeat this for about 1000 particle pairs and average the resulting κ, giving $\kappa = 4 \times 10^{-6}$ N/m. To convert the potential of mean force into the inter-particle potential, we must average over the interactions with the surrounding particles. We do this in an approximate way assuming that the potential of mean force can be built up by linear superposition of pair-wise contributions with all neighbours. Averaging over the different angles then gives a spring constant for a single particle-pair $k = 0.25\kappa \approx 1 \cdot 10^{-6}$ N/m. The 2D Young's modulus of a hexagonal spring network is then $E = 2k/\sqrt{3} \approx 1 \cdot 10^{-6}$ N/m.

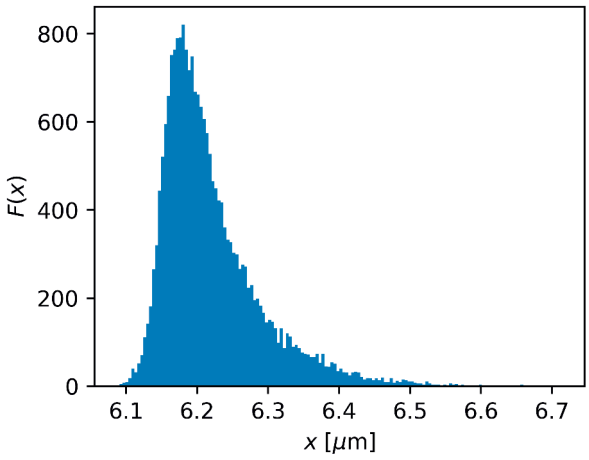

Figure 2.6: Example of a histogram of inter-particle distances between neighbouring particles in our colloidal crystal sample.

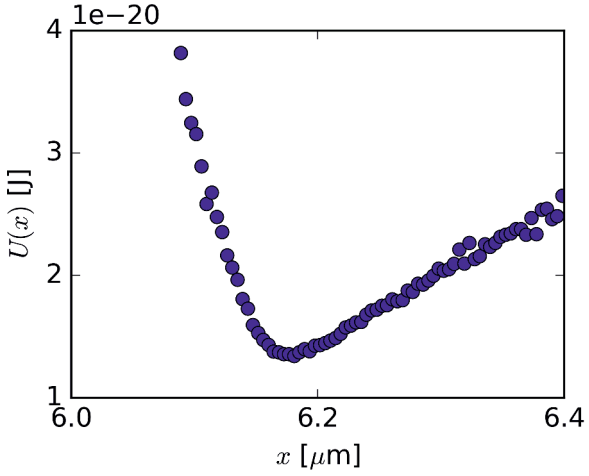

Figure 2.7: Example of a potential of mean force, reconstructed with the Boltzmann equation and the histogram in figure 2.6.

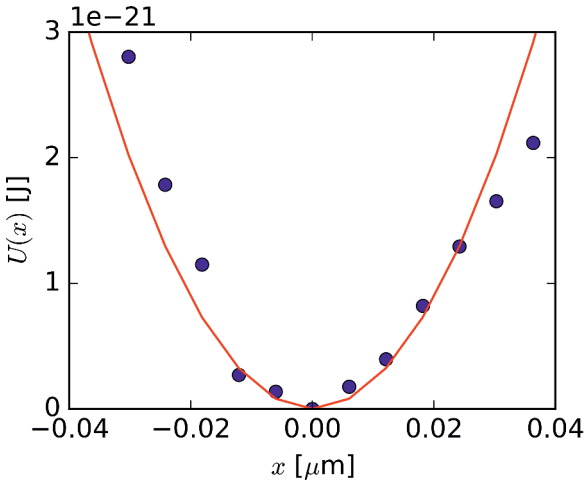

Figure 2.8: Example of a fit (*red*) of a harmonic potential to the harmonic part of our measured pair potential in our colloidal crystal sample (*blue circles*). The effective potential of mean force spring constant determined by this fit is $\kappa = 2 \cdot 10^{-6}$ N/m.

Appendix D: Determination of friction coefficient γ, Reynolds number Re and Deborah number De

We experimentally determine the two-dimensional friction coefficient ξ by tracking a dilute suspension of silica beads over time. We calculate their ensemble-averaged 2D mean squared displacement (Fig. 2.9). Using $\langle r^2 \rangle = 4D\tau$ we find $D \approx 9.0 \times 10^{-14}$ m^{2}s^{-1}. With the Einstein equation, $D = k_B T/\xi$, we find $\xi = 4.6 \times 10^{-8}$ Ns/m. In our continuum description of the material, we need the friction per unit area γ, which we estimate as $\gamma \approx \xi/d^2$ with d the particle diameter; this gives $\gamma \approx 2.9 \cdot 10^3$ Ns/m^3.

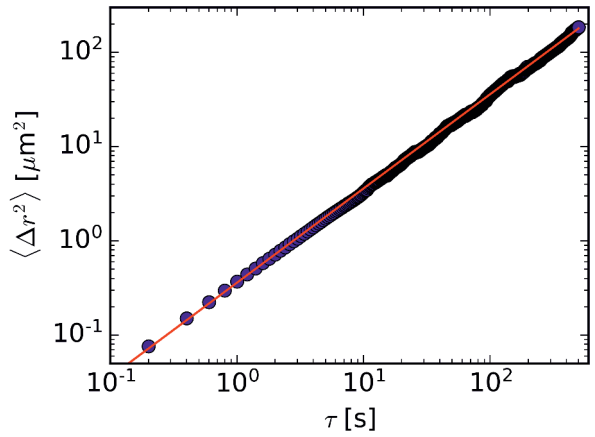

Figure 2.9: Linear fit (*red*) to the mean square displacement curve of dilute particles sedimented on the glass surface of the cover slip (*blue circles*).

We estimate the Reynolds number in our experiment, $Re = \rho v L/\eta$ by taking the maximum velocity of the probe particle $v = \omega A$ with A the amplitude of the oscillation, and ρ and η the density and viscosity of the medium. This gives, with $A = 2$ μm for the highest frequency $Re \approx 4 \times 10^{-6}$. Since $Re \ll 1$, our experiments are in the overdamped regime.

The Deborah number $De = \omega\tau$ with ω the angular frequency of our mechanical excitation and τ the intrinsic relaxation time in the solid set by the self-diffusion time of the particles. We estimate $\tau \approx 16s$ and with our excitation frequency range find that during our experiments $2 < De < 2 \cdot 10^2$.

Appendix E: Dynamic and structural characterization of crystals

We investigate the dynamics and structure of our experimental system to confirm that we are indeed looking at colloidal crystals. Crystals are characterized by long-ranged order and arrested dynamics. As a measure for the dynamics we measure the Mean Squared Displacement (MSD) (Fig. 2.10). At short τ we observe a localization plateau which highlights the arrested dynamics that are typical for colloidal crystals.

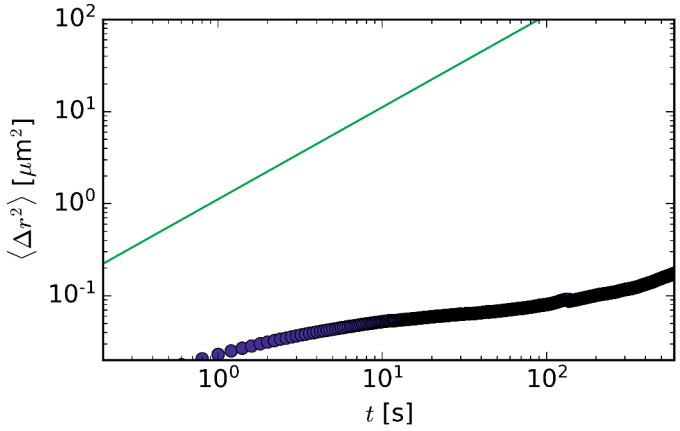

Figure 2.10: MSD (*blue circles*) for a colloidal crystal that is not mechanically excited. The green line represents a slope equal to one.

Figure 2.11 shows a microscopy image of the colloidal crystal, clearly showing the hexagonal ordering of the particles. The packing fraction is estimated from the number of particles per unit area and the particle diameter, giving a packing fraction of 0.89. We further confirm the presence of long-ranged order by obtaining the pair-correlation function $g(r)$ from the microscopy images, which is in excellent agreement with the $g(r)$ expected for a two-dimensional hexagonal packed crystal (Fig 2.12). In addition we calculate the two dimensional structure factor $S(q_x, q_y)$, which shows discrete peaks in a six-fold symmetry at fixed distances from the origin and each other (Fig 2.13). Even at large q_x and q_y we see discrete peaks, which confirms the presence of long-ranged order in our system.

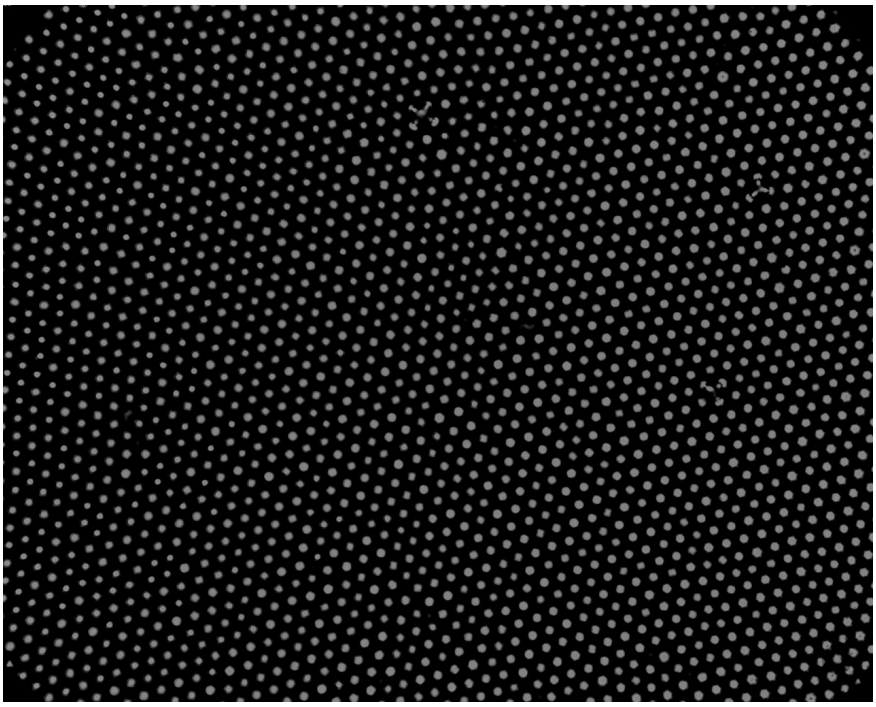

Figure 2.11: Microscopy image of our colloidal crystal sample

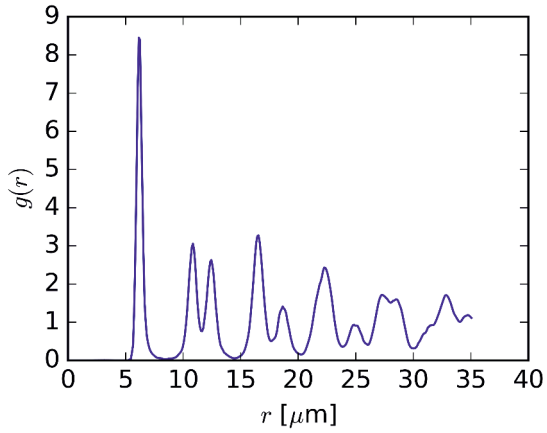

Figure 2.12: Pair-correlation function for the colloidal crystal sample

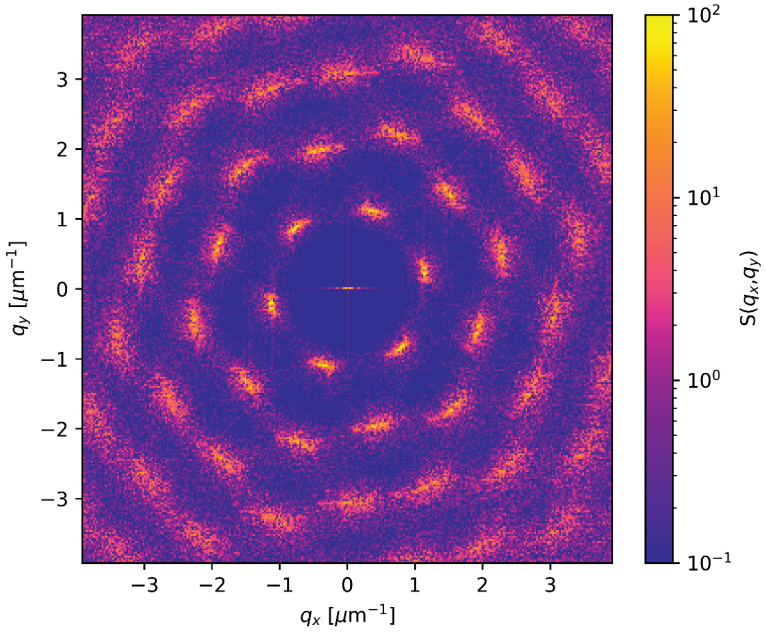

Figure 2.13: Two dimensional structure factor for the colloidal crystal samples

Appendix F: Dynamic and structural characterization of colloidal glasses

Colloidal glasses are characterized by arrested dynamics while having a disordered liquid-like structure. To confirm that we indeed have arrested dynamics, we measure the mean squared displacement curves for our colloidal glass samples (Figures 2.14,2.15 and 2.16). As we prepare our glass samples with a bidisperse mixture of particles we show separate curves for the dynamics of both large and small particles and for the combined dynamics. All MSD curves show a localization plateau for intermediate τ that indicates arrested dynamics for all types of particles. The upturn for large τ might be due to long-wavelength fluctuations in the sample or to cage-breaking events that are typical for colloidal glasses. Figure 2.17 shows a microscopy image of the colloidal glass, showing no apparent ordering. Indeed, in contrast to our crystalline samples, the pair-correlation functions for the glasses show a liquid-like structure that highlights the disordered nature of our glasses (Figures 2.18,2.19 and 2.20). Furthermore the two-dimensional structure factors show no distinct dots and are isotropic, indicating that we have no long-ranged order in these systems (Figures 2.21,2.22 and 2.23).

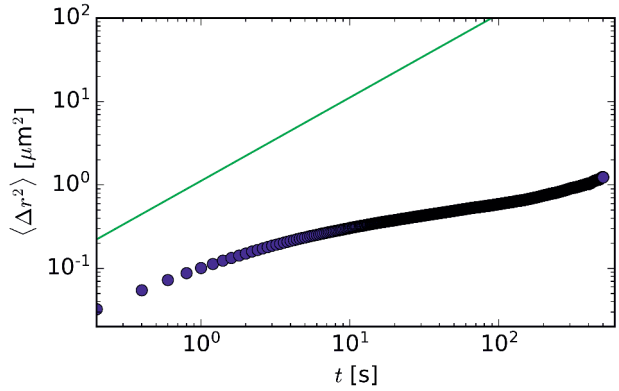

Figure 2.14: MSD (*blue circles*) for the small and large particles in a colloidal glass that is not mechanically excited. The green line represents a slope equal to one.

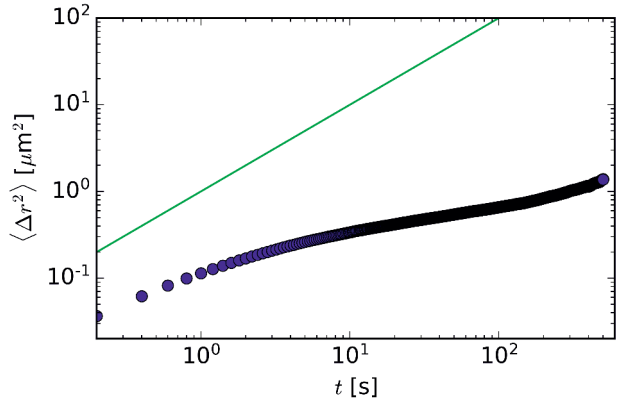

Figure 2.15: MSD (*blue circles*) for the small particles in a colloidal glass that is not mechanically excited. The green line represents a slope equal to one.

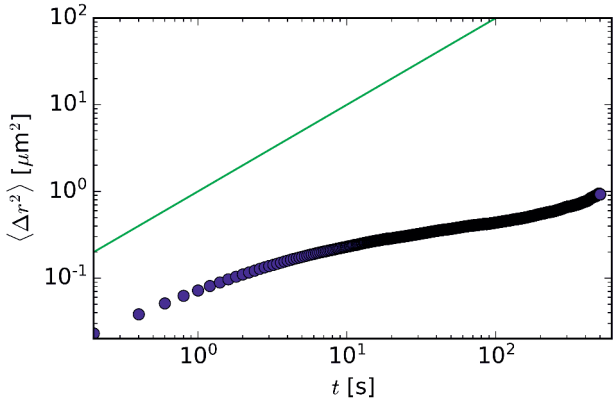

Figure 2.16: MSD (*blue circles*) for the large particles in a colloidal glass that is not mechanically excited. The green line represents a slope equal to one.

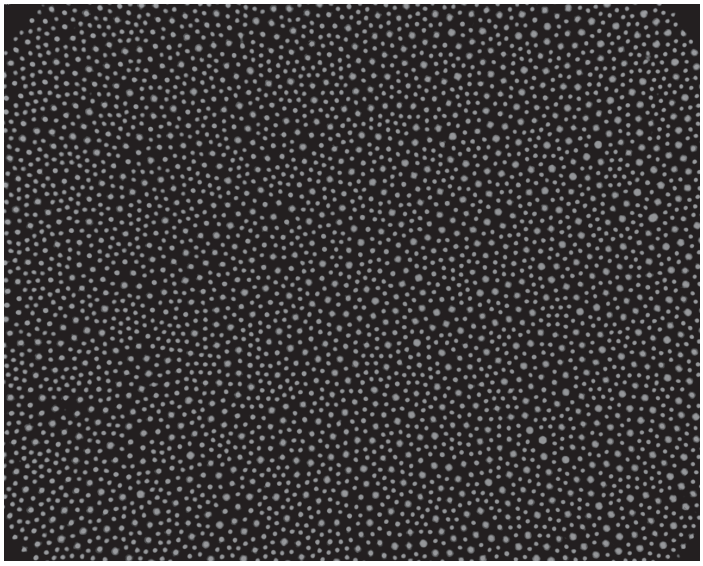

Figure 2.17: Microscopy image of our colloidal glass sample

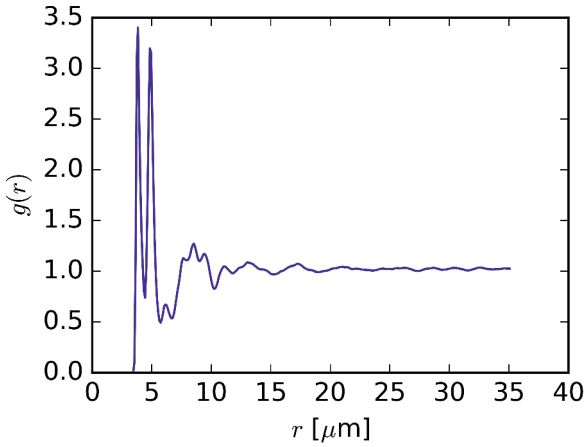

Figure 2.18: Pair-correlation function for large and small particles in the colloidal glass samples

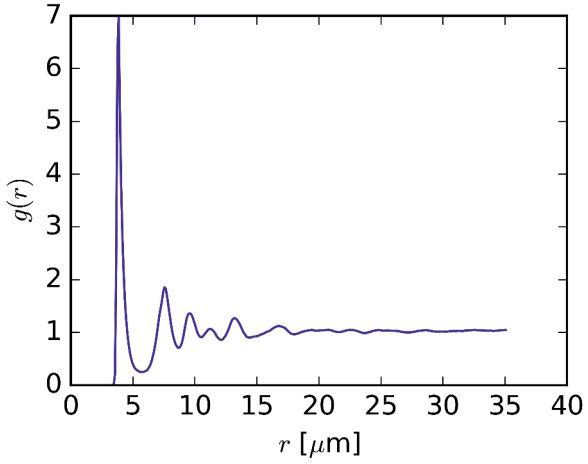

Figure 2.19: Pair-correlation function for the small particles in the colloidal glass samples

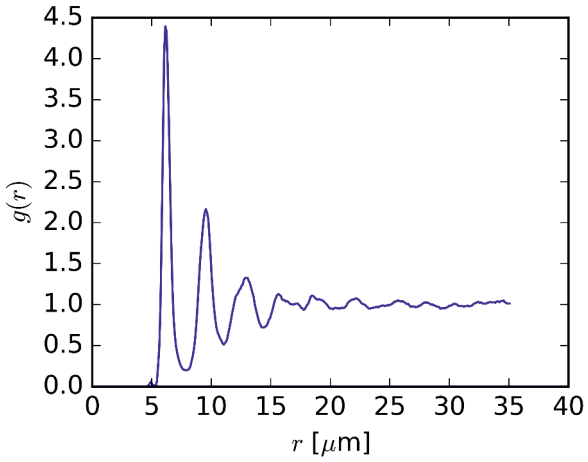

Figure 2.20: Pair-correlation function for the large particles in the colloidal glass samples

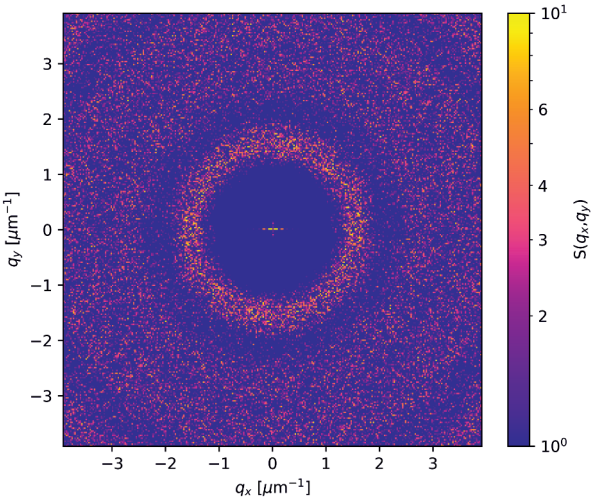

Figure 2.21: Two dimensional structure factor for large and small particles in the colloidal glass samples

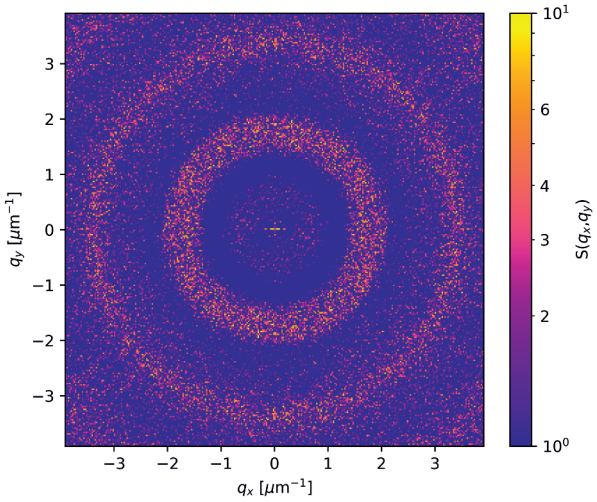

Figure 2.22: Two dimensional structure factor for the small particles in the colloidal glass samples

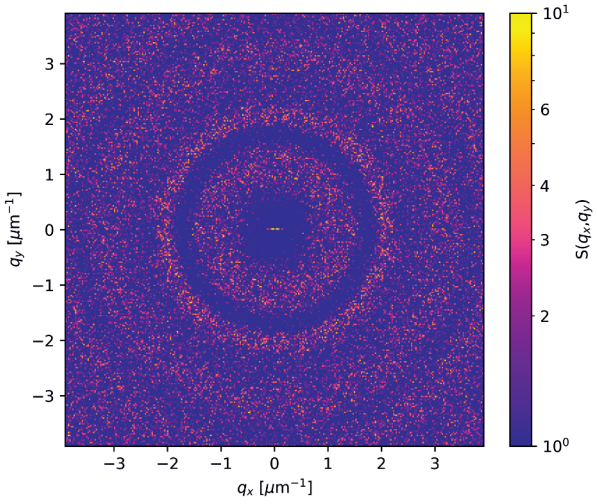

Figure 2.23: Two dimensional structure factor for the large particles in the colloidal glass samples

Appendix G: Effect of the Poisson ratio

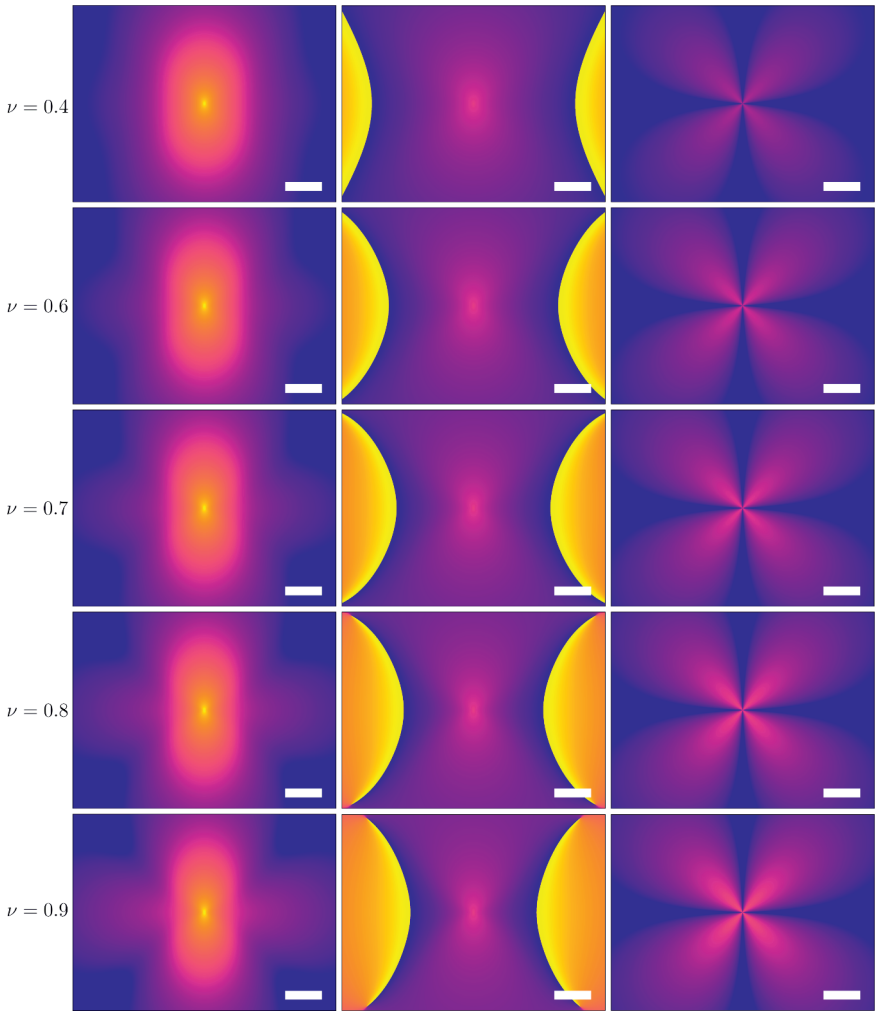

Figure 2.24: Amplitude and phase patterns for varying Poisson factors. From left to right the columns represent the amplitude of the parallel displacement component, the phase of the parallel displacement component, and the amplitude of the perpendicular displacement component, respectively. The perpendicular phase pattern is not affected by the Poisson ratio. Scalebar represents 40 μm.

Bibliography

[1] Daniel B. Allan, Thomas Caswell, Nathan C. Keim, and Casper M. van der Wel. trackpy: Trackpy v0.4, April 2018.

[2] Bertram Alexander Auld. *Acoustic fields and waves in solids*. , 1973.

[3] David Boal. *Mechanics of the Cell*. Cambridge University Press, 2 edition, 2012.

[4] Lydéric Bocquet, Annie Colin, and Armand Ajdari. Kinetic theory of plastic flow in soft glassy materials. *Phys. Rev. Lett.*, 103:036001, Jul 2009.

[5] Chase P Broedersz, Xiaoming Mao, Tom C Lubensky, and Frederick C MacKintosh. Criticality and isostaticity in fibre networks. *Nature Physics*, 7(12):983, 2011.

[6] Ivo Buttinoni, Jinwoong Cha, Wei-Hsun Lin, Stéphane Job, Chiara Daraio, and Lucio Isa. Direct observation of impact propagation and absorption in dense colloidal monolayers. *Proceedings of the National Academy of Sciences*, 2017.

[7] Daniel T.N. Chen, Qi Wen, Paul A. Janmey, John C. Crocker, and Arjun G. Yodh. Rheology of soft materials. *Annual Review of Condensed Matter Physics*, 1(1):301–322, 2010.

[8] Dennis E. Discher, Paul Janmey, and Yu-li Wang. Tissue cells feel and respond to the stiffness of their substrate. *Science*, 310(5751):1139–1143, 2005.

[9] Gustavo Düring, Edan Lerner, and Matthieu Wyart. Phonon gap and localization lengths in floppy materials. *Soft Matter*, 9(1):146–154, 2013.

[10] Leopoldo R. Gómez, Ari M. Turner, Martin van Hecke, and Vincenzo Vitelli. Shocks near jamming. *Phys. Rev. Lett.*, 108:058001, Jan 2012.

[11] J Goyon, A Colin, G Ovarlez, A Ajdari, and L Bocquet. Spatial cooperativity in soft glassy flows. *Nature*, 454(7200):84, 2008.

[12] Pol Grasland-Mongrain, Ali Zorgani, Shoma Nakagawa, Simon Bernard, Lia Gomes Paim, Greg Fitzharris, Stefan Catheline, and Guy Cloutier. Ultrafast imaging of cell elasticity with optical microelastography. *Proceedings of the National Academy of Sciences*, 115(5):861–866, 2018.

[13] George Neville Greaves, AL Greer, RS Lakes, and T Rouxel. Poisson's ratio and modern materials. *Nature materials*, 10(11):823, 2011.

[14] Gary L Hunter and Eric R Weeks. The physics of the colloidal glass transition. *Reports on Progress in Physics*, 75(6):066501, 2012.

[15] Donald E. Ingber. From cellular mechanotransduction to biologically inspired engineering. *Annals of Biomedical Engineering*, 38(3):1148–1161, Mar 2010.

[16] Diana E Jaalouk and Jan Lammerding. Mechanotransduction gone awry. *Nature reviews Molecular cell biology*, 10(1):63, 2009.

[17] Alex J Levine and T C Lubensky. One- and Two-Particle Microrheology. *Phys. Rev. Lett.*, 85(8):1774–1777, aug 2000.

[18] L D Landau & E M Lifshitz. *Theory of Elasticity (Volume 7 of A Course of Theoretical Physics)*. Pergamon Press, 1970.

[19] Robert Mallet. On the dynamics of earthquakes; being an attempt to reduce their observed phenomena to the known laws of wave motion in solids and fluids. *The Transactions of the Royal Irish Academy*, 21:51–105, 1846.

[20] T G Mason and D A Weitz. Optical Measurements of Frequency-Dependent Linear Viscoelastic Moduli of Complex Fluids. *Phys. Rev. Lett.*, 74(7):1250–1253, feb 1995.

[21] PH Mott and CM Roland. Limits to poisson's ratio in isotropic materials. *Physical review B*, 80(13):132104, 2009.

[22] RJ Poole. The deborah and weissenberg numbers. *British Soc. Rheol. Rheol. Bull*, 53:32–39, 2012.

[23] Simon Rogers. Large amplitude oscillatory shear: Simple to describe, hard to interpret. *Physics Today*, 71(7):34–40, jul 2018.

[24] Leonardo E. Silbert, Andrea J. Liu, and Sidney R. Nagel. Vibrations and diverging length scales near the unjamming transition. *Phys. Rev. Lett.*, 95:098301, Aug 2005.

[25] Veronique Trappe, V Prasad, Luca Cipelletti, PN Segre, and David A Weitz. Jamming phase diagram for attractive particles. *Nature*, 411(6839):772, 2001.

[26] Skanda Vivek, Colm P. Kelleher, Paul M. Chaikin, and Eric R. Weeks. Long-wavelength fluctuations and the glass transition in two dimensions and three dimensions. *Proceedings of the National Academy of Sciences*, 114(8):1850–1855, 2017.

[27] Alessio Zaccone and Enzo Scossa-Romano. Approximate analytical description of the nonaffine response of amorphous solids. *Phys. Rev. B*, 83:184205, May 2011.

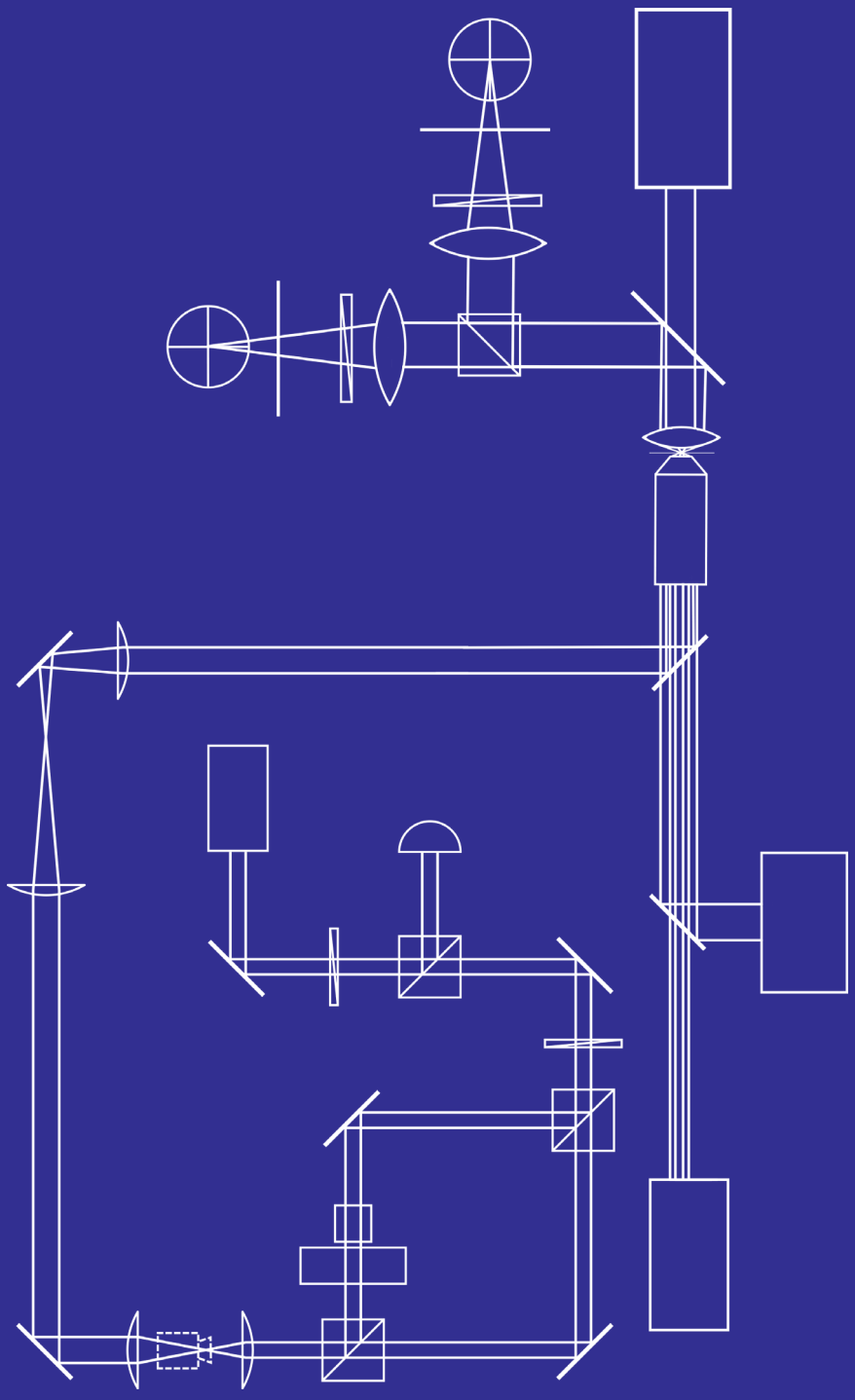

CHAPTER 3

Calibration of deflected AOD intensity for optical tweezers

Acousto Optical Deflectors (AODs) together with optical tweezers are widely used to manipulate colloidal particles at high frequencies. The intensity of the steered beam depends heavily on the deflection angle of the AODs. For quantitative use of optical tweezers these intensity variations are undesirable. Here we describe a procedure for measuring and correcting the intensity inhomogeneities. Intensity variance is reduced with a factor 27.3. Furthermore we describe a distributed real-time particle tracking method to verify the effect of the correction on force constant consistency. Improved intensity control allows to employ AODs for quantitative force measurements and microrheology at high frequencies.

Manuscript in preparation as:
J.M. van Doorn, R. Higler, R. Fokkink, R. Wegh, J. Sprakel and J. van der Gucht: *Calibration of deflected AOD intensity field for optical tweezers*

Introduction

Optical trapping has become a widely used tool in the field of soft matter[6, 1]. The ability to spatially organize and move particles and the possibility to accurately measure pico-Newton forces have made optical tweezers an excellent method to characterize mechanics at the micro scale[11]. Moving particles requires moving of the optical trap and thus steering of the trapping beam. This can be readily achieved with either moving mirrors, Spatial Light Modulators (SLMs) and Acousto Optical Deflectors (AODs). Whereas moving mirrors and SLMs are relatively slow, AODs are used in situations where high-frequency displacements are required and low inertia is crucial. However, with AODs the spatial intensity field suffers from strong heterogeneities, as compared to, for example, SLMs[14].

Crystals that are applied in AODs consist of materials that exhibit the acousto-optical effect. The efficiency of this effect, which determines the deflected intensity, depends mainly on the type of material, the acoustic frequency and the acoustic amplitude[13]. The acoustic frequency also controls the diffraction angle and is mainly used for beam steering. Because the efficiency varies for different acoustic frequencies and thus for different angles, the deflected intensity is spatially heterogeneous. This results in a non-constant trap stiffness and optical forces during trap motion. This is problematic, especially for applications in micro mechanical characterization, which assume a constant optical force along the entire particle trajectory [11].

In this chapter we present a software-based method to quantify and correct for spatial intensity variations due to AOD beam steering; this is implemented by means of a feedback algorithm which dynamically controls the amplitude of the acoustic waves imposed on the deflecting crystals. This results in a significant increase in the homogeneity of the intensity field, yet can also be used to design an intensity field on demand without the requirement for holographic projections. We combine this approach with direct dig-

ital synthesizers that support fast switching and facile control over acoustic frequency and amplitude. This allows to pre-calculate corrections for a specific trajectory of a trapped bead across the field-of-view and execute the trajectory at high frequency. Finally we discuss how our set-up is capable of both fast QPD detection and distributed real-time particle tracking for obtaining large amounts of particle displacement statistics. The combination of different detection methods and multiple ways of bead manipulation offers great flexibility and improved accuracy which opens up new ways to study spatially-resolved dynamics at small time scales.

Acousto optical deflection

The functioning of AODs is based on the acousto-optical effect. When an acoustic wave with frequency f_a, amplitude A_a and velocity $v_a = \lambda a \cdot f_a$ propagates trough a crystal it locally deforms the crystal. In acousto-optical materials, such as dioxide, this strain causes a local shift in refractive index. This allows to establish dynamic diffraction gratings within the crystal with a slit-size equal to the acoustic wavelength $\lambda_a \sin\theta_n = n\lambda_o$. Within the small-angle approximation and only considering first-order diffraction, the diffraction angle that results from the acoustic frequency shift, is given as

$$\Delta\theta_d = \frac{\lambda_o}{v_a}\Delta f_a \tag{3.1}$$

where $\Delta\theta_d$ is the shift in diffraction angle. The change in refractive index due to acoustic strains is proportional to the amplitude of the acoustic wave so that [13]

$$\Delta n_0 = \sqrt{\frac{1}{2}MI_a} \tag{3.2}$$

where $I_a = A_a^2$ is the acoustic intensity and M a material constant related to the efficiency of the acousto-optical effect [13].

As the diffraction is caused by reflections within the crystal, the intensity of the diffracted beam is governed by the reflectance R on the parts with a

higher refractive index Δn_0. A higher difference in refractive index and thus a higher reflectance will cause more light to be defracted by the crystal. At the Bragg angle, $\theta = \theta_n$, it follows that [13]

$$\frac{I_d}{I_i} = 2\pi^2 n^2 \frac{L^2 \lambda_a^2}{\lambda_o^4} \Delta n_0^2 = 2\pi^2 n^2 \frac{L^2 \lambda_a^2}{\lambda_o^4} M A_a^2 \tag{3.3}$$

where L is the length of the crystal and n the refractive index of the unperturbed crystal. The above equation permits the reflectance to increase above 1 which is physically impossible as no light is created upon reflection. When saturation processes are taken into account the ratio between the intensity of the incident and the diffracted beam $\frac{I_d}{I_i}$does not exceed unity and can be expressed as[13, 9]

$$\frac{I_d}{I_i} = \sin^2 \sqrt{2\pi^2 n^2 \frac{L^2 \lambda_a^2}{\lambda_o^4} M A_a^2} \tag{3.4}$$

which relates the intensity of the diffracted beam to the acoustic power exerted on the crystal and also to the acoustic wavelength λ_a. The local intensity fluctuations are caused by the λ_a^4 dependence. We can however use the quadratic dependence of output power on the acoustic amplitude A_a to correct for these local intensity variations.

Experimental setup

Optics

We use a near infrared laser beam for optical trapping. This beam with λ = 1064nm and a Gaussian intensity profile is generated with a 1.5 W Nd:YAG laser (Laser Quantum Ventus IR). After reflection by mirror M1 [Fig. 3.1], the laser beam is linearly polarized with a half-lambda waveplate ($\frac{\lambda}{2}$)(Newport). A polarizing beam splitter cube (PBS) (Optosigma, 20.0 mm) decomposes the beam into its two polarization components. To minimize power fluctuations

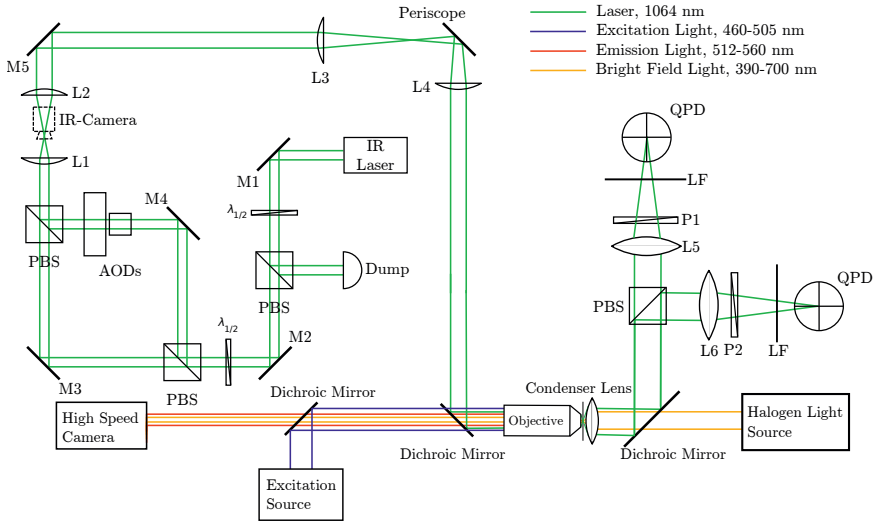

Figure 3.1: Schematic drawing of the optical tweezers setup. The laser path is depicted in green. The position of the IR camera for calibration measurement is indicated with the intermittent lines

the laser is operated at full power and the incident intensity into the microscope is controlled by adjusting the rotation angle of the half-lambda waveplate. The reflected component is directed into a beam dump and the transmitted component is split a second time again with an identical $\frac{\lambda}{2}$/PBS construction. The transmitted component is guided into the microscope directly to create a stationary optical trap.

The reflected component is guided to a pair of Acousto Optical Deflectors (AODs)(AA Opto-Electronic, DTSXY 250), to create a mobile trap that can be steered. Both beams for the static and mobile trap are recombined with a third PBS. To fit the rear aperture of the microscope objective, the diameter of the exiting beam is increased by a factor of 3.4 with a Keplerian beam expander consisting of lenses L1 (Sill Optics, f=50.0mm) and L2 (OptoSigma, f=170.0mm) [Fig. 3.1]. A combination of a second beam expander, consisting

of lenses L3 (OptoSigma, f=350.0mm) and L4 (OptoSigma, f=350.0mm), and a periscope guides the beam into the microscope (Nikon, ecplipse Ti). The second beam expander ensures that the beam for the mobile trap always hits the rear aperture of the objective regardless of the AOD deflection angle. After reflection by a dichroic mirror (Chroma, z1064rdc-SP), a water-immersion objective (Nikon, CFI Plan Apo IR SR 60X WI, NA=1.27) focuses both beams in diffraction limited spots that act as optical traps. Sample chambers are mounted on a motorized and computer controlled stage (Pi, Piline m-687). The forward scattered light is collected by the condenser lens of the microscope and reflected by a dichroic mirror (Thorlabs, DMSP805L). The scattering patterns from the static and mobile trap are separated with a PBS (Edmund optics, 50mm) and both exiting beams are focused with lenses L5 and L6 (Thorlabs, Biconvex f=100.0mm) on a Quadrant PhotoDiode (QPD)(OSI optoelectronics, SPOT-9DMI) to detect positions of optically trapped beads [5]. Rotatable polarizers (Thorlabs, LPVIS100) reduce the scattered light intensity to prevent saturation of the QPDs. Additionally 1064 nm laser line filters (Thorlabs, FL1064-10) are employed to exclude environmental light. Two separate QPDs allow for cross-power spectral analysis of the static and mobile trap[2, 15]. In addition, trapped beads can be imaged with bright-field microscopy using a high-speed camera (Fasttec Imaging, HiSpec 2g Mono). Epifluorescence microscopy allows to detect positions of fluorescently-labelled beads, which can for example be refractive-index matched as not to experience trapping forces. Vibrations are minimized by mounting the set-up on an air-suspended optical table (TMC, 78 Series CleanTop®) while all power supplies and controllers are positioned on a separate table.

Sample chambers are prepared by attaching two rectangular cover slips (21 $\times$ 26 mm) to a microscope slide (76 $\times$ 26 mm) with Norland Optical Adhesive 61 (NOA61). On top of the rectangular coverslips a circular cover slip ($\oslash$ = 50 mm) is glued. To prevent drift the formed channel is sealed with two component epoxy glue (Bison).

Electronics

Acoustic waves in the AODs are generated with direct digital synthesizers (AA Opto-Electronic, DDSPA 15 bits 10-400MHz) and analog amplifiers (AA Opto-Electronic, AMPA-B-34). The digital synthesizers are controlled using two National Instruments NI-6323 computer cards that share their internal clock. Each card sends out a 31 bit instruction integer consisting of a 23 bit instruction for its AOD and 8 bits for triggering external devices(Table 3.1).

Triggering	AODFrequency	AODAmplitude
8 bits	15 bits	8 bits

Table 3.1: The 31 bit instruction integer that is send out by the NI-6323 computer cards. The 23 bits for the AOD instructions are directly connected to the synthesizers.

The 23 bit AOD intstruction contains 15 bits for specifying the acoustic frequency and 8 bits for specifying the acoustic amplitude. An array of 2000 computer generated instruction integers can be stored in the internal memory of the computercards and can be executed either linearly or in a loop. Because the acoustic wave has to propagate trough the AOD crystal the minimal time between instructions is set to 9μs which corresponds to a maximal clockrate of 111kHz.

QPDs are mounted on custom electronic boards that output three voltages: X, Y, SUM [Fig. 3.2]. After conversion of the currents to voltages, the analog signal of each quadrant is amplified with a low noise electrometer amplifier(Analog devices, AD8513). The resulting signals are summed electronically such that

$$X = (I_{TopRight} + I_{BottomRight}) - (I_{TopLeft} + I_{BottomLeft}) \tag{3.5}$$

$$Y = (I_{TopRight} + I_{TopLeft}) - (I_{BottomRight} + I_{BottomLeft}) \tag{3.6}$$

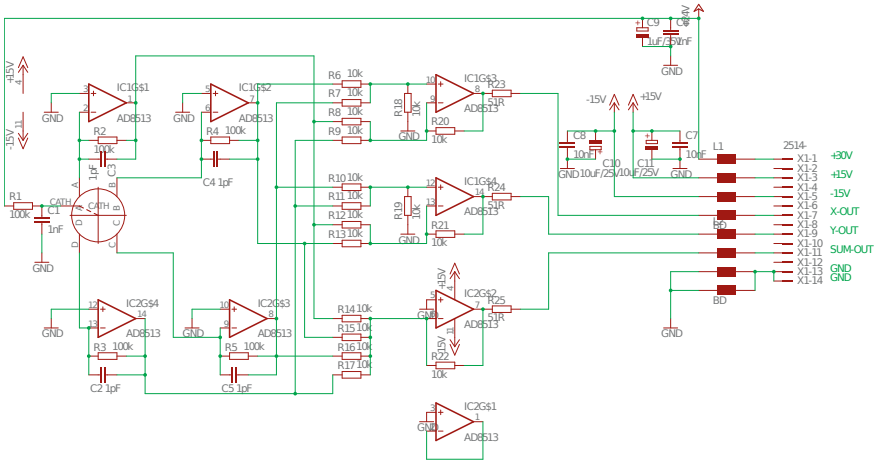

Figure 3.2: Electric circuit drawing of the custom QPD electronics.

$$SUM = I_{TopRight} + I_{TopLeft} + I_{BottomRight} + I_{BottomLeft} \tag{3.7}$$

Data acquisition is performed by a National Instruments NI-6143 computer card. This card digitizes 8 channels at 250 kS/s simultaneously. Each QPD occupies 3 channels and the remaining channels measure the triggers sent to the AODs in order to synchronize trap positions with QPD force measurements. To reduce noise the QPD electronics are powered with a floating power supply.

Software

To orchestrate all components of the setup custom software has been developed. The software interfaces with the National instrument cards, the high-speed camera and the motorized stage. It includes an easy interface with Matlab scripts to calibrate the force constant of the optical trap with power-spectral analysis[3, 7]. Furthermore the software can calibrate the force constant using the Boltzmann method[4]. The software is available upon request.

Distributed real time particle tracking

High-speed video microscopy produces vast amounts of data. In order to reduce hard disk usage and facilitate efficient data transport, real-time particle tracking is applied. This is carried out by streaming images obtained from the high-speed camera over a gigabit ethernet network to worker computers. The worker computers perform particle tracking using the python version of established particle tracking routines[12]. ZeroMQ is used for setting up the stream between the acquisition computer and the worker computers[8]. After obtaining an image from the camera stream, the acquisition CPU copies the image in binary form together with its timestamp to a ZMQ message which is sent out to the workers. The worker CPUs locate the particles and output their coordinates and timestamp to a HDF5 or .csv datafile. When the experiment is finished, particle trajectories are reconstructed from the separate datafiles and sorted by their timestamp. Scaling up the processing capability can be easily achieved by adding more workers as the images are automatically distributed over all available workers.

Epifluorescence microscopy and force detection

Structural changes and dynamics are monitored with epifluorescence video microscopy. To demonstrate this a cropped epifluorescence picture of a colloidal gel is shown in figure 3.3 (a). The depletion gel consists of a=1.55μm tFEMA/tBMA core-shell particles in a refractive index matched solvent[10]. A Gaussian blurred (30pix) version of the raw image is subtracted and the result is treated with a bandpass filter to make it suitable for particle tracking [Fig. 3.3(b)]. Kilfoil particle tracking routines are used to track particles[12]. The results are shown in figure 3.3(c). Particle tracking can be executed real-time by streaming the images to worker CPUs as is described in the previous section. The frame rate that can be achieved depends mainly on the photostability of the fluorescent dye applied in the particles and the available pro-

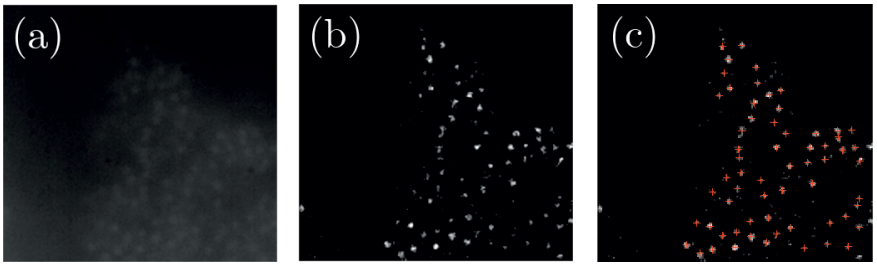

Figure 3.3: (*a*) Cropped epifluorescence image of a colloidal depletion gel consisting of a=1.55μm core-shell particles.(*b*) Image after proccesing with Gaussian blur and bandpass filters.(*c*) Results of particle tracking, located particles are indicated with a red +.

cessing power. Force measurements are carried out using back-focal-plane inferometry [5]. Figure 3.4 shows a force curve of a trapped particle that experiences a drag force induced by moving the microscope stage. The force fluctuations before moving the stage are caused by Brownian motion whereas the fluctuations after the particle escaped resemble electronic noise.

AOD intensity field calibration

We correct for inhomogeneities in the AOD intensity field by calibrating the acoustic amplitude for a desired intensity. The intensity field is flattened by locally decreasing the acoustic amplitude such that the intensity of the diffracted beam is the same for every angle. The intensity of the diffracted laser beam is measured with a NIR camera (Basler, acA1300-60gmNIR) that is placed after lens L1 [Fig. 3.1]. L1 focusses the beam to make sure all possible paths of the diffracted beam end up at the sensor of the camera. The laser power is set at 1450 mW in order to maximize stability. The laser power is attenuated with both $\frac{\lambda}{2}$/PBS constructions such that no pixel on the NIR camera is saturated [Fig. 3.5]. Intensities are measured from the 8-bit im-

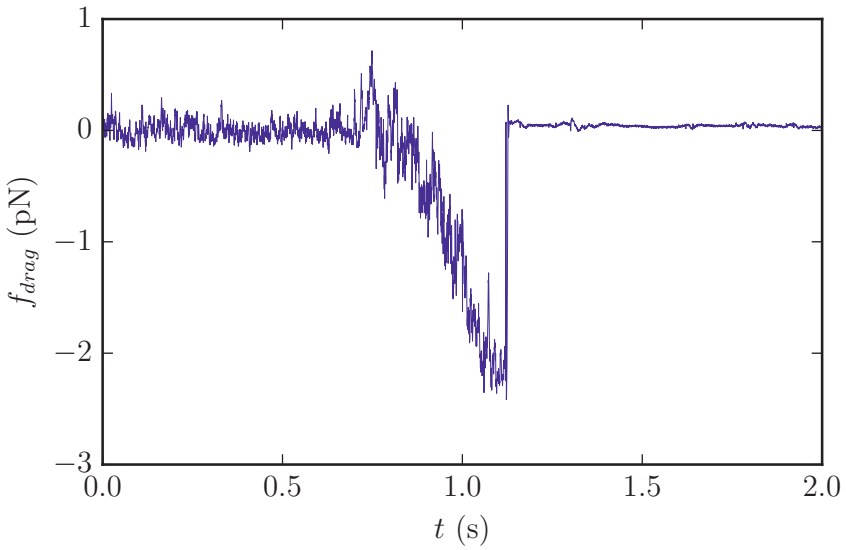

Figure 3.4: Example of force measurements on a 2μm trapped silica bead with a QPD. The stage starts moving at $t = 0.8$s. This causes a drag force on the particle and at $t = 1.1$s the particle escapes the optical trap.

ages by taking a time-averaged pixel intensity. To suppress camera noise and to increase the dynamic range, pixels with a intensity value <8 are excluded from the average.

According to equation 3.4 the relation between the acoustic amplitude and the diffracted beam intensity is non-linear and depends on material constants. Therefore the amplitude-intensity relation is calibrated by measuring the diffracted beam intensity along the amplitude range in the center of the intensity field [Figure 3.6]. The resulting data is fitted with a third-order polynomial. The coefficients are stored and used to calculate the required amplitude for a desired decrease in intensity. At lower amplitudes the intensity levels off due to the exclusion of pixels with an intensity lower than 8; however, as such small amplitudes are not used in practice this does not

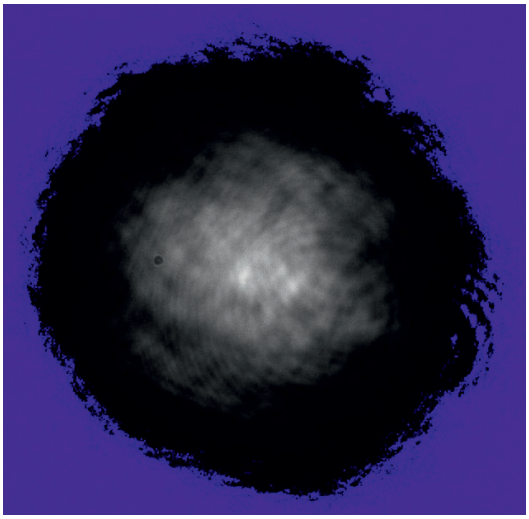

Figure 3.5: Typical image of laser spot as detected by the camera. Pixels with intensity lower than 8 are indicated with blue whereas pixels with an intensity of 255 are colored red

present an issue.

Heterogeneities in the intensity field are recorded by dividing the AOD frequency range in a user-specified number of steps. The software scans these steps and measures the diffracted beam intensity at each position with maximum acoustic amplitude. This results in a two-dimensional array with intensity values before calibration [Figure 3.7(a)]. The array is stored on the computers harddrive and used to calculate corrected amplitude values for each AOD with the following equation

$$A_{ac} = c_3(\sqrt{\frac{I_{bl}}{I_{rpb}}})^3 + c_2(\sqrt{\frac{I_{bl}}{I_{rpb}}})^2 + c_1\sqrt{\frac{I_{bl}}{I_{rpb}}} + c_0 \qquad (3.8)$$

Where I_{bl} is the lowest intensity in the array, I_{rpb} is the intensity value in the array nearest to the requested point and c_n are the coefficients obtained from the fit in figure 3.6. Because both AODs together have to reduce the

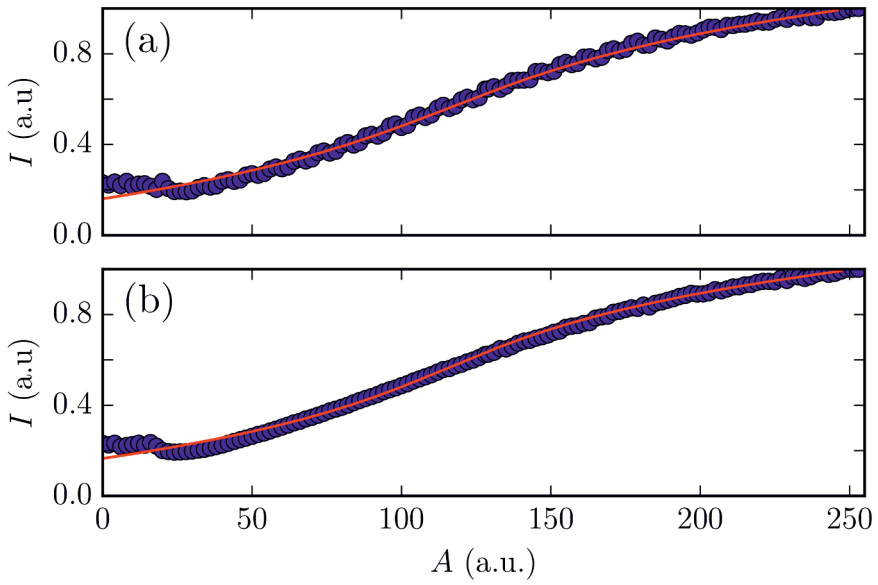

Figure 3.6: Normalized intensities (*circles*) for 128 points along the entire 8 bit amplitude range. A third-order polynomial (*solid*) is fitted through the data as an approximation.

intensity by a factor of $\frac{I_{bl}}{I_{rpb}}$ and the AODs are placed after each other, each separate AOD has to reduce the intensity by $\sqrt{\frac{I_{bl}}{I_{rpb}}}$. After calibration, the heterogeneities in intensity are substantially reduced [Fig. 3.7(b)]. Histograms of the intensity values before and after calibration[Fig. 3.7(c) and Fig. 3.7(d)] indicate that the spread in intensity values decreases strongly, with the intensity variance reduced by a factor 27.3. The distribution of intensities after calibration exhibits a Gaussian shape, which suggests that the remaining variance is due to measurement inaccuracies and the fact that the acoustic amplitude can only be varied in discrete steps. To test the effect of the calibration on the force constant of the optical trap a 2μm silica bead was dragged from the lower left corner to the upper right corner of the field of view, in a 10 w/w% glycerol/H_2O solution. The position of the particle is monitored with real-

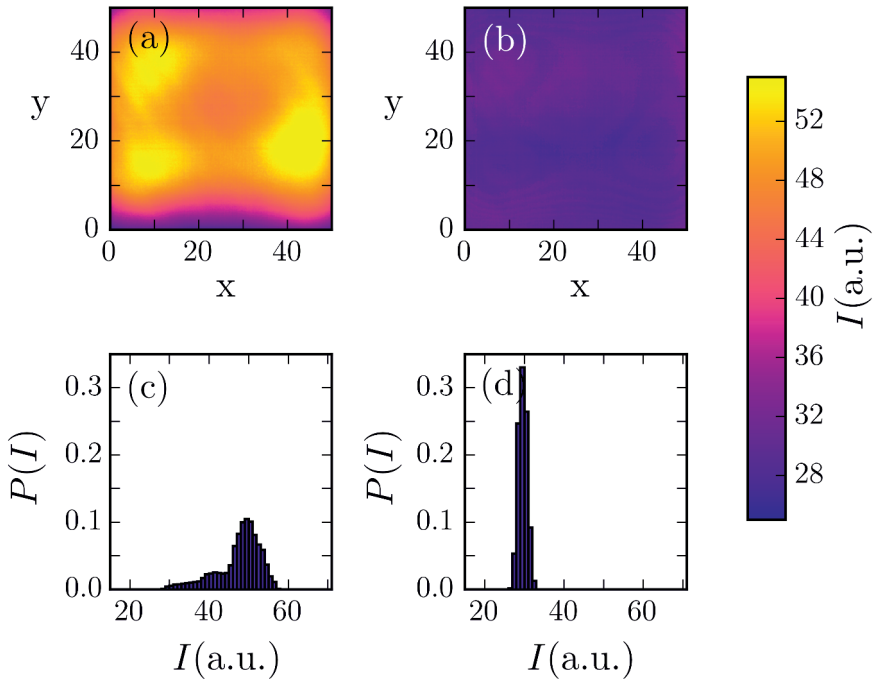

Figure 3.7: Comparison between the intensity field before (*a*) and after (*b*) calibration. (*c,d*) Histograms of intensity values measured with an IR camera. The variance changes dramatically after calibration.

time particle tracking at 164 fps. Position fluctuations perpendicular to the drag direction are obtained by rotation with a rotation matrix such that all drag motion is exerted along one axis. The data is subsequently binned in 100 bins. The standard deviation of each bin $\sigma_\perp(d)$ is plotted in figure 3.8 as a function of the traveled distance d. For the uncalibrated field the positional fluctuations at the edges are clearly larger than in the center. Larger fluctuations mean that the optical trap is weaker, which indicates that the force constant is smaller at the edges than in the center. This agrees with the field in figure 3.7(a) since higher intensity corresponds to a higher force constant. The data for the calibrated field shows much more constant positional fluctu-

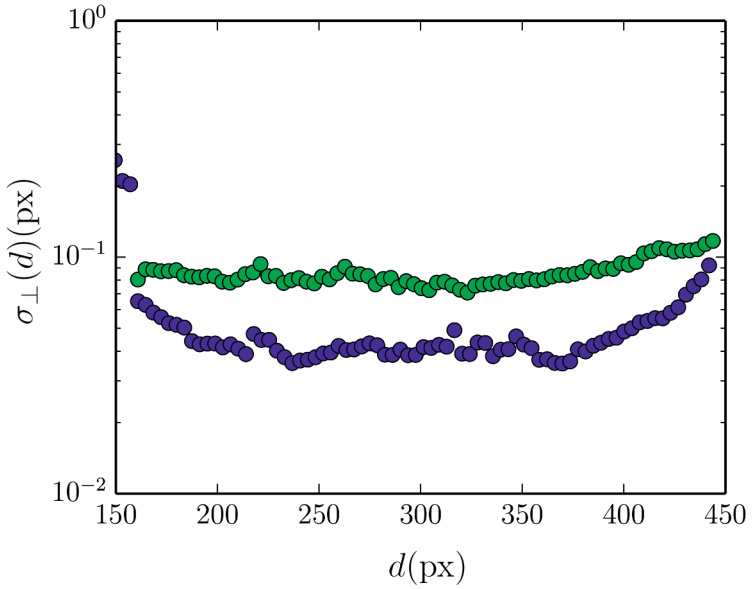

Figure 3.8: Standard deviations of the positional fluctuations before (*blue*) and after (*green*) calibration. Before calibration the fluctuations at the edges increase with respect to the fluctuations in the center. After calibration fluctuations are more constant with position.

ations with trap position. This suggests that the calibration indeed improved force constant consistency across the whole AOD range.

Conclusions

We have developed a procedure to measure and correct intensity variations in AODs. The correction dramatically improves intensity variance with a factor of 27.3. This allows for better control over the optical forces that are exerted on trapped beads across the AOD range. This is demonstrated experimentally by monitoring Brownian fluctuations of a bead dragged across the AOD field. The improved force constant consistency is particularly important for quan-

titative applications of AOD-based optical tweezers. When combined with speed of digitally controlled AODs and an high-speed camera this calibration allows to explore a new area of high-speed mechanics with optical tweezers.

Bibliography

[1] A. Ashkin, J. M. Dziedzic, J. E. Bjorkholm, and Steven Chu. Observation of a single-beam gradient force optical trap for dielectric particles. *Optics Letters*, 11(5):288, may 1986.

[2] M. Atakhorrami, K. M. Addas, and C. F. Schmidt. Twin optical traps for two-particle cross-correlation measurements: Eliminating cross-talk. *Review of Scientific Instruments*, 79(4):043103, apr 2008.

[3] Kirstine Berg-Sorensen and Henrik Flyvbjerg. Power spectrum analysis for optical tweezers. *Review of Scientific Instruments*, 75(3):594, 2004.

[4] E.-L. Florin, A. Pralle, E.H.K. Stelzer, and J.K.H. Hörber. Photonic force microscope calibration by thermal noise analysis. *Applied Physics A: Materials Science & Processing*, 66(7):S75–S78, mar 1998.

[5] Frederick Gittes and Christoph F Schmidt. Interference model for back-focal-plane displacement detection in optical tweezers. *Opt. Lett.*, 23(1):7–9, jan 1998.

[6] David G Grier. A revolution in optical manipulation. *Nature*, 424(6950):810–6, aug 2003.

[7] Poul Martin Hansen, Iva Marija Tolic-Norrelykke, Henrik Flyvbjerg, and Kirstine Berg-Sorensen. tweezercalib 2.1: Faster version of MatLab package for precise calibration of optical tweezers. *Computer Physics Communications*, 175(8):572–573, oct 2006.

[8] iMatix Corporation. http://zeromq.org/, 2015.

[9] Blaž Kavčič, Dušan Babić, Natan Osterman, Boštjan Podobnik, and Igor Poberaj. Rapid prototyping system with sub-micrometer resolution for microfluidic applications. *Microsystem Technologies*, 18(2):191–198, sep 2011.

[10] Thomas E Kodger, Rodrigo E Guerra, and Joris Sprakel. Precise colloids with tunable interactions for confocal microscopy. *Scientific Reports*, 5:14635, sep 2015.

[11] D Mizuno, D A Head, F C MacKintosh, and C F Schmidt. Active and Passive Microrheology in Equilibrium and Nonequilibrium Systems. *Macromolecules*, 41(19):7194–7202, 2008.

[12] Vincent Pelletier, Naama Gal, Paul Fournier, and Maria L Kilfoil. Microrheology of Microtubule Solutions and Actin-Microtubule Composite Networks. *Phys. Rev. Lett.*, 102(18):188303, 2009.

[13] Bahaa E A Saleh, Malvin Carl Teich, and Bahaa E Saleh. *Fundamentals of photonics*, volume 22. Wiley New York, 1991.

[14] Gabriel C Spalding, Johannes Courtial, and Roberto Di Leonardo. *Holographic optical tweezers*. Academic Press, 2008.

[15] Yann von Hansen, Alexander Mehlich, Benjamin Pelz, Matthias Rief, and Roland R Netz. Auto- and cross-power spectral analysis of dual trap optical tweezer experiments using Bayesian inference. *The Review of scientific instruments*, 83(9):095116, sep 2012.

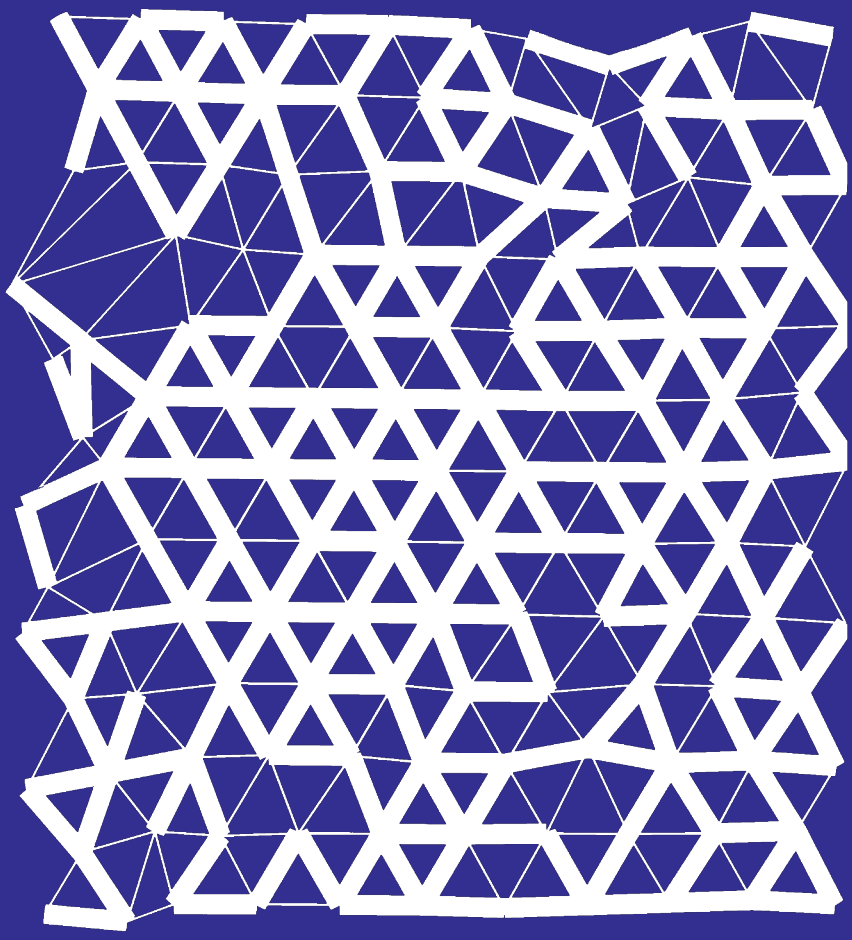

CHAPTER 4

Criticality and mechanical enhancement in composite fiber networks

Many biological materials consist of sparse networks of disordered fibers, embedded in a soft elastic matrix. The interplay between rigid and soft elements in such composite networks leads to mechanical properties that can go far beyond the sum of those of the constituents. In this chapter we present lattice-based simulations to unravel the microscopic origins of this mechanical synergy. We show that the competition between fiber stretching and bending and elastic deformations of the matrix gives rise to distinct mechanical regimes, with phase transitions between each regime that are characterized by critical behavior and diverging strain fluctuations and with different mechanisms leading to mechanical enhancement.

This chapter was published as:

J.M. van Doorn, L. Lageschaar, J. Sprakel and J. van der Gucht: *Criticality and mechanical enhancement in composite fiber networks*, Phys. Rev. E 95, **(2017)**, 042503

Introduction

Many materials, ranging from textiles and paper to connec- tive tissue and the cytoskeleton of living cells, have a micro-scopic structure that consists of crosslinked fibers. Theoretical progress in the last decades has led to a detailed understanding of the physics of such fiber networks[1]. Because stiff fibers resist not only stretching, but also bending, the mechanical behavior of fiber networks differs significantly from that of networks of flexible polymers. Different mechanical regimes can be observed: at high densities fiber networks deform affinely and the elasticity is governed by fiber stretching, while at lower densities there is a crossover to a nonaffine, bending-dominated regime[2, 3, 4, 5, 6].

Although experiments on model networks give support to the existence of different mechanical regimes[7, 8, 9], the current theories fall short in describing real biomaterials. An important reason for this is that natural materials are almost without exception composite materials that consist of mixtures of elements of different rigidity: the cytoskeleton is a complex network of (partially bundled) actin filaments, intermediate filaments, and microtubules [10]; the extracellular matrix consists of stiff collagen fibers in a matrix of more flexible polymers[11]; and also many synthetic high-performance materials are composites of soft and rigid fibers[12, 13, 14, 15, 16]. Recent experimental work has shown that networks of stiff fibers embedded in an elastic matrix can have an elastic modulus that significantly exceeds the sum of the moduli of the two individual networks[17, 18]. It was hypothesized that this mechanical enhancement was caused by a suppression of nonaffine deformation modes in the rigid fiber network due to the reaction forces in the softer network. However, a theoretical underpinning of this hypothesis was missing. Previous models considered the effect of sparse rigid inclusions in a softer base network[19, 20, 21, 22, 23, 24]. These models indeed showed that the interplay between stiff and soft components can strongly affect the defor-

mation modes and stiffness of a composite network. However, there has been no systematic investigation of how the mechanical response of a composite network depends on the connectivity of the fiber network and on the stiffness of the individual constituents. Here, we present a model that allows us to explore the mechanics of composite networks over a large range of parameters and compositions, both for sparse fiber networks and for highly connected fibers.

Model

We use numerical simulations to study the mechanics of disordered composite networks, consisting of crosslinked fibers embedded in a soft elastic matrix. Both the fibers and the polymers that constitute the background matrix are arranged on a two-dimensional (2D) triangular lattice with lattice spacing l_0, as shown in Fig. 4.1. The effects of connectivity are explored by randomly removing segments of the fiber network with a probability $1 - p$, so that the average connectivity equals $z = 6p$. Sequences of contiguous colinear fiber segments are treated as elastic rods, characterized by a stretch modulus μ_1 and a bending modulus κ_1. Since fibers in biomaterials are typically much softer with respect to bending than to stretching[1], we will only consider the case that $\kappa_1 \ll \mu_1 l_0^2$. Intersecting fibers are assumed to be crosslinked with permanent but freely hinged bonds. The background matrix is modelled as a homogeneous network of undiluted central force springs with stretch modulus μ_2. The two networks are linked to each other at each vertex of the lattice. To investigate the mechanical response of the composite network, we calculate the linear shear modulus G by applying a shear strain $\gamma = 10^{-2}$ to the network by translating the horizontal boundaries to which the fibers and springs are attached. The network is then relaxed by minimizing the total

mechanical energy

$$E = \frac{1}{2}\frac{\mu_1}{l_0}\sum_{<ij>} g_{ij}^{(1)}(\Delta l_{ij})^2 + \frac{1}{2}\frac{\kappa_1}{l_0^3}\sum_{<ijk>} g_{ij}^{(1)} g_{jk}^{(1)}(\Delta\theta_{ijk})^2 + \frac{1}{2}\frac{\mu_2}{l_0}\sum_{<ij>}(\Delta l_{ij})^2 \quad (4.1)$$

where l_0 is the lattice spacing, Δl_{ij} the extension of the segment between vertices i and j, $\Delta\theta_{ijk}$ the angle between neighboring bonds i-j and j-k, and $g_{ij}^{(1)} = 1$ if there is a fiber segment between vertices i and j, while $g_{ij}^{(1)} = 0$ otherwise. The first term represents the stretch energy of the fibers, the second term the bending energy, and the third term the elastic energy of the matrix. The first and third summations extend over all bonds i-j, while the second summation extends only over colinear neighboring bonds. This energy can be expressed in terms of the node displacements[6] using $\Delta l_{ij} = (\mathbf{u}_j - \mathbf{u}_i)\cdot\hat{\mathbf{r}}_{ij}$ with $\hat{\mathbf{r}}_{ij}$ the unit vector along the i-j bond, and $\Delta\theta_{ijk} = (\mathbf{u}_k + \mathbf{u}_i - 2\mathbf{u}_j)\times\hat{\mathbf{r}}_{ij}$. The energy is minimized using lower upper (LU) decomposition, giving the equilibrium nodal displacements. The shear modulus is calculated as $G = (2/A)(E/\gamma^2)$ where A is the area of the network. In our simulations we have used $A = 4\times10^4 l_0^2$. Results for other system sizes are shown in Fig. 4.7 in Appendix B.

Results

Mechanical regimes

In Fig. 4.2, we show the shear modulus as a function of the connectivity p for various values of the matrix stiffness μ_2. For $\mu_2 = 0$, G vanishes when the connectivity is lower than a critical rigidity threshold. For fibers with no bending rigidity ($\kappa_1 = 0$, dashed line), this threshold is $p_{\rm cf} \approx 0.651$, as given by Maxwell's criterion for isostatic networks of central force springs[25]. For nonzero κ_1, however, the rigidity threshold shifts discontinuously to a lower value, $p_{\rm b} \approx 0.442$, which is independent of κ_1 for $\kappa_1 > 0$ (black line). The

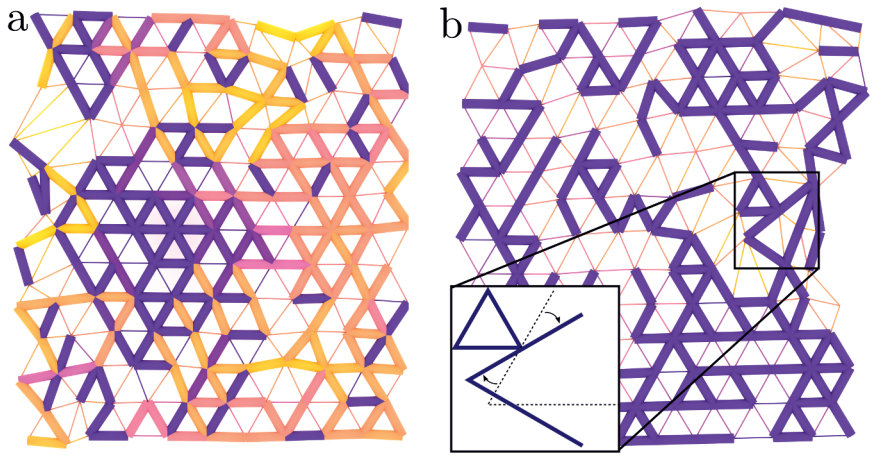

Figure 4.1: Composite networks on a triangular lattice. A small section of a deformed network of fibers in a soft matrix, with $\kappa_1/(\mu_2 l_0^2) = 10^{-6}$ and $\mu_2/\mu_1 = 10^{-12}$ for (a) $p = 0.65$ and (b) $p = 0.45$. Thick segments represent fiber segments, color-coded for their bending energy (yellow: strongly bent, blue: weakly bent), and thin segments represent the background matrix, color-coded for stretching energy (yellow: strongly stretched; blue: weakly stretched). Inset in (b) shows an example of a rigid rotation of a fiber cluster.

results for different values of the bending rigidity are shown in Fig. 4.6 in Appendix A. In the presence of an elastic matrix with nonzero stretch modulus μ_2, the network is mechanically stable for any value of p. However, features of the mechanical transitions at p_{cf} and p_{b} can still be seen, as the shear modulus decreases very steeply with decreasing p around these points [Fig. 4.2]. This suggests that both points mark a transition between distinct mechanical regimes in the composite network. To investigate the nature of these different regimes, we examine both crossover regions in more detail. For low values of μ_2, the mechanical response of the composite network is dominated by the fiber network for p sufficiently above p_{b}. We therefore expect that the crossover region at p_{cf} is similar to the one observed in single-component fiber networks. As shown previously[6], in such networks the central force

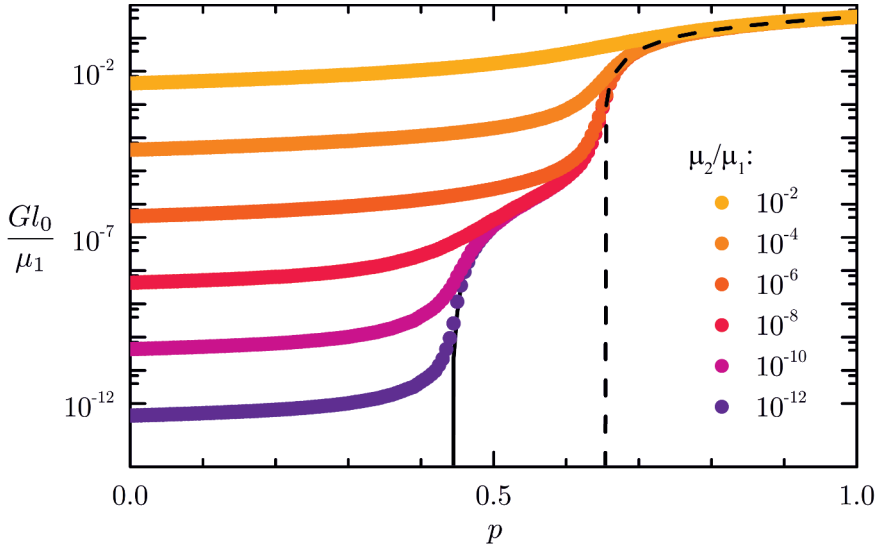

Figure 4.2: Elasticity of composite networks. Shear modulus G (in units μ_1/l_0) as a function of the bond probability p for $\kappa_1/\mu_1 l_0^2 = 10^{-6}$ and for a range of stiffnesses of the background matrix. The black line corresponds to $\mu_2 = 0$ and the dashed line to $\mu_2 = 0$ and $\kappa_1 = 0$.

threshold coincides with a transition from a stretching-dominated regime for $p > p_{\text{cf}}$ to a bending-dominated regime for $p < p_{\text{cf}}$. The presence of an elastic matrix as embedding medium is expected to affect this transition, because fiber bending is a nonaffine deformation mode, which inevitably leads to additional strain in the medium. The elastic energy stored in the matrix due to the bending of an embedded fiber increases proportionally to the matrix stiffness μ_2[27]. We therefore expect the resistance to bending to increase linearly with μ_2. Indeed, we find that we can collapse our data by introducing an effective bending rigidity, which is the sum of the intrinsic bending rigidity and a matrix-induced bending resistance [see Appendix C]:

$$\kappa_{\text{eff}} = \kappa_1 + \mu_2 l_0^2 \tag{4.2}$$

This is shown in Fig. 4.3(a), where we plot the scaling form

$$G = \frac{\mu_1}{l_0}|\Delta p_{\text{cf}}|^{\beta}\mathcal{G}^{\text{cf}}_{\pm}\left(\frac{\kappa_{\text{eff}}}{\mu_1 l_0^2}|\Delta p_{\text{cf}}|^{-\alpha}\right) \tag{4.3}$$

with $\Delta p_{\text{cf}} = p - p_{\text{cf}}$ and with scaling exponents $\alpha = 3.0$ and $\beta = 1.4$, in agreement with previous findings[6]. The universal scaling function $\mathcal{G}^{\text{cf}}_{\pm}(x)$ consists of three branches that characterize three different mechanical regimes. For $x \ll 1$, $\mathcal{G}^{\text{cf}}_{+}(x) \sim$ const and $\mathcal{G}^{\text{cf}}_{-}(x) \sim x$. This implies a stretching-dominated regime with $G \sim \mu_1|\Delta p_{\text{cf}}|^{\beta}$ above the transition ($\Delta p_{\text{cf}} > 0$), and a bending-dominated regime with $G \sim \kappa_{\text{eff}}|\Delta p_{\text{cf}}|^{\beta-\alpha}$ below the transition ($\Delta p_{\text{cf}} < 0$). In the bending-dominated regime, the shear modulus is governed by the effective bending resistance of the fibers [equation 4.2]: for very soft matrices ($\mu_2 < \kappa_1 l_0^{-2}$) the response is dominated by the intrinsic bending rigidity of the fibers, $G \sim \kappa_1$, while for stiffer matrices ($\mu_2 > \kappa_1 l_0^{-2}$) the shear modulus is determined by the induced bending rigidity due to the matrix: $G \sim \mu_2$. Very close to the critical threshold, we find a crossover regime with anomalous scaling[6] $G \sim \kappa_{\text{eff}}^{\beta/\alpha}\mu_1^{1-\beta/\alpha}$ independent of Δp_{cf}, as observed from the critical branch in Fig. 4.3(a).

At $p = p_{\text{b}}$ there is a second transition, now from a bending-dominated regime to a matrix-dominated regime. Again, we can capture the different regimes around this transition by a scaling form

$$G = \frac{\kappa_1}{l_0^3}|\Delta p_{\text{b}}|^{\delta}\mathcal{G}^{\text{b}}_{\pm}\left(\frac{\mu_2 l_0^2}{\kappa_1}|\Delta p_{\text{b}}|^{-\gamma}\right) \tag{4.4}$$

with $\Delta p_{\text{b}} = p - p_{\text{b}}$ and $\mathcal{G}^{\text{b}}_{\pm}(x)$ another universal scaling function. The data is found to collapse with critical exponents $\gamma = 4.5$ and $\delta = 3.0$. Again, we see three branches, corresponding to three different mechanical regimes. Above the transition for $x \ll 1$ we find $\mathcal{G}^{\text{b}}_{+}(x) \sim$ const and $G \sim \kappa_1|\Delta p_{\text{b}}|^{\delta}$, which corresponds to the rigidity percolation scaling of a bending-dominated network[6]. Below the transition, for $x \ll 1$ we find $\mathcal{G}^{\text{b}}_{-}(x) \sim x$ and $G \sim \mu_2|\Delta p_{\text{b}}|^{\delta-\gamma}$. In this regime the fiber network is below its rigidity threshold,

and the composite network consists of an elastic matrix with embedded, non-percolating fiber clusters. Indeed, the scaling that we find is very similar to the one found for a central force network with rigid inclusions[28, 29]. Very close to the transition we again find an anomalous scaling regime in which the modulus becomes independent of Δp_{b} and is governed by both bending and matrix contributions, with $G \sim \kappa_1^{1-\delta/\gamma}\mu_2^{\delta/\gamma}$. The different mechanical regimes that we find for our composite network are summarized in the phase diagram in Fig. 4.3(c), which clearly highlights the rich behavior of composite networks.

It is well-established that the mechanics of weakly-connected disordered networks are governed by nonaffine deformation modes[1, 2, 3, 4, 5, 6]. This raises the question whether the different mechanical regimes that we observe originate from a transition between different nonaffine modes. We examine the the nonaffine fluctuations by calculating the mean-square deviation from a uniform, affine strain field[30]:

$$\Gamma = \frac{1}{\gamma^2 l_0^2}\left\langle \left(\mathbf{u} - \mathbf{u}^{(\mathrm{aff})}\right)^2 \right\rangle \tag{4.5}$$

Here $\mathbf{u}$ and $\mathbf{u}^{(\mathrm{aff})}$ are the actual displacement and the affine displacement of a node, respectively. We find a strong, cusp-like increase of the nonaffine fluctuations in the vicinity of both p_{cf} and p_{b}, highlighting the critical state of the fiber network at these points [Fig. 4.4(a)]. From Fig. 4.1 it is clear, however, that the nature of the nonaffine modes is very different in these two regimes. For $p \approx p_{\mathrm{cf}}$, the deformation field is characterized by large and heterogeneous bending fluctuations [Figs.4.1(a) and 4.4(b)]. This is in agreement with earlier work[2, 3, 4, 5, 6], where the central force threshold was shown to mark a transition from an affine, stretching-dominated regime for $p > p_{\mathrm{cf}}$ to a nonaffine, bending-dominated regime for $p < p_{\mathrm{cf}}$. By contrast, the increase in Γ at $p \approx p_{\mathrm{b}}$ is not associated with bending fluctuations [Fig. 4.1(b)], but can be ascribed to rigid body motions of fibers or fiber clusters [inset Fig. 4.1(b) and Fig. 4.4(c)] that become more and more prominent as the connec-

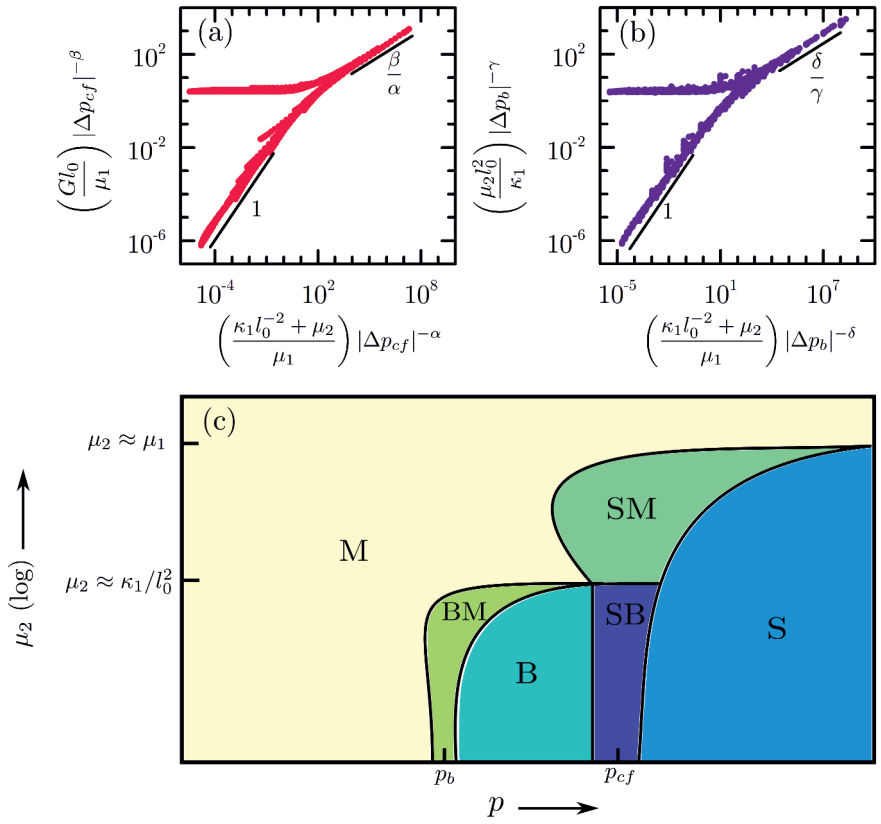

Figure 4.3: Mechanical regimes in composite networks. Scaling analysis of the shear modulus in the vicinity of (a) the central force isostatic point $p_{\rm cf}$ and (b) the rigidity threshold $p_{\rm b}$, for a wide variety of values of κ_1 and μ_2. Values of the critical exponents: $\alpha = 3.0$, $\beta = 1.4$, $\gamma = 4.5$, $\delta = 3.0$. (c) Mechanical phase diagram of composite networks: S: stretching-dominated ($G \sim \mu_1$), B: bending-dominated ($G \sim \kappa_1$), M: matrix-dominatd ($G \sim \mu_2$), SB: stretch-bend coupled ($G \sim \mu_1^{1-x}\kappa_1^x$), SM: stretch-matrix coupled ($G \sim \mu_1^{1-x}\mu_2^x$), BM: bend-matrix coupled ($G \sim \kappa_1^{1-y}\mu_2^y$).

tivity of the network decreases. At the rigidity threshold $p_{\rm b}$, the fiber network becomes floppy and all the strain can be accommodated by such rigid body motions without elastic energy cost in the fiber network[6, 26, 31]. However,

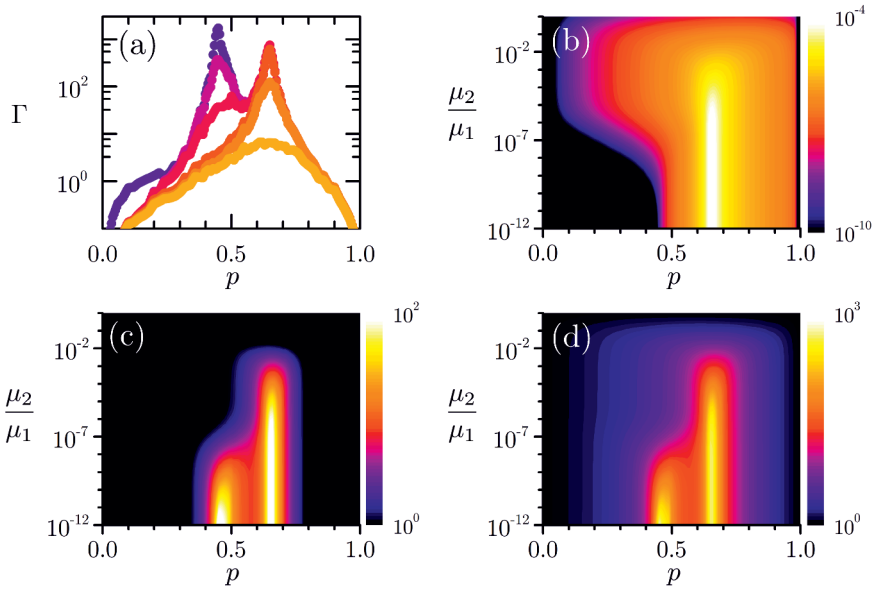

Figure 4.4: Nonaffine deformations in composite networks. (a) Non-affinity as a function of connectivity p for several values of μ_2 (same color coding as in Fig. 4.2). (b) Bending energy per unit area and unit strain, $E_b/A\gamma^2$, as a function of p and μ_2. (c) Rigid body rotations: mean-squared rotation angle of the end-to-end vector of fibers, averaged over all fibers in the network $\langle\Delta\phi^2\rangle$, compared to that for the affinely deformed network as a function of p and μ_2. (d) Relative deformation energy of the background matrix, compared to the affinely deformed network, $E_2/E_2^{(\mathrm{aff})}$, as a function of p and μ_2. The bending rigidity $\kappa_1 = 10^{-6}\mu_2 l_0^2$ in all cases.

while the nonaffine modes are soft modes for the fiber network, they lead to additional deformations in the background matrix, so that the elastic energy of the matrix is strongly increased in regions where the nonaffine fluctuations are large [Fig. 4.4(d)]. This means that the final deformation field in a composite network is a compromise between energy stored in the fiber network (which can be reduced by nonaffine modes) and energy stored in the matrix (which is enhanced by nonaffine deformations). As the matrix becomes stiffer, the nonaffine fluctuations are increasingly suppressed [Fig. 4.4]. The scaling

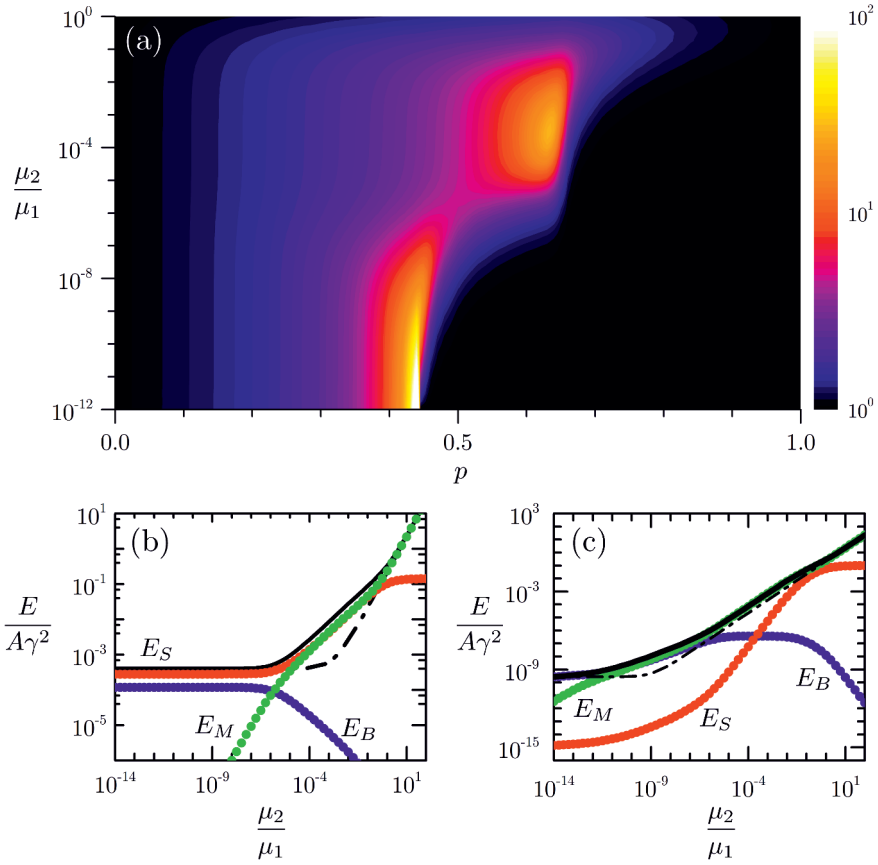

Figure 4.5: Mechanical enhancement in composites. (a) Enhancement of the shear modulus with respect to the summed moduli of the individual networks, $G/(G_1 + G_2)$ as a function of p and μ_2 for $\kappa_1 = 10^{-6}\mu_2 l_0^2$. (b,c) Different energy contributions to the shear modulus (E_b (blue): fiber bending; E_s (red): fiber stretching; E_m (green): matrix deformation) as a function of μ_2 for (b) $p = 0.65$ and (c) $p = 0.45$. The black line gives the total elastic energy and the dashed line the sum of the energies of the separate networks, so that the difference between the solid and the dashed line represents the mechanical enhancement.

of the nonaffine fluctuations with μ_2 and κ_1 is discussed in Appendix B [Fig. 4.7].

Mechanical enhancement

The main reason for the interest in composite materials is that the interplay between the different components can lead to highly synergistic properties, such as enhanced strength and rigidity[12, 13, 14, 15, 16, 17, 18]. We therefore consider the enhancement of the modulus of the composite network in comparison with the sum of the moduli of the individual networks [Fig. 4.5(a)]. The highest enhancement, with a modulus that exceeds those of the individual networks by up to a factor 10^2, is observed in the two crossover regions labeled SM and BM in Fig. 4.3(c). We can understand the origin of the enhancement in these regimes, by considering the different contributions to the modulus. At $p \approx p_{\mathrm{cf}}$ [Fig.4.5(b)], the modulus is dominated by bending contributions for small μ_2. These bending modes are suppressed by the elastic matrix when μ_2 increases [Fig. 4.4(b)], leading to a more affine deformation. However, this goes at the cost of increased fiber stretching, and this increase in stretching energy stiffens the network. As discussed above, at $p \approx p_{\mathrm{b}}$, the deformation of the fiber network is characterized by floppy modes, in which large clusters of fibers undergo rigid body motions without being strained. As the matrix becomes stiffer, these rigid body motions are suppressed at the cost of increased fiber bending [Figs. 4.4(b) and 4.4(c)]. Thus, while the enhancement around p_{cf} is caused by the suppression of bending modes, the enhancement around p_{b} is associated with an increase in fiber bending [Fig.4.5(c)].

Discussion

We have revealed a very rich mechanical behavior of composite networks. Small variations in composition can lead to large differences in mechanical response. This may be an important reason why composite structures are so abundant in biology, where adaptiveness is often crucial. Indeed, it has been argued that many biological networks have a connectivity in the vicinity of a critical regime[9], where they are most susceptible to small changes. Our

results show that these are also the regions where mechanical synergy is to be expected. As Fig. 4.5(a) shows, a non-trivial crosstalk between the two networks occurs only for specific compositions and stiffness ratios between the two networks. For densely cross-linked fiber networks ($p > p_{\mathrm{cf}}$), where the mechanics of the fiber network is dominated by affine stretching modes even in the absence of an elastic matrix, there is no enhancement. However, for bending-dominated fiber networks ($p_{\mathrm{b}} < p < p_{\mathrm{cf}}$), there is a significant range of matrix stiffnesses where strong enhancement is expected to occur. Recent experiments report the modulus of a mixture of two protein fiber networks with varying composition[17]. The network of the stiffest fibers was kept constant, while the stiffness of the soft background matrix was varied over a large range. A significant mechanical enhancement was found over approximately six decades in modulus of the soft network, with a maximum enhancement factor of approximately 3 with respect to the sum of the moduli of the separate networks. These experiments correspond to a vertical cross-section in Fig. 4.5(a), i.e. a variation in μ_1 at constant connectivity of the stiff network p. Even though the precise value of p is not known for the experimental system, it presumably lies between p_{b} and p_{cf}, since the network was argued to be in the bending-dominated regime. As shown in Fig. 4.5(a), our model also predicts a modulus enhancement in this regime over a range spanning approximately 6 decades in μ_1. The maximum enhancement of 3 found in the experiment suggests that the network is significantly below p_{cf}, and that an even stronger enhancement may be obtained for p values closer to the central force threshold.

While our focus has been on linear elasticity, we expect that also the non-linear response of composite networks will differ greatly from that of single-component networks. Fiber networks are known to become stiffer as the strain increases[7] due a transition from bending to stretching-dominated elasticity[32]. Recent experiments have shown that this strain stiffening can be suppressed completely when the fibers are embedded in a soft elastic ma-

trix [17]. Our results suggest that this may be the result of a suppression of bending modes already in the linear regime. Finally, the suppression of non-affine fluctuations by the background matrix leads to a more homogeneous stress distribution in the network. This should have large consequences for the nucleation and propagation of cracks in the material, and may thus contribute to the large increase in fracture strength found in double network hydrogels[15, 16].

Appendix A: The effect of the fiber bending rigidity

To investigate the effect of the fiber bending rigidity on the shear modulus of composite networks, we repeat the calculations of Fig. 4.2 for different values of κ_1. Results are shown in Fig. 4.6. For $\kappa_1 = 0$, the single fiber network becomes unstable at the central force isostatic threshold $p_{\text{cf}} = 0.651$ [Fig. 4.6(a)]. For this case, our simulations of composite networks are identical to previous findings for the so-called superelastic problem[29], consisting of central force spring networks, where a fraction p of the bonds have a stretch modulus $\mu_1 + \mu_2$ and a fraction $1 - p$ of the bonds have a stretch modulus μ_2. For all $\kappa_1 > 0$, the rigidity threshold is at $p_{\text{b}} \approx 0.442$ [Figs. 4.6(b-f)]. We see evidence for a bending to stretching transition at p_{cf} when the bending modulus is small, as a strong decrease of the shear modulus when p drops below p_{cf}. However, for $\kappa_1/\mu_1 l_0^2 \leq 10^{-2}$, bending becomes too costly so that this transition vanishes and the shear modulus is stretching-dominated for all $p > p_{\text{b}}$. The results of Fig. 4.6 have been used, together with those in Fig. 4.2, to characterize the different mechanical regimes of composite networks as a function of p, κ_1, and μ_2, as shown in Fig. 4.3.

Appendix B: The magnitude of the nonaffine fluctuations

As shown in Fig. 4.4(a), the nonaffine fluctuations show cusp-like peaks a both $p = p_{\text{cf}}$ and $p = p_{\text{b}}$. The peak in Γ at the central force isostatic point,

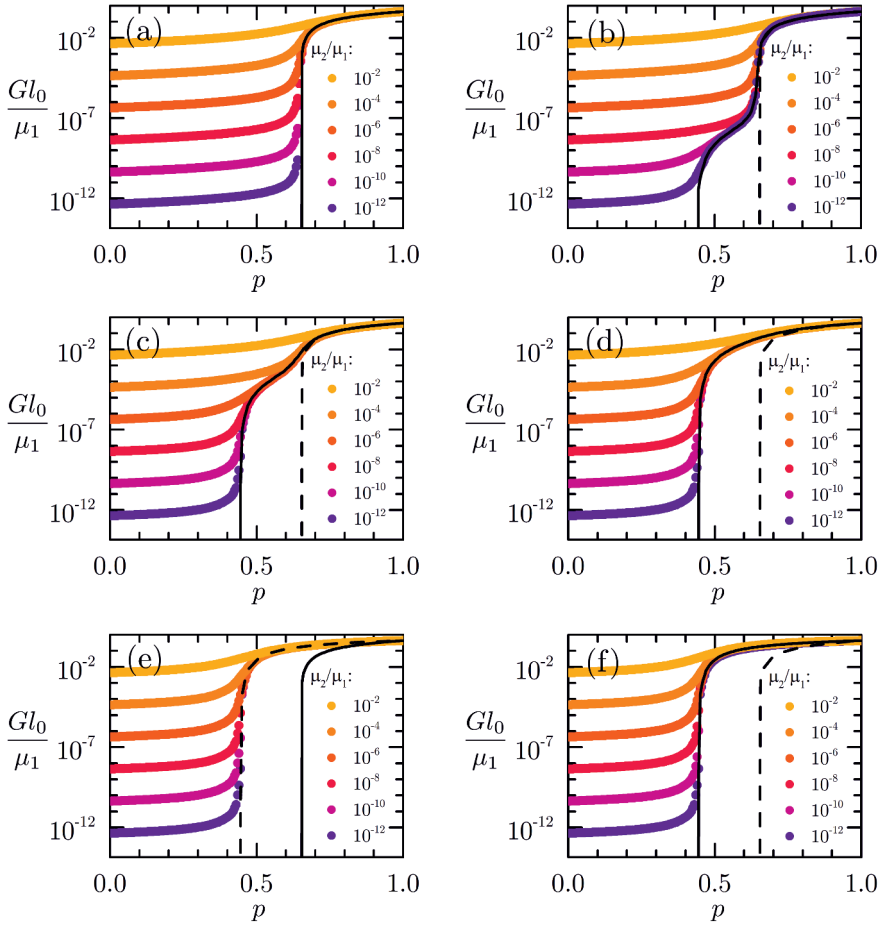

Figure 4.6: Elasticity of composite networks for different bending rigidity. Shear modulus G (in units μ_1/l_0) as a function of the bond probability p for a range of stiffnesses of the background matrix for different values of $\kappa_1/\mu_1 l_0^2$: (a) 0, (b) 10^{-8}, (c) 10^{-4}, (d) 10^{-2}, (e) 1, (f) 10^2 . The black line corresponds to $\mu_2 = 0$ and the dashed line to $\mu_2 = 0$ and $\kappa_1 = 0$. In each figure, the values of μ_2/μ_1 are (from top to bottom): 10^{-2}, 10^{-4}, 10^{-6}, 10^{-8}, 10^{-10}, 10^{-12}.

Γ_{cf}, is due to nonaffine bending fluctuations [Figs. 4.1(a) and 4.4(b)]. These fluctuations are reduced as the effective bending rigidity, $\kappa_{\text{eff}} = \kappa_1 + \mu_2 l_0^2$ increases. We find that $\Gamma_{\text{cf}} \sim (\mu_1/\kappa_{\text{eff}})^x$ with $x = 0.53 \approx 1 - \beta/\alpha$ [Fig.

4.7(a)].

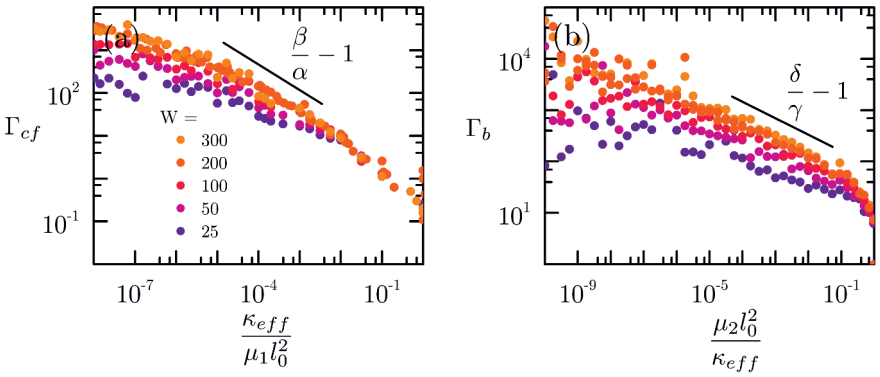

Figure 4.7: Nonaffine fluctuations in the two critical regions. (a) Peak in Γ at $p = p_{\mathrm{cf}}$ as a function of $\kappa_{\mathrm{eff}}/\mu_1$, and (b) peak in Γ at $p = p_{\mathrm{b}}$ as a function of $\mu_2/\kappa_{\mathrm{eff}}$, both for various lattice sizes.

The shear modulus at this point is determined by the bending energy, so that $G_{\mathrm{cf}} \sim \kappa_{\mathrm{eff}}\Gamma_{\mathrm{cf}} \sim \kappa_{\mathrm{eff}}^{\beta/\alpha}\mu_1^{1-\beta/\alpha}$. Note that a deviation from the scaling of Γ_{cf} is observed for small values of κ_{eff}, which we attribute to a finite-size effect: the finite size of the lattice limits the maximum size of the collective nonaffine modes. Indeed, we find that Γ_{cf} decreases as the lattice size decreases [Fig. 4.7(a)]. The peak in Γ at the bending rigidity threshold, Γ_{b} is determined by rigid rotations of fiber clusters [Fig. 4.1(b) and 4.4(c)]. An increase of the matrix stiffness suppresses these modes, so that Γ_{b} decreases as μ_2 increases [Fig. 4.7(b)]. However, this suppression goes at the cost of increased bending, so that the nonaffine fluctuations at this point are determined by a compromise between matrix stretching and fiber bending. We find that $\Gamma_{\mathrm{b}} \sim (\kappa_{\mathrm{eff}}/\mu_2)^y$ with $y = 0.33 \approx 1 - \delta/\gamma$, highlighting the critical state of the network for $\mu_2 \to 0$. The shear modulus at this point is mainly determined by the elastic energy of the matrix, so that $G_{\mathrm{b}} \sim \mu_2\Gamma_{\mathrm{b}} \sim \mu_2^{\delta/\gamma}\kappa_1^{1-\delta/\gamma}$. Again, we observe deviations from the scaling of Γ_{b} for small lattice sizes and small μ_2.

Appendix C: Effective bending rigidity of a fiber in an elastic medium

We consider an elastic rod of length L embedded in an infinite 2D elastic medium. Here, we treat the matrix as a continuous medium with shear modulus G_2. A bending deformation of the rod increases the total energy of the system[27]:

$$E = \frac{\kappa_1}{2} \int_0^L \left(\frac{\mathrm{d}^2 u}{\mathrm{d}x^2} \right)^2 \mathrm{d}x + \frac{\alpha_2}{2} \int_0^L u^2 \mathrm{d}x \tag{4.6}$$

where $u(x)$ is the transversal displacement of the rod as a function of the axial coordinate along the rod, and where the parameter α_2 represents the effective spring constant of the matrix, which is proportional to the shear modulus G_2 as discussed below. The first term represents the bending energy of the rod and the second term represents the elastic energy due to the deformation of the matrix. We have assumed that the length of the rod does not change upon bending so that we can neglect the stretching energy. We assume a deformation of the form

$$u(x) = u_0 \sin\left(\frac{n\pi x}{L}\right) \qquad \text{with } n = 1, 2, \ldots \tag{4.7}$$

Substitution in equation 4.6 then gives

$$E = \frac{n^4 \pi^4 u_0^2}{4L^3} \left[\kappa_1 + \alpha_2 (L/n\pi)^4 \right] \tag{4.8}$$

This can be interpreted as a the energy of a bent rod with an effective bending rigidity $\kappa_{\text{eff}} = \kappa_1 + \alpha_2 (L/n\pi)^4$.

While for a 3D medium, the effective spring constant is related to the shear modulus of the medium as $\alpha_2 \approx 4\pi G_2 / \ln(L/d)$ with a the diameter of the rod[27], for a 2D medium we can derive [33] $\alpha_2 \approx 4\pi G_2 / L$. Since the shear modulus of a triangular spring network is equal to $G_2 = \frac{1}{4}\sqrt{3}\mu_2 / l_0$, we finally find

$$\kappa_{\text{eff}} = \kappa_1 + A \mu_2 l_0^2 \tag{4.9}$$

with $A = \frac{\sqrt{3}}{n^4 \pi^3} (L/l_0)^3$. The prefactor A depends on the rod length L and on the mode number n. Around the central force isostatic point, the average

fiber length is $L = l_0/(1 - p_{\text{cf}}) \approx 2.8l_0$. Assuming that the dominant bending mode is the lowest energy mode, $n = 1$, we find $A \approx 1.3$, close to the value of unity used to collapse the data in Fig. 4.3.

Bibliography

[1] Broedersz, C. P. & MacKintosh, F. C. Modeling semiflexible polymer networks. *Rev. Mod. Phys.* **86**, 995–1036 (2014).

[2] Wilhelm, J. & Frey, E. Elasticity of stiff polymer networks. *Phys. Rev. Lett.* **91**, 108103 (2003).

[3] Head, D., Levine, A. & MacKintosh, F. Deformation of cross-linked semiflexible polymer networks. *Phys. Rev. Lett.* **91**, 108102 (2003).

[4] Head, D., Levine, A. & MacKintosh, F. Distinct regimes of elastic response and deformation modes of cross-linked cytoskeletal and semiflexible polymer networks. *Phys. Rev. E* **68**, 061907 (2003).

[5] Das, M., MacKintosh, F. C. & Levine, A. J. Effective medium theory of semiflexible filamentous networks. *Phys. Rev. Lett.* **99**, 038101 (2007).

[6] Broedersz, C. P., Mao, X., Lubensky, T. C. & MacKintosh, F. C. Criticality and isostaticity in fibre networks. *Nature Phys.* **7**, 983–988 (2011).

[7] Gardel, M. *et al.* Elastic Behavior of cross-linked and bundled actin networks. *Science* **304**, 1301–1305 (2004).

[8] Lieleg, O., Claessens, M. M. A. E., Heussinger, C., Frey, E. & Bausch, A. R. Mechanics of bundled semiflexible polymer networks. *Phys. Rev. Lett.* **99**, 088102 (2007).

[9] Sharma, A. *et al.* Strain-controlled criticality governs the nonlinear mechanics of fibre networks. *Nature Phys.* **12**, 584–587 (2016).

[10] Bausch, A. & Kroy, K. A bottom-up approach to cell mechanics. *Nature Phys.* **2**, 231–238 (2006).

[11] Wegst, U. & Ashby, M. The mechanical efficiency of natural materials. *Philos. Mag.* **84**, 2167–2181 (2004).

[12] Munch, E. *et al.* Tough, Bio-Inspired Hybrid Materials. *Science* **322**, 1516–1520 (2008).

[13] Wegst, U. G. K., Bai, H., Saiz, E., Tomsia, A. P. & Ritchie, R. O. Bioinspired structural materials. *Nature Mater.* **14**, 23–36 (2015).

[14] Jang, K.-I. *et al.* Soft network composite materials with deterministic and bio-inspired designs. *Nature. Comm.* **6**, 6566 (2015).

[15] Gong, J., Katsuyama, Y., Kurokawa, T. & Osada, Y. Double-network hydrogels with extremely high mechanical strength. *Adv. Mater.* **15**, 1155+ (2003).

[16] Sun, J.-Y. *et al.* Highly stretchable and tough hydrogels. *Nature* **489**, 133–136 (2012).

[17] Rombouts, W. H., Giesbers, M., van Lent, J., de Wolf, F. A. & van der Gucht, J. Synergistic Stiffening in Double-Fiber Networks. *Biomacromol.* **15**, 1233–1239 (2014).

[18] Rombouts, W. H., Colomb-Delsuc, M., Werten, M. W. T., Otto, S., de Wolf, F. A. & van der Gucht, J. Enhanced rigidity and rupture strength of composite hydrogel networks of bio-inspired block copolymers. *Soft Matter* **9**, 6936–6942 (2013).

[19] Huisman, E. M., Heussinger, C., Storm, C. & Barkema, G. T. Semiflexible Filamentous Composites. *Phys. Rev. Lett.* **105**, 118101 (2010).

[20] Bai, M., Missel, A. R., Klug, W. S. & Levine, A. J. The mechanics and affine-nonaffine transition in polydisperse semiflexible networks. *Soft Matter* **7**, 907–914 (2011).

[21] Zhang, L., Lake, S. P., Barocas, V. H., Shephard, M. S. & Picu, R. C. Cross-linked fiber network embedded in an elastic matrix. *Soft Matter* **9**, 6398–6405 (2013).

[22] Wada, H. & Tanaka, Y. Mechanics and size-dependent elasticity of composite networks. *EPL* **87**, 58001 (2009).

[23] Das, M. & MacKintosh, F. C. Mechanics of soft composites of rods in elastic gels. *Phys. Rev. E* **84**, 061906 (2011).

[24] Shahsavari, A. S. & Picu, R. C. Exceptional stiffening in composite fiber networks. *Phys. Rev. E* **92**, 012401 (2011).

[25] Maxwell, J. C. On the calculation of the equilibrium and stiffness of frames. *Phil. Mag.* **27**, 294–299 (1864).

[26] Mao, X., Stenull, O. & Lubensky, T. C. Effective-medium theory of a filamentous triangular lattice. *Phys. Rev. E* **87**, 042601 (2013).

[27] Brangwynne, C. *et al.* Microtubules can bear enhanced compressive loads in living cells because of lateral reinforcement. *J. Cell. Biol.* **173**, 733–741 (2006).

[28] Sahimi, M. & Arbabi, S. Mechanics of disordered solids. 2. Percolation on elastic networks with bond-bending forces. *Phys. Rev. B* **47**, 703–712 (1993).

[29] Garboczi, E. & Thorpe, M. Effective-medium theory of percolation on central-force elastic networks. 3. The superelastic problem. *Phys. Rev. B* **33**, 3289–3294 (1986).

[30] DiDonna, B. & Lubensky, T. Nonaffine correlations in random elastic media. *Phys. Rev. E* **72**, 066619 (2005).

[31] Heussinger, C. & Frey, E. Floppy modes and nonaffine deformations in random fiber networks. *Phys. Rev. Lett.* **97**, 105501 (2006).

[32] Onck, P., Koeman, T., van Dillen, T. & van der Giessen, E. Alternative explanation of stiffening in cross-linked semiflexible networks. *Phys. Rev. Lett.* **95**, 178102 (2005).

[33] Levine, A. J., Liverpool, T. B. & MacKintosh, F. C. Dynamics of rigid and flexible extended bodies in viscous films and membranes. *Phys. Rev. Lett.* **93**, 038102 (2004).

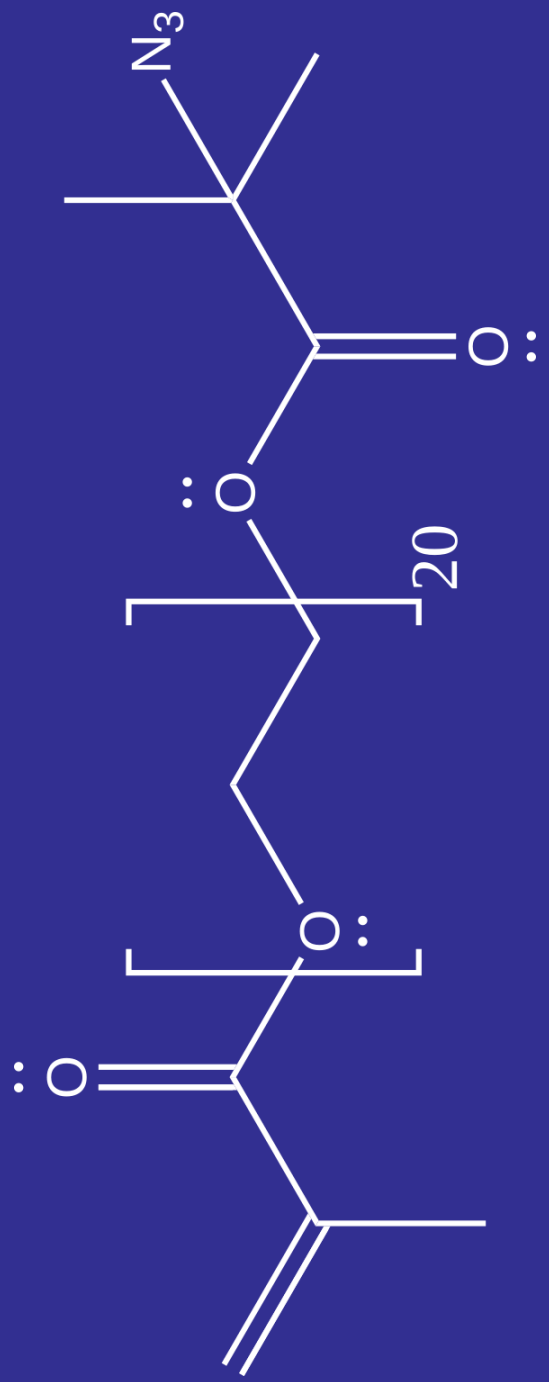
N3
O
O
20
O
O

CHAPTER 5

Synthesis of azide functionalized polymer colloids

Surface properties dictate interactions between colloids. Tuning these properties to assemble large structures of multiple colloids is a central theme in colloidal synthesis. To bring the flexibility of click chemistry to the surface of polymeric colloids we propose one-step synthesis of azide-functionalized colloids. For this we synthesize an azide-functionalized monomer that is co-polymerized during particle synthesis. By varying the amount of azide monomer we are able to tune the surface concentration of azide groups. This is particularly useful when working with supra molecular interactions as binding dynamics are exponentially dependent on the number of supramolecular bonds. Our results suggest a two order of magnitude increase of surface concentration compared to previously reported methods.

Manuscript in preparation as:
J.M. van Doorn, P.Hage, T. van de Laar, I.Voets and J. Sprakel: *Simple one-step synthesis of azide functionalized polymer colloids*

Introduction

Colloidal materials are defined by their inter-particle interactions. Repulsive interactions often lead to colloidal crystals or, if polydispersity is sufficiently high, to colloidal glasses. Conversely, attractive interactions lead to the formation of aggregates or at sufficiently high volume fraction colloidal gels. Making more complex structures would require more complex potentials which are more difficult to realize experimentally[14, 13]. The surface properties of colloidal particles are the key factor that determine the shape of the inter-particle potential. Controlling this surface chemistry gives much control over eventual potentials and opens up the way for engineered potentials. Many strategies exist to control surface chemistry such as surface intialized RAFT or ATRP, co-polymerization of charged monomers, silane chemistry and click chemistry[9, 4, 6, 3]. Click chemistry offers great versatility and efficiency in modifying any surface with a vast number of molecules[11]. However either an azide or an alkyne group has to be present on the surface. For inorganic particles this is readily achieved however the particle bulk material properties such as density and refractive index are much more difficult to control for inorganic particles[7, 10]. These properties are easily tunable in polymeric particles by changing the ratio of monomers. Functionalizing polymeric surfaces, however, requires either swelling of the polymeric particles or a solvent that dissolves the particles during modification[1, 8, 2]. Furthermore in many cases the strength of the interaction between particles depends greatly on the concentration of functional surface groups control of which is difficult to achieve with current methods.

In this chapter we present a simple one-step synthesis of polymeric azide-functionalized particles. By co-polymerizing azide-monomers in different quantities we have excellent control of the amount of azide groups on the surface. Our chemistry is compatible with previously reported methods that allow for refractive index and density matching, which greatly enhances the

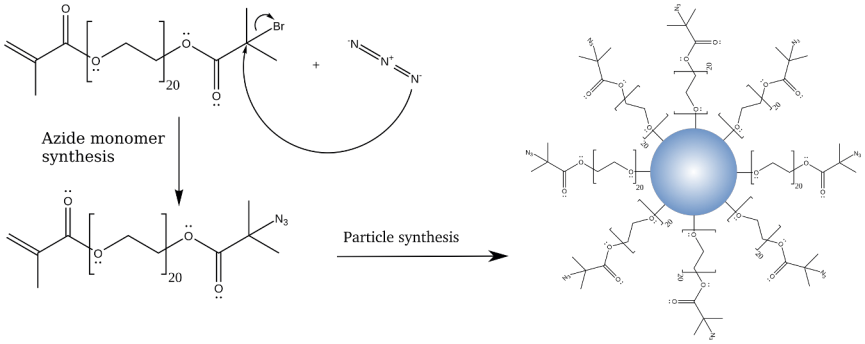

Figure 5.1: Schematic drawing of our synthesis.

versatility and applicability this modification.

Results and Discussion

Inspired by surface initiated polymerization methods we design an azide-functionalized co-monomer that can deliver azide groups to the surface of the polymeric particles[Fig. 5.1][5, 12]. Within this monomer a polymerizable methaclate group and a functional azide group are separated by a ≈20 unit PEG linker. This approach ensures maximal flexibility and accessibility of the azide goups once attached to the particle surface. To synthesize this monomer we first prepare,2-(2-bromoisobutyryloxy)-PEG-methacrylate . For this we perform a nucleophilic substitution reaction between Poly(ethylene glycol) methacrylate (PEG-MA) and α-Bromoisobutyryl bromide. Next we substitute the terminal bromine with an azide group by reacting with sodium azide to obtain our functionalized azide monomer[Fig. 5.1].

We synthesize our polymeric particles using a dispersion polymerization with Polyvinylpyrrolidone (PVP) as adsorbing polymer that will act as a steric stabilizer. Similar to previously reported syntheses we use a mixture of monomers that can be tuned for a desired refractive index and density. This will reduce excessive scattering and improve image quality when studying

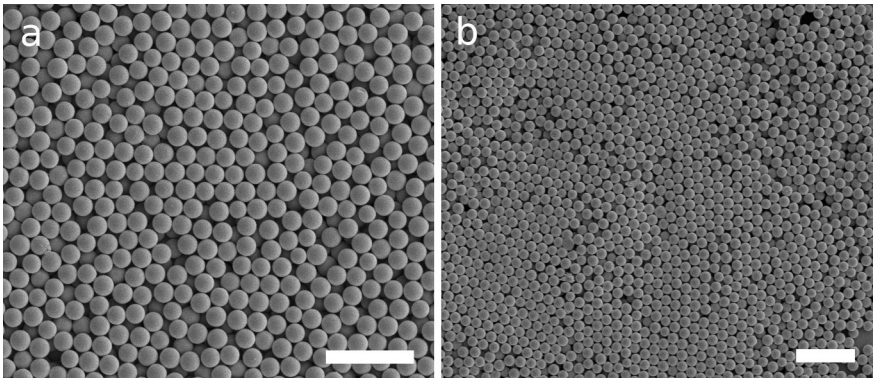

Figure 5.2: SEM image of colloids with (a) 0.1% and (b)3.0% azide monomer. Scalebars represent 5μm.

these particles with fluorescence microscopy. Density tuning of these particles reduces sedimentation which is particularly important when the modified surface induces attractive interactions that lead to the formation of large particle clusters. Our newly synthesized azide monomer that will provide the azide groups on the surface will act as a third monomer in this particle synthesis. Adding the azide monomer does not affect the quality of the particles. This is confirmed by Scanning Electron Microscopy (SEM) images that reveal low particle polydispersity and a consistent size throughout different reactions [Fig 5.2].

As surface properties largely define the inter particle potential, precise control over the surface concentration of azide groups is essential. We achieve this by varying the amount of azide monomer during the particle synthesis. To check whether we indeed have control over the surface concentration we attach a fluorescent Fluor 488-Alkyne dye to our particles via click-chemistry[Fig. 5.3]. After reacting with the dye we wash the particles 5 times with demineralized water to exclude any non-covalently bound dye molecules so that only dye molecules that are linked with the click reaction remain. We hypothesize that when more azide groups are present on the sur-

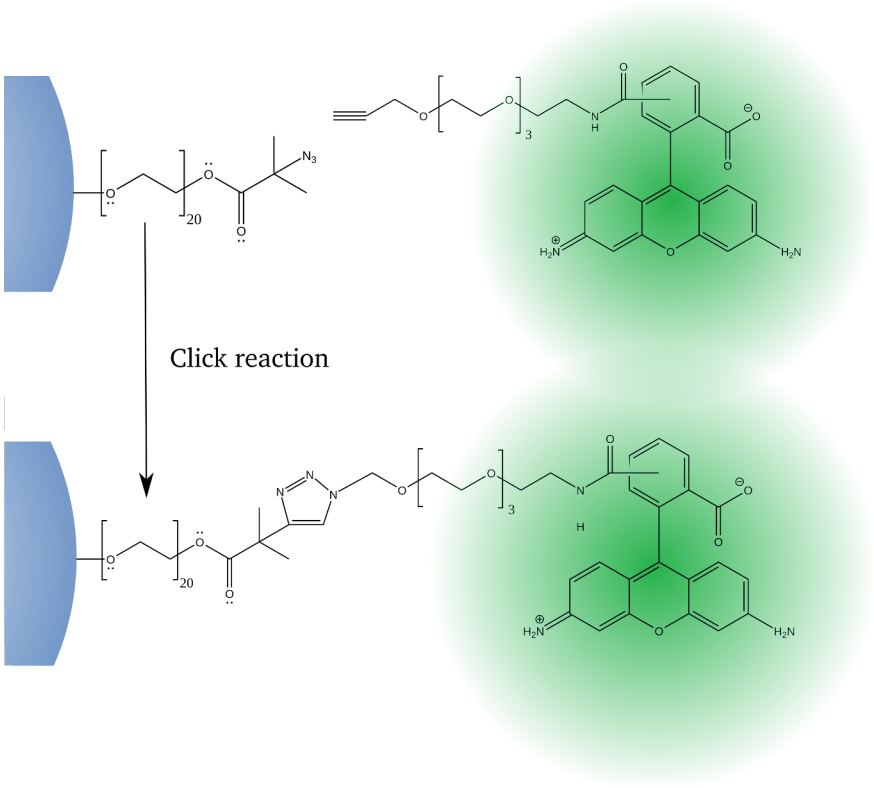

Figure 5.3: Schematic drawing click functionalization with a fluor 488 dye

face more dye molecules will attach and give a brighter fluorescence signal.

To test this hypothesis we synthesize five batches of particles, each with a different concentration of azide monomer and perform a click reaction with the Fluor 488 dye. For particles with a high concentration of azide mononer (3.0 % of the monomer) we expect that many dye molecule have attached to the surface. Indeed when we study particles with confocal microscopy, even though the molecules are much smaller than the diffraction limit, we see a bright fluorescent layer around the particles confirming that large amounts of dye are present on the surface[Fig. 5.4(b)]. However when we decrease the concentration of azide monomer to 0.1% of the monomer we expect a

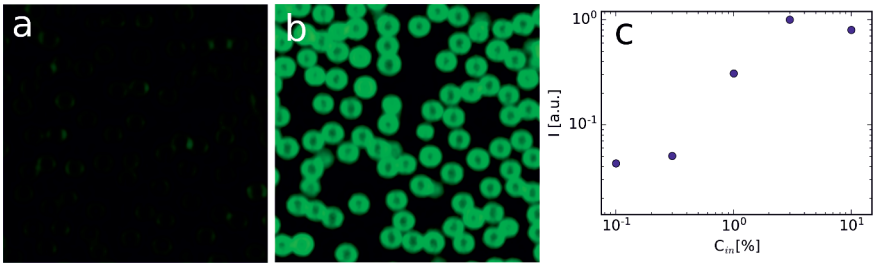

Figure 5.4: Confocal image of fluor-488 modified colloids with (a) 0.1% and (b)3.0% azide monomer. Intensity in (a) is enhanced 8 times.(c) Intensity versus azide monomer concentration. Intensity increases proportional with concentration until a plateau value is reached.

weak to no fluorescent signal and we indeed find a rather weak signal even after increasing the acquisition by a factor of 8 [Fig. 5.4(a)]. We quantify and compare the amount of fluorescence for the different azide monomer concentrations in figure 5.4(c) and find the fluorescence signal increases proportional to the azide monomer concentration until a plateau is reached around 3.0%. At this point saturation occurs either because the surface is saturated with azide groups or because previously attached dye molecules are hindering the attachment of additional dye molecules. We estimate the number of dye molecules on the surface by calculating the ratio of the available particle surface to the surface that one monomer occupies $d = \frac{A_a}{A_m}$ while assuming a homogeneous distribution of the azide monomer throughout the particle. For our sample with highest fluorescence and thus highest surface coverage we find $\frac{0.03 \cdot 4\pi \cdot 10^{-6}}{10^{-18}} = 3.7 \cdot 10^7$ dye molecules per particle as an upper limit. For the lower limit we use the 1.0% inimer point and find $\frac{0.01 \cdot 4\pi \cdot 10^{-6}}{10^{-18}} = 1.2 \cdot 10^7$ dye molecules per particle. Although crude estimates, these values suggests a two order of magnitude increase over previously reported densities for particles of similar size[8].

Conclusion

We have shown a simple one step method to functionalize polymeric colloidal particles. Our method combines the versatility of polymeric particles with easy surface modification previously only possible for inorganic particles. Furthermore our excellent control over surface concentration pushes the maximum surface coverage and paves the way for studying the complex assembly of particles via supra-molecular interactions.

Materials and methods

Preparation of 2-(2-bromoisobutyryloxy)-PEG-methacrylate

We add a mixture of 18.6 mL of α-*iso*-bromo-butyrylbromide in 60 mL dicholomethane (DCM) dropwise to a mixture of 50g poly(ethylene glycol)-methacrylate (PEG-MA), 15.2g triethylamine in 500mL DCM on ice in about 60 minutes under refluxing conditions. Once fully added we let the mixture react overnight. We filter the reaction mixture using a whatman filter and concentrate by rotary evaporation. We add clean DCM and wash four times against brine (saturated NaCl in H_2O) to remove impurities. We add $MgSO_4$ as a drying salt and filter before concentrating with rotary evaporation.

Azide modification

We add 26.19g of previously prepared 2-(2-bromoisobutyryloxy)-PEG-methacrylate to 5.24 g of sodium azide in 125 mL dimethylFormamide (DMF) and stir overnight at room temperature. We add 100 mL of demineralized water and 100mL chloroform and collect the organic layer. After washing the organic layer three times with demineralized water, we add $MgSO_4$ as a drying salt and filter before concentrating with rotary evaporation obtaining a viscous pale yellow liquid.

C_{am} [%]	V_{am} [μl]	R_h [nm]
0.1	10	549
0.3	30	521
1.0	100	457
3.0	300	512
10.0	1000	595

Table 5.1: Amounts of azide monomer used in particle synthesis to obtain various surface concentrations and resulting hydrodynamic radii obtained with dynamic light scattering (DLS).

Particle synthesis

To a 250mL round bottom flask we add 85 mL methanol, 15 mL demineralized water, 2.8mL 2,2,2-Trifluoroethyl methacrylate (TFEMA), 7.2 mL tert-Butyl methacrylate (tBMA), a volume of azide monomer according to table 5.1, 4g polyvinylpyrrolidone (PVP) and 200mg azobisisobutyronitril (AIBN). We buble the mixture with N_2 for 15 minutes and react overnight while tumbling at 65° C. After reacting, we filter the reaction mixture over a coffee filter and wash against water three times using centrifugation. This results in 100mL of particle suspension with an approximate volume fraction of ϕ =0.1.

Click reaction

In a 1.5mL eppendorf reaction vessel we add 400μl 1mM tris(3-hydroxypropyltriazolylmethyl)amine (THPTA) solution, 28.5μl 4mM Cu(II)SO_4, 50μl particle suspension, 200μl dye solution (excess) and 400μl 6.25mM sodium ascorbate. We let the mixture react for 2h in an incubator shaker at 25° C. After reacting we wash the modified particles five times with demineralized water to remove dye that has not bound to the particles.

Scanning Electron Microscopy

To conduct Scanning electron microscpy (SEM) on the polymer particles, a small amount of washed particles was transferred onto an SEM grid and dried at room temperature. The samples were sputter coated with a layer of gold for 1 min at 25mA prior to analysis (Emitech K550). Particles were analyzed using a FEI Quanta 3D FEG instrument (SEM/FIB). The voltage and spot size were set at 3kV and 4.5 respectively.

Confocal Microscopy and analysis

Confocal experiments are carried out with a Nikon C2 confocal microscope with a 60x immersion objective. All surface concentration were imaged with identical settings. For samples with low fluorescence signal multiple images are taken and summed into a resulting 16 bit image. The images are subsequently analyzed by taking the average intensity while excluding pixels with a value lower than 50 and higher than 65535 to exclude noise and saturated pixels respectively. Finally all average intensities are normalized to the highest intensity found in all samples (3% azide monomer).

Bibliography

[1] Dana R. Breed, Raymond Thibault, Fang Xie, Qian Wang, Craig J. Hawker, and David J. Pine. Functionalization of polymer microspheres using click chemistry. *Langmuir*, 25(8):4370–4376, 2009. PMID: 19260650.

[2] Rémi Dreyfus, Mirjam E. Leunissen, Roujie Sha, Alexei Tkachenko, Nadrian C. Seeman, David J. Pine, and Paul M. Chaikin. Aggregation-disaggregation transition of dna-coated colloids: Experiments and theory. *Phys. Rev. E*, 81:041404, Apr 2010.

[3] Anthony J. Kim, Paul L. Biancaniello, and John C. Crocker. Engineering dna-mediated colloidal crystallization. *Langmuir*, 22(5):1991–2001, 2006. PMID: 16489780.

[4] Anthony J. Kim, Vinothan N. Manoharan, and John C. Crocker. Swelling-based method

for preparing stable, functionalized polymer colloids. *Journal of the American Chemical Society*, 127(6):1592–1593, 2005. PMID: 15700965.

[5] Thomas E Kodger, Rodrigo E Guerra, and Joris Sprakel. Precise colloids with tunable interactions for confocal microscopy. *Scientific reports*, 5:14635, 2015.

[6] Yu Li and Brian C. Benicewicz. Functionalization of silica nanoparticles via the combination of surface-initiated raft polymerization and click reactions. *Macromolecules*, 41(21):7986–7992, 2008.

[7] Marie-Alexandra Neouze and Ulrich Schubert. Surface modification and functionalization of metal and metal oxide nanoparticles by organic ligands. *Monatshefte für Chemie - Chemical Monthly*, 139(3):183–195, Mar 2008.

[8] Joon Suk Oh, Yufeng Wang, David J Pine, and Gi-Ra Yi. High-density peo-b-dna brushes on polymer particles for colloidal superstructures. *Chemistry of Materials*, 27(24):8337–8344, 2015.

[9] C. Perruchot, M. A. Khan, A. Kamitsi, S. P. Armes, T. von Werne, and T. E. Patten. Synthesis of well-defined, polymer-grafted silica particles by aqueous atrp. *Langmuir*, 17(15):4479–4481, 2001.

[10] Reisa A Sperling and Wolfgang J Parak. Surface modification, functionalization and bioconjugation of colloidal inorganic nanoparticles. *Philosophical Transactions of the Royal Society A: Mathematical, Physical and Engineering Sciences*, 368(1915):1333–1383, 2010.

[11] Christian Spiteri and John E Moses. Copper-catalyzed azide–alkyne cycloaddition: Regioselective synthesis of 1, 4, 5-trisubstituted 1, 2, 3-triazoles. *Angewandte Chemie International Edition*, 49(1):31–33, 2010.

[12] Jan Maarten van Doorn, Joris Sprakel, and Thomas E Kodger. Temperature-triggered colloidal gelation through well-defined grafted polymeric surfaces. *Gels*, 3(2):21, 2017.

[13] Francesco Varrato, Lorenzo Di Michele, Maxim Belushkin, Nicolas Dorsaz, Simon H. Nathan, Erika Eiser, and Giuseppe Foffi. Arrested demixing opens route to bigels. *Proceedings of the National Academy of Sciences*, 109(47):19155–19160, 2012.

[14] Yu Wang, Yufeng Wang, Xiaolong Zheng, Étienne Ducrot, Jeremy S Yodh, Marcus Weck, and David J Pine. Crystallization of dna-coated colloids. *Nature communications*, 6:7253, 2015.

Part II

Strength

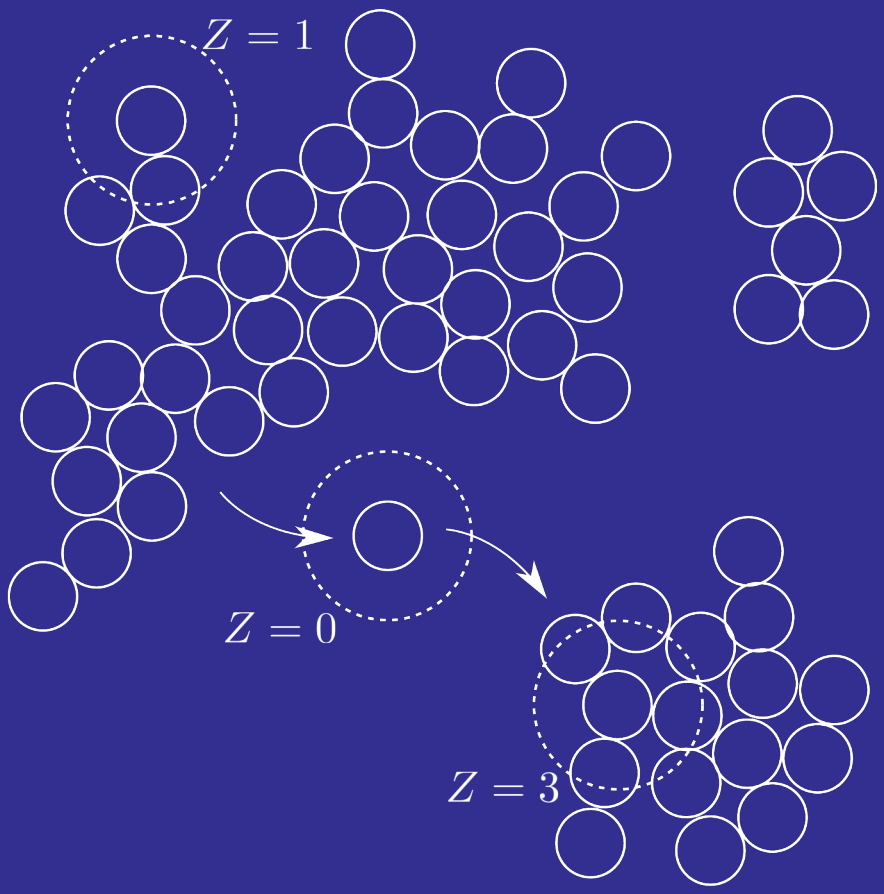
$Z = 1$
$Z = 0$
$Z = 3$

CHAPTER 6

Linking particle dynamics to local connectivity in colloidal gels

Colloidal gels are a prototypical example of a heterogeneous network solid whose complex properties are governed by thermally-activated dynamics. In this chapter we experimentally establish the connection between the intermittent dynamics of individual particles and their local connectivity. We interpret our experiments with a model that describes single-particle dynamics based on highly cooperative thermal debonding. The model, in quantitative agreement with experiments, provides a microscopic picture for the structural origin of dynamical heterogeneity in colloidal gels and sheds new light on the link between structure and the complex mechanics of these heterogeneous solids.

This chapter was published as:

J.M. van Doorn, J. Bronkhorst, R. Higler, T. van de Laar and J. Sprakel: *Linking Particle Dynamics to Local Connectivity in Colloidal Gels*, Physical Review Letters, 118, **(2017)**, 188001

Introduction

Attractive interactions can drive a dilute colloidal suspension towards a solid state formed by a sample-spanning and mechanically rigid particle network [28, 26]. These colloidal gels are nonequilibrium solids, kinetically arrested en route to their equilibrium state of solid-liquid coexistence [19]. Particle gels are characterized by strong heterogeneity in local connectivity, mesoscopic structure and their dynamics and mechanics [8, 5, 10, 6]. The microstructure and internal dynamics of colloidal gels can be directly observed with optical microscopy at the single-particle level. As a consequence, gels form a testing ground to explore the complex and length-scale dependent mechanics of heterogeneous solids. Colloidal gels derive their rigidity from physically bonded gel strands and nodes that form a percolating elastic network. The linear elasticity of gels is governed by the network architecture and its thermal fluctuations [15, 23]. By contrast, the gradual aging of gels to a denser state [3, 28] and their nonlinear response to applied stresses [25, 13], is governed by events occuring at the much smaller length scale of individual particles. Since the bonds between the particles are typically weak, single particles can debond from strands in the gel by thermally activated bond breaking [17]. On longer time scales, this results in the restructuration of the gel network, causing it to coarsen, age and relax internal stresses built up during gelation [20]. Moreover, thermal activation at the single-particle level plays a crucial role in processes of fatigue that preempt stress-induced failure of the gel [25]. To date, quantitative descriptions of these thermally activated phenomena have relied on mean-field approximations [17]. Yet, the inhomogeneity in local coordination that is intrinsic to gels, must play a large role in the intermittent debonding dynamics that are at the origin of this complex nonlinear behavior. As a result, linking the structure of colloidal gels to their nonlinear mechanics has remained challenging, in particular as the relationship between local connectivity and thermally activated dynamics of single

particles is not clearly established.

In this chapter we explore the connection between the local connectivity and intermittent bonding-debonding dynamics of individual particles in colloidal gels. We use quantitative three-dimensional microscopy to experimentally probe this relationship in colloidal gels formed from colloids that interact by means of short-ranged attractions. We show how the experimental data can be quantitatively described with a microscopic model that describes particle debonding as a strongly cooperative thermally-activated event depending on the local bonding structure. This allows us to explain how the complex ensemble-averaged mean-squared displacement results from the convolution of different particle species within a single gel. Our results illustrate how the heterogeneous dynamics characteristics of strongly disordered solids emerge from their complex and inhomogeneous local network structure.

We study gels formed from poly(methyl methacrylate) (PMMA) particles, synthesized as detailed in Ref. [1]. The particles have a radius $a = 709$ nm and a polydispersity of $\sim 5\%$, as determined from static light scattering. The particles are suspended at a volume fraction $\phi = 0.20$ in an index- and density-matching solvent mixture. The solvent is saturated with tetrabutylammonium bromide (TBAB) to screen charge interactions; we note that even at saturation, weak electrostatic interactions remain [22]. Attractive forces are induced by the addition of polystyrene ($M_w = 105$ kg/mol, $M_w/M_n = 1.06$, $c^* = 41.6$ mg/ml) as a depletant, which has a radius of gyration $R_g \approx 10$ nm, resulting in a short-range depletion attraction with $R_g/a = 0.014$. Three-dimensional image stacks are acquired with confocal fluorescence microscopy, from which particle positions and trajectories are determined with a resolution $dr_{res,xy} = 10$ nm and $dr_{res,z} = 40$ nm [11]. We benchmarked this locating approach with state-of-the-art iterative methods [14], yielding identical results (see Appendix).

Upon increasing the polymer concentration c_p, calculated in the free (liquid) volume, the structure of the sample transitions from a fluid of isolated parti-

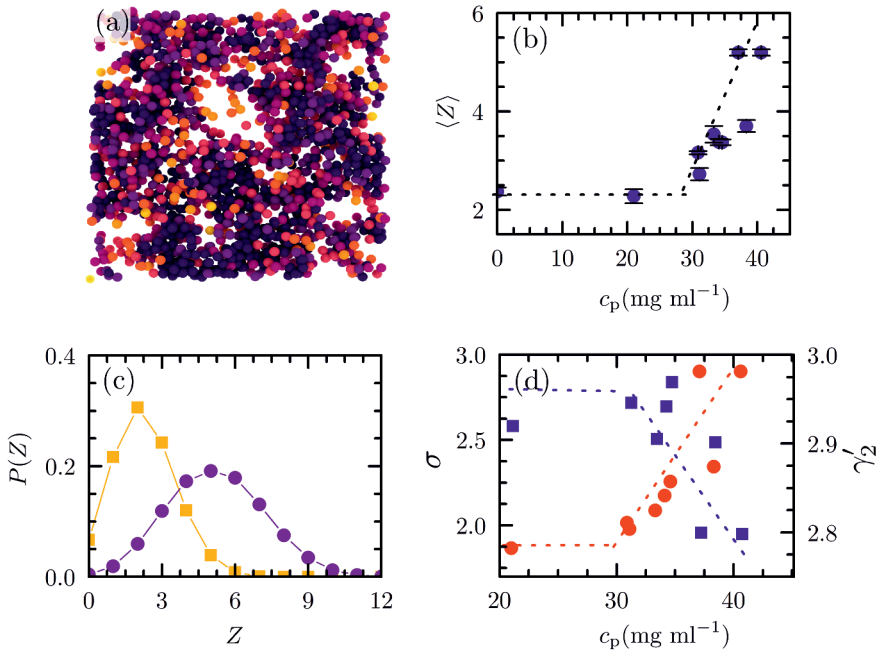

Figure 6.1: (a) Computer-generated rendering of a gel ($c_p = 37.1$ mg/ml); particles color coded with their value of Z (from dark blue $Z \geq 6$ to yellow $Z = 1$). (b) $\langle Z \rangle$ as a function of c_p; dotted lines to guide the eye. (c) $P(Z)$ for a liquid $c_p = 21.0$ mg/ml (squares) and a gel $c_p = 37.1$ mg/ml (circles). (d) Distribution width σ (circles) and kurtosis γ_2' (squares) of the distribution $P(Z)$ as a function of c_p; dotted lines to guide the eye.

cles, into a fluid of small and dynamic clusters [18]. At a threshold depletant concentration a sample-spanning gel forms [Fig. 6.1(a)]. The phase behavior of this experimental system was studied in detail previously [19, 21]. To evaluate the sample microstructure, we first calculate the ensemble-averaged and static coordination number $\langle Z \rangle$ from snapshots of the three-dimensional gel structure, where Z is determined based on proximity, with a cutoff at the first minimum in the pair correlation function. We note that the exact choice of this criterion varies between different studies [16, 19, 24], but has no substantial influence on the result (see appendix). We confirm that the large majority

of neighbors identified in this way are mechanically bonded, by considering their debonding kinetics (see appendix). As the attraction strength increases we see a transition from a low, but finite, value of $\langle Z \rangle$ in the liquid state, and a rapid growth in the coordination number as the sample transforms into an aggregated colloidal gel [Fig. 6.1(c)] [5]. However, the average coordination number does not provide insight into the strong intrinsic heterogeneity in the microstructure of colloidal gels, which becomes visible in a computer-generated representation of our experimental system in which the particles are color coded according to their instantaneous value of Z [Fig. 6.1(a)]. Indeed, calculation of the probability $P(Z)$ reveals a relatively wide distribution; the local structure becomes noticeably more heterogeneous, evidenced from the increase in width σ and decrease of the kurtosis γ_2', which is 3 for a pure Gaussian, above the gel point [Figs. 6.1(c) and 6.1(d)].

The microscopic dynamics of colloidal systems are conventionally probed by the time- and ensemble-averaged mean-squared displacements (MSD) $\langle \Delta r^2 \rangle$ [Fig. 6.2(a)]. At low attraction strengths a diffusive $\langle \Delta r^2 \rangle \propto t$ is found [Fig. 6.2(a)]. Increasing c_p leads to an increase in the depletion attraction, which is partially countered by electrostatic repulsion; this leads to a gel transition at $c_p \sim 33$ mg/ml, where the depletion attraction U becomes large enough to result in percolation. This can also be seen by plotting the value of the MSD at $t = 498$s as a proxy for the low-frequency particle mobility [Fig. 6.2(b)]. As a consequence, the material behaves as a solid and $\langle \Delta r^2 \rangle$ exhibits a time-independent localization plateau at short t which turns into diffusive behavior at larger t.

The self-part of the MSD is a measure for the local dynamics of single particles. To illustrate the fact that the internal gel dynamics are strongly length-scale dependent, we compare these data to the distinct part of the MSD $\langle \Delta r^2 \rangle_D$ [Figs. 6.2(c) and 6.2(d)]. The distinct, or two-point, mean-squared displacement, computed as described elsewhere [4], probes the correlated motion of particles transmitted through the medium. As such they are

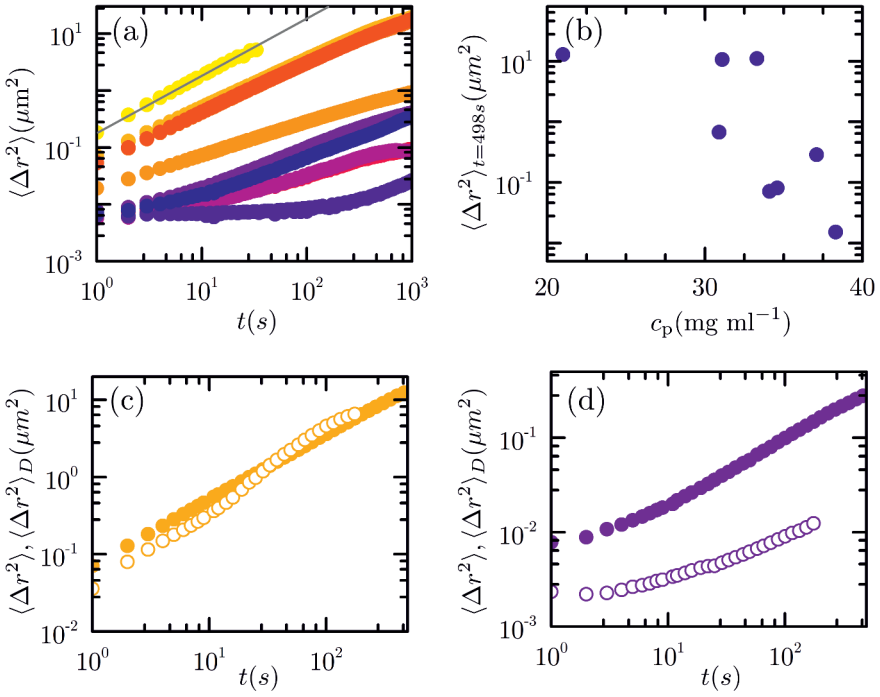

Figure 6.2: (a) $\langle \Delta r^2 \rangle$ for (top to bottom) c_p =0, 21.0, 30.9, 31.1, 33.3, 34.1, 34.6, 37.1, 38.3, 40.6 mg/ml. (b) $\langle \Delta r^2 (t = 498\text{s}) \rangle$ versus c_p. (c),(d) self (closed symbols) and distinct part (open symbols) of the MSD for a liquid (c)($c_p = 21.0$ mg/ml) and gel (d)($c_p = 37.1$ mg/ml).

a measure for the global, rather than local, properties of the gel. For samples in the fluid, just prior to the liquid-solid transition, the self- and distinct-parts of the MSD overlap within experimental error [Fig. 6.2(c)]. This indicates that there are no appreciable differences between local and global dynamics. By contrast, just above the gel threshold the distinct $\langle \Delta r^2 \rangle_D$ is almost an order of magnitude lower than the self-part of the MSD [Fig. 6.2(d)]. The gel is more rigid at the macroscopic scale, than that what is experienced by individual particles locally. Apparently, the dynamics of single particles in the gel are strongly affected by local structures; insight into these effects cannot be

obtained by ensemble averaging.

We hypothesize that single-particle dynamics, as measured by the self-part of the MSD, can be described by a specific sequence of events. Particles are first bonded to their neighbors in the gel network by bonds of strength U/k_BT. Under the action of thermal fluctuations, particles spontaneously debond from the gel with a characteristic rate $k_{d,Z}$; after debonding a particle will diffuse through the viscous medium with a rate D. This motion persists, until the particle collides with the gel network and re-attaches by forming new bonds. Thus, particles can exist in two states, bound and free, each characterized by different dynamics.

We can experimentally evidence the existence of these two populations by determining the probability distribution $P(\Delta r^2(t))$ of MSD values for individual particles at a particular lag time $t = 498$ s. A sample in the fluid states exhibits a distribution with a single population of freely diffusing particles [Fig. 6.3(a)], also illustrated by the linear dependence of the ensemble-averaged MSD with time [Fig. 6.2(a)]. By contrast, a sample in the gel state reveals two populations; a major fraction of the particles is bonded and exhibits a low mobility, whereas a secondary peak signals the particles which have debonded and diffuse through the solution [Fig. 6.3(b)]. Note that this diffusive population has a lower effective diffusion coefficient than particles in the repulsive liquid, probably due to the fact that not only singlets, but also small clusters debond and diffuse. These two populations are clearly visible, except for the shortest correlation times, where their Δr^2 values overlap, so that a single peak remains [Figs. 6.3(c) and 6.3(d)].

Assuming no significant contribution by small diffusing clusters, the self-part of the MSD of a single particle $\Delta r^2(t)$ can be split into two contributions. (i) In the first, free diffusion occurs during a characteristic time τ_f, during which $\Delta r^2(t) = 6Dt$. (ii) In the second thermal fluctuations of a particle in its bonded state, during a time τ_b, can be decomposed into two contribu-

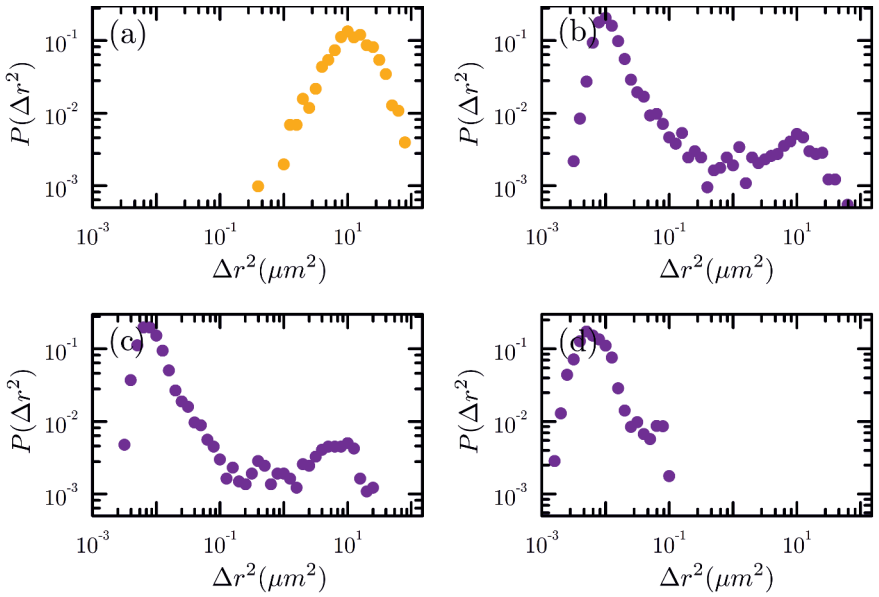

Figure 6.3: Probability distributions P of single-particle MSD at $t = 498$s for $c_p = 21.0$ (a) and 37.1 mg/ml at $t = 498$s (b), $t = 248$s (c) and $t = 1$s (d).)

tions: (a) bonded particle pairs will exhibit bond-length fluctuations in the attractive potential well, with a characteristic amplitude, from dimensional analysis, $\delta_{BL} \sim (k_B T R_g^2/U)^{1/2}$. (b) the gel network as a whole will exhibit collective fluctuations, which displaces particles within the same strand in sync. These collective fluctuations are mechanical excitations of the solid as a whole and their amplitude scales as $\delta_C \sim (k_B T/G)^{1/3}$, with $G \sim U/a^3$ the shear modulus of the gel. If we define $\alpha_b = \tau_b/(\tau_b + \tau_f)$ as the fraction of time a particle resides in a bonded configuration, the time-averaged MSD of a single particle can be approximated as

$$\Delta r^2(t) = (1 - \alpha_b)6Dt + \alpha_b({\delta_{BL}}^2 + {\delta_C}^2). \tag{6.1}$$

Based on realistic estimates for $R_g \approx 10$ nm, U of order $k_B T$ and $a = 709$ nm, we find that $\delta_{BL} \ll \delta_C$, such that $({\delta_{BL}}^2 + {\delta_C}^2) \approx {\delta_C}^2$. We note that, in our experiments, only vibrations that exceed the spatial resolution dr_{res} of

the particle locating algorithm can be detected. Smaller vibrations will result in a observed MSD plateau of ${\delta_C}^2 \approx dr_{res}^2$.

For the sake of simplicity, we presume that the diffusion of debonded species occurs at a rate $D = {}^{k_B T}/_{6\pi\eta a}$, where $\eta = 2$ mPa·s is the viscosity of the suspending medium. The time a debonded particle remains free τ_f is governed by the diffusion-limited collisions of free colloids with the gel strands. The characteristic time a particle resides in a bound state is governed by thermally activated dynamics. In an Eyring approach, the rate of dissociation of a single bond is described as $k_{d,1} = \omega_0 \exp\left[-U/k_B T\right]$, where ω_0 is the attempt frequency [9]. For a particle to detach from the gel network, all Z bonds that connect it to its neighbors must be ruptured. Breaking one bond, while the particle stays in place due to the remaining $Z - 1$ bonds, leads to rapid restoration of the broken bond with a rate k_a. Assuming that $k_a \gg k_{d,1}$, particle detachment from the network will only occur if all Z bonds break simultaneously [17]. Thus particle detachment is strongly cooperative with a rate $k_{d,Z} = (k_{d,1})^Z$. The typical time a particle remains bonded becomes $\tau_b = \frac{1}{\omega_0}\left[\exp\left(ZU/k_B T\right) - 1\right]$,where the term -1 ensures that the bonding time vanishes as $Z \to 0$. Substituting these results in Eq.6.1 gives a microscopic expression for the single-particle mean-squared displacement as

$$\Delta r^2(Z,t) = 6Dt + \frac{e^{ZU/k_B T} - 1}{e^{ZU/k_B T} - 1 + \omega_0 \tau_f}\left({\delta_C}^2 - 6Dt\right). \qquad (6.2)$$

This expression predicts a distinct dependence of the single-particle dynamics on its local coordination number Z. From our experimental data, we determine the value of $\Delta r^2(Z,t)$ at a fixed lag time $t = 498$s, and plot these as a function of the average Z for the particle during the length of our experimental observations [symbols in Fig. 6.4(a)]. To avoid mathematical complexity we use the time-average coordination number as a proxy for the single-particle connectivity. We note that this is an approximation; a comprehensive theory would require taking into account the entire time path of connectivity for each particle $Z(t)$.

We fit these experimental data to the theoretical model [Eq. 6.2]; we determine δ_C from the plateau in the MSD at high values of Z, and fit the parameters U and $\omega_0\tau_f$, the ratio of the frequency of debonding attempts and reassociations. The predictions from the microscopic theory are in excellent agreement with the experimental data [symbols in Fig. 6.4(a), see appendix for the fitting values]. Both data sets, for different polymer concentrations, can be fitted with $\omega_o\tau_f \ll 1$, thus confirming the validity of the assumption that $k_a \gg k_{d,1}$. Moreover, we find that the weaker the gel, i.e. at lower c_p, the larger the amplitude of collective fluctuations; $\delta_C = 0.33$ μm for gels at $c_p = 30.9$ mg/ml and $\delta_C = 0.12$ μm for 34.1 mg/ml. This is consistent with the qualitative trend predicted by the scaling relation above.

The effective bonding energies we need to fit the data in proximity to the gel point are of the order of $\sim$ 1-2 k_BT. This is of the correct order of magnitude, but a factor of 2 smaller than the value reported previously for gels of the same particles at similar ϕ but for a slightly longer-ranged attraction with $R_g/a = 0.059$[19], while for our gels $R_g/a = 0.014$. We also note that this is almost an order of magnitude lower than the depth of the depletion attraction calculated with the Asakura-Oosawa model [2], which assumes only hard sphere repulsions. We attribute this to the still significant electrostatic repulsion known to act between PMMA particles in apolar solvents even in presence of the TBAB electrolyte [22]. In particular for small depletants, the presence of residual charges can lead to drastic weakening of the effective attractions.

These data illustrate the intimate link between single-particle dynamics and local connectivity. To further substantiate these findings we probe the evolution of the coordination number for a single particle as a function of time. For a weakly connected particle, strongly intermittent fluctuations occur between bonded $Z > 0$ and unbonded $Z = 0$ states [Fig. 6.5(a)]; the continuous debonding and diffusion allows the particle to travel significant distances over the course of several minutes before it exits the field of view

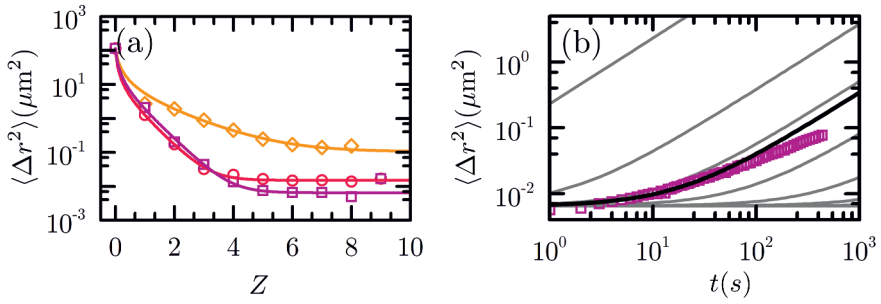

Figure 6.4: (a) Single-particle MSD at $t = 498$ s versus Z from experiments (symbols) and model described in the text (solid lines) for $c_p = 30.9$ mg/ml(diamonds), 34.1 mg/ml (circles) and 34.6 mg/ml (squares). (b) Experimental ensemble-averaged $\langle \Delta r^2 \rangle$ (symbols, $c_p = 34.6$ mg/ml) and prediction by Eq. 6.3 (solid black line). The gray lines are the contributions to $\langle \Delta r^2 \rangle$ for different (top to bottom) $Z = 0$, 1, 2, 3, 4, 5, 6.

[Fig. 6.5(c)]. By contrast, a strongly coordinated particle shows fluctuations in coordination number of ± 1 [Fig. 6.5(b)], but remains connected over the entire length of the experiment of 5000s, and as a consequence only exhibits strongly localized positional fluctuations [Fig. 6.5(d)].

Finally, with a quantitative microscopic description for the effect of connectivity on single-particle dynamics [Eq.6.2], we attempt to reconstruct the ensemble-averaged mean-squared displacement. To do so, we must weight the ensemble-average using the distribution of coordination numbers $P(Z)$ as a weighting function:

$$\langle \Delta r^2(t) \rangle = \sum_Z P(Z) \Delta r^2(Z,t). \tag{6.3}$$

With the values of U and $\omega_0 \tau_f$ determined from our experimental data [Fig. 6.4(a)] and $P(Z)$ obtained directly from the static structure of the gel, we can now predict the ensemble-averaged MSD. Indeed, without adjustable parameters, we find that the reconstructed $\langle \Delta r^2(t) \rangle$ based on our model for single

particle dynamics is in reasonable quantitative agreement with the ensemble-averaged MSD determined directly from experiments [Fig. 6.4(b)]. This highlights the self-consistency of our description. Moreover, it enables us to deconvolve the ensemble-average into the different populations of particles with different local coordination numbers Z [solid gray lines, Fig. 6.4(b)]. This provides a direct and quantitative explanation for the distinct dynamical heterogeneities characteristic of colloidal gels. We have presented experimental

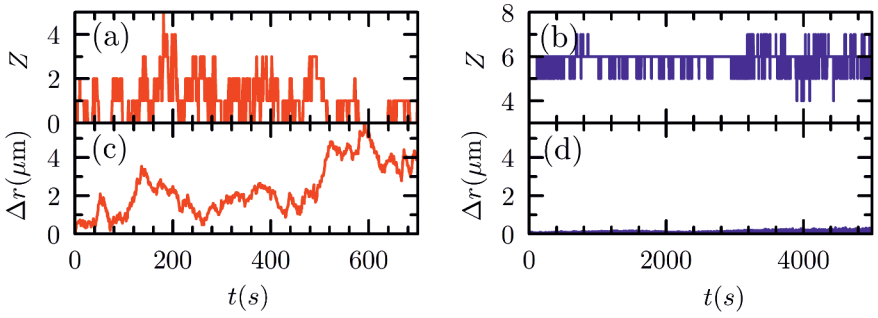

Figure 6.5: Thermal fluctuations in Z of a single particle (a),(b) and its corresponding displacement Δr (c),(d) for a weakly connected (a),(c) and highly connected (b),(d) particle in the same gel at $c_p = 37.1$ mg/ml.

data and theoretical analysis that explains how the heterogeneous dynamics of colloidal gels derives from the large inhomogeneities in local connectivity. The quantitative description of single-particle dynamics based on the local structure could form a stepping stone to develop microscopic descriptions of processes, such as aging, syneresis or stress-induced fatigue, in which the local microstructure evolves over time under the action of thermally activated particle rearrangements. Here, we have only considered particle rearrangements to occur through debonding and reassociation onto the gel network. Even though this provides a reasonable approximation, given the agreement between our experiments and the model, other thermally-activated modes of particle motion, such as the sliding of a particle along a gel strand without debonding entirely, also exist and must be accounted for, to arrive at a

complete description of gel dynamics.

Appendix

Experimental system

PMMA-PHSA particles of 700 nm radius are synthesized using dispersion polymerisation of methyl-methacrylate (MMA, Sigma) in hexane and dodecane (80 degrees celsius, 2 hours) using AIBN as a radical initiator [27]. The particles are stabilized by a comb polymer of polyhydroxy stearic acid (PHSA) grafted onto a PMMA backbone. The PHSA-comb is covalently linked to the particle surface using an epoxide-carboxylic coupling in a second step after the dispersion polymerization. Nile red is incorporated into the particles to enable excitation by a 534 nm laser and subsequent detection of light in a fluorescent microscope.

PMMA-PHSA particles are dried by rotary evaporation to remove solvents from the particle suspension, creating a PMMA-PHSA particle powder. The depletant is a polystyrene polymer bought at Polymer Source Inc, which was $M_n = 99,000$g/mol, $M_w = 105,500$g/mol and $PDI = 1.06$ as determined by the supplier using gel permeation chromatography. The overlap concentration c_p^* is calculated using $c_p^* = 3Mw/4\pi R_g^3 N_A$ with $R_g = 10$nm and $Mw = 105,500$g/mol, resulting in $c_p^* = 42$g/l. We determine the radius of our PMMA particles using Static Light Scattering (SLS) using a custom-built instrument. A dilute suspension was prepared in cis-decalin in a quartz cuvette, and the scattering intensity was measured in a range of $\theta = 20^\circ$ to 120° . The scattering intensity as a function of angle ($I(\theta)$) was fitted to the form factor for polydisperse hard spheres, yielding a radius of gyration of 709nm and a polydispersity of $\sim$ 5%.

Refractive index and density matching

The particle suspension was refractive-index and density matched by repeatedly adding small amounts of either CXB or tetralin to a suspension of PMMA-PHSA particles in a w/w 80% CXB, 16% cis-decalin and 4% tetralin solution. A final mixture of w/w 70.5% CXB, 19.8% tetralin and 9.6% cis-decalin ($\rho = 1.26$, $n_r = 1.504$) was prepared that did not have any observable sedimentation after 60 minutes of centrifugation at 2000g.

Sample preparation

Samples are prepared by weighing the required amount of particles to create a $\phi = 0.2$ suspension with a certain amount of added depletant. Index and density matching solution is added (CXB, Tetralin, Decalin mixture) and the sample is left to tumble on a rotating wheel overnight.
Sample chambers are built by glueing (Norland 61) two cover slips (rectangle, 21x26mm) to a microscope slide with a few mm 2D channel in between, which are cured by exposure to a strong UV lamp. A third circular microscope slide ($\oslash = 50mm$) is placed on top after application of more glue to create a 3D channel. Sample chambers are left overnight in a 50 $^{\circ}C$ oven to make sure all glue is cured. Approximately 100 μl of sample is transferred into the chamber, which is then sealed using a two component epoxy glue.

Measurements & analysis

Confocal images of each sample are taken by a Visitech VT-infinity3 with a Hamamatsu ORCA Flash 4.0 camera. 60 minutes of equilibration time is given to each sample glued to the microscope stage, after which 5000 z-stacks of 41x41x20.7 μm are taken at 1 Hz. Imaging is performed at least 10 μm from the glass sample interface to avoid wall effects.
We have taken experimental precautions to avoid drift occurring in our samples that include clamping down the sample tightly onto the microscope, me-

chanical equilibration after placing the sample of at least 1h, having the microscope on an actively-damped optical table and having the entire set-up in a climate control room in which temperature and humidity are controlled to an accuracy of 0.1 $^{\circ}C$ and 1-3% humidity.
Particle locating and tracking is performed using established routines [12], determining centroids of each particle and creating single particle trajectories. Z was determined by doing a range search over the centroid location data over a distance of 2.1μm. $Z(\tau)/Z_0$ is determined by analyzing all neighbor's identities during each individual trajectory. MSD of particle trajectories were determined by analyzing the locations data, of which we assume that $\tau_{max} = 0.2 * 5000s$. Increasing τ to more than 20% of measurement time was assumed not to be statistically viable.
After particle tracking we compute the ensemble-averaged affine drift magnitude and direction. Particle positions are then updated by removing this drift, and we re-run the tracking algorithm for a refinement of the trajectories. This process is iterated 30x which leads to a complete minimization of any coherent motion, as was shown extensively for suspensions even in strong flows in a recent paper by Duits et al.[7]. The typical drift velocities we determine in our experiments never exceed 0.1 μm/s.

Dynamical nearest neighbor analysis

To check whether bonds determined with our analysis are persistent and can be regarded as mechanically bonded, we calculate the decay of the number of original bonds. For different lag times we calculate the number of original bonds with a cutoff of $3a$, where a is the radius of the particles. We ensemble and time-average all decays to yield adequate statistics, which results in the decays shown in Fig. 6.6. For a colloidal liquid none of the original bonds are present after 5s [Fig. 6.6 (a)], which indicates that none of the bonds are long-lived and cannot be regarded as mechanically bonded. For a colloidal gel however most of the original bonds are still present after 5s which indicates

that these bonds have a much higher persistence than the bonds in the liquid sample and can therefore be regarded as mechanically bonded [Fig. 6.6 (b)]. Furthermore, we confirm that these data are independent of the exact choice

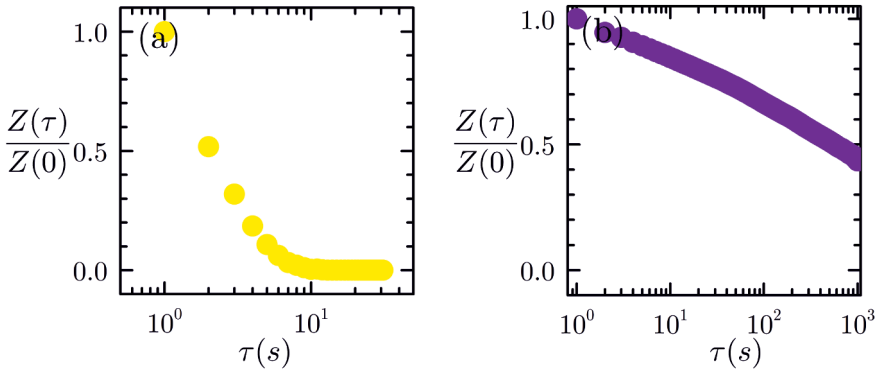

Figure 6.6: Decay curves for the fraction original bonds $\frac{Z(\tau)}{Z(0)}$ at lagtime τ for a colloidal liquid ($c_p = 0$ mg/ml) (a) and a colloidal gel ($c_p = 37.1$ mg/ml)(b).

for the cutoff distance [Fig. 6.7]. Previous studies have used different values for this cutoff([16, 19, 24]); here we choose to proceed our analysis with a cutoff of approximately 1.5 times the particle diameter such that the entire first peak in the pair correlation function is counted as the nearest neighbor shell. This results in a good signal-to-noise ratio for the nearest-neighbor data and accounts for the fact that (i) residual electrostatic interactions between the particles result in a broadening of the bonding distance and (ii) there is a finite resolution of determining the particle centroid in our experiment.

Parameters Fig. 6.4(a)

Table 6.1 shows the parameters for the fits shown in figure 6.4(a) in the main text. Fitting is carried out using the trust-region algorithm in the MATLAB® Curve Fitting Toolbox™. $\frac{U}{k_B T}$ and $\omega_0 \tau_f$ are fitting parameters and δ_C is determined from experimental data.

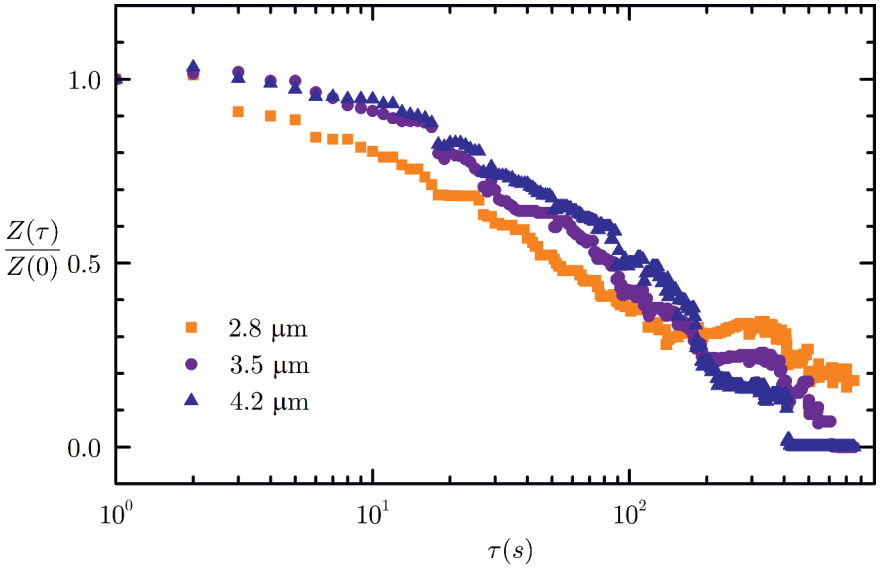

Figure 6.7: Decay curves for the fraction original bonds $\frac{Z(\tau)}{Z(0)}$ at lagtime τ for a sticky liquid ($c_p = 21.0$ mg/ml) for cutoff distances 2.8 μm, 3.5 μm and 4.2 μm (squares, circles and triangles respectively).

Table 6.1: Parameters used for curves in Fig. 6.5 (a). $\frac{U}{k_BT}$ and $\omega_0\tau_f$ are fitting parameters and δ_C is determined from experimental data.

c_p [mg/mL]	$\frac{U}{k_BT}$	$\omega_0\tau_f$	δ_C [μm]
30.9	0.8	0.06	0.33
34.1	2.0	0.07	0.12
34.6	1.9	0.09	0.08

Comparison of particle locating to iterative particle locating

To demonstrate the validity of our located particles we compare the locating method that was used for all analysis in this paper with a state-of-the-art iterative locating method[14] for two representative samples. Directly after locating we exclude all particles with an integrated intensity over I_{int}=40000 to make sure all found particles are real particles [Fig.6.8]. After filtering

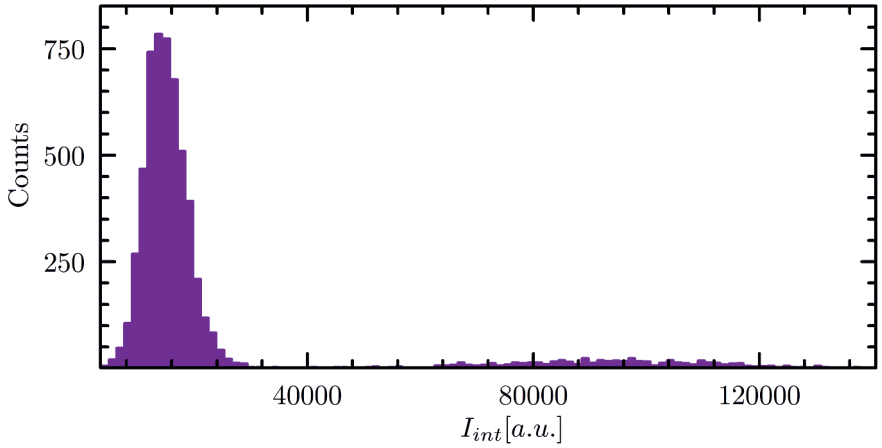

Figure 6.8: Histogram of the integrated intensities of particles found with an iterative particle locating algorithm for c_p=37.1mg/mL.

and tracking we find 8984 trajectories for both the iterative algorithm and the original locating algorithm for the c_p=37.1mg/mL sample. For the c_p = 21.0mg/mL sample we also find 1173 trajectories for both algorithms.

To fully appreciate the impact of the iterative algorithm on our measured single particle dynamics we compare the single particle mean-squared displacement probability distributions obtained with the different algorithms [Fig. 6.9]. Besides one slightly shifted point on the right in Fig. 6.9f all distributions are identical. This indicates that results obtained with the locating method we used for all analysis are nearly-identical to the results obtained with current the state-of-the-art locating algorithms.

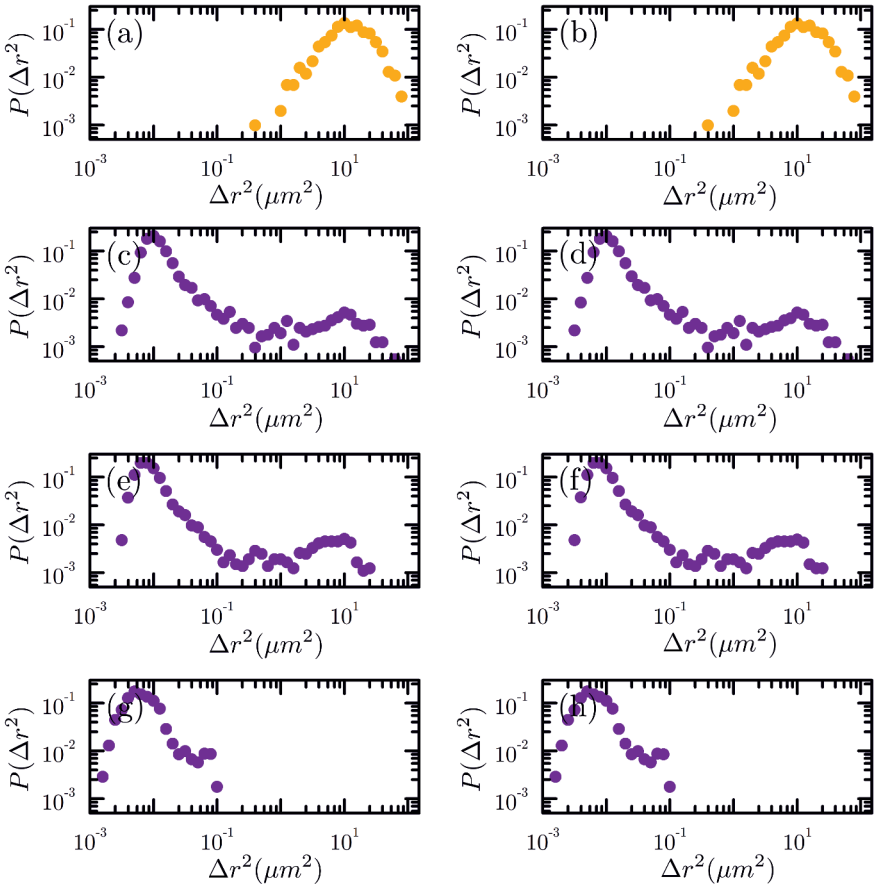

Figure 6.9: Comparison of the probability distributions P of single particle mean-squared displacements obtained with conventional locating (*left*) and iterative locating (*right*) for lagtimes (top to bottom) 498s, 248s and 1s.

Bibliography

[1] L Antl, JW Goodwin, RD Hill, Ronald H Ottewill, SM Owens, S Papworth, and JA Waters. The preparation of poly (methyl methacrylate) latices in non-aqueous media. *Colloids and Surfaces*, 17(1):67–78, 1986.

[2] Sho Asakura and Fumio Oosawa. Interaction between particles suspended in solutions of macromolecules. *Journal of polymer science*, 33(126):183–192, 1958.

[3] Luca Cipelletti, Suliana Manley, RC Ball, and DA Weitz. Universal aging features in the restructuring of fractal colloidal gels. *Physical review letters*, 84(10):2275, 2000.

[4] John C Crocker, Megan T Valentine, Eric R Weeks, Thomas Gisler, Peter D Kaplan, Arjun G Yodh, and David A Weitz. Two-point microrheology of inhomogeneous soft materials. *Physical Review Letters*, 85(4):888, 2000.

[5] Clare J Dibble, Michael Kogan, and Michael J Solomon. Structural origins of dynamical heterogeneity in colloidal gels. *Physical Review E*, 77(5):050401, 2008.

[6] A D Dinsmore and D A Weitz. Direct imaging of three-dimensional structure and topology of colloidal gels. *Journal of Physics: Condensed Matter*, 14(33):7581, 2002.

[7] M. H. G. Duits, S. Ghosh, and F. Mugele. Measuring advection and diffusion of colloids in shear flow. *Langmuir*, 31(21):5689–5700, 2015. PMID: 25965857.

[8] Agnes Duri and Luca Cipelletti. Length scale dependence of dynamical heterogeneity in a colloidal fractal gel. *EPL (Europhysics Letters)*, 76(5):972, 2006.

[9] Henry Eyring. The activated complex in chemical reactions. *The Journal of Chemical Physics*, 3(2):107–115, 1935.

[10] Y Gao and ML Kilfoil. Direct imaging of dynamical heterogeneities near the colloid-gel transition. *Physical review letters*, 99(7):078301, 2007.

[11] Yongxiang Gao and Maria L Kilfoil. Accurate detection and complete tracking of large populations of features in three dimensions. *Optics express*, 17(6):4685–4704, 2009.

[12] Yongxiang Gao and Maria L. Kilfoil. Accurate detection and complete tracking of large populations of features in three dimensions. *Optics Express*, 17(6):4685, 2009.

[13] Thomas Gibaud, Christophe Perge, Stefan B Lindström, Nicolas Taberlet, and Sébastien Manneville. Multiple yielding processes in a colloidal gel under large amplitude oscillatory stress. *Soft matter*, 12(6):1701–1712, 2016.

[14] K. E. Jensen and N. Nakamura. Note: An iterative algorithm to improve colloidal particle locating. *Review of Scientific Instruments*, 87(6):066103, 2016.

[15] A. H. Krall and D. A. Weitz. Internal dynamics and elasticity of fractal colloidal gels. *Phys. Rev. Lett.*, 80:778–781, Jan 1998.

[16] Shir R. Liber, Shai Borohovich, Alexander V. Butenko, Andrew B. Schofield, and Eli Sloutskin. Dense colloidal fluids form denser amorphous sediments. *Proceedings of the National Academy of Sciences*, 110(15):5769–5773, 2013.

[17] Stefan B Lindström, Thomas E Kodger, Joris Sprakel, and David A Weitz. Structures, stresses, and fluctuations in the delayed failure of colloidal gels. *Soft Matter*, 8(13):3657–3664, 2012.

[18] Peter J Lu, Jacinta C Conrad, Hans M Wyss, Andrew B Schofield, and David A Weitz. Fluids of clusters in attractive colloids. *Physical Review Letters*, 96(2):028306, 2006.

[19] Peter J Lu, Emanuela Zaccarelli, Fabio Ciulla, Andrew B Schofield, Francesco Sciortino, and David A Weitz. Gelation of particles with short-range attraction. *Nature*, 453(7194):499–503, 2008.

[20] Ajay Singh Negi and Chinedum O Osuji. Dynamics of internal stresses and scaling of strain recovery in an aging colloidal gel. *Physical Review E*, 80(1):010404, 2009.

[21] PN Pusey, Wilson CK Poon, SM Ilett, and P Bartlett. Phase behaviour and structure of colloidal suspensions. *Journal of Physics: Condensed Matter*, 6(23A):A29, 1994.

[22] C. Patrick Royall, Wilson C. K. Poon, and Eric R. Weeks. In search of colloidal hard spheres. *Soft Matter*, 9:17–27, 2013.

[23] CJ Rueb and CF Zukoski. Viscoelastic properties of colloidal gels. *Journal of Rheology (1978-present)*, 41(2):197–218, 1997.

[24] Kirill Sandomirski, Elshad Allahyarov, Hartmut Lowen, and Stefan U Egelhaaf. Heterogeneous crystallization of hard-sphere colloids near a wall. *Soft Matter*, 7(18):8050–8055, 2011.

[25] Joris Sprakel, Stefan B. Lindström, Thomas E. Kodger, and David A. Weitz. Stress enhancement in the delayed yielding of colloidal gels. *Phys. Rev. Lett.*, 106:248303, Jun 2011.

[26] Veronique Trappe and Peter Sandkühler. Colloidal gels—low-density disordered solid-like states. *Current opinion in colloid & interface science*, 8(6):494–500, 2004.

[27] T. van de Laar, R. Higler, K. Schroën, and J. Sprakel. Discontinuous nature of the repulsive-to-attractive colloidal glass transition. *Scientific Reports*, 6(October 2015):22725, 2016.

[28] Emanuela Zaccarelli. Colloidal gels: equilibrium and non-equilibrium routes. *Journal of Physics: Condensed Matter*, 19(32):323101, 2007.

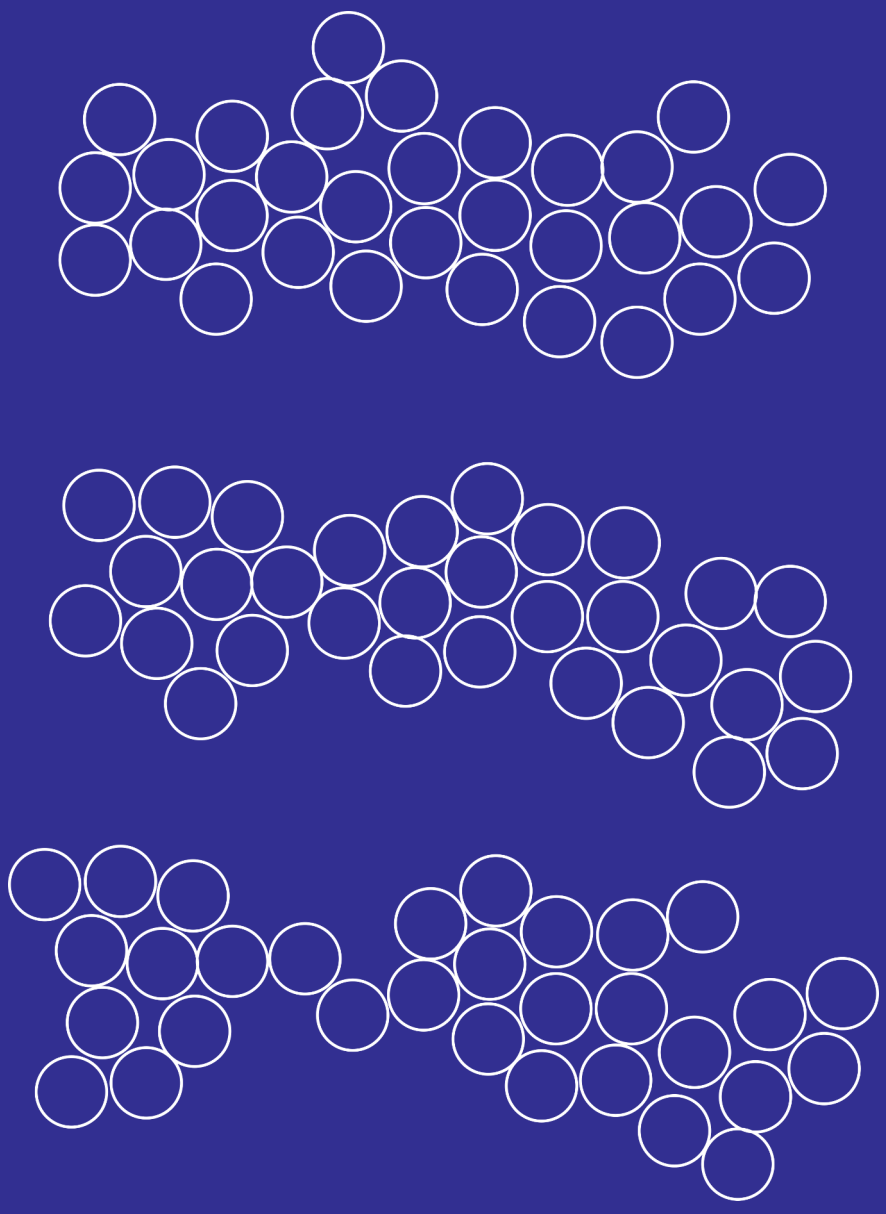

CHAPTER 7

Strand plasticity governs fatigue in colloidal gels

The repeated loading of a solid leads to microstructural damagecsc that ultimately results in catastrophic material failure. While posing a major threat to the stability of virtually all materials, the microscopic origins of fatigue, especially for soft solids, remain elusive. Here we explore fatigue in colloidal gels as prototypical inhomogeneous soft solids by combining experiments and computer simulations. Our results reveal how mechanical loading leads to irreversible strand stretching, which builds slack into the network that softens the solid at small strains and causes strain hardening at larger deformations. We thus find that microscopic plasticity governs fatigue at much larger scales. This gives rise to a new picture of fatigue in soft thermal solids and calls for new theoretical descriptions of soft gel mechanics in which local plasticity is taken into account.

This chapter was published as:
J.M. van Doorn, J.E. Verweij, J. Sprakel and J. van der Gucht: *Strand plasticity governs fatigue in colloidal gels*, Physical Review Letters, 120, **(2018)**, 208005

Introduction

The application of repeated load to a solid material can lead to the erosion of its microstructure, in a process that is known as fatigue. While the initial stages of this process often go unnoticed, the gradual accumulation of damage that can ultimately lead to the sudden and catastrophic failure of the material. Understanding the microscopic origins of fatigue is therefore crucial for the reliable prediction of a material's lifetime and for the development of strategies to improve mechanical stability. In materials such as steel and concrete, fatigue is characterized by the accumulation and growth of small microcracks [15, 10]. However, the mechanisms of fatigue in disordered soft materials are much less understood. A prototypical class of soft heterogeneous solids is comprised of colloidal gels. These are nonequilibrium structures consisting of aggregated colloidal particles that form a sample-spanning network [28].

The arrested dynamics of the aggregated particles lead to solidlike behaviour, with elastic properties that are determined by the structure and connectivity of the network [12, 25]. When subjected to a large enough stress, colloidal gels will eventually fluidize or fracture, often after a latent period of apparent stability [8, 3, 2, 7, 9, 27, 16]. The microstructural changes responsible for this delayed failure have been attributed to the brittlelike rupture of network strands due to force-activated breaking of interparticle bonds [17, 5, 26]. Such models assume that no restructuring of the network due to plastic particle rearrangements takes place. Yet, it is known that such rearrangements do occur [13, 23], even for colloidal gels at rest [29], where they lead to aging, coarsening, and slow relaxation of internal stresses [4, 21, 6]. While it is known that under a large deformation aggregates break into smaller clusters [30], the response of aggregated structures to repeated small deformations remains unclear. To establish a link between the stability of colloidal gels and their microstructure, it is therefore needed to understand the role of

plasticity in gel failure and fatigue.

In this Letter, we report fatigue measurements on model colloidal gels subjected to cyclic loading. By combining experiments and computer simulations, we show that the gradual weakening that occurs in these gels is due to plastic deformations within individual gel strands. Our results thus shed new light on the mechanism of damage accumulation in colloidal gels and suggest that the current models for colloidal gel failure must be revised to take this plastic softening into account.

We investigate colloidal gels consisting of monodisperse polystyrene particles synthesized as described in Ref. [1], with a volume fraction ϕ =0.18. The particles have a diameter $a = 90$ nm as determined by dynamic light scattering. Attraction is induced by coating the particles with a thermoresponsive surfactant layer of approximately 8 nm thickness, as synthesized in Ref. [11]. To screen electrostatic repulsion between the particles, 100 mM NaCl is added to all samples. Rheological measurements are performed with a stress-controlled rheometer (MCR-501, Anton Paar) with a concentric cylinder geometry (CC10/Ti). The gels are formed *in situ* by heating the samples to 45°C, above the critical aggregation temperature of the surfactant, which results in gels with thick strands, each composed of many particles in its cross section, in which it is established that significant rearrangements occur [11]. To minimize initial transient effects, samples are equilibrated for 1 h before initiating measurements. Fatigue in the gels is studied by cyclically deforming the samples with a sawtooth strain profile [inset in Fig. 7.1]. After 14 cycles at the same strain amplitude $\gamma_{\max}$, we allow the sample to rest for 120 s, before starting a new set of deformation cycles at a higher strain amplitude, with increment $\Delta\gamma_{\max} = 0.005$.

For the smallest amplitude the stress-strain curve exhibits a linear elastic response [Fig. 7.1]. For larger strain amplitudes, however, the stress increases nonlinearly with increasing strain and shows a hysteresis loop, which indicates dissipative losses during the deformation cycle [14] [see also ap-

pendix F, Fig. 7.15(a)]. The first cycle for every strain amplitude differs qualitatively from the subsequent cycles: With increasing strain, the stress increases strongly, until a threshold value of approximately 470 Pa is reached, after which it levels off, indicating that the material undergoes plastic flow at this stress level. For every subsequent cycle, the observed stress is lower than that in the first cycle, signalling a progressive, irreversible weakening of the material. The stress-strain curve then gradually approaches a limit cycle, with an enclosed area that reflects the viscoelastic dissipation in the network due to solvent flow or reversible particle rearrangements. Note that the viscous contribution to the stress is negative in the unloading branch of the cycle, leading to a negative overall stress as the strain returns to zero.

Because the timescale at which plastic rearrangements take place can be relatively long for these strongly aggregated particles, we expect the amount of plasticity to depend on the loading rate. Indeed, when we increase $\dot{\gamma}$ by a factor of 10, to 10^{-1} s^{-1}, we observe a much more elastic response, with the onset of nonlinear plastic behaviour shifted to much larger strains and stresses [Fig. 7.2(a)].

To analyze the nature of the observed plasticity in colloidal gels in more detail, we first disentangle the elastic and viscous contributions to the mechanical response, by averaging the loading and unloading curve for each cycle [20]. This averages out the viscous contribution to the stress, so that only the elastic stress σ_{el} remains [Fig. 7.2(b)]. For the smallest strain amplitude, the stress-strain response is linear; however, at higher strains, when the gels have undergone plastic deformation, the curves become strongly nonlinear. The shapes of the non-linear response of all cycles are very similar. After an initial linear response, characterized by a linear modulus G_0, the gels show pronounced strain hardening: At a characteristic strain amplitude γ^*, there is a sharp upturn of the stress. The linear modulus that characterizes the initial slope of the stress-strain curves decreases with increasing strain amplitude [Fig. 7.2(c)], signaling the progressive weakening of the gels resulting from

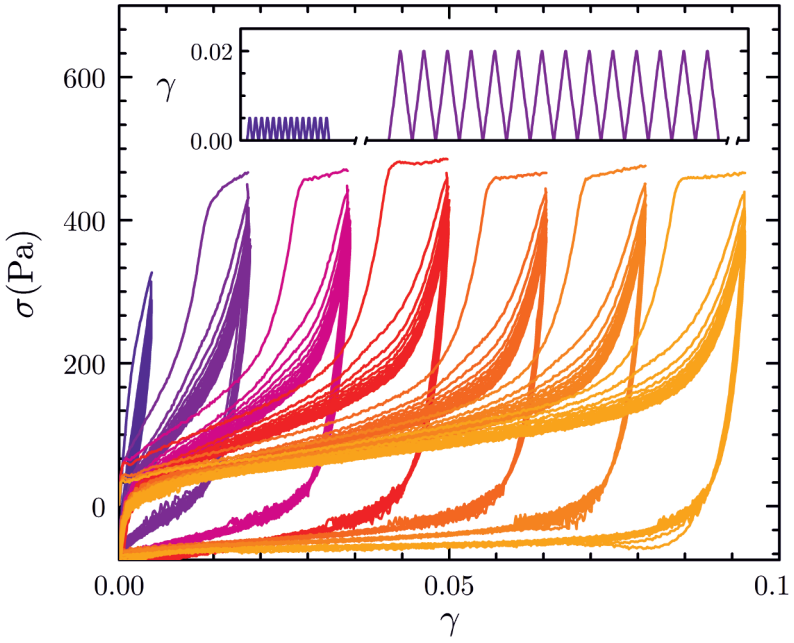

Figure 7.1: Stress-strain curves as a result of sawtooth strain cycles shown in the inset (only the first two sets are shown) with $\dot{\gamma}$=10^{-2} s^{-1}. From blue to yellow: γ_{max} = 0.005, 0.02, 0.035, 0.05, 0.065, 0.08, 0.095 (note that only a selection of the sets is shown).

the gradual erosion of the network structure during the fatigue cycles. We obtain γ^* by superimposing the different stress-strain curves for both strain rates by plotting the normalized stress σ_{el}/σ^*, where $\sigma^* = G_0\gamma^*$, as a function of the rescaled strain γ/γ^* [Fig. 7.2(d) and appendix F, Fig. 7.15(b)]. The excellent collapse indicates that the physical mechanism that underlies the mechanical response of the gels remains the same during the fatigue cycles. We find a linear increase of γ^* with increasing maximum strain amplitude [inset in Fig. 7.2(c)], indicating that the strain hardening response is delayed by the fatigue process.

While our data demonstrate the importance of plasticity for fatigue in colloidal gels, the microscopic nature of this plastic deformation remains to be

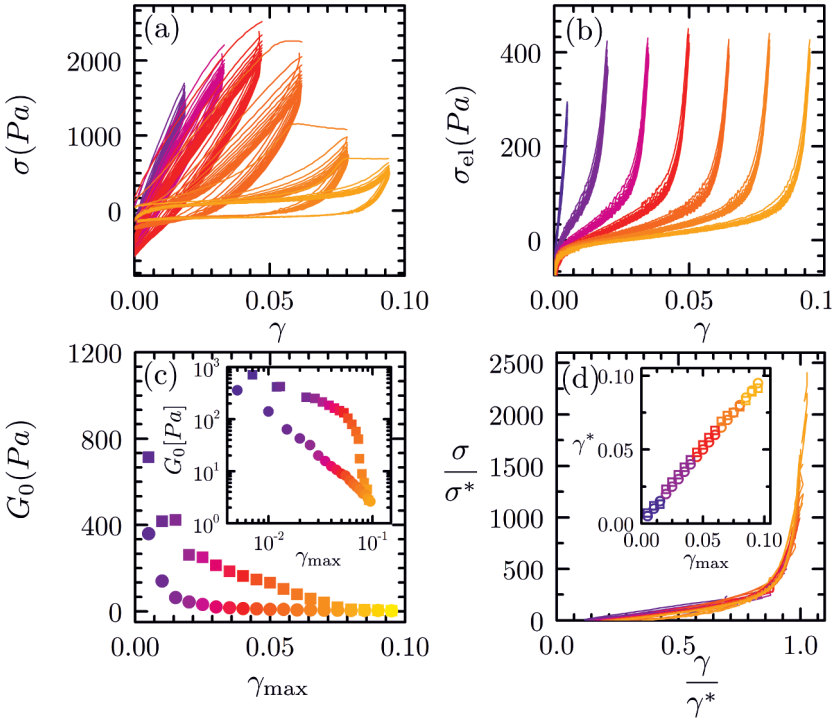

Figure 7.2: (a) Stress-strain curves for $\dot{\gamma}$=10^{-1} s^{-1}, from blue to yellow: γ_{max} = 0.005, 0.02, 0.035, 0.05, 0.065, 0.08, 0.095. (b) Elastic midlines for curves in Fig.7.1. c) The initial modulus as function of γ_{max} for $\dot{\gamma}$=10^{-1} s^{-1} (squares) and $\dot{\gamma}$=10^{-2} s^{-1} (circles). The inset shows the same data on a double-logarithmic scale. (d) Collapse of every second elastic midline for both strain rates. The inset shows the dependence of γ^* on γ_{max} for $\dot{\gamma}$=10^{-1} s^{-1} (squares) and $\dot{\gamma}$=10^{-2} s^{-1} (circles).

uncovered. Given that colloidal gels are networks of connected strands consisting of aggregated particles, the observed weakening must be caused either by the rupture of gel strands, leading to a decrease in network connectivity, or by softening of the gel strands, leading to a lower effective spring constant of the strands. To identify which of these scenarios is the dominant one, we need detailed information at the single strand level. Since this is extremely difficult to obtain experimentally for our system, we perform Brownian Dy-

namics (BD) computer simulations on single gel strands [Fig. 7.3]. The strands are composed of 256 particles of diameter a interacting through a Morse potential [24], with an interaction strength $\epsilon = 10k_BT$ and interaction range parameter $\rho_0 = 33$, which corresponds to a well width of approximately $\Delta = 0.09a$, similar to the experimental system [appendix A, Fig. 7.5]. Following the experimental protocol, the gel strands are deformed cyclically with a sawtooth strain profile (see appendix A for further details about the simulation method). To connect our simulation results to the experimental findings, we calculate the force needed to deform the strand as a function of the strain [1]. The force-strain curves for non-fractured gel strands show features that are very similar to the macroscopic curves measured experimentally [Fig. 7.4(a)]. Like in the experimental curves, we find that the first force-strain curve for each strain amplitude differs qualitatively from the subsequent cycles, showing a plateau above a critical force that indicates plastic deformation within the gel strand.

We use a similar procedure to rescale the force-strain curves as in Fig. 7.2(d). Again, we average the force in the loading and unloading curve and plot the rescaled elastic force f_{el}/f^*, with $f^* = k\gamma^*$ the scaled stiffness of the strand in the linear regime as a function of the rescaled strain γ/γ^*. This yields a curve that shows similar features to the experimental one [Fig. 7.4(b)], with a linear response regime, followed by a strain-hardening response at higher strains. The linear spring constant of the gel strands k decreases in a similar fashion with the strain amplitude γ_{max} as the elastic modulus in the experiments [Fig. 7.4(c)]. Furthermore, the onset of strain hardening shifts to higher strains with increasing strain amplitude [Fig. 7.4(d)], also in agreement with experiments [inset in Fig. 7.2(c)]. Since broken strands have been excluded from the analysis, the observed weakening in the simulated force-strain curves can be attributed completely to plastic rearrangements within

[1] The force f on the simulation walls is related to the stress measured in the experiment as $\sigma \approx \frac{f}{\xi^2}$, with ξ the mesh size of the network.

the strands. This suggests that also the weakening observed at the macroscopic scale in our fatigue experiments can be explained by plastic deformation and softening in individual gel strands, without the need to invoke a rupture of strands.

To verify that this finding is not specific to the geometry of the simulated gel strands, we have carried out simulations for strands of different lengths and widths and for larger gel networks consisting of many interconnected gel strands. In all cases, the force-strain loops show similar features to the curves in Fig. 7.4(a) and Figs. 7.11 -7.13, which affirms that gel strand plasticity is a mechanism for fatigue in a wide class of colloidal gels, irrespective of the precise structure of the gel strands.

To unravel the microscopic mechanism that underlies the plastic deforma-

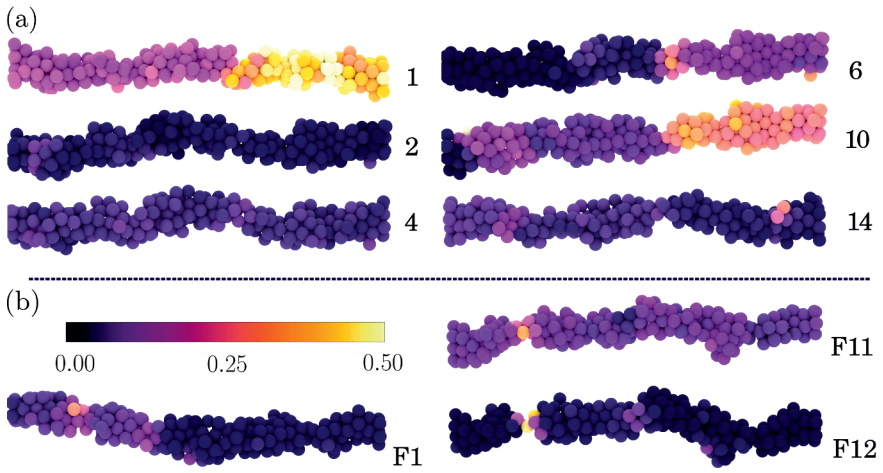

Figure 7.3: (a) Visual representation of the noncumulative average plastic deformation per particle in oscillation cycles 1,2,4,6,10, and 14 of a single gel strand ($\gamma_{max} = 0.04$, data in supplemental Fig 2.). The color bar indicates the non-cumulative plastic deformation m_i per particle in each cycle from low (purple) to high (yellow). The cumulative plastic deformation of this gel strand is shown in appendix F Fig. 7.14(b) Plastic deformation in a gel strand after the first cycle ($F1$), before fracture ($F11$) and after fracture ($F12$).

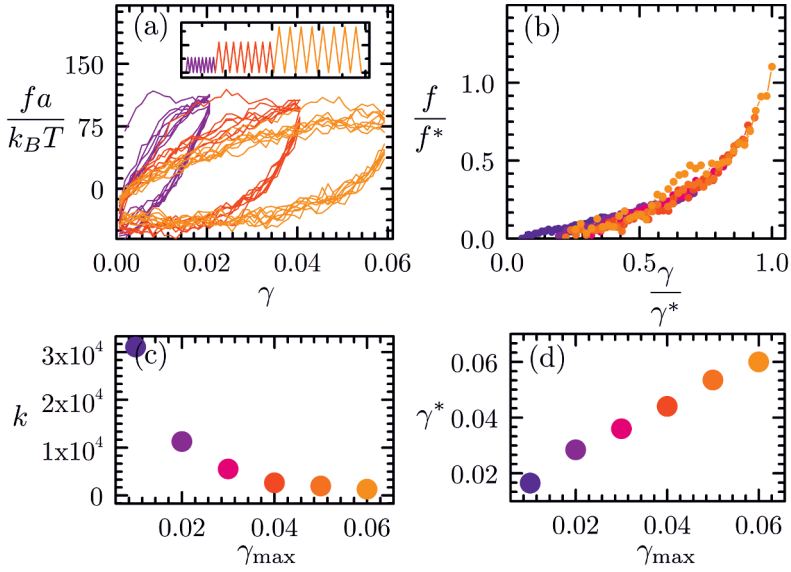

Figure 7.4: (a) Force-strain curves for BD simulations of 24 (8 × 3) oscillations of a single gel strand at strain amplitudes (purple to orange) $\gamma_{max} = 0.02$, 0.04 and 0.06. (b) Collapse of the average force-strain curves (positive parts of the loading and unloading curve) of the fourth oscillation cycle scaled by γ^* on the x-axis and $k \cdot \gamma^*$ on the y-axis. Data are obtained from appendix A, Fig. 7.8(c) Spring constant k (in units k_BTa^{-1}) as a function of γ_{max}. (d) γ^* as a function of γ_{max}.

tion of the gel strands, we analyze the rearrangements of individual particles and quantify the average plastic strain for each particle in an oscillation c_n as

$$m_i(c_n) = \frac{1}{\mathcal{N}_i a^2} \sum_{j=1}^{\mathcal{N}_i} \langle (\mathbf{r}_{ij}(0) - \mathbf{r}_{ij}(t))^2 \rangle \tag{7.1}$$

where $\mathbf{r}_{ij}(0)$ and $\mathbf{r}_{ij}(t)$ denote the separation vector between particle i and neighboring particles j at the start of the cycle and after a time t, respectively, $\mathcal{N}_i$ is the number of nearest neighbors of particle i, and the average is taken over the entire oscillation.

During the strain cycles, the amount of plastic strain gradually increases, with most of the plastic rearrangements occurring during the first cycle. For larger

strain amplitudes, the amount of plastic strain is also larger [Fig. appendix B, 7.7(b)]. These irreversible particle rearrangements and the associated rupture of inter-particle bonds are responsible for the large energy dissipation in the first strain cycles. As the gel strands are several particle diameters wide [Fig. 7.3], the breaking of a single bond does not immediately lead to rupture of the whole strand [17]. The overall integrity of the strand is maintained by adjacent bonds and due to thermal fluctuations, new bonds can form [20, 6, 27]. This provides a mechanism for the plastic deformation of the gel strands.

Visual inspection of computer-rendered images of the simulated strands suggest that the plastic rearrangements of particles result in the irreversible lengthening of the strands after deformation, leading to the build-up of slack in the strands and buckling during unloading [Fig. 7.3(a)]. The linear increase of γ^* with increasing γ_{max} [inset in Fig. 7.2(a) and Fig. 7.4(d)] furthermore suggests that this slack is proportional to the applied extension. During the next cycle the slack induced by previous cycles is pulled out first, which results in little resistance and explains the initial soft linear elastic response of the gels. When the strands are pulled taut, the resistance to further stretching increases strongly as the strand entropy vanishes and the physical bonds between the particles become perturbed. This results in the observed strain hardening in our colloidal gels. We note that these phenomena are reminiscent of observations made for networks of biopolymer bundles [20].

Interestingly, the plastic rearrangements do not occur homogeneously in the gel strand but are strongly localized to specific regions [Fig. 7.3]. This leads to the formation of thicker and thinner regions in the gel strand, reminiscent of the Rayleigh-Plateau instability in liquid jets, which highlights the arrested liquid state of colloidal gels [18]. This is further corroborated by looking at the average number of bonds per particle, which gradually increases during the oscillations [Appendix B, Fig. 7.7(d)], suggesting that fatigue in colloidal gels is reminiscent of activated aging, in which the nonequilibrium gel structure tends to coarsen by increasing the number of bonds [19].

At high strains, the localization of plastic deformation ultimately leads to a rupture of the gel strand at the weakest spot, i.e. at a local necking region [Fig. 7.3(b)]. The percentage of broken strands increases with increasing strain amplitude and reaches about 65 % for a strain of 0.06 [appendix B, Fig.7.9]. As the strands become longer and thinner, a rupture occurs more frequently, but in all cases it is preceded by a significant plastic deformation within the strands [appendix D, Fig. 7.12 and appendix E, Fig. 7.13. Since our analysis focuses on the microscopic plastic events within strands, preceding their rupture, the role of strand rupturing for the mechanical stability of the gel as a whole remains to be understood.

To investigate the effect of the deformation rate, we also deform the gel strands at higher strain rates. Increasing the strain rate by a factor of 100 leads to a considerably higher number of ruptured strands [appendix B, Fig. 7.9(c)]. From the average plastic deformation per oscillation cycle [appendix B, Fig. 7.10 as a function of increasing strain rate we observe a clear decline in the plasticity of the gel strands. These data suggest that colloidal gels with hardly any options to deform plastically will rupture in a brittle fashion. Macroscopically, the extended linear regime in Figure 7.2(a) signals the onset of a transition to brittle failure. This is supported by the fact that G_0 decreases very rapidly at high γ^* for $\dot{\gamma}$=10^{-1} s^{-1} , suggesting that a larger part of the damage is caused by brittle fracture [inset in Fig. 7.2(c)].

Our results highlight how fatigue in colloidal gels results from plasticity at much smaller scales. This feature results from the strongly hierarchical and multiscale structure of networks of colloidal particles. To date, strand plasticity has been overlooked in describing the mechanics of colloidal gels but has also received little attention as a possible mechanism of fatigue in a wider variety of heterogeneous solids, while our data clearly indicate its pivotal role in deciding the material's fate under repeated loading. Strand stretching and the buildup of slack has also been identified as a mechanism for strain softening in networks of biological fibers [20]. This raises the question whether

localized plasticity, which remains obscured in macroscopic mechanical testing, may have a more universal role in the fatigue mechanisms of a wider class of inhomogeneous soft solids with a hierarchical microstructure. If so, a universal description of these effects could have pronounced implications for the predictability of the nonlinear mechanical response of soft materials, which remains an open challenge in the field. Finally, while our work has focused on fatigue induced by external loading, other failure mechanisms driven by internal stresses are known to exist for these inhomogeneous thermal solids, such as aging and syneresis [4, 21, 6]. The plasticity we describe here results from the rearrangement of particles by thermally activated debonding [29], in which the mechanical stress imposes a directional bias that leads to irreversible strand stretching. Based on our observations here, we hypothesize that internal stress can give rise to similar effects, where e.g. contractile internal stresses could bias rearrangements that lead to isotropic condensation of the structure, ultimately resulting in syneresis. While this remains unexplored to date, it could open the way to a universal description of the failure of these nonequilibrium solids.

Appendix A: Simulation details

Multiple strain amplitudes

Brownian Dynamics (BD) simulations were performed to study the effect of repeated deformation on the microscopic scale only. We consider a gel strand with 256 particles which interact through the Morse potential [24]:

$$\beta U(r) = \beta\epsilon \, \exp(\rho_0[a-r]) \, (\exp[\rho_0(a-r)] - 2) \tag{7.2}$$

with $\beta = 1/k_BT$, $\rho_0 = 33$, energy scale $\beta\epsilon = 10$ and particle diameter $a = 2r_a$ [Fig. 7.5]. The parameter ρ_0 determines the width of the potential,

which becomes approximately $\Delta = 0.09\ a$ for $\rho_0 = 33$ [2]. In this way it matches the experimental interaction range, which is known to be around 8 nm for the thermo-responsive surfactant that coats the particles ($r_p = 45$ nm) [11].

The motion of a particle i with position $\boldsymbol{r}_i$ is obtained by solving the overdamped Langevin equation:

$$\dot{\boldsymbol{r}}_i(t) = \beta D_0[-\nabla_i U(t)] + \sqrt{2D_0}\boldsymbol{\xi}_i(t) \tag{7.3}$$

where $\boldsymbol{\xi}_i(t)$ is random white noise, sampled with zero mean and unit variance, to model the thermal fluctuations of the particles. $D_0 = k_B T/\zeta_f$ is the short-time diffusion coefficient with ζ_f the friction coefficient, set to unity. The time step δt for the numerical integration is set to $\delta t = 1 \times 10^{-6}\ \tau_B$. We express the unit of time in terms of the short-time self-diffusion $\tau_B = a^2/D_0$.

Individual strands are formed between two attractive walls, with a particle-wall interaction given also by Eq. 7.2 (with $\rho_0 = 33$, $\beta\epsilon = 10$). We use periodic boundary conditions in the y and z direction. We place particles initially in a face centered cubic (fcc) lattice in a 4 x 4 (height x width) arrangement (N = 256). The system is then equilibrated for 568 τ_B, which leads to aggregation of the particles and the formation of a gel strand between the two walls [3]. During equilibration, the particle positions are randomized, leading to a different internal strand structure for each simulation. Note that the distances between the particles in the initial configuration are larger than the range of

[2] Here, Δ is determined by taking the end of the well at 10% of the original well-depth (1 $k_B T$). To determine the fraction of broken inter-particle bonds χ_n, the number of bonds per particle N_b and the irreversible displacements of particles m, the cut-off between the particles' center-to-center distance is set to 1.16 (1% of the original well-depth). The visual representations in Figure 7.3 and appendix F, Figure 7.14 are made with a cut-off of 1.5

[3] Varying the equilibration time doesn't influence the obtained force-strain curves. However, for too short equilibration times the average number of bonds is still substantially increasing in the zero measurement; see appendix A, Figures 7.6 and 7.7 for the zero measurement (blue curve, $\gamma = 0$) of these simulations.

the potential.

Similarly to the experiment, the single gel strand in the BD simulations

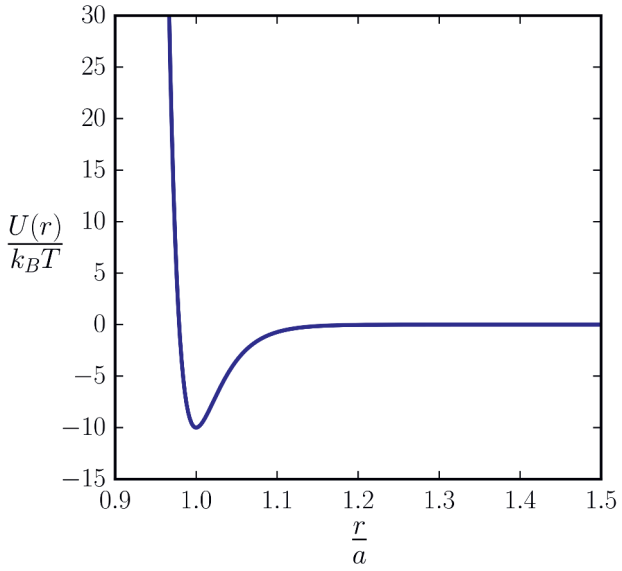

Figure 7.5: Morse potential with interaction range parameter $\rho_0 = 33$ and interaction strength $\beta\epsilon = 10$. The cutoff of the potential is set to 1.5.

is cyclically deformed with a sawtooth strain profile [inset in Fig. 7.1(a)]. One of the walls is moved outward, leading to an expansion at a fixed strain rate $\dot{\gamma} = 0.00284\ \tau_B^{-1}$. Note that this strain rate is comparable to a strain rate of $\dot{\gamma} = 1.7\ \mathrm{s}^{-1}$ in the experiment. After 8 successive oscillations the strain amplitude is increased from $\gamma = 0.02$ to $\gamma = 0.04$ and $\gamma = 0.06$ respectively. More than 65 $\%$ of the gel strands break after 24 oscillatory expansions at successive strain amplitudes of $\gamma = 0.02, 0.04$ and 0.06.

We note that the fracture of individual strands is highly ductile and occurs by strong necking. Moreover, fracture only occurs when a single bond connects the two halves. In all simulations a percentage of the strands is fractured (either by detaching from the wall or by breaking into clusters, see appendix B, Fig. 7.10). To focus on plastic mechanisms, data of broken strands is ex-

cluded in further analysis. Each strain amplitude contains data of at least 30 statistically different gel strands.

Single strain amplitudes

For single strain amplitudes, simulations are performed exactly as described above, however, in this case we do not impose a higher strain after a certain amount of cycles. Data is shown both for expansion [appendix A, Fig. 7.6] and compression [appendix B, Fig. 7.7] of single gel strands. In the latter case the distance between the walls is first decreased, leading to compression of the gel strand, after which the walls are brought back to their original position. We impose 14 oscillations in total for strain amplitudes $\gamma = 0.02$, 0.04 and 0.06. The fourth oscillation for these strain amplitudes (expansion) is used to re-scale the force-strain curves as shown in Fig. 7.4(b).

At higher strain amplitudes, compression favors the increase in number of bonds compared to expansion. Both the amount of dissipated energy and the fraction of inter-particle bonds that break per oscillation cycle is lower for compression, i.e. compression enhances the reformation of inter-particle bonds over expansion.

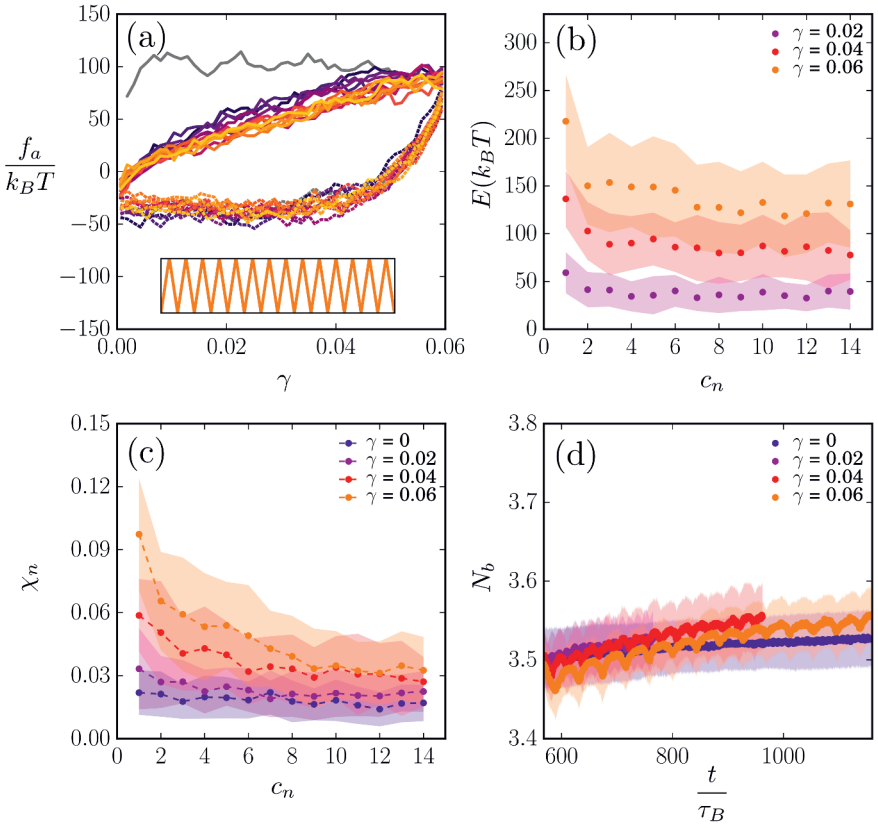

Figure 7.6: (a) Force-strain curve for BD simulations upon 14 oscillatory *expansions* of a single gel strand at strain amplitude $\gamma_{max} = 0.06$. The strain profile is shown in the inset. The loading branch of each cycle is indicated with a solid line. The dotted line indicates the unloading branch. The different oscillations (1-14) are plotted from purple to yellow. To highlight the first oscillation cycle this one is plotted in gray. (b) Dissipated energy in each oscillation number c_n for strain amplitudes $\gamma_{max} = 0.02$, 0.04 and 0.06 obtained through integration of the force-strain curves. (c) The fraction of bonds that break per oscillation. The dotted line is drawn to guide the eye. (d) Average number of bonds in time. The shaded areas indicate the standard deviation.

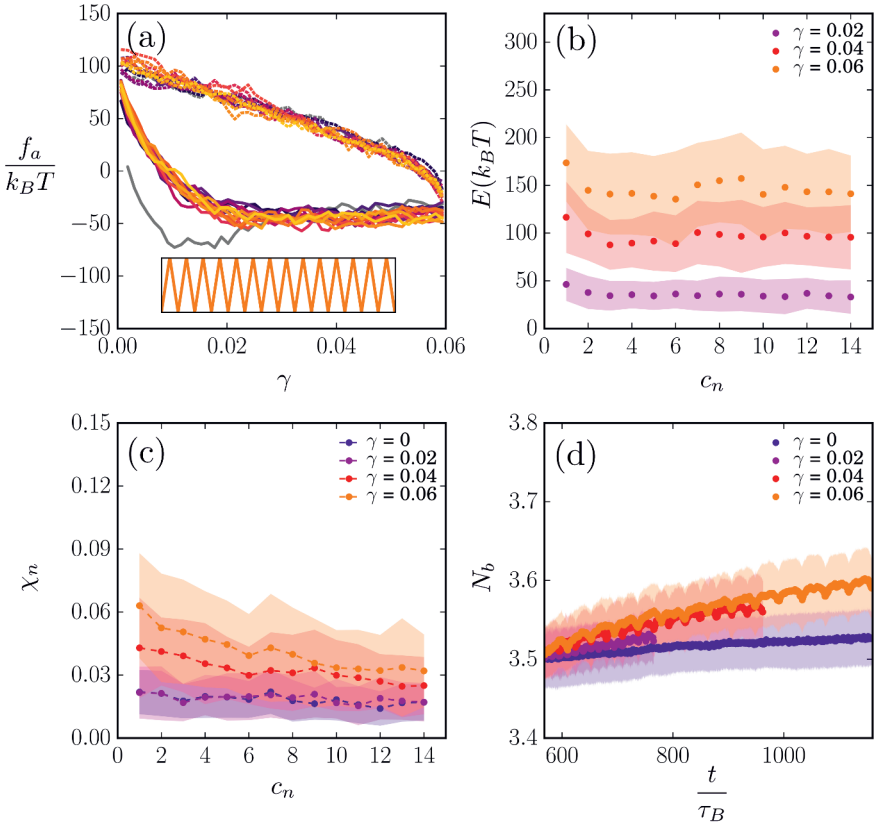

Figure 7.7: Data of BD simulations upon 14 oscillatory *compressions*. See appendix A, Fig. 7.6 for the explanation of each subplot.

Appendix B: Analysis details

Bond rearrangements

To quantify bond rearrangements, we calculate the average fraction of inter-particle bonds that is broken per oscillation cycle:

$$\chi_n(c_n) = \frac{\langle n_i(c_n) - n_i(c_n + 1)\rangle_p}{N_b(c_n)}, \tag{7.4}$$

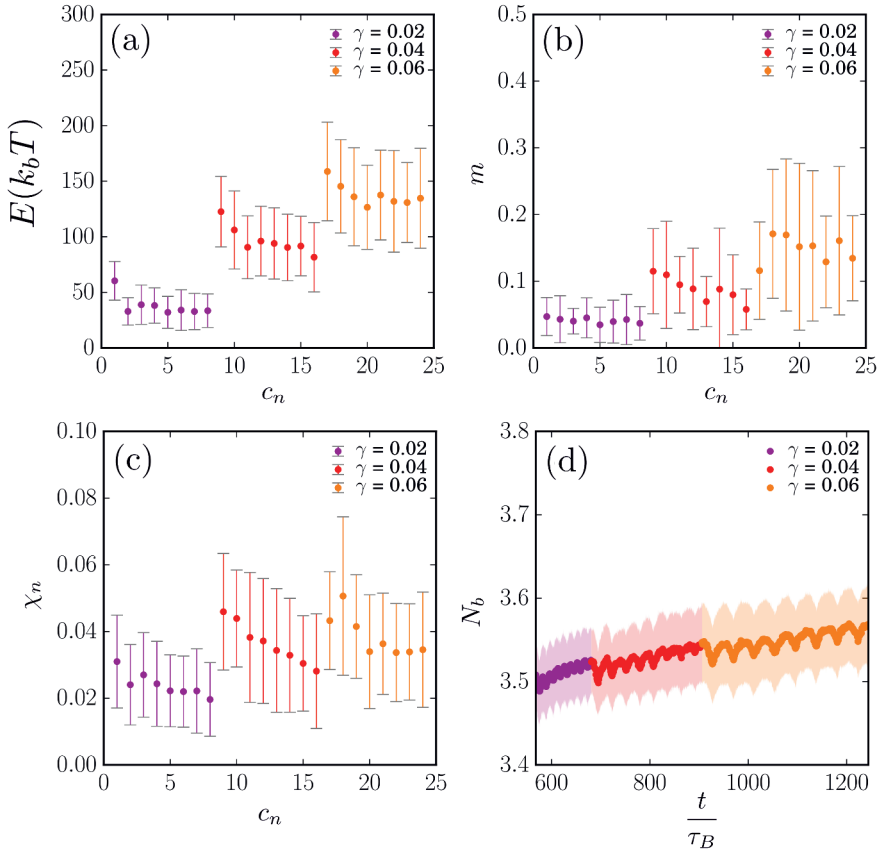

Figure 7.8: (a) Dissipated energy per oscillation for strain amplitudes $\gamma_{max} = 0.02$, 0.04 and 0.06, obtained by integration of the force-strain curves [Fig. 7.4(a)]. (b) Average plastic deformation per oscillation [Eq. 7.1]. (c) The fraction of broken bonds per oscillation. (d) Number of bonds in time. The shaded area indicates the standard deviation.

where $n_i(c_n)$ is the number of nearest neighbors of particle i at the start of a certain oscillation, $n_i(c_n + 1)$ is the number of these neighbors that remain at the end of this oscillation and the average is taken over all particles p in the strand. The number of broken inter-particle bonds is normalized by the average number of bonds per particle N_b. We find that the number

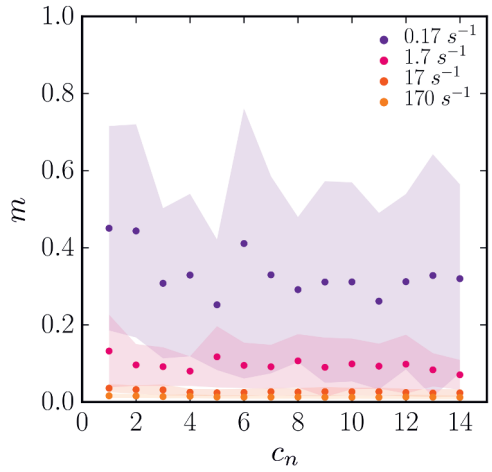

Figure 7.9: Average plastic deformation per oscillation cycle as a function of the strain rate $\dot{\gamma}$.

of broken bonds is highest in the first deformation cycle and decreases gradually [appendix A, Fig. 7.8(c)]. As described earlier, the average number of bonds per particle in the gel strand N_b increases in time [appendix A, Fig. 7.8(d)] [22]. Repeated oscillatory deformation hence is reminiscent to activated aging, in which the non-equilibrium gel structure tends to coarsen to increase the number of bonds in the network.

Broken gel strands

Gel strands that break during the simulation are not included in further analysis. Statistics of the broken strands [Fig. 7.10] show the percentage of strands that detach from the wall or break into clusters. The number of gel strands that break upon expansion is higher compared to compression. Yet, for expansion the majority of the strands break into clusters whereas for compression the effect of breaking at the wall or into clusters is more evenly distributed. Deformation of gel strands at different strain rates $\dot{\gamma}$ only shows

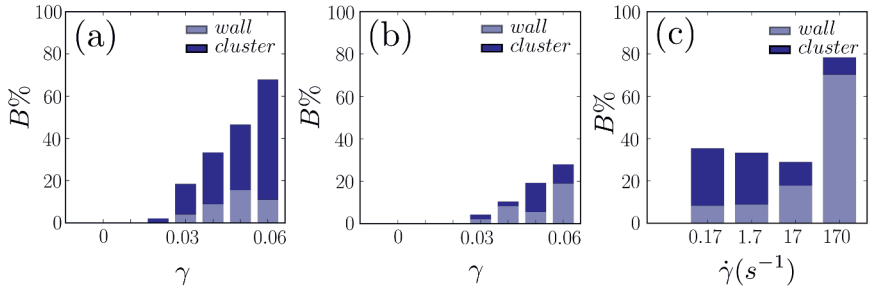

Figure 7.10: Breakage percentage (B %) for (a) expansion and (b) compression of gel strands at strain amplitudes $\gamma = 0.01$ - 0.06. (c) Breakage statistics of gel strands that are deformed with strain rates $\dot{\gamma} = 0.17$, 1.7, 17 and 170 s^{-1} respectively (expansion, $\gamma_{max} = 0.04$).

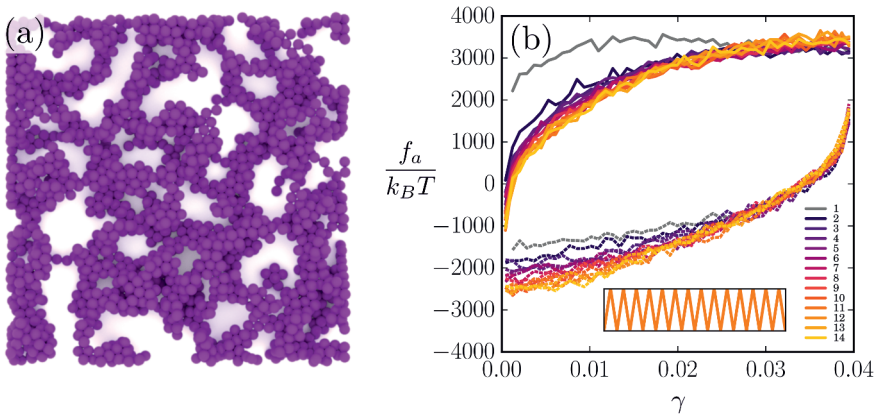

Figure 7.11: (a) Small slab (N=1880) of a large 3D colloidal gel (N=13500) at volume fraction $\phi = 0.2$. (b) Force-strain curves upon 14 oscillatory expansions of a large gel ($\gamma_{max} = 0.04$).

different breakage statistics at a strain rate of 170 s^{-1}. Here, the amount of broken strands increases drastically and strands start to break profoundly at the wall instead of breaking into clusters. This indicates that the amount of broken gel strands is not affected by the strain rate used in the simulations (1.7 s^{-1}).

Appendix C: Comparing a single gel strand with a network of strands

Deformation of a large 3D gel ($N = 13500$, $\phi = 0.2$) is performed in the same way as described for the single gel strands. The gel is formed between two attractive walls, starting from a random particle configuration, and equilibrated for 11 τ_B. Expansion is performed by moving both walls outward. To make simulations feasible, the strain rate is increased to $\dot{\gamma} = 0.0284\ \tau_B^{-1}$. This is comparable to an experimental strain rate of $\dot{\gamma} = 17\ s^{-1}$. The results are averaged over ten independent runs.

The obtained network structure [Fig. 7.11(a)] is highly heterogeneous. To get a clear picture we only show a small slab of the total gel. In Fig. 7.11(b) the force-strain curve of the large gel is shown. Similar to the single gel strands we see irreversible weakening of the network structure, by plastic rearrangements during the first deformation cycle. This confirms that simulations on single gel strands are representative for a large colloidal gel network.

Appendix D: Length independence of simulation data

Gel strands of different lengths are deformed using the same method as presented earlier. The different strands consist of N_{short} = 128, N_{normal} = 256 and N_{long} = 384 particles and are named A, B and C respectively [Fig. 7.12(a)]. Recall that the simulation data in figures 7.3 and 7.4 refers to type B only.

From the percentage of gel strands that break [inset in Fig. 7.12(c)] it is clear that longer gel strands (c) break more often. However, these broken strands are not included in the analysis. When we plot the force-strain curves of the oscillatory expansion of these different gel strands, they fall on top of

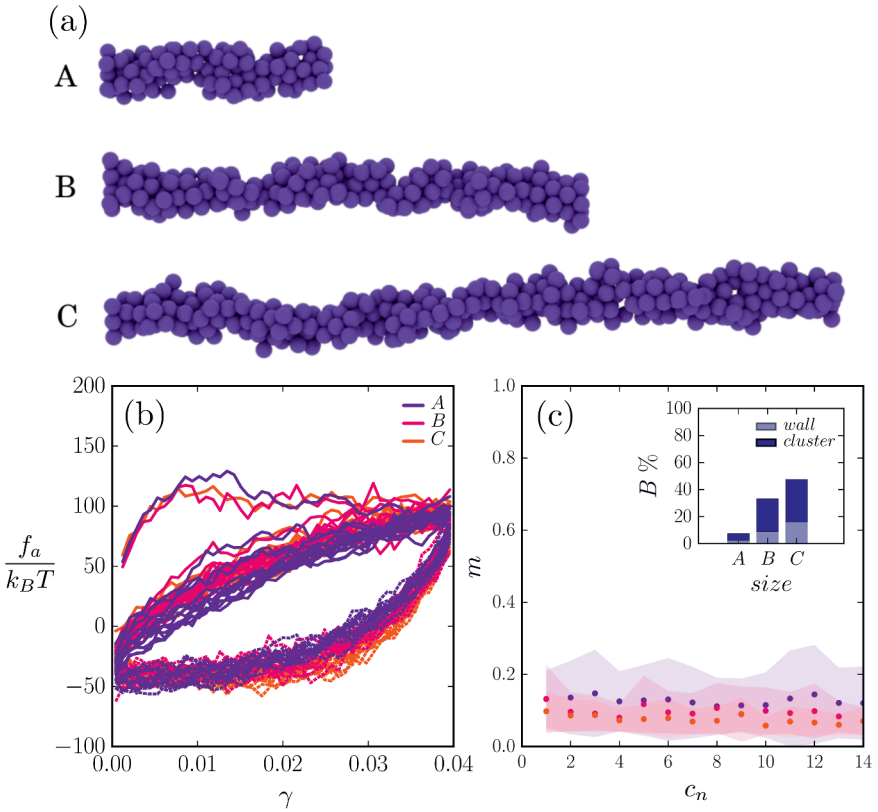

Figure 7.12: (a) Visual representation of gel strands of different lengths. (b) Force-strain curves for 14 oscillatory expansions of gel strands A,B and C ($\gamma_{max} = 0.04$). (c) Average plasticity of the particles per oscillation cycle. The inset shows the percentage of broken strands for A,B and C.

each other. Also the average plasticity in each oscillation cycle [Fig. 7.12(c)] is similar for strands of different lengths. This shows that the plastic deformation in the simulated gel strands does not depend on the length of the strands.

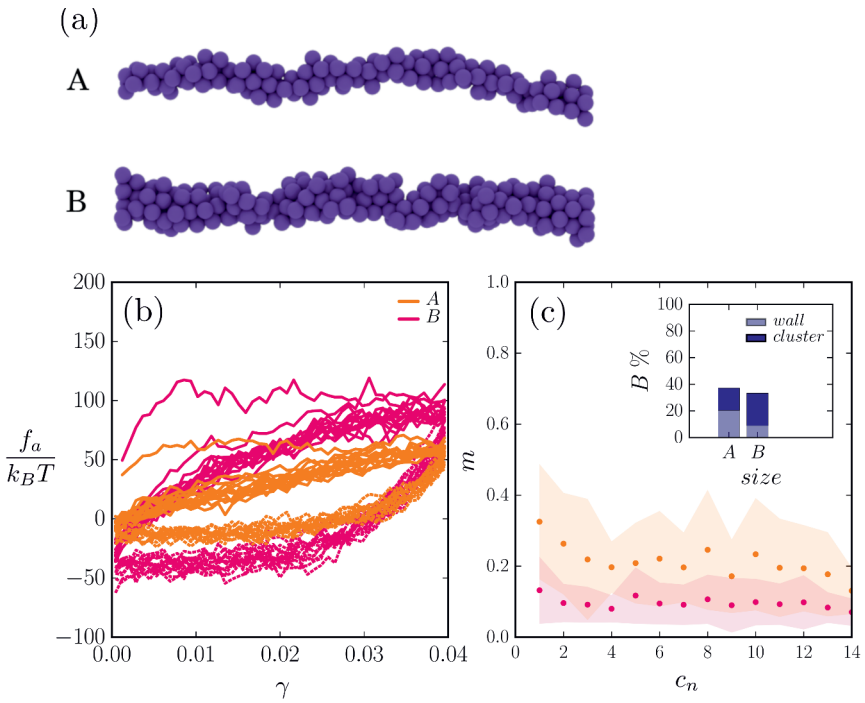

Figure 7.13: (a) Visual representation of two gel strands of different thickness. (b) Force-strain curves for 14 oscillatory expansions of gel strands A and B ($\gamma_{max} = 0.04$). (c) Average plasticity of the particles per oscillation cycle. The inset shows the percentage of broken strands for A and B.

Appendix E: Plasticity increases for thinner strands

With the same simulation method as described before we deform a thinner gel strand. In this case the initial configuration of this thinner strand is a face centered cubic lattice in a 2 × 2 arrangement (N_{thin} = 144). Comparison with strands of type B (as shown in figures 7.3 and 7.4) shows an increase in plasticity when strands are thinner [Fig. 7.13(b)]. From the breakage statistics [inset in Fig. 7.13(b)] we see that, as expected, these thinner strands also break more frequently. This data shows that upon varying the diameter of the gel

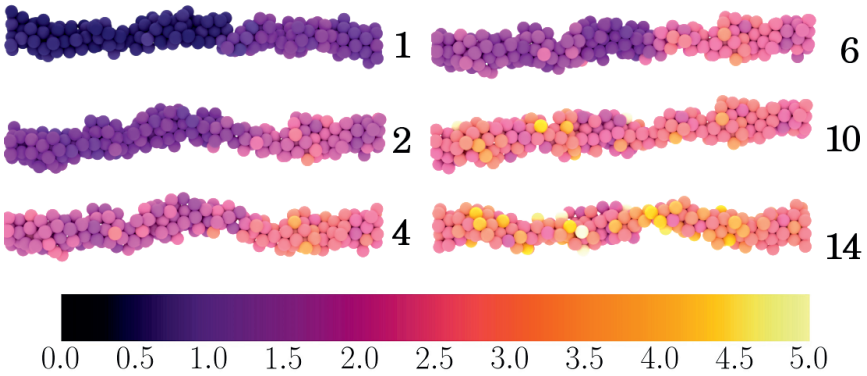

Figure 7.14: Visual representation of the cumulative average plastic deformation in cycles 1,2,4,6,10 and 14 of a single gel strand (γ_{max} = 0.04). The color bar indicates the cumulative irreversible displacements of the particles from low (purple) to high (yellow).

strands plasticity is still a generic mechanism for fatigue.

Appendix F: Additional data

Figure 7.14 contains the same data as shown in Figure 7.3(a). Yet, here the plasticity is plotted in a cumulative fashion. After each oscillation the particle positions are always compared to the configuration at the start of cycle 1. For the non-cumulative plasticity particle positions at the start of cycle 1 are compared with the start of cycle 2, the start of cycle 2 with the start of cycle 3 etc. Figure 7.15 contains additional experimental data.

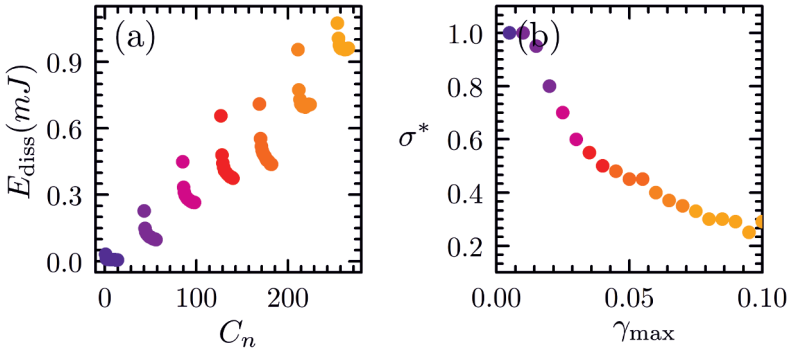

Figure 7.15: (a)Dissipated energy for every cycle (c_n) shown in Fig. 1. The data points are color coded to their respective γ_{max} value. The dissipated energy is highest in the first cycle for a given strain amplitude and then gradually decreases to a plateau value as the stress-strain curve approaches a limit cycle. This limiting dissipated energy reflects the viscoelastic dissipation in the network due to solvent flow through the network or to reversible rearrangements, while the additional dissiptaion in the first cycle reflects the irreversible plastic deformation that occurs during loading of the gels. (b)Characteristic stress σ^* (with $\sigma^* = G_0\gamma^*$) used to rescale experimental data presented in Fig. 7.2 as function of γ_{max}. Data points are color-coded to their respective γ_{max} value.

Bibliography

[1] Jeroen Appel, Niek de Lange, Hanne M. van der Kooij, Ties van de Laar, Jan Bart ten Hove, Thomas E. Kodger, and Joris Sprakel. Temperature Controlled Sequential Gelation in Composite Microgel Suspensions. *Particle & Particle Systems Characterization*, 32(7):764–770, jul 2015.

[2] P. Bartlett, L.J. Teece, and M.A. Faers. Sudden collapse of a colloidal gel. *Phys. Rev. E*, 85:021404, 2012.

[3] Mehdi Bouzid and Emanuela Del Gado. Network topology in soft gels: Hardening and softening materials. *Langmuir*, 34(3):773–781, 2018. PMID: 28977748.

[4] Luca Cipelletti, S. Manley, R. C. Ball, and D. A. Weitz. Universal aging features in the restructuring of fractal colloidal gels. *Phys. Rev. Lett.*, 84:2275–2278, Mar 2000.

[5] J. Colombo and E. Del Gado. Stress localization, stiffening, and yielding in a model colloidal gel. *J. Rheol.*, 58:1089, 2014.

[6] Jader Colombo, Asaph Widmer-Cooper, and Emanuela Del Gado. Microscopic picture of cooperative processes in restructuring gel networks. *Phys. Rev. Lett.*, 110:198301, May 2013.

[7] Thomas Gibaud, Christophe Perge, Stefan B. Lindstrom, Nicolas Taberlet, and Sebastien Manneville. Multiple yielding processes in a colloidal gel under large amplitude oscillatory stress. *Soft Matter*, 12:1701–1712, 2016.

[8] V. Gopalakrishnan and C.F. Zukoski. Delayed flow in thermo-reversible colloidal gels. *J. Rheol.*, 51:623, 2007.

[9] J. Kim, D. Merger, M. Wilhelm, and M.E. Helgeson. Microstructure and nonlinear signatures of yielding in a heterogeneous colloidal gel under large amplitude oscillatory shear. *J. Rheol.*, 58:1359, 2014.

[10] Mirko Klesnil and Petr Lukáš. *Fatigue of metallic materials*, volume 71. Elsevier, 1992.

[11] Thomas E. Kodger and Joris Sprakel. Thermosensitive Molecular, Colloidal, and Bulk Interactions Using a Simple Surfactant. *Advanced Functional Materials*, 23(4):475–482, jan 2013.

[12] A. H. Krall and D. A. Weitz. Internal Dynamics and Elasticity of Fractal Colloidal Gels. *Physical Review Letters*, 80(4):778–781, jan 1998.

[13] B.J. Landrum, W.B. Russell, and R.N. Zia. Delayed yield in colloidal gels: Creep, flow, and re-entrant solid regimes. *J. Rheol.*, 60:783–807, 2016.

[14] M. Laurati, S. U. Egelhaaf, and G. Petekidis. Plastic rearrangements in colloidal gels investigated by laos and ls-echo. *Journal of Rheology*, 58(5):1395–1417, 2014.

[15] M.K. Lee and B.I.G. Barr. An overview of the fatigue behaviour of plain and fibre reinforced concrete. *Cement and Concrete Composites*, 26(4):299 – 305, 2004.

[16] M. Leocmach, C Perge, T. Divoux, and S. Manneville. Creep and Fracture of a Protein Gel under Stress. *Phys. Rev. Lett.*, 113:038303, 2014.

[17] Stefan B. Lindstrom, Thomas E. Kodger, Joris Sprakel, and David A. Weitz. Structures, stresses, and fluctuations in the delayed failure of colloidal gels. *Soft Matter*, 8:3657–3664, 2012.

[18] Peter J Lu, Emanuela Zaccarelli, Fabio Ciulla, Andrew B Schofield, Francesco Sciortino, and David A Weitz. Gelation of particles with short-range attraction. *Nature*, 453(7194):499–503, 2008.

[19] Esmaeel Moghimi, Alan R. Jacob, Nick Koumakis, and George Petekidis. Colloidal gels tuned by oscillatory shear. *Soft Matter*, 13:2371–2383, 2017.

[20] Stefan Münster, Louise M Jawerth, Beverly A Leslie, Jeffrey I Weitz, Ben Fabry, and David A Weitz. Strain history dependence of the nonlinear stress response of fibrin and collagen networks. *Proceedings of the National Academy of Sciences of the United States of America*, 110(30):12197–202, jul 2013.

[21] Ajay Singh Negi and Chinedum O. Osuji. Dynamics of internal stresses and scaling of strain recovery in an aging colloidal gel. *Phys. Rev. E*, 80:010404, Jul 2009.

[22] Jun Dong Park, Kyung Hyun Ahn, and Seung Jong Lee. Structural change and dynamics of colloidal gels under oscillatory shear flow. *Soft Matter*, 11:9262–9272, 2015.

[23] S. Roy and M. S. Tirumkudulu. CYielding in a strongly aggregated colloidal gel. Part I: 2D simulations. *J. Rheol.*, 60:559–574, 2016.

[24] C. Patrick Royall, Jens Eggers, Akira Furukawa, and Hajime Tanaka. Probing colloidal gels at multiple length scales: The role of hydrodynamics. *Phys. Rev. Lett.*, 114:258302, Jun 2015.

[25] C. J. Rueb and C. F. Zukoski. Viscoelastic properties of colloidal gels. *Journal of Rheology*, 41(2):197–218, 1997.

[26] B. Saint-Michel, T. Gibaud, and S. Manneville. Predicting and assessing rupture in protein gels under oscillatory shear. *Soft Matter*, 13:2643, 2017.

[27] Joris Sprakel, Stefan B. Lindström, Thomas E. Kodger, and David A. Weitz. Stress enhancement in the delayed yielding of colloidal gels. *Phys. Rev. Lett.*, 106:248303, Jun 2011.

[28] VERONIQUE Trappe, V Prasad, Luca Cipelletti, PN Segre, and DAVID A Weitz. Jamming phase diagram for attractive particles. *Nature*, 411(6839):772–775, 2001.

[29] Jan Maarten van Doorn, Jochem Bronkhorst, Ruben Higler, Ties van de Laar, and Joris Sprakel. Linking particle dynamics to local connectivity in colloidal gels. *Phys. Rev. Lett.*, 118:188001, May 2017.

[30] Alessio Zaccone, Hua Wu, Daniele Gentili, and Massimo Morbidelli. Theory of activated-rate processes under shear with application to shear-induced aggregation of colloids. *Phys. Rev. E*, 80:051404, Nov 2009.

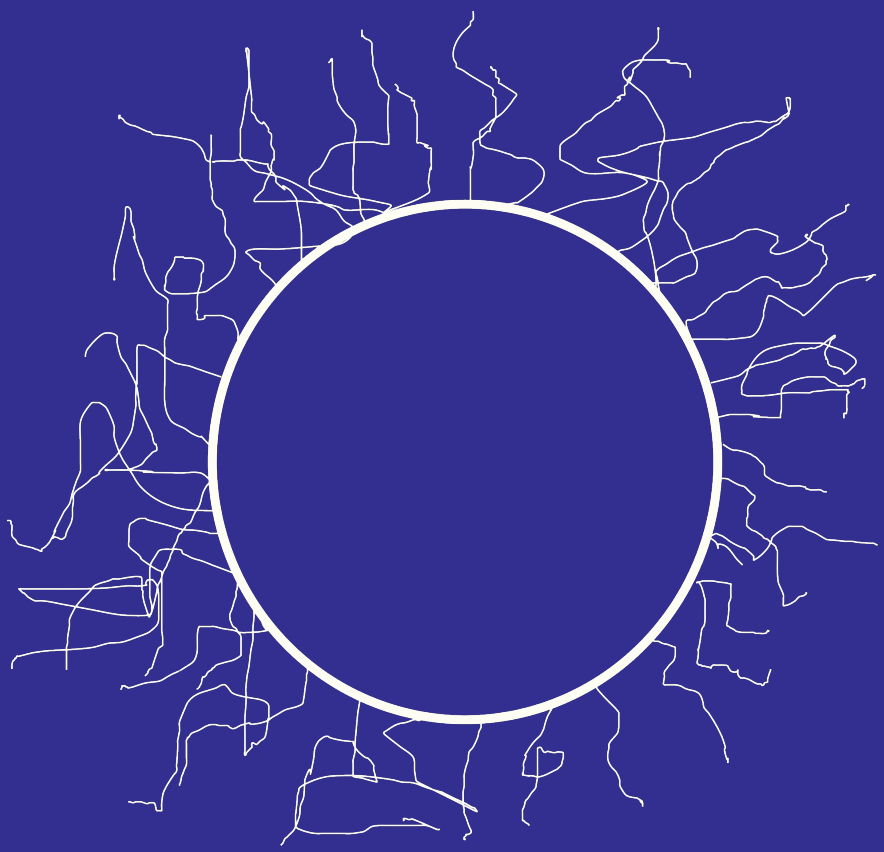

CHAPTER 8

Synthesis of pNIPAM grafted colloids

Sufficiently strong interparticle attractions can lead to aggregation of a colloidal suspension and, at high enough volume fractions, form a mechanically rigid percolating network known as a colloidal gel. We synthesize a model thermo-responsive colloidal system for systematically studying the effect of surface properties, grafting density and chain length, on the particle dynamics within colloidal gels. After inducing an attraction between particles by heating, aggregates undergo thermal fluctuation which we observe and analyze microscopically; the magnitude of the variance in bond angle is larger for lower grafting densities. Macroscopically, a clear increase of the linear mechanical behavior of the gels on both the grafting density and chain length arises, as measured by rheology, which is inversely proportional to the magnitude of local bond angle fluctuations. This colloidal system will allow for further elucidation of the microscopic origins to the complex macroscopic mechanical behavior of colloidal gels including bending modes within the network.

This chapter was published as:

J.M. van Doorn, J. Sprakel and T.E. Kodger: *Temperature-triggered colloidal gelation through well-defined grafted polymeric surfaces*, Gels, 3, **(2017)**, 21

Introduction

Colloidal particles are of significant importance to various fields in science and engineering and to consumer products, such as foods and paints. Upon inducing sufficiently strong attraction to a colloidal suspension, colloidal particles will aggregate and form a mechanically rigid percolating network above a critical volume fraction[26]. These structures, known as colloidal gels, can be regarded as a model for soft heterogeneous solids. Differing from polymeric gels, the bonds between particles in colloidal gels have a non-permanent nature enabling bonds to reform and individual particles to rearrange due to mechanical deformation or thermal fluctuations[2, 22, 25]. These rearrangements mainly govern the mechanical behavior of these soft solids and are of paramount importance to understanding the mechanics of soft heterogeneous solids[9, 5].

Many efforts studying the particle dynamics within colloidal gels focus on the attraction strength as control parameter. Systematic investigations on colloidal gels typically employ a depletion attraction [21], where both the range and depth of interaction may be tuned. However, apart from longitudinal fluctuations such as detaching and attaching, particles can also exhibit transverse modes of rearrangement such as sliding[22]. Where the first mode is mainly influenced by the inter-particle potential, the details of the other modes are difficult to unravel, but thought to be governed by the surface properties of the particles such as their friction coefficients[8]. The implications of such parameters on the assembly of colloidal systems may be profound, and are only briefly discussed in the literature; this is partly due to the fact that there does not yet exist an experimental means to investigate their effects.

In this chapter, we synthesize a colloidal model system that is suitable for systematically studying the effect of particle surface properties such as grafting density and chain length, on the dynamics within colloidal gels. We

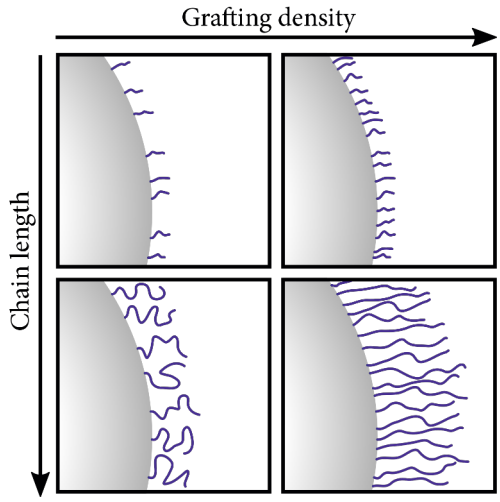

Figure 8.1: Controlled grafting density and chain length using surface initiated ATRP of pNIPAM.

control the grafting density and chain length by using surface initiated atom transfer radical polymerization (ATRP): The grafting density is tuned by copolymerizing a known volume of an ATRP initiator-monomer during particle formation and the chain length is tuned by adding a sacrificial initiator to the bulk solution during the ATRP reaction. We grow a temperature sensitive polymer, poly(N-isopropylacrylamide), from the particle surface to alter the interparticle potential dynamically. After inducing an attraction between particles by heating, a clear dependence on the magnitude of local bond angle fluctuations and linear mechanical behavior of the gel arises from both the grafting density and chain length. Lastly, we disperse these particles in a refractive index matching aqueous solution allowing for 3D confocal imaging during gelation.

Results and Discussion

The origin of the interparticle attraction between colloidal particles can be varied; common examples are depletion[21], electrostatic[24], or van der Waals; however, these sources of attraction can not be easily triggered. Here, we induce inter-particle attraction using a temperature sensitive surface grafted polymer, poly N-isopropylacrylamide (pNIPAM)[18]. This polymer has a Lower Critical Solution Temperature (LCST) in water around 32°C. Above this temperature the polymers expel water and demixes from the aqueous solution which induces interparticle attraction[20]. When the temperature is lowered below the LCST, the polymer solubility is enhanced, resulting in good solvent for T$\ll$LCST, and the interparticle potential becomes sterically repulsive. The precise value of the LCST is sensitive to the composition of the solvent[30] and as a result, we design our system to be stable in water. One of the challenges with studying concentrated particle suspensions is that the refractive index, n, mismatch between the water, $n = 1.333$, and the material of which the colloids are formed impedes experimental optical techniques due to multiple light scattering. To overcome this challenge, we synthesize monodispersed particles from poly(2,2,2-trifluoroethyl methacrylate) (ptFEMA) which has a relatively low refractive index of n =1.42 which is suitable for refractive index matching. By forming particles with diameters between 0.5μm and 3μm, they are large enough to be easily visualized by optical microscopy and also small enough to undergo thermal fluctuations; here we synthesize 1.00μm diameter particles. Additionally, these particles are co-polymerized with 2-(2-bromoisobutyryloxy) ethyl methacrylate (BIEA) which acts as a monomer during particle synthesis and as a initiator for Atom Transfer Radical Polymer (ATRP)[15]. Due to its two sided functionality, this molecule is called an *inimer* [19]. Varying the co-polymerization volume percentage from 0.1% to 3.0% of *inimer* during particle synthesis enables tuning of the grafting density on the particle surface. Additionally, ATRP al-

lows for precise control over the length of these grafted polymers[11]; resulting in the independent ability to tune both the length and density of polymer present on the particle surface as depicted in Fig. 8.1.

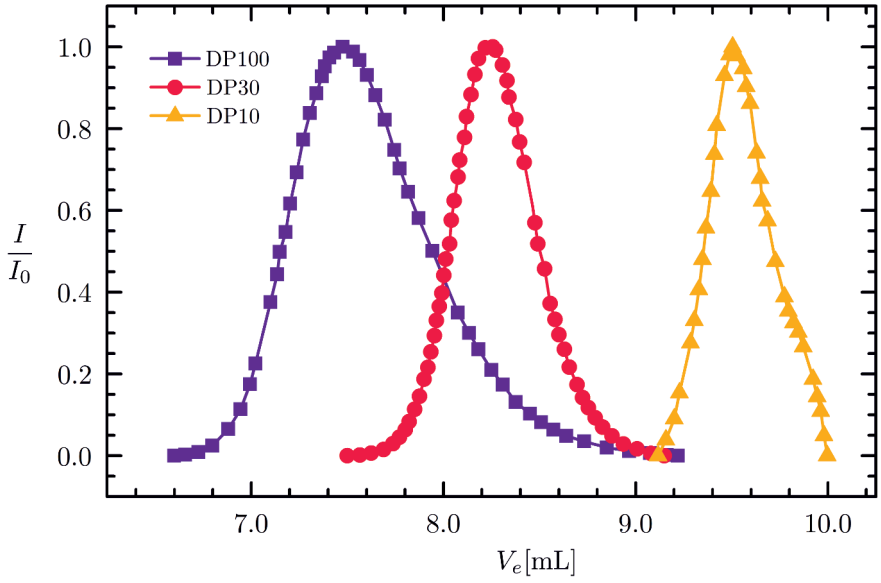

Figure 8.2: Gel permeation chromatography (GPC) elution profiles for polymers with different degrees of polymerization; with the elution volume of the polymers being inversely proportional to their respective degree of polymerization. DP=10, Mn=2.9×10^2 g/mol, Mw=3.1×10^2 g/mol, PDI=1.10; DP=30, Mn=3.1×10^3 g/mol, Mw=3.6×10^3 g/mol, PDI=1.2; DP=100, Mn=9.3×10^3 g/mol, Mw=1.5×10^4 g/mol, PDI=1.6.

During a typical ATRP reaction, the degree of polymerization is controlled by the molar ratio of the initiator to monomer. However, the precise molar value of surface available *inimer* molecules is difficult to determine. This leaves choosing the appropriate amount of monomer to establish a desired ratio challenging. To nevertheless control the length of the grafted polymers, we add a conventional ATRP initiator with identical ATRP initiation rate to the grafting reaction. This yields free linear polymer with the

same degree of polymerization (DP) as the polymers which are simultaneously grown from the surface[27]. Gel permeation chromatography (GPC) analysis of the linear polymer results in a clear dependence in the chain length for the desired DP, while still retaining a fairly monodisperse distribution as seen in Fig. 8.2.

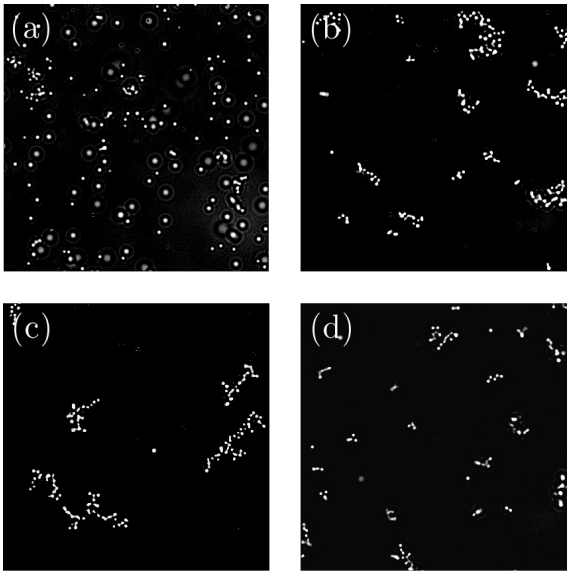

Figure 8.3: Optical microscopy images for different grafting densities at 32°C in 30mM NaCl for DP=100. 0.1%(a), 0.3%(b), 1.0% (c), and 3.0%(d).

To obtain a temperature triggerable interaction, a pNIPAM surface modification is insufficient; electrostatic repulsion between particles must also be tuned. A controlled concentration of salt, 30mM NaCl, is added to screen electrostatic repulsions to approximately the length scale of the shortest surface polymers; the calculated Debye screening length is κ^{-1}= 1.7nm. It must be noted that at higher [NaCl], the LCST of pNIPAM decreases below room temperature[30] and additionally electrostatic repulsion is insufficient to prevent aggregation by van der Waals forces between particles; the precise salt

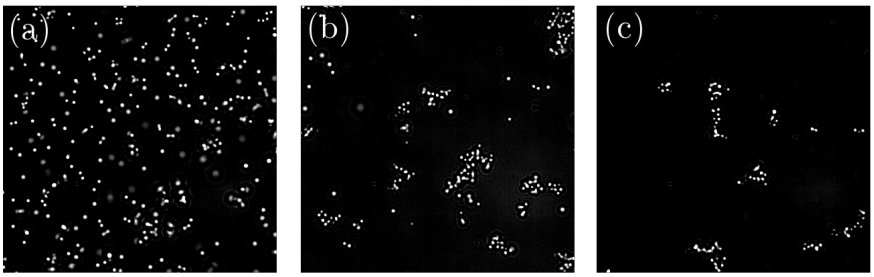

Figure 8.4: Optical microscopy images for different chain lengths at 32°C in 10mM NaCl for a grafting density of 3.0%. DP=10 (a), DP=30 (b), and DP=100 (c).

concentration is crucial to obtain a temperature sensitive interaction potential via the pNIPAM grafted surfaces.

To study the structure and dynamics of aggregated surface modified particles, we employ bright-field microscopy. A two-dimensional array of colloidal particles is formed by simply letting the relatively dense ptFEMA colloids sediment onto the capillary wall. To prevent particles adhering to the capillary walls, the capillaries are coated with a polyeletrolyte multilayer which has been shown to eliminate wall interactions for pNIPAM layers [31, 16]. Once sedimented, the sample is heated to a temperature slightly below the LCST of pNIPAM in pure water, the particles begin to form two-dimensional aggregates as seen in Fig.8.3. For the lowest grafting density, only a few aggregates are found at this temperature and volume fraction, ϕ, while at higher grafting density, large extended aggregates are visible. Correspondingly, for particles with a constant grafting density but differing chain length, the effects are similar: At the short chain lengths, the degree of aggregation is limited while at longer chain lengths, very few individual particles exist as seen in Fig. 8.4. Aggregates of particles with the highest grafting density seem to be smaller than aggregates composed of particles with lower grafting densities. This may be due to particles with lower grafting densities rearranging more easily. Within each aggregate, the magnitude of the thermal fluctuations be-

tween particles appears to be directly related to the chain length and grafting density of the surface polymer. By measuring the angle between neighboring

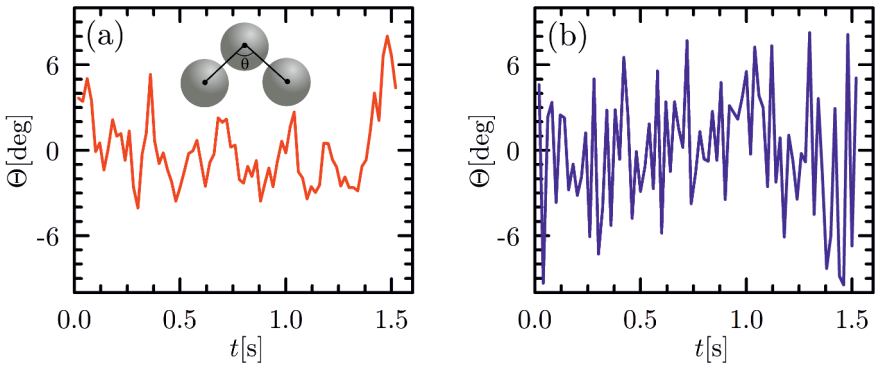

Figure 8.5: Bond angle fluctuations for samples of DP=100 with 0.3% (a) and 3% (b) grafting density. The variance of the fluctuations are 6.7 $(\text{deg})^2$ and 19.2 $(\text{deg})^2$ respectively. Inset; schematic representation of bond angle calculation between neighboring particles.

particles over time, we are able to directly quantify the amplitude of the bond angle fluctuations as a proxy for the friction coefficient. Centers of neighboring particle are first located and tracked over time; after which the angle, $\theta(t)$, is calculated as seen in Fig.8.5 inset. The fluctuations about the mean angle, $\Theta(t) = \theta(t) - \langle\theta(t)\rangle$, are shown for two grafting densities in Fig. 8.5. At lower grafting density, angular fluctuations are large. Conversely, at a higher grafting density, the angular fluctuations are minimized. A smaller amplitude in Θ corresponds to more hindrances in thermally activation motion between particles occurring which points at a higher friction between the particle surfaces [16]. Polymer brushes, with their high grafting densities, have repeatably been found to be low friction interfaces seemingly contradictory to the above observations[14, 23, 4]. However, temperature sensitive polymer brushes tethered to a substrate have been shown to switch from low to high friction above the LCST of pNIPAM which supports the different

amplitudes of Θ seen in Fig. 8.5[12, 17]. Therefore, increasing grafting density, also increases the friction between particles; the consequences of this increased friction may be profound. We hypothesize that colloidal gels with lower friction coefficients and therefore more flexible bonds are capable of relaxing applied stresses and would result in a lower elastic modulus.

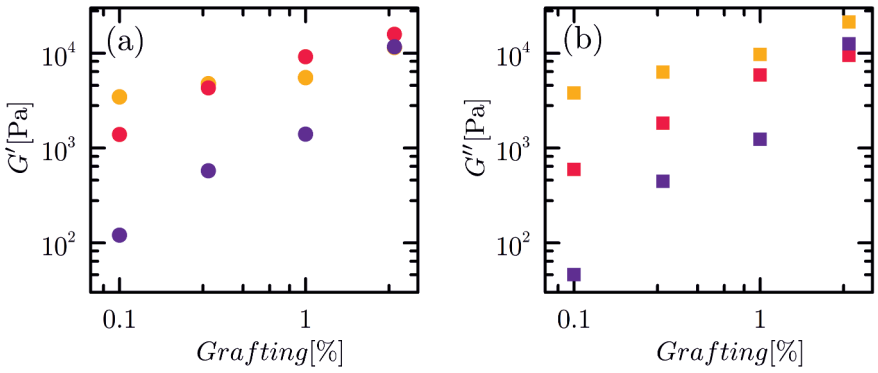

Figure 8.6: Storage (a) and loss moduli (b) after heating dispersions at $\phi = 0.28$ with 30mM NaCl to $45°C$ for DP=10 (yellow), DP=30 (red) and DP=100 (purple). All moduli are measured at 1Hz and γ<0.03.

To directly investigate whether more flexible bonds lead to a lower elastic modulus, we use bulk rheology. At a higher volume fraction, ϕ=0.28$\pm$0.02, the particle dispersions form elastic 3D colloidal gels upon heating above the LCST. We compare the mechanical behavior of colloidal gels with differing grafting densities and chain length of the surface pNIPAM polymer. Though the precise volume fraction of the dispersion is not known, the resulting differences of linear mechanical response in these gels are larger than the variance caused by the uncertainty in ϕ as seen in Fig. 8.6. The elastic modulus of colloidal gels has been shown to scale as, $G^{'} = (\kappa_0/a)(\phi - \phi_c)^p$ where κ_0 is the two-particle spring constant, a is the particle size, p is a scaling exponent which depends on the nature of the network deformation, and ϕ_c is the critical volume fraction which is typically $\phi_c \leq 0.08$[21, 13]. Here,

$\phi = 0.28 >> \phi_c$, therefore, the uncertainty in ϕ cannot account for the large variation in the elastic moduli seen in Fig.8.6; it must arise from changes in κ_0. For the highest grafting densities, the elastic and viscous responses of the gels converge for all chain lengths. By contrast, at lower grafting densities the gels are significantly weaker by nearly to two orders of magnitude for the longest chain length; this drop in elasticity corresponds well with the larger magnitude in Θ observed microscopically as seen in Fig. 8.5.

Colloidal networks resist mechanical deformation by stretching inter-particle bonds and bending particle strands composed of multiple particles. These bending modes result in angular changes between individual particles, $\Delta\theta$, and have been shown to contribute significantly to the elastic response of colloidal networks[21]. Therefore, hindering these bending modes can directly increase the elastic response which is seen in Fig.8.6. How precisely the microscopic changes, grafting density and chain length, manifest as differences in the macroscopic rheology including yielding is beyond the scope of this work and has been the subject of extensive simulation studies[1, 7, 6].

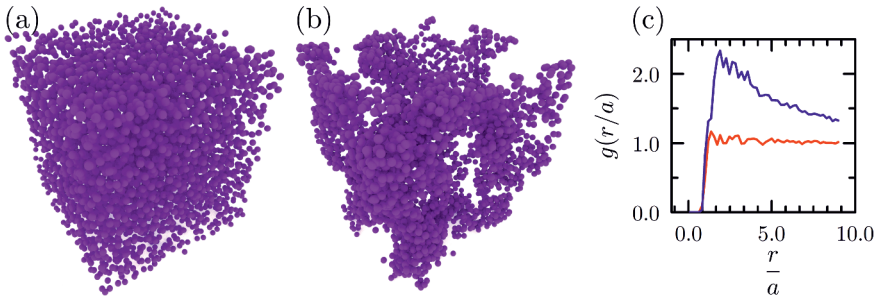

Figure 8.7: Computer-reconstructed visualizations of a sample with particle coordinates obtained from three dimensional confocal microscopy data. The field of view is 67x67x75μm. (A) a liquid dispersion of particles, $\phi \approx 0.15$, at 25°C in 50wt% Sucrose with 10mM NaCl. (B) a colloidal gel of the same dispersion at 50°C. (C) Calculated radial distribution functions normalized for particle size, a, for gel (red, A) and liquid (blue, B) dispersion.

Finally, these model ptFEMA particles may be fluorescently labeled and dispersed in an refractive index matching solution of 50wt% sucrose with 10mM NaCl. By refractive index matching the particles to the suspending solution, light scattering is minimized and by combining fluorescent labeling, 3D confocal microscopy images may be captured. As the thermo-responsive nature of the polymer brush is retained in the sucrose solution, the dispersion may still be heated from a colloidal liquid into a colloidal gel while being imaged deep into the sample, $\approx 75\mu$m as shown in Fig. 8.7. From the individual particle locations, the radial distribution function, $g(r/a)$, was calculated and shown in Fig.8.7C; the $g(r/a)$ clearly show a transition from a liquid dispersion of particles to a colloidal gel by heating. This ability to dynamically induce gelation by heating this particle dispersion with its controlled pNIPAM surface polymer is similar to previous work where the authors quantified the kinetics and structure of pNIPAM grafted nanoparticles [29]. In these dynamic light scattering studies, only the fractal dimension was determined as individual particle kinetics are not available. From this work, a detailed kinetic aggregation framework was proposed to connect the local particle-level dynamics to the macroscopic rheology effectively describing many experimental rheology results on colloidal gels [28]. The model system proposed here will allow for a detailed study of this kinetics framework to different gelation processes and directly observing microscopic sliding dynamics between particles after gelation in three dimensions using confocal microscopy.

Conclusions

We have developed a thermally responsive colloidal system with controlled grafting density and chain length of pNIPAM polymer on the particle surface. Upon heating, such dispersions form a colloidal gel. Both the microscopic bond angle fluctuations and macroscopic elastic moduli exhibit a clear dependence on both grafting density and chain length. The unique com-

bination of complete transparency, tunable particle surface properties and temperature-triggerable interactions paves the way to the study of gelation kinetics in three-dimensions with high resolution.

Materials and Methods

All materials were purchased from TCI Europe and used as received unless otherwise noted. N-isopropyl acrylamide (NIPAM) monomer was recrystallized from n-hexane prior to use. Additionally, the $inimer$ monomer, 2-(2-bromoisobutyryloxy) ethyl methacrylate (BIEA), was synthesized as previously reported[19, 15].

Particle Synthesis

We synthesize poly(2,2,2-trifluoroethyl methacrylate) (ptFEMA) colloidal particles co-polymerized with 2-(2-bromoisobutyryloxy) ethyl methacrylate using free radical dispersion polymerization [15]. To a 500ml round bottom flask is added 30ml water, 270ml methanol, 25ml 2,2,2-trifluoroethyl methacrylate, 250mg 2,2′-azobis(2-methylpropionitrile), 250mg 3-sulfopropyl methacrylate potassium salt (Sigma-Aldrich) and 25μL of BIEA (0.1vol% to monomer). The flask is placed under reflux conditions in a silicone oil bath preheated to 80°C and allowed to polymerize for 4hrs. The resulting particles have a hydrodynamic diameter, $a = 1.00\mu$m with a polydispersity index, PDI = $(\sigma(a)/\langle a \rangle) = 0.01$ as determined by Dynamic Light Scattering. The reaction is repeated with 75μL, 250μL, and 750μL of BIEA to arrive at 0.3vol%, 1.0vol% and 3.0vol% of *inimer* respective to monomer, with no measurable change to particle diameter or polydispersity.

Surface Initiated ATRP

Particle dispersions were washed three times by centrifugation at 250g into a 1wt% solution of L23 surfactant (Sigma-Aldrich) to a final volume of 200ml.

To graft polymers from the particle surface, 50g dimethylformamide, 2g NIPAM (1.7×10^{-2} moles), 0.47ml tris[2-(dimethylamino)ethyl]amine (1.7×10^{-3} moles), 0.253mL ethyl α-bromoisobutyrate (1.7×10^{-3} moles) are added to a 250ml round bottom flask. The solution is bubbled with nitrogen for 15 minutes, after which 0.168g of Cu(I)Cl (1.7×10^{-3} moles) is added to initiate the polymerization. The above procedure yielded a DP=10 as shown in Fig. 8.2. For DP=30, 50ml particle dispersion, 50g dimethylformamide, 2g NIPAM (1.7×10^{-2} moles), 0.156ml tris[2-(dimethylamino)ethyl]amine (0.56×10^{-3} moles), 0.084mL ethyl α-bromoisobutyrate (0.56×10^{-3} moles) are added to a 250ml round bottom flask, bubbled, and initiated with 0.056g of Cu(I)Cl (0.56×10^{-3} moles). For DP=100, 50ml particle dispersion, 50g dimethylformamide, 2g NIPAM (1.7×10^{-2} moles), 0.047ml tris[2-(dimethylamino)ethyl]amine (1.7×10^{-4} moles), 0.025mL ethyl α-bromoisobutyrate (1.7×10^{-4} moles) are added to a 250ml round bottom flask and initiated with 0.017g of Cu(I)Cl (1.7×10^{-4} moles). These procedures are repeated for each BIEA volume ratio, 0.1%, 0.3vol%, 1.0vol% and 3.0vol%, to yield a total of 12 different particle dispersions each with a unique grafting density and chain length. After surface modification, the dispersions were centrifuged and the supernatant collected and purified before GPC measurements. The sedimented particles were redispersed in 20ml of demineralized water and each particle dispersion was dialyzed for 10 days again deionized water to remove Cu(I)Cl and the surfactant L23. The hydrodynamic diameters of the particles after surface modification have been characterized by DLS using a second-order cumulants fit to the correlation functions. The results show an increasing trend only for the with highest surface grafting density, 3%, from $a = 1020 \pm 68nm$ for the bare particles to DP=10, $a = 996 \pm 63nm$; DP=30, $a = 1044 \pm 31nm$; and DP=100, $a = 1112 \pm 40nm$.

The supernatant was heated to $80°C$ overnight to remove water and then precipitated in diethyl ether, dissolved in chloroform, and precipitated again, a total three times. The precipitate was dried and dissolved in water and

mixed bed resins (AG501-X8, Bio-Rad) added to remove copper salts. The resins were filtered away and the now clean pNIPAM polymer was freeze dried. GPC measurements were performed in at 5mg/ml in a solution of tetrahydrofuran with 5 vol % triethylamine at a flow rate of 1ml/min at 35°C on an Agilent Technologies 1200, PLgel 5μm Mixed-D column[3]. The column was calibrated prior to use with linear polystyrene dissolved in the above solvent.

Fluorescent Labeling

A single dispersion, 1vol% BIEA with DP=100, was fluorescently labeled. A miniemulsion was prepared by tip sonication, containing 0.2ml toluene, 5mg boron-dipyrromethene 543 dye (Excition, Inc.), and 4ml 1wt% solution of L23 surfactant. To this miniemulsion 1.5ml of particle dispersion at $\phi = 0.30$ was added. This dispersion was mixed for 3 days to allow the particles to swell and take up the dye. Subsequently dry nitrogen was blown over the top of the dispersion to remove toluene and kinetically trap the dye inside the particles. This fluorescently labeled dispersion was dialyzed against deionized water to remove L23. Sucrose was then added as a powder and dissolved to a final concentration of 50wt% which resulted in a refractive index matched dispersion.

Microscopy

Bright field and confocal microscopy experiments were performed in capillaries of 40x4x0.2mm inner dimensions coated with polyelectrolyte multilayers. Capillaries were first plasma treated, then submerged into a 1M NaCl solution with 1wt% poly(diallydimethyl ammonium) chloride (Mw $\approx 5 \times 10^5$ g/mol, Sigma-Aldirch), then washed extensively with deionized water, then submerged in a 1M NaCl solution with 1wt% poly(styrene sulfonate) (Mw $\approx 2 \times 10^5$ g/mol, Sigma-Aldrich) and finally washed extensively with deion-

ized water. This layer-by-layer treatment was repeated three times for a total of 6 layers. A dilute suspension of each particle dispersion, $\phi = 0.001$, was prepared by diluting with either a 10mM or 30mM NaCl solution, loaded into a coated capillary, allowed to sediment over 1hr and finally heated to the desired temperature using a home built objective and capillary heater. Samples were allowed to equilibrate for 10 minutes at each temperature before imaging. Images were then captured using a Nikon microscopy with a 60X water immersion objective at 50fps using a Fastec HiSpec1 camera. Confocal microscopy 3D images were captured using a Zeiss LSM5 Pascal with 488nm excitation and 100X oil immersion objective. The refractive index matched dispersion in 50wt% sucrose with 10mM NaCl was first imaged at room temperature then quickly heated to $50°$C. Particle centers were located using standard locating software [10] using Matlab.

Rheology

For rheology measurements, each dialyzed dispersion was allowed to sediment over several days and the supernatant removed until the dispersion obtained a high volume fraction, $\phi > 0.30$. Each dispersion's volume fraction was measured by drying a known mass of dispersion, $\approx 1.00g$, in an 80°C oven overnight; this method exhibited repeatability within 6% of the mean. To this measured dispersion, a small volume of water and 2.0M NaCl was added to obtain $\phi = 0.28$ in 100mM NaCl for each dispersion which was measured using a Anton Paar MCR501 rheometer with a 50mm diameter cone-plate geometry. A solution of tetradecane was added around the geometry to minimize evaporation. The dispersion was heated to $45°C$ in 10 minutes and allowed to gel further over 1hr then measured at 1Hz with an applied strain from $\gamma = 0.001$ to $\gamma = 1.00$ and an average value taken within the linear regime typically $\gamma < 0.03$.

Bibliography

[1] Eric Dickinson Joost H. J. van Opheusden Bert H. Bijsterbosch, Martin T. A. Bos and Pieter Walstra. Brownian dynamics simulation of particle gel formation: from argon to yoghurt. *Faraday Discussions*, 101:51–64, 1995.

[2] Richard Buscall, Tahsin H. Choudhury, Malcolm A. Faers, James W. Goodwin, Paul A. Luckham, and Susan J. Partridge. Towards rationalising collapse times for the delayed sedimentation of weakly-aggregated colloidal gels. *Soft Matter*, 5:1345–1349, 2009.

[3] Merve Cetintas and Marleen Kamperman. Self-assembly of ps-b-pnipam-b-ps block copolymer thin films via selective solvent annealing. *Polymer*, 107:387–397, 2016.

[4] M Chen, WH Briscoe, SP Armes, and J Klein. Lubrication by biomimetic surface layers at physiological pressures. *Science*, 323:1698–1700, 2009.

[5] Luca Cipelletti, S Manley, R C Ball, and D A Weitz. Universal Aging Features in the Restructuring of Fractal Colloidal Gels. 2000.

[6] Jader Colombo and Emanuela Del Gado. Stress localization, stiffening, and yielding in a model colloidal gel. *Journal of Rheology*, 58(5):1089–1116, 2014.

[7] Jader Colombo, Asaph Widmer-Cooper, and Emanuela Del Gado. Microscopic picture of cooperative processes in restructuring gel networks. *Physical review letters*, 110(19):198301, 2013.

[8] Jean-Michel Condre, Christian Ligoure, and Luca Cipelletti. The role of solid friction in the sedimentation of strongly attractive colloidal gels. *Journal of Statistical Mechanics: Theory and Experiment*, 2007(02):02010, Feb 2007.

[9] A Coniglio, L De Arcangelis, E Del Gado, A Fierro, and N Sator. Percolation , gelation and dynamical behaviour in colloids. *J . Phys . : Condens . Matter*, 16:4831–4839, 2004.

[10] Yongxiang Gao and Maria L. Kilfoil. Accurate detection and complete tracking of large populations of features in three dimensions. *Optics Express*, 17(6):4685, 2009.

[11] J. D. Jeyaprakash, S. Samuel, R. Dhamodharan, and Jürgen Rühe. Polymer brushes via atrp: Role of activator and deactivator in the surface-initiated atrp of styrene on planar substrates. *Macromolecular Rapid Communications*, 23(4):277–281, 2002.

[12] D.M. Jones, J.R. Smith, W.T.S. Huck, and C. Alexander. Variable adhesion of micropatterned thermoresponsive polymer brushes: Afm investigations of poly(n-isopropylacrylamide) brushes prepared by surface-initiated polymerizations. *Advanced Materials*, 14(16):1130–1134, 2002.

[13] Yacov Kantor and Itzhak Webman. Elastic properties of random percolating systems. *Physical Review Letters*, 52(21):1891–1894, May 1984.

[14] Jacob Klein, Eugenia Kumacheva, Diana Mahalu, Dvora Perahia, Lewis J Fetters, et al. Reduction of frictional forces between solid surfaces bearing polymer brushes. *Nature*, 370(6491):634–636, 1994.

[15] Thomas E Kodger, Rodrigo E Guerra, and Joris Sprakel. Precise colloids with tunable interactions for confocal microscopy. *Scientific reports*, 5:14635, 2015.

[16] Thomas E. Kodger and Joris Sprakel. Thermosensitive molecular, colloidal, and bulk interactions using a simple surfactant. *Adv. Funct. Mater.*, 23(4):475–482, Sep 2012.

[17] Ibrahim B. Malham and Lionel Bureau. Density effects on collapse, compression, and adhesion of thermoresponsive polymer brushes. *Langmuir*, 26(7):4762–4768, 2010. PMID: 19961208.

[18] Giancarlo Masci, Laura Giacomelli, and Vittorio Crescenzi. Atom transfer radical polymerization of n-isopropylacrylamide. *Macromolecular rapid communications*, 25(4):559–564, 2004.

[19] Krzysztof Matyjaszewski, Scott G. Gaynor, Anthony Kulfan, and Matthew Podwika. Preparation of hyperbranched polyacrylates by atom transfer radical polymerization. 1.acrylic ab* monomers in atom transfer radical polymerizations. *Macromolecules*, 30:5192–5194, 1997.

[20] Robert Pelton. Poly(n-isopropylacrylamide) (pnipam) is never hydrophobic. *Journal of Colloid and Interface Science*, 348:673–674, 2010.

[21] V. Prasad, V. Trappe, A. D. Dinsmore, P. N. Segre, L. Cipelletti, and D. A. Weitz. Rideal lecture. *Faraday Discussions*, 123:1–12, Nov 2002.

[22] Bharath Rajaram and Ali Mohraz. Microstructural response of dilute colloidal gels to nonlinear shear deformation. *Soft Matter*, 6:2246–2259, 2010.

[23] Uri Raviv, Suzanne Giasson, Nir Kampf, Jean-François Gohy, Robert Jérôme, and Jacob Klein. Lubrication by charged polymers. *Nature*, 425(6954):163–165, 2003.

[24] E.R. Russell, J. Sprakel, T.E. Kodger, and D.A. Weitz. Colloidal gelation of oppositely charged particles. *Soft Matter*, 8:8697, 2012.

[25] Joris Sprakel, Stefan B. Lindstrom, Thomas E. Kodger, and David A. Weitz. Stress enhancement in the delayed yielding of colloidal gels. *Physical Review Letters*, 106(24), Jun 2011.

[26] Veronique Trappe, V Prasad, Luca Cipelletti, PN Segre, and David A Weitz. Jamming phase diagram for attractive particles. *Nature*, 411(6839):772–775, 2001.

[27] T. W. von Werna, D. S. Germack, E. C. Hagberg, V. V. Sheares, C. J. Hawker, and K. R. Carter. A versatile method for tubing the chemistry and size of nanoscopic features by living free radical polymerization. *Journal of the American Chemical Society*, 125:3831, 2003.

[28] A Zaccone, HH Winter, M Siebenbürger, and M Ballauff. Linking self-assembly, rheology, and gel transition in attractive colloids. *Journal of Rheology*, 58(5):1219–1244, 2014.

[29] Alessio Zaccone, Jerome J Crassous, Benjamin Béri, and Matthias Ballauff. Quantifying the reversible association of thermosensitive nanoparticles. *Physical review letters*, 107(16):168303, 2011.

[30] Yanjie Zhang, Steven Furyk, David E Bergbreiter, and Paul S Cremer. Specific ion effects on the water solubility of macromolecules: Pnipam and the hofmeister series. *Journal of the American Chemical Society*, 127(41):14505–14510, 2005.

[31] Haipeng Zheng, Ilsoon Lee, and Michael F. Rubner. Two component particle arrays on patterned polyelectrolyte multilayer templates. *Advanced Materials*, 14:569–572, 2002.

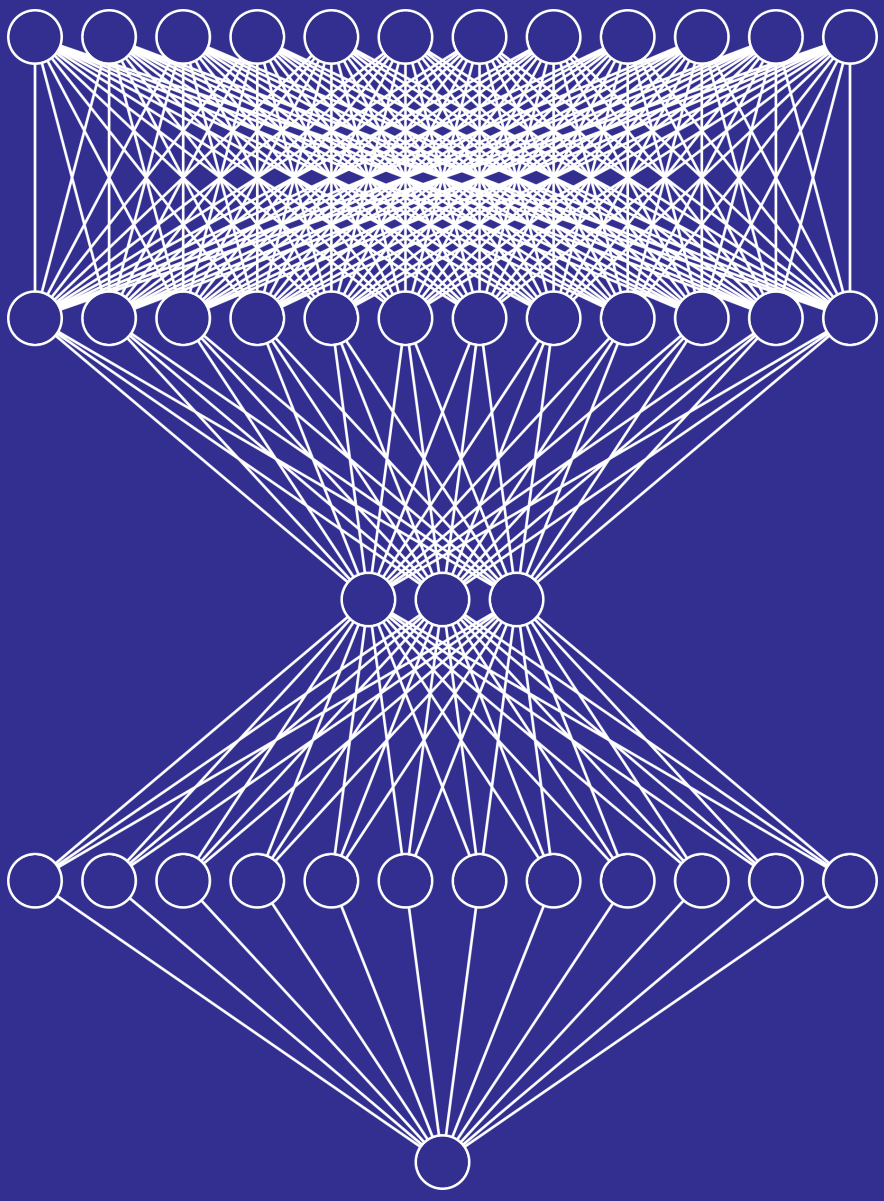

CHAPTER 9

Learn to Break: Predicting mechanical failure in dilute fiber networks with machine learning

Mechanically loading solids too far leads to irreversible fracture. The critical stress at which fracture occurs is highly stochastic and difficult to predict. Especially for disordered fiber networks that are characterized by their non-linear mechanics and large amounts of non-affine deformation the fracture processes is highly complex. In this chapter we explore how recently developed methods in machine learning can aid the prediction of the critical fracture stress to asses the lifetime of materials. We obtain excellent predictions for the critical fracture stress of random fiber networks solely based on structural and topological input parameters. Furthermore we circumvent the black box behavior of neural networks to shed light on the physical mechanisms underlying fracture by identifying parameters that are essential for a good prediction.

Manuscript in preparation as:
J.M. van Doorn, S. Dussi and J van der Gucht: *Learn to Break: Predicting mechanical failure in dilute fiber networks with machine learning*

Introduction

When a material is loaded beyond its limits it will break[1]. Depending on the materials properties this failure will be brittle, ductile or a combination of both[2]. In all cases fracture is driven by a random process and a complex interplay of mechanical and structural features[3] and a small change in one of these properties may change the fracture behaviour completely. Typically a crack is initiated at a weak spot and, if dissipation via plastic deformation plays a small role, this crack will propagate until the material splits in two or more parts[4, 5]. The mechanics in the crack tip are extreme and deviating strongly from the approximations of linear elasticity. They are characterised by a strong non-affinity, an extreme sensitivity to local features in the material nanostructure, making fracture extraordinarily difficult to predict from averaged material properties using traditional methods[6].

Mechanical failure in fibrous materials is even more complex; yet of crucial importance in a wide variety of biological settings, such as the cytoskeleton, muscles and connective tissues, or engineered fibrous materials such as paper or fibrillar nanocomposites[3]. These materials consist of dilute and disordered fiber networks. Even without fracture these networks exhibit a highly non-linear mechanical response[7, 8]. These non-linearities allow nature to tune the mechanics to a specific biological function. Predicting fracture in these networks solely from their structure could lead to a set of design rules that allow for engineered tissues with a tailored mechanical response. Recent advances in machine learning led to the development of artificial neural networks that are capable to capture highly non-linear processes and that have been shown to give accurate predictions for greatly different and complex problems[9, 10, 11, 12, 13].

In this chapter we train artificial neural networks to predict fracture and the mechanics leading up to fracture in highly non-linear dilute networks. Machine learning cannot only be used as a means to predict features that are

difficult to predict by other means, but despite it's 'black box' nature they can be utilized as a stepping stone to unveil new physical mechanisms. By systematically varying input parameters we identified three structural and topological parameters that are crucial in predicting fracture. Our results open up the way to a more integral understanding of failure in dilute networks.

Results

Non-linear elasticity

Machine learning requires training through input of a large numbers of statistically independent target structures. Here we create these by means of spring-network simulations. We carry out simulations on spring networks consisting of equidistant springs of length l_0 and with identical spring constants μ on a triangular lattice with $L \times L$ nodes. To create disorder in the network structure and topology, we remove a fraction of the bonds $(1 - p)$ randomly in each fully connected spring network[Fig.9.1(a)]. For each p and L we generate a dataset of 10^3 spring networks to train our neural networks. We subject all networks to uniaxial extension deformation and after minimizing the energy with an highly optimized structural relaxation algorithm (the Fast Inertial Relaxation Engine, FIRE), we record the overall stress[Fig. 9.1(b)][14, 15]. Networks with dilutions $p = 0.5, 0.56, 0.6$ are below the rigidity threshold for triangular lattices and do not meet the Maxwell criterion for rigidity and can therefore not be considered mechanically rigid[16, 7, 17]. As a result of this dilution, networks with a dilution of bonds around the rigidity percolation threshold exhibit a highly non-linear, difficult to predict, stress-strain response as has been observed earlier [Fig. 9.1(c)][7, 8, 18, 19]. The goal is to predict fracture based solely on structural metrics of the material. We thus identify a large number of structural metrics

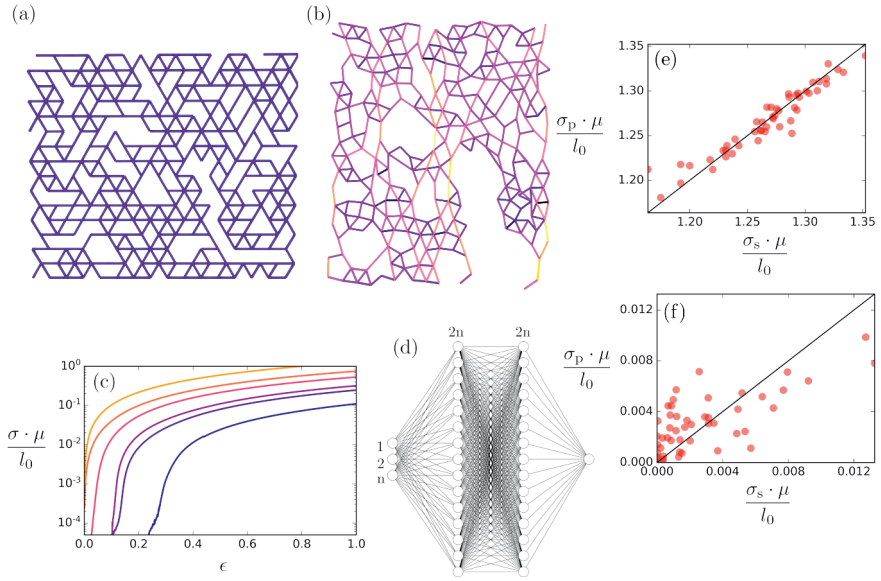

Figure 9.1: (a) Example of a spring network without deformation. (b) A uniaxialy loaded spring network, bonds with a brighter color carry more load than darker bonds. (c) Stress-strain curves for various network dilutions as a result of uniaxial extension. Colors represent from blue to yellow $p = 0.5, 0.56, 0.6, 0.7, 0.9$. (d) Neural network architecture used in this work. (e)Scatter plot of predicted vs simulated stress values for $p = 0.9$, $\epsilon = 1.0$ (f)Scatter plot of predicted vs simulated stress values for $p = 0.56$, $\epsilon = 0.1$ and $L = 16$

to explore. We train fully connected neural networks that consist of an input layer with n input nodes, two hidden layers of $2n$ nodes and one output layer with one node[Fig. 9.1(d)][20, 21]. As input we calculate coarse grained parameters that quantify the structure and topology of our spring networks. These parameters include the average number of bonds per node, the variance, kurtosis and skewness of the bond angle and cycle length distributions, a complete overview is given in table 9.1 allong with an explanantion of most parameters in appendix A. We use 85% of the spring network configurations in our dataset for training, 10% for validation and 5% for testing our predic-

tions.

As the non linear stress strain response depends greatly on the dilution of bonds we start with prediction for spring networks with $p = 0.9$ at $\epsilon = 1$ as relatively linear case[7]. To test how well the neural network predicts the stress at a given strain we plot for each spring network in the testing set the predicted stress values σ_{p} as a function of the stress values obtained with simulations σ_{s}. For a perfect prediction all points would lie on the line $\sigma_{\mathrm{p}} = \sigma_{\mathrm{s}}$ and for this relatively easy case we find that most values are indeed close to this line[Fig.9.1(e)]. However for a more complex and non-linear case of $p = 0.56$ and $\epsilon = 0.1$ we find many more points deviating from this ideal line indicating that the neural network has much more difficulty in predicting a more non-linear mechanical response[Fig.9.1(f)].

To appreciate the predictive capabilities of our trained neural networks more quantitatively we calculate the Pearson correlation coefficient ρ between the simulated stress values and the predicted stress values. A perfect prediction corresponds to a perfect correlation and therefore $\rho = 1$. A more strict measure is the S-score which quantifies the improvement of the prediction over using the mean of the test data as an estimate for the stress of a specific spring network[11]:

$$S = 1 - \frac{[\sum_i (\sigma_{\mathrm{s},i} - \sigma_{\mathrm{p},i})^2]}{[\sum_i (\sigma_{\mathrm{s},i} - \langle \sigma_{\mathrm{s},i} \rangle)^2]} \tag{9.1}$$

Here $S = 0$ would correspond to a prediction that is equally good as using the mean of the stress values from simulations and $S = 1$ to a perfect prediction. For the cases in figure 9.1 (e,f) we obtain $S = 0.89$ and $S = 0.48$ respectively. This suggests that even in difficult non-linear cases we can predict mechanical stress much better than using conventional estimates such as statistical means.

To investigate how predictability evolves along the stress-strain response we train a series of neural networks, each at a different strain for spring networks at increasing dilution[Fig. 9.2]. As spring networks exhibit a more

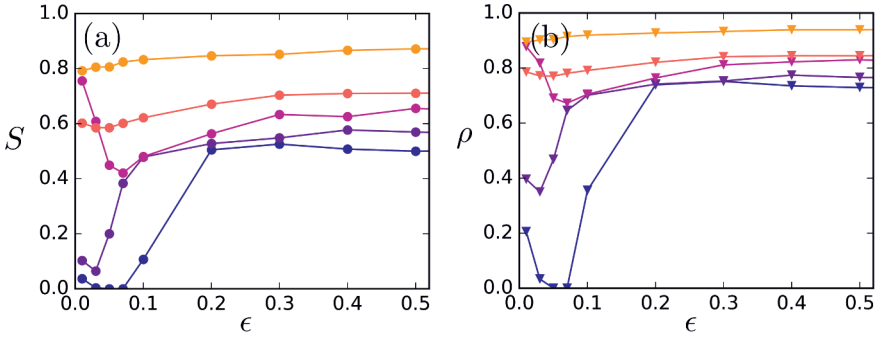

Figure 9.2: (a) Prediction quality measured with the S-score for neural networks trained for spring networks with different dilutions at increasing strain. Colors correspond to: from blue to yellow $p =, 0.50, 0.56, 0.6, 0.7, 0.9$. (b) Prediction quality measured with the Pearson correlation coefficient for that same neural networks shown in (a).

non-linear response with increasing dilution we expect prediction to become more challenging for a dilute network. Indeed we observe decreasing S and ρ scores with decreasing p. Strikingly, spring networks with $p = 0.6$ and $p = 0.56$ have a minimum in their predictability. As these networks are diluted below the rigidity threshold they do not resist deformation at small strains. However when the networks undergo deformations, segments of the network are pulled taut, which induced strain-induced rigidity, allowing mechanical stress to be stored in the network under sufficient strain[8]. Around this critical strain non-affine deformations dominate and make prediction particularly difficult[7, 22, 23, 24, 18]. The minimum in predictability highlights this complex non-affine behavior of the critical spring networks.

So far all our spring networks consist of equidistant springs of length l_0. However in realistic materials, fibers have a wide distribution of lengths[25]. To demonstrate the broad applicability of our approach we try to predict stress-strain responses in more geometrically disordered networks. For this we move the nodes in the original triangular lattice to a random position within a circle around the original position of the node with radius $D_R \cdot l_0$.

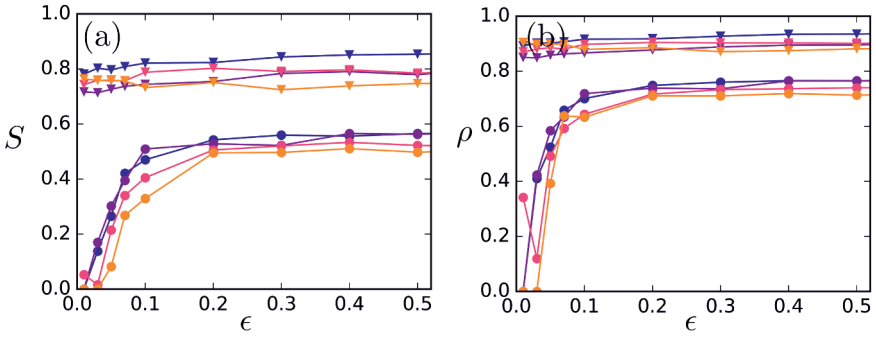

Figure 9.3: (a)Prediction quality measured with the S-score for neural networks trained for spring networks with different bond length distributions at increasing strain with dilution $p = 0.9$ (triangles) and $p = 0.56$ (circles). Colors correspond to: from blue to yellow $D_R = 0.1, 0.2, 03, 0.4$. (b) Prediction quality measured with the Pearson correlation coefficient for that same neural networks shown in (a).

Here D_R is the degree of distortion. We set the lengths of the resulting bonds as rest lengths and keep the spring constants identical for all bonds. Similar to the dilution dependence we quantify the performance of our neural networks with ρ and S[Fig. 9.3]. As observed earlier we find spring networks with a lower dilution more easy to predict than networks with a higher dilution. Surprisingly the distortion does not have a dramatic effect on the predictability. This means that despite significant disorder the neural network is still able to make reasonable predictions for the stress-response. Moreover the effect of distortion seems to be smaller for a highly diluted network [Fig 9.3(a)]. Apparently for spring networks that already exhibit large connectivity disorder, extra distortion does not make mechanics more complex.

Fracture

To study fracture, we introduce a critical breaking threshold t to the bonds in our spring network. When a bond is stretched above this critical strain value it will be removed from the network. We define the maximal stress as

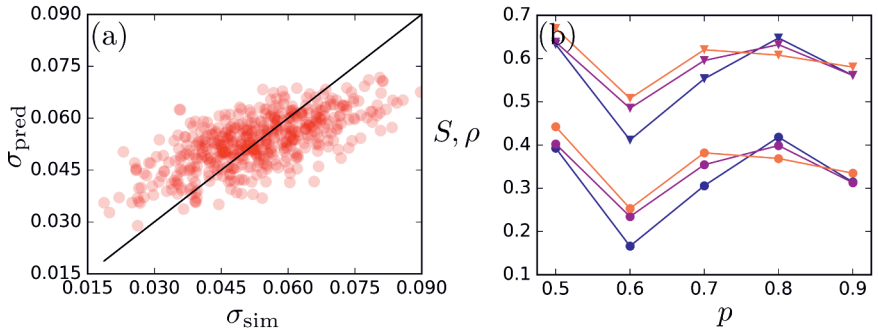

Figure 9.4: (a) Scatter plot of predicted vs simulated fracture stresses for spring networks with $L = 16$, $t = 0.30$ and $p = 0.50$. (b) Pearson correlation coefficient (triangles) and S-score (circles) of fracture stresses predictability dependent on system dilution p. Colors correspond to from blue to yellow $t = 0.03, 0.1, 0.3$.

the network's strength and we aim to predict this quantity. For the fracture stress prediction, we generate a larger dataset of 10^4 spring networks per dilution and we include additional topological information as input parameters for the neural network, an overview can be found in table 9.2 in appendix A. After training, we quantify the quality of the predictions of the neural networks with the Pearson correlation coefficient and the S-score. A scatter plot reveals a lower slope than the ideal $\sigma_p = \sigma_s$ line[Fig. 9.4(a)]. This means that the neural network is conservative in its prediction as the range of the predicted values is smaller than the range of the fracture stresses from the simulations; high fracture stresses are underestimated and low fracture stresses are overestimated. However for networks with high dilution, $p = 0.50$, we find similar S-scores as for the stress prediction in figure 9.2. Surprisingly when we increase the number of bonds in a network, the prediction quality decreases in contrast to the results obtained for stress prediction[Fig. 9.4(b)]. At $p = 0.6$ a minimum is observed which corresponds to a dilution close to the isostatic point. Around this point the spring networks behave highly non-linear with a large amount of non-affine deformation and have a larger fraction of broken bonds[14, 3].

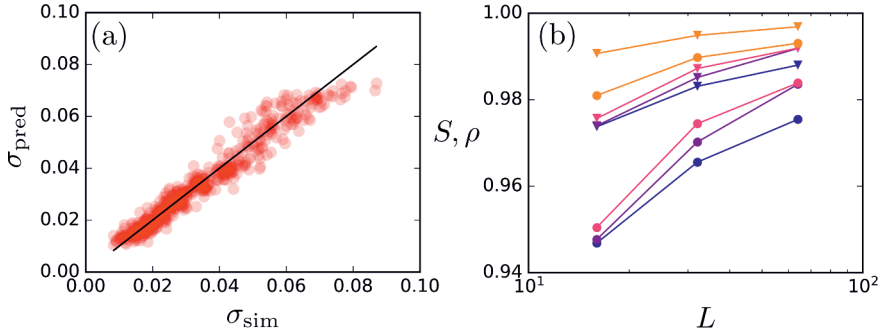

Figure 9.5: (a) Scatter plot of predicted vs simulated fracture stresses for spring networks with $L = 16$ and $t = 0.03$ and a random dilution. (b) Pearson correlation coefficient (triangles) and S-score (circles) of fracture stresses predictability dependent on system size. Colors correspond to from blue to yellow $t = 0.03, 0.1, 0.3$.

For more diluted networks we find an increased predictability when we increase the fracture threshold. When the breaking threshold is increased spring networks tend to break more brittle. Because bonds live longer, stress has a higher probability of being redistributed over the network. This leads to increased loading on the weakest point in the network, which makes the fracture of the whole network easier to predict using only structural and topological parameters. For networks with a smaller dilution this effect is less pronounced, probably because in these networks a clear weak spot is hard to define.

As fracture mechanics are largely dependent on the system size, we study the prediction quality for sizes $L = 16, 32$ and 64[6]. To avoid predicting extreme values we do not train our neural networks for spring networks with a specific dilution but instead create a dataset of 10^4 spring networks with a random dilution without using this dilution as an input for our neural network. A scatter plot for the smallest system size and the lowest threshold, however, reveals excellent predictability[Fig. 9.5 (a)]. Strikingly this is even better than for the results of the stress-strain prediction shown earlier and again we find a positive correlation with the breaking threshold of the bonds.

Surprisingly, predictability increases with increasing system size. As system size increases, stresses are more easily distributed which makes the global behaviour less dependent on local heterogeneity's. Moreover the coarse grained input parameters we use to train our neural networks will probably represent the structure and topology better in large networks leading to a better prediction. As simulating large systems is computationally expensive and our neural networks perform particularly well on large networks, our approach may offer an opportunity to greatly reduce the cost of assessing the load capacity of large networks. However, the cost of calculating topological input parameters might still be significant.

Our results show that neural networks have the excellent capability to predict the fractures stresses in spring networks. However this does not give much insight in the physics governing the fracture mechanics as a trained neural network behaves as a black box. To get around this, we investigate which input parameters are essential for achieving a good prediction of the fracture stress. For this we train multiple neural networks for a single dataset of spring networks that have $L = 16$, $t = 0.30$ and $p = 0.50$ with different sets of input parameters. We start by training a neural network with all available input parameters as a benchmark for the best prediction possible with our input data with a resulting S-score of 0.42. Next we search for combinations of input parameters that give an equally good prediction by eliminating input parameters from our original set. Strikingly we find a set of only three input parameters that result in a S-score that is as good as for all input parameters combined[Fig 9.6(a)]. These parameters are the kurtosis of the distribution of bond angles in a spring network (S20), the variance of the distribution of cycle lengths in a spring network(T5) and the variance of the distribution of the edge betweenness centrality (EBC) of all bonds in a spring network(T18). A definition and short explanation of these quantities can be found in appendix A. As a negative control we train a neural network with three different input parameters and find a S-score of 0.08 indicating that our

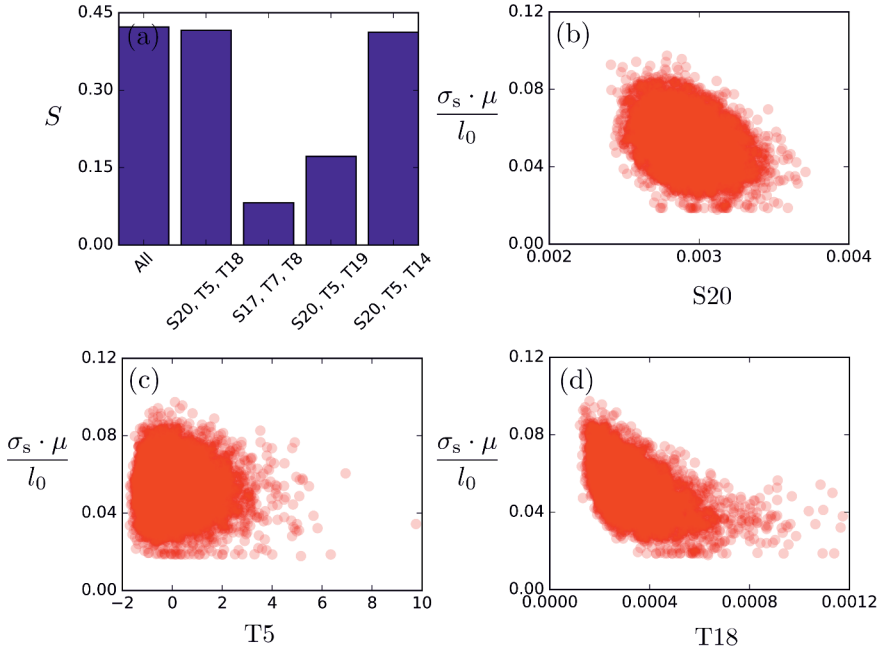

Figure 9.6: (a) Comparison of prediction quality for different input parameters listen in appendix A. (b) Scatterplot of fracture stress vs the kurtosis of the bond angle distribution. (c) Scatterplot of fracture stress vs the variance of the cycle length distribution for cycles greater than 3. (d) Scatterplot of fracture stress vs variance of the edge betweeness centrality distribution.

three parameters carry most information necessary for predicting fracture stresses. When we replace the variance of the EBC distribution(T18) with the kurtosis of the EBC distribution (T19) prediction quality drops dramatically. However if we replace T18 with the variance of a related quantity, the node betweenness centrality, the S-score remains the same[Fig 9.6(a)]. This indicates that the variance in an edge betweenness centrality distribution carries the information about critical fracture stress. Recent work on granular packings also identified the betweenness centrality as a key parameter for forecasting stresses and fracture[25, 26]. As stress in disordered networks usually takes the shortest path available the EBC contains information which bonds

carry the most load and are thus are the most likely to break[27]. Also the cycle length distribution plays an important role in rigidity as the cycle length distribution is found to change dramatically after the jamming transition in granular materials [28]. This supports that similar mechanisms govern stress distribution in granular packings and fiber networks [29].

Based on our findings we conclude that three appropriate quantities describing (i) network orientation e.g. S20, (ii) network bottlenecks e.g. T8, (iii) network redundancy e.g. T5 are necessary and sufficient to predict network fracture based exclusively on information when the network is at rest. These three parameters individually do not show a clear correlation with the observed fracture stress[Fig. 9.6(b-d)]. This highlights that the combination of these parameters is crucial to making good predictions and that neural networks are particularly suitable to screen large datasets and identify which are the crucial parameters to monitor when studying fracture mechanics.

Conclusion

In this chapter we have shown how neural networks can be employed for predicting fracture and mechanics leading up to fracture using only structural and topological information. Fracture becomes more and more nonlinear when more disorder is introduced which is highlighted by a decreasing predictability for networks with higher dilution and higher distortion of the nodes. By studying the prediction quality depending on the input parameters, neural networks prove an excellent tool for identifying crucial parameters that govern the physical mechanisms of fracture. Combined with state of the art machine learning techniques our work paves the way for prediction of often delayed mechanical failure[30, 31].

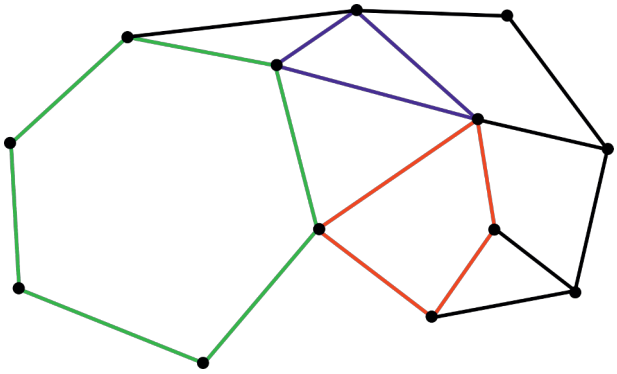

Figure 9.7: A random graph with different cycle lengths. Colors highlight a cycle of length three (*blue*), four (*red*), and six (*green*)

Appendix A: Input parameters

Cycle length distribution

When bonds in a triangular are lattice are removed, loops or cycles larger than a triangle are introduced. The size of these cycles is quantified with the cycle length. For our diluted networks we extract a distribution of the lengths of all cycles present in the spring network using an established algorithm. As we are interested in the effect of dilution we only consider graphs with a length larger than 3. We summarize this distribution with common statistical quantities such as mean, median, variance and kurtosis. We use these quantities as input for our neural networks.

Betweenness centrality

The betweenness centrality is a measure that quantifies the importance of nodes or bonds in the network to the available shortest paths in the network. These shortest path are important as stress in mechanical networks usually travels the shortest path which means that central nodes or bonds carry more load. If a node or bond has a high value for betweenness centrality it is im-

portant to many shortest paths in the network. If a node or bond has a low value it is relatively isolated as little shortest paths will cross the node or bond. Mathematically for a node this is defined as

$$g(v) = \sum_{s \neq v \neq t} \frac{\sigma_{st}(v)}{\sigma_{st}} \tag{9.2}$$

where σ_{st} is the total number of shortest paths from node s to node t and $\sigma_{st}(v)$ the number of shortest path that cross node v. In addition to nodes a similar quantity can also be define for edges or bonds and this is known as the edge betweenness centrality. We calculate distributions for both quantities in our spring networks and summarize these with statistical quantities such as mean, median, variance and kurtosis which we use as input for our neural networks.

Nematic director

To calculate the nematic director for all bonds in the bead spring network, nem_ dir$_x$ and nem_ dir$_y$, we first calculate the nematic tensor[32]

$$Q_{\alpha\beta} = \frac{1}{N} \sum_i u_{i\alpha} u_{i\beta} - \delta_{\alpha\beta} \tag{9.3}$$

Here $\vec{u_i} = (u_x, u_y)$ is the unit vector describing direction of a bond, $\delta_{\alpha\beta}$ the Kronecker delta function and N the total number of bonds. From diagonalizing $Q_{\alpha\beta}$ we obtain the largest eigenvalue which corresponds to the nematic order parameter, nem_ op and the associated eigenvector $\hat{n} = (n_x, n_y)$ that is the nematic director.

Fourier coefficients

To quantify any translational order we calculate the Fourier coefficients of the bonds

$$f_{hk} = |\sum_j e^{i2\pi(h \cdot x_j + k \cdot y_j)}| \tag{9.4}$$

Where j sums over all bonds or nodes and (x_j, y_j) is the bond middle position of bond or node j.

Table 9.1: Structural parameters considered as input for our neural networks

Parameter ID	Parameter
S1	Number of bonds in horizontal direction, L_x
S2	Number of bonds in vertical direction, L_y
S3	Total number of nodes
S4	Total number of bonds
S5	Mean of distribution of nearest neighbors, Z_{average}
S6	Variance of distribution of nearest neighbors, Z_{variance}
S7	Skewness of distribution of nearest neighbors, Z_{skew}
S8	Kurtosis of distribution of nearest neighbors, Z_{kurtosis}
S9	$f02_{\text{bond}}$
S10	$f03_{\text{bond}}$
S11	$f04_{\text{bond}}$
S12	$f05_{\text{bond}}$
S13	$f06_{\text{bond}}$
S14	nem_op
S15	$\text{nem\_dir}_{\text{x}}$
S16	$\text{nem\_dir}_{\text{y}}$
S17	Mean of distribution of bond angles, θ_{average}
S18	Variance of distribution of bond angles, θ_{variance}
S19	Skewness of distribution of bond angles, θ_{skew}
S20	Kurtosis of distribution of bond angles, θ_{kurtosis}
S21	Mean of distribution of bond lengths, $l_{0\text{average}}$
S22	Variance of distribution of bond lengths, $l_{0\text{variance}}$
S23	Skewness of distribution of bond lengths, $l_{0\text{skew}}$

Continuation of Table 9.1	
Parameter ID	**Parameter**
S24	Kurtosis of distribution of bond lengths, $l_{0\text{kurtosis}}$
S25	$f01$
S26	$f02$
S27	$f03$
S28	$f04$
S29	$f05$
S30	$f10$
S31	$f11$
S32	$f12$
S33	$f13$
S34	$f14$
S35	$f15$
S36	$f20$
S37	$f21$
S38	$f22$
S39	$f23$
S40	$f24$
S41	$f25$
S42	$f30$
S43	$f31$

Table 9.2: Topological parameters considered as input parameters for our neural networks. Cycle length parameters are for the distribution of cycle lengths greater than 3 which excludes the cycles native to the triangular lattice.

Parameter ID	Parameter
T1	Number of cliques
T2	Degree of assortativity
T3	Mean of the distribution of cycle lengths
T4	Median of the distribution of cycle lengths
T5	Variance of the distribution of cycle lengths
T6	Kurtosis of the distribution of cycle lengths
T7	Average clustering
T8	Mean of the distribution of node degree centrality
T9	Median of the distribution of node degree centrality
T10	Variance of the distribution of node degree centrality
T11	Kurtosis of the distribution of node degree centrality
T12	Mean of the distribution of node betweeness centrality
T13	Median of the distribution of node betweeness centrality
T14	Variance of the distribution of node betweeness centrality
T15	Kurtosis of the distribution of node betweeness centrality
T16	Mean of the distribution of edge betweeness centrality
T17	Median of the distribution of edge betweeness centrality
T18	Variance of the distribution of edge betweeness centrality
T19	Kurtosis of the distribution of edge betweeness centrality
T20	Global efficiency
T21	Wiener index

Bibliography

[1] Leonardo Da Vinci. I libri di meccanica, reconstructed from the original notes by arturo uccelli. *Kraus Reprint, Nendeln, Liechtenstein*, 1972.

[2] Flake C Campbell. *Fatigue and fracture: understanding the basics*. ASM International, 2012.

[3] Michelle M. Driscoll, Bryan Gin-ge Chen, Thomas H. Beuman, Stephan Ulrich, Sidney R. Nagel, and Vincenzo Vitelli. The role of rigidity in controlling material failure. *Proceedings of the National Academy of Sciences*, 113(39):10813–10817, 2016.

[4] Alan Arnold Griffith and Geoffrey Ingram Taylor. Vi. the phenomena of rupture and flow in solids. *Philosophical Transactions of the Royal Society of London. Series A, Containing Papers of a Mathematical or Physical Character*, 221(582-593):163–198, 1921.

[5] Costantino Creton. 50th anniversary perspective: Networks and gels: Soft but dynamic and tough. *Macromolecules*, 50(21):8297–8316, 2017.

[6] Mikko J. Alava, Phani K. V. V. Nukala, and Stefano Zapperi. Statistical models of fracture. *Advances in Physics*, 55(3-4):349–476, 2006.

[7] Chase P Broedersz, Xiaoming Mao, Tom C Lubensky, and Frederick C MacKintosh. Criticality and isostaticity in fibre networks. *Nature Physics*, 7(12):983, 2011.

[8] A Sharma, AJ Licup, KA Jansen, R Rens, M Sheinman, GH Koenderink, and FC MacKintosh. Strain-controlled criticality governs the nonlinear mechanics of fibre networks. *Nature Physics*, 12(6):584, 2016.

[9] David Silver, Aja Huang, Chris J Maddison, Arthur Guez, Laurent Sifre, George Van Den Driessche, Julian Schrittwieser, Ioannis Antonoglou, Veda Panneershelvam, Marc Lanctot, et al. Mastering the game of go with deep neural networks and tree search. *nature*, 529(7587):484, 2016.

[10] Yann LeCun, Yoshua Bengio, and Geoffrey Hinton. Deep learning. *nature*, 521(7553):436, 2015.

[11] Henri Salmenjoki, Mikko J Alava, and Lasse Laurson. Machine learning plastic deformation of crystals. *Nature communications*, 9(1):5307, 2018.

[12] E. D. Cubuk, S. S. Schoenholz, J. M. Rieser, B. D. Malone, J. Rottler, D. J. Durian, E. Kaxiras, and A. J. Liu. Identifying structural flow defects in disordered solids using machine-learning methods. *Phys. Rev. Lett.*, 114:108001, Mar 2015.

[13] Samuel S Schoenholz, Ekin D Cubuk, Daniel M Sussman, Efthimios Kaxiras, and Andrea J Liu. A structural approach to relaxation in glassy liquids. *Nature Physics*, 12(5):469, 2016.

[14] Leyou Zhang, D. Zeb Rocklin, Leonard M. Sander, and Xiaoming Mao. Fiber networks below the isostatic point: Fracture without stress concentration. *Phys. Rev. Materials*, 1:052602, Oct 2017.

[15] Erik Bitzek, Pekka Koskinen, Franz Gähler, Michael Moseler, and Peter Gumbsch. Structural relaxation made simple. *Phys. Rev. Lett.*, 97:170201, Oct 2006.

[16] D. J. Jacobs and M. F. Thorpe. Generic rigidity percolation: The pebble game. *Phys. Rev. Lett.*, 75:4051–4054, Nov 1995.

[17] J. Clerk Maxwell F.R.S. Xlv. on reciprocal figures and diagrams of forces. *The London, Edinburgh, and Dublin Philosophical Magazine and Journal of Science*, 27(182):250–261, 1864.

[18] P. R. Onck, T. Koeman, T. van Dillen, and E. van der Giessen. Alternative explanation of stiffening in cross-linked semiflexible networks. *Phys. Rev. Lett.*, 95:178102, Oct 2005.

[19] Jingchen Feng, Herbert Levine, Xiaoming Mao, and Leonard M. Sander. Nonlinear elasticity of disordered fiber networks. *Soft Matter*, 12:1419–1424, 2016.

[20] Martín Abadi, Ashish Agarwal, Paul Barham, Eugene Brevdo, Zhifeng Chen, Craig Citro, Greg S. Corrado, Andy Davis, Jeffrey Dean, Matthieu Devin, Sanjay Ghemawat, Ian Goodfellow, Andrew Harp, Geoffrey Irving, Michael Isard, Yangqing Jia, Rafal Jozefowicz, Lukasz Kaiser, Manjunath Kudlur, Josh Levenberg, Dan Mané, Rajat Monga, Sherry Moore, Derek Murray, Chris Olah, Mike Schuster, Jonathon Shlens, Benoit Steiner, Ilya Sutskever, Kunal Talwar, Paul Tucker, Vincent Vanhoucke, Vijay Vasudevan, Fernanda Viégas, Oriol Vinyals, Pete Warden, Martin Wattenberg, Martin Wicke, Yuan Yu, and Xiaoqiang Zheng. TensorFlow: Large-scale machine learning on heterogeneous systems, 2015. Software available from tensorflow.org.

[21] Francois Chollet et al. Keras. https://keras.io, 2015.

[22] Jan Wilhelm and Erwin Frey. Elasticity of stiff polymer networks. *Phys. Rev. Lett.*, 91:108103, Sep 2003.

[23] Moumita Das, F. C. MacKintosh, and Alex J. Levine. Effective medium theory of semiflexible filamentous networks. *Phys. Rev. Lett.*, 99:038101, Jul 2007.

[24] D. A. Head, A. J. Levine, and F. C. MacKintosh. Distinct regimes of elastic response and deformation modes of cross-linked cytoskeletal and semiflexible polymer networks. *Phys. Rev. E*, 68:061907, Dec 2003.

[25] Tatyana M. Svitkina, Elena A. Bulanova, Oleg Y. Chaga, Danijela M. Vignjevic, Shinichiro Kojima, Jury M. Vasiliev, and Gary G. Borisy. Mechanism of filopodia initiation by reorganization of a dendritic network. *The Journal of Cell Biology*, 160(3):409–421, 2003.

[26] Estelle Berthier, Mason A Porter, and Karen E Daniels. Forecasting failure locations in two-dimensional disordered lattices. *arXiv preprint arXiv:1812.08025*, 2018.

[27] Jonathan E Kollmer and Karen E Daniels. Betweenness centrality as predictor for forces in granular packings. *Soft matter*, 15(8):1793–1798, 2019.

[28] Roberto Arévalo, Iker Zuriguel, and Diego Maza. Topology of the force network in the jamming transition of an isotropically compressed granular packing. *Phys. Rev. E*, 81:041302, Apr 2010.

[29] Hadrien Laubie, Farhang Radjai, Roland Pellenq, and Franz-Josef Ulm. Stress transmission and failure in disordered porous media. *Phys. Rev. Lett.*, 119:075501, Aug 2017.

[30] Hanne M. van der Kooij, Simone Dussi, Gea T. van de Kerkhof, Raoul A. M. Frijns, Jasper van der Gucht, and Joris Sprakel. Laser speckle strain imaging reveals the origin of delayed fracture in a soft solid. *Science Advances*, 4(5), 2018.

[31] Jordan Hoffmann, Yohai Bar-Sinai, Lisa M. Lee, Jovana Andrejevic, Shruti Mishra, Shmuel M. Rubinstein, and Chris H. Rycroft. Machine learning in a data-limited regime: Augmenting experiments with synthetic data uncovers order in crumpled sheets. *Science Advances*, 5(4), 2019.

[32] R Eppenga and Daan Frenkel. Monte carlo study of the isotropic and nematic phases of infinitely thin hard platelets. *Molecular physics*, 52(6):1303–1334, 1984.

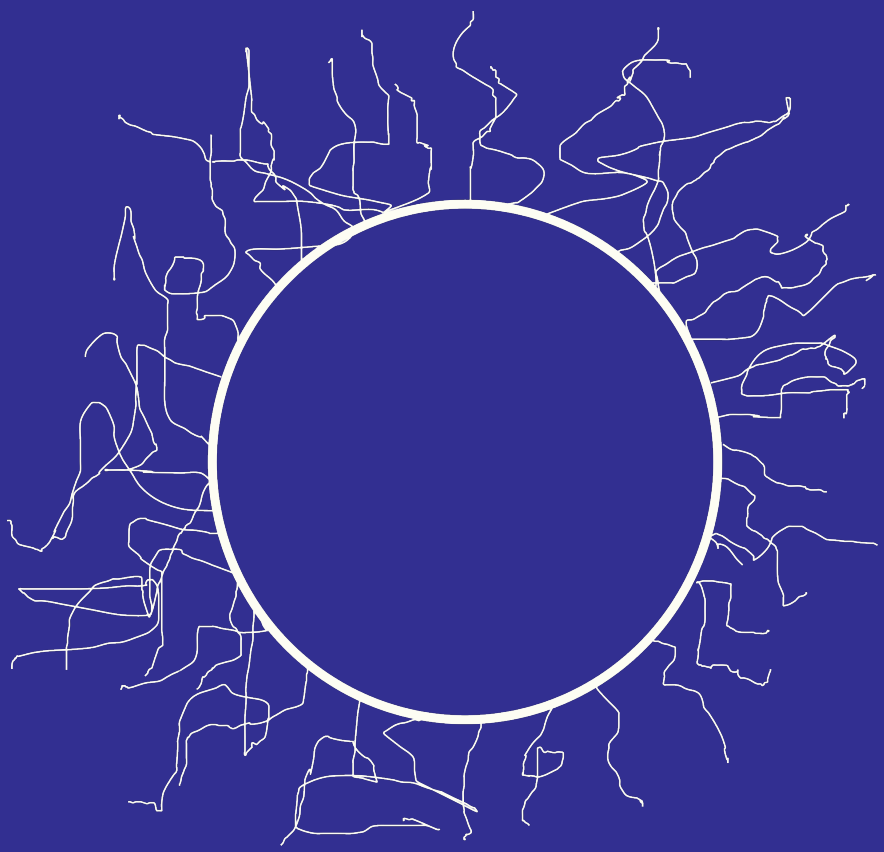

CHAPTER 10

General Discussion

In this thesis we aimed to understand mechanics of systems in the limit of vanishing strength and stiffness from their underlying structure and dynamics. In particular for hypersoft materials, we studied how dynamics could be interpreted in terms of mechanics and for hyperweak materials we looked at how failure mechanics arise from underlying structure and dynamics. Moreover we developed new experimental techniques and systems that allow for further studying these concepts. In this last chapter we evaluate the steps we have taken towards the aim of the thesis that is set out in the introduction. Furthermore we discuss how our results relate to each other and established research and we discuss how they can be used as stepping stones for future research.

Reversible mechanics: Stiffness

The main aim of this part of the thesis is to link structure and dynamics to the mechanics of hypersoft materials. In chapter 2 we present direct measurements of infrasonic elastic waves in ultrasoft solids. We showed how these waves can be interpreted in terms of linear elastic properties with a newly developed theoretical framework that directly links the dynamics in hypersoft materials to their mechanics. We observe these infrasonic waves in both ordered and disordered solids. This makes these waves especially

suitable for studying ultrasoft disordered solids such as marginal fiber networks and jammed systems. Close to the percolation threshold the mechanics in disordered systems can depend greatly on the local structure as a large part of the sample may consist of floppy regions that do not contribute to the overall rigidity[1, 2, 3, 4]. Which parts of marginal disordered solids are rigid and which are floppy is often not immediately clear from their initial structure[5, 6]. Making the link between structure and mechanics is therefore vital for an integral understanding of marginal solids. Electromagnetic waves and mechanical waves that propagate at high Reynolds numbers are known to scatter, refract and reflect on structural defects or boundaries within materials [7, 8, 9]. Observing these events closely has led to enormous insight in the structure of these materials and is crucial to today's materials and biological sciences[10, 11]. In chapter 2 we observed the first signs of the structure dependence of wave propagation at low Reynolds numbers as a distorted wave pattern for our disordered samples. Systematically analyzing these distortions around crystal defects, grain boundaries or in entirely disordered materials could lead to insight on how disordered liquid-like structures lead to rigidity. During the observation of mechanical waves we also monitor the evolution of a materials structure. This offers a unique opportunity to firmly establish the link between structure and mechanics in disordered solids. Analogous to elastographic methods that are widely used in medical imaging, a map of elastic properties such as the floppy and rigid regions could be constructed with wave propagation measurements[12, 13]. This spatially resolved mechanical map could then be compared with maps of parameters quantifying structural parameters such as described in chapters 6 and 9[14]. The main challenge of this approach would be to break the diffraction limit of our infrasonic waves as, for proper sampling, the wavelengths of our infrasonic waves are required to be at least several particle diameters. To circumvent this limitation, our method may be extended by combining the wave patterns for different experiments with different excitation angles or locations.

Similar techniques are also applied to ultrasonic testing where phased array excitation's are employed to generate maps of structural defects in building materials and metal pipes[15].

While we studied the propagation of infrasonic waves in ultrasoft two dimensional materials, the much greater realm of three dimensional materials remains unexplored. Directly applying our method in three dimensions poses technical challenges. For the imaging of three dimensional colloidal systems the microscope objective has to move along the z axis to scan different imaging planes. As the optical trap is formed in the focal plane of the objective it also moves along the z axis and would drag trapped particles with it. To circumvent this problem optical tweezers setups with multiple objectives have been developed to separate the imaging and the trapping functions of the objective[16, 17]. Such setups however are challenging to align and rather costly. To go around this problem, we propose a simpler experiment where a three-dimensional sample is excited in a two-dimensional plane and the resulting infrasonic wave is detected in the same plane. For three dimensional confocal microscopy optically transparent samples are essential for good image quality. This is even more important when working with optical tweezers as the optical trap may affect out-of-plane particles that are not properly refractive index matched. This problem can be minimized by minimizing the intensity of the laser and maximizing the refractive index of the probe bead that is embedded in the transparent material[18]. Studying the 2D projection of the propagating waves would allow us to obtain all mechanical information as the extra dimension would yield an extra transverse mode that, in an isotropic material, would be identical to the transverse mode that can be observed in the imaging plane[19]. To interpret these results the theoretical framework proposed in chapter 2 will have to be generalized for a three-dimensional material. A two-dimensional projection of the resulting response functions could then be used to directly interpret the mechanical waves observed in the imaging plane.

Hybrid networks

In chapter 4 we presented an *in silico* model to study the reinforcement of weak marginal fiber networks with a secondary elastic network. We show how this leads to new mechanical regimes and synergistic mechanical enhancement. Furthermore we elucidate the mechanisms underlying this mechanical enhancement. Depending on the mechanical regime, the secondary elastic network suppresses different non affine deformation modes that are abundant in dilute fiber networks[1, 5].

Studying these mechanisms experimentally is highly challenging as current hybrid networks consist of polymers that are invisible with optical microscopy. To make hybrid networks that can be studied with optical microscopy and gain experimental access to the dynamics of these systems we have to look at hybrid colloidal gels. These systems however require highly specific interactions as particles belonging to one network may not have an attractive interaction with the particles from the other network[20]. As a first step towards these interactions, we developed a simple surface modification method in chapter 5 based on click chemistry. As click chemistry is widely used, a large range of possible modification molecules are available such as DNA oligos with a custom sequence[21]. Surfaces with these DNA sequences induce complex interaction potentials between colloidal particles that lead to the formation of hybrid colloidal gels[20, 22]. As we have evidenced in chapter 6 and 7, local structure and dynamics are crucial for the global mechanics in colloidal gels. Therefore to get a complete picture of three dimensional hybrid colloidal gels, information on the single particle level is required. This can be achieved with confocal microscopy for which it is crucial that the colloids forming the hybrid network are refractive index matched with the suspending liquid. As these solvents are often non-aqueous and DNA hybridization is driven by hydrogen bonds and the hydrophobic effect, this poses challenges for the attractive interaction between the DNA oligomers on the sur-

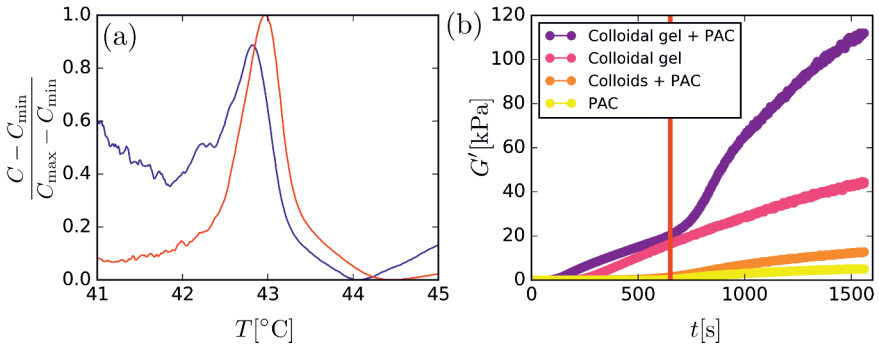

Figure 10.1: (a) Differential scanning calorimetry (DSC) curves of herring sperm DNA in classic DNA binding buffer (red) and classic binding buffer with 50 wt. % sucrose (blue). For both conditions we observe a hybridization peak at approximately 43°C. (b) Storage moduli monitored over time for a colloidal gel network embedded in a polymeric polyacrylamide (PAC) gel and various control experiments (see legend). The red line indicates the point at which the UV light is switched on. Temperature is held constant for all samples at 45°C except for the sample with the non-aggregated colloidal particles (*orange*) which was held at 5°C.

face of the particles[23, 24]. In chapter 8 we have shown that even in 50 wt% sucrose in water solutions pNIPAM retained its LCST behaviour and could therefore still be used to trigger a temperature dependent interaction. As the colloids we used in chapter 5 have a similar refractive index as the colloids in chapter 8, we can match the refractive index of the DNA coated colloids by suspending them in a 50% wt sucrose in water solution. To test whether DNA can still hybridize in this environment, we carry out a differential scanning calorimetry (DSC) experiment[Fig. 10.1 (a)]. Surprisingly we observe similar hybridization peaks for DNA in a classic binding buffer and in a classic binding buffer with 50% sucrose. This opens up the way to form transparent hybrid colloidal gels with our azide modified colloidal particles and to study synergistic mechanisms experimentally.

A simpler way of studying the effect of a secondary elastic matrix on a colloidal gel is by embedding the colloidal gel in a polymeric gel. As col-

loidal particles cannot move in an elastic polymeric matrix, the colloidal gel must form before the polymeric gel is formed. To implement this we use the same colloidal system as we use in chapter 7 that provides a temperature trigger and add acrylamide monomers with a photo-initiator to provide a photo-activated trigger for the secondary network. This way we can form the colloidal gel first by increasing temperature and, when the colloidal gel has sufficiently aged, illuminate with UV light to form the secondary acrylamide network. To check whether this system indeed exhibits synergistic mechanical enhancement, we study our samples with rheology by monitoring the evolution of the storage modulus G' over time at $\gamma = 0.01$ and $\omega = 1$ rad·s^{-1}[Fig. 10.1 (b)]. First the temperature is raised to 45°C and the colloidal gel forms and ages. Remarkably after triggering the formation of the second network with a UV light source the storage modulus rises rapidly. A sample where only the acrylamide network is formed shows a much lower storage modulus which means that the increase seen in the hybrid network is larger than the sum of the two constituents and therefore synergistic[25]. For another control experiment we do not heat the sample, which prevents the colloidal network from forming but we do trigger the formation of the second network. This results in slight increase over the storage modulus for the acrylamide network only because of the filler effect[26]. This highlights that, for the hybrid network sample, the dramatic increase in stiffness is caused by reinforcement of the colloidal network, as we had predicted theoretically in chapter 4.

Strength

The main focus of this part of the thesis is to explain the irreversible mechanics of hyperweak materials from their structure and dynamics. In chapter 6 we took the first step by directly linking the dynamics in hyperweak solids to their heterogeneous structure. In chapter 7 we take this further and

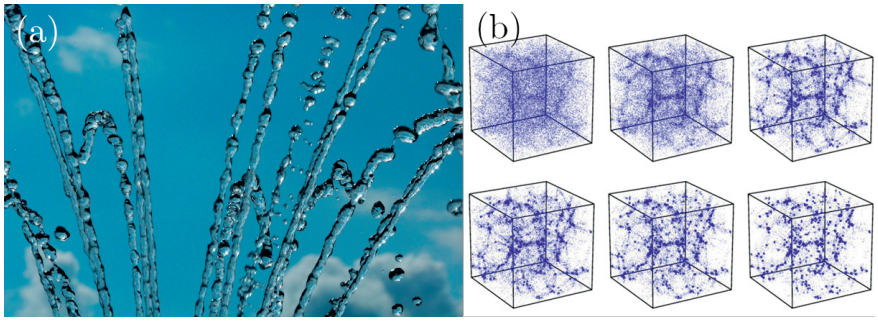

Figure 10.2: (a) The break up of a liquid column in spherical droplets. This everyday phenomenon is know as the Rayleigh-Plateau instability and is driven by the surface tension of the air-liquid interface[28]. (b) Simulation snapshots of clustering galaxies driven by gravity as attractive interaction. The resulting structure is formed via a similar mechanism as the Rayleigh-Plateau instability and reminiscent of that of colloidal gels. Reprinted by permission from Springer Nature [27], copyright (2003).

show how single particle mobility contributes to fatigue and mechanical failure in these ultraweak systems, providing the link between failure mechanics and dynamics. Remarkably the weakening of colloidal gels can be largely explained by exclusively looking at the weakening of single strands and neglecting the overall topology and structure of the network. In Chapter 8 we propose a new model system for hyper weak materials that allows for a controlled study of the influence of colloidal surface mechanics on the overall mechanics. Finally in chapter 9 we explore how the possibilities of machine learning can aid in understanding and predicting fracture mechanics in marginal networks. This provides the link of network structure and topology to fracture mechanics.

We have shown in chapters 6 and 7 that kinetically arrested solids are never at rest but continuously evolve. In contrast to fatigue in biological fiber networks, these aging dynamics are amplified under external load, which results in local weak spots that erode the strength of the material as a whole[29]. The external force F decreases bond lifetimes as $\tau \propto e^{-F \cdot \delta / k_B T}$ with δ as a

microscopic lengthscale. This increases the probability of particles that have multiple bonds to detach and explore the material for a more favorable position as shown in chapter 6. This new position maximizes the number of bonds and is closer to the equilibrium state of the material. This picture suggests that fatigue and aging in colloidal gels have similar mechanisms and that fatigue can be regarded as mechanically accelerated aging. Moreover, the restructuring of the colloidal strands in thin and thick regions we observe is remarkably similar to the Rayleigh-Plateau instability of liquid jets[Fig. 10.2 (a)]. Here a cylindrical fluid column breaks up in multiple spherical droplets driven by the minimization of surface area and thus surface energy[28]. Colloidal particles at the interface of strands in a colloidal gel have fewer bonds than particles within the strands. This gives them a higher amount of free energy. Minimizing the number of particles on the interface of the strand would thus minimize overall free energy. This suggests that the aging and break up of colloidal strands is a manifestation of the Rayleigh-Plateau instability. A similar mechanism can also be observed on the much larger scale of galaxy clusters where small clusters of galaxies are formed from the break up of much larger ones, which results in a structure similar to colloidal gels[Fig. 10.2 (b)][27, 28].

From a commercial point of view fatigue, aging and the resulting weakening are often undesirable[30]. Yogurt, a prototypical example of a colloidal gel, is prone to the phenomenon of syneresis[31]. Here, after scooping or waiting for a sufficient period of time, liquid is expelled out of the yogurt leading to a layer of liquid on top of the yogurt which is often unappetizing. Many consumers perceive this liquid layer as a defect and a lot of effort is taken to understand an prevent syneresis[32]. For yogurt and cheese curd syneresis is linked to internal stresses inside the colloidal gels as a result of their internal dynamics[30]. Also in low-fat mayonaise syneresis has been observed[33]. Restraining these internal dynamics would stabilize the internal stresses and prevent syneresis. An approach to accomplish this could be the implemen-

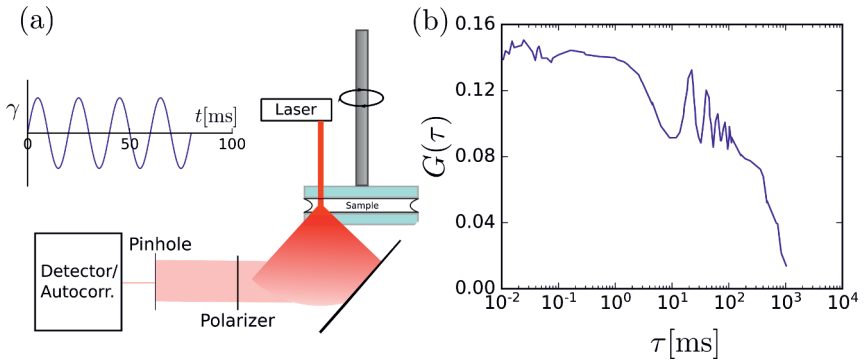

Figure 10.3: (a) Schematic overview of our echo-DWS setup. The sample is sheared with a transparent (glass) plat-plate geometry. A linearly polarized laser illuminates the sample through the top plate. The scattered light is then reflected by a mirror and fed into the detector. A linear polarizer is placed before the detector to make sure only multiply scattered photons reach the detector. A pinhole ensures that the detector measures a single speckle. The applied strain profile is displayed in the inset. (b) The normalized intensity correlation function as measured by the detector/correlator combination for a colloidal gel sample. The peaks between 10 and 100 ms are the echos of the recovering structure as a result of the shear deformation depicted in the inset in (a). The decay of the echo peaks highlights the plastic deformations inside the colloidal gel.

tation of a secondary elastic matrix. This would make the entire system a composite network of colloidal particle strands and for example a polymeric hydrogel. As shown in figure 10.1(b) polymeric hydrogel is an efficient way of immobilizing colloidal particles and reinforcing a colloidal network. In addition this would transform a colloidal gel from a ultra soft and ultra weak material into a strong and stiff material characterized by reversible mechanics as described in chapter 4.

The reversibility of the mechanics in these systems can be studied by monitoring the integrity of the structure after several deformation cycles. This can be readily achieved with echo diffusing wave spectroscopy (echo-DWS)[34, 35][Fig. 10.3(a)]. When measuring a sample of immobilized parti-

cles with classic DWS the signal will not decorrelate because the sample is non-ergodic[36]. However when subjecting the sample to oscillatory strain the signal will decorrelate and recover when the strain is released [Fig. 10.3(b)]. In the ideal case with full reversibility the signal will be exactly the same as before deformation. However if internal rearrangements or relaxations occurred during the straining of the sample, the correlation function will not entirely return to its original value. As DWS relies in interference of light it can detect small displacements in the order of nanometers, which makes it an extremely sensitive approach to measuring the slightest irreversible deformation. While echo-DWS is highly suitable for studying the changes in the material as a whole, it does not provide information at the single particle level, which could give access to microscopic mechanisms. Inspired by previous work, to study plasticity on the microscopic level, we propose an echo method that is based on deformation induced with optical tweezers [38]. This method consists of embedding a scattering melamine probe bead ($d \approx 4.0\mu$m) in an optically transparent colloidal gel of tFEMA/tBMA core-shell particles($d \approx 1.5\mu$m) [Fig.10.4 (a)][37]. The probe bead is subsequently driven by an optical trap with an amplitude $A = 2.0\mu$m and a frequency $f = 0.5$Hz, while the positions of the colloidal particles in the gel are monitored with epifluorescence microscopy. Analogous to DWS, these positions are then autocorrelated in time. When the sample is completely reversible the correlation function will show peaks of equal height as a result of the oscillatory strain induced by the optical trap. However in case of irreversible rearrangements the peaks will decay and ultimately completely decorrelate[Fig.10.4 (b)]. For short lag times the reversible decorrelation is centered around the probe particle[Figs.10.4 (c),(e)], however for longer lag times the decorrelation and plasticity spread towards the edges of the field of view [Fig. 10.4(f)]. Interpreting the resulting dynamics in terms of propagating waves as described in chapter 2 will be challenging as the irreversible rearrangements make the material locally fluid and will greatly attenuate wave

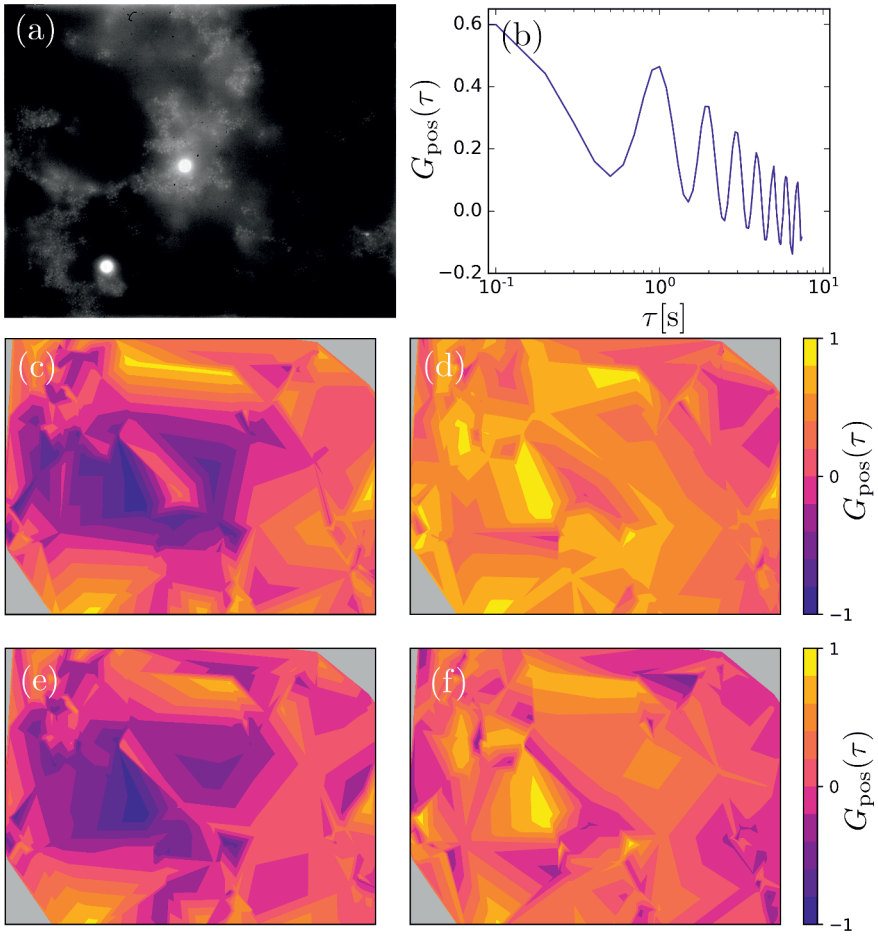

Figure 10.4: (a) Epifluorescence microscopy image of a optically transparent depletion gel of tFEMA/tBMA core-shell particles. The large bright particle in the center is a refractive index mismatched melamine sphere that functions as the probe. (b) Position autocorrelation function averaged for all particles in the field of view as a function of lagtime τ. (c-f) Contour plots of spatially resolved position auto correlation values for $\tau = 0.5, 1.0, 1.5, 4.0$s respectively. No correlation data is available for the grey areas because of the lack of particles.

propagation. However for cases with moderate amounts of plasticity, comparing the measured wave propagation patterns with the patterns that are

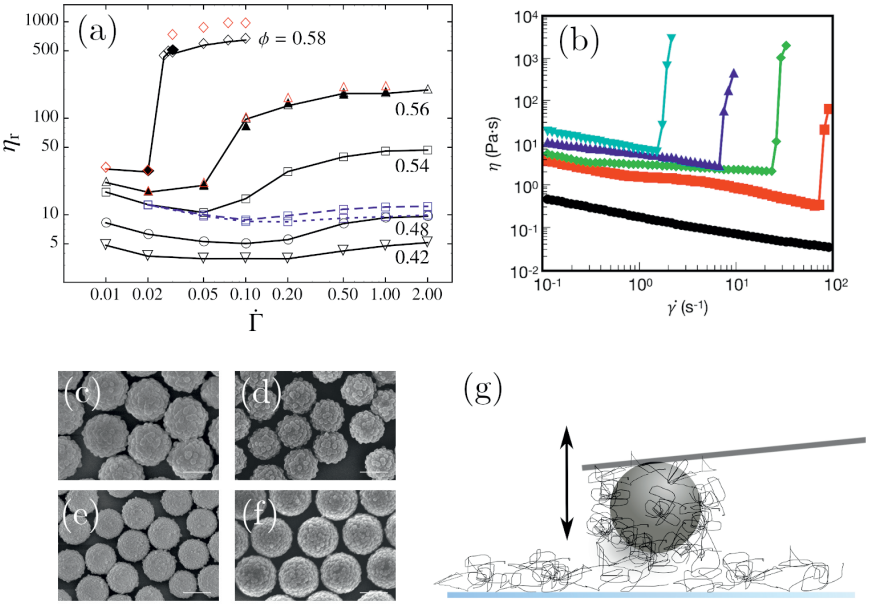

Figure 10.5: (a) Shear jamming as observed in a simulation of granular frictional hard spheres for various volume fractions ϕ, reprinted with permission from [39], copyright 2013 by the American Physical Society. For high volume fraction a sudden increase in relative viscosity η_r is observed with increased shear rate $\dot{\Gamma}$. (b) Shear thickening for smooth(black) and frictional colloidal raspberry particles of, from left to right, decreasing roughness. For the rough particles a sudden increase in viscosity η is observed with increasing shear rate $\dot{\gamma}$[40]. (c-f) Electron microscopy images of raspberry colloids with decreasing roughness[40]. (g) Schematic representation of a pull-off experiment with AFM.

expected for a fully linear solid as described by our theory may shed new light on the floppy and rigid regions in marginal solids.

Friction

In chapter 8 we have found indications that mechanical surface properties may play a significant role in the overall mechanics of colloidal gels. In the granular world it is well-known that friction drives a shear rate induced ar-

rest known as discontinuous shear thickening[41, 42, 43, 44]. Here a sudden increase in viscosity is observed for dense granular suspensions at a critical shear rate[39]. Above this critical shear rate, the suspension is in a jammed state which is similar to dense suspensions that are above the critical jamming volume fraction[Fig. 10.5 (a)]. Also for dense colloidal systems friction has been linked to a discontinuous shear thickening transition [Fig. 10.5 (b-f)][40]. While the pronounced effects of friction have been intensively studied for dense, sheared and repulsive systems, the effects of friction on the mechanics of attractive systems such as colloidal gels have been largely ignored. Introducing inter particle friction would hinder the sliding and rotational migration of weakly connected particles over the colloidal strands. As we have seen in chapters 6 and 7 the migration of single particles can have a large contribution to the overall mechanics of these systems. Hindering these migrations could have a pronounced effect on the overall mechanics and resistance to fatigue. This could provide another mechanism in preventing failure and syneresis in commercial products. Additionally, when particles are hindered in their rational movement, overall bending resistance will be introduced in the colloidal strands. In chapter 4 we have shown how bending resistance in fiber networks leads to a rich phase diagram of different mechanical regimes[1]. Harnessing friction in colloidal gels would therefore open up the way to soft materials with a tailored mechanical response.

The experimental system proposed in chapter 8 provides a good starting point to systematically study the effects of friction in more detail. It is however challenging to directly translate the grafting density of polymers on the surface of the colloidal particle to a friction coefficient. Frictional forces depend on both the friction coefficient and the normal force. While this normal force is indirectly related to the inter particle attraction en thus to the amount of polymeric material present on the surface, a direct measurement is preferred. This can be achieved by measuring the pull-off force of a pNIPAM-grafted colloidal particle from a surface spin-coated with ex-

actly the same material with atomic force microscopy (AFM)[Fig. 10.5 (g)][45]. Subsequently, when the normal force is known, the particle can be dragged over the surface to determine the frictional force and the corresponding friction coefficient with either optical tweezers or AFM[46, 47]. Once the relation between grafting density, polymer length and friction coefficient has been established its effect on fatigue can be tested with the same experiments as described in chapter 7.

Predicting the life span of colloidal gels

In the last chapter on the prediction of fracture in dilute fiber networks we have seen that the new methods of machine learning can provide an effective tool in identifying the critical parameters in complex problems. For fiber networks we found that, with only three structural or topological parameters describing the networks structure, a reasonable prediction of the critical fracture stress could be obtained. This suggests that network structure is key in mechanical failure in fiber networks. This contrasts with the results we obtained for colloidal gels in chapter 7. Here we found that the weakening of the individual strands or bonds in the network largely explains the global mechanical failure. This contrast implies that the introduction of bond weakening by internal dynamics completely changes the failure mechanism. To study this further and to predict the lifespan of a colloidal gel based on its initial structure, the methods developed in chapter 9 can be applied to colloidal gels. As this is a much more complex problem than the fracture of fiber networks, a first step could be taken by simplifying a colloidal gel as a fiber network with spring constants that are weakened as a function of their maximal extension and break when the spring constant has decreased below a threshold value. To simulate the heterogeneity in strand length and thickness, the initial spring constants can be drawn from a normal distribution. The mean, variance, kurtosis etc. of this distribution can then be used combined with the structural and topological parameters described in chapter 9

as input for the neural networks to investigate if they hold predictive power for the lifetime of the network as a whole.

Conclusion

In the individual chapters in this thesis we established the links that tie together the complex network of structure, dynamics and mechanics in hypersoft and hyperweak materials. In this final chapter we have worked towards a broader understanding of this complex network by discussing each link in a broader context and bringing them together. While we advanced our knowledge about colloidal gels significantly, this is mainly focused on idealized frictionless particles in single colloidal networks.

However we found that the microscopic surface frictional properties and an elastic background matrix can have considerable impact on the macroscopic mechanics. Immobilizing the particles in the colloidal network with an elastic background matrix could prevent fatigue and syneresis. Increasing friction between particles reduced the sliding of particles and may induce increased bending rigidity in colloidal strands. Studying these mechanisms will offer many design opportunities for colloidal gels with specifically tuned mechanical properties. Furthermore we mainly treated hypersoft and hyperweak as separate classes of materials. Most hyperweak materials such as colloidal gels are often hypersoft as well. Measuring the linear infrasonic elastic wave measurements with echo measurements could help in clearing up the transition from reversible to irreversible mechanics in colloidal gels. Finally we explored how machine learning methods could be applied to complex mechanical problems. While predictions by these methods are based on black boxes, the main feature of machine learning is the identification of important physical parameters in complex phase spaces that can be the subject of further study.

Bibliography

[1] Chase P Broedersz, Xiaoming Mao, Tom C Lubensky, and Frederick C MacKintosh. Criticality and isostaticity in fibre networks. *Nature Physics*, 7(12):983, 2011.

[2] D. J. Jacobs and M. F. Thorpe. Generic rigidity percolation: The pebble game. *Phys. Rev. Lett.*, 75:4051–4054, Nov 1995.

[3] T. S. Majmudar, M. Sperl, S. Luding, and R. P. Behringer. Jamming transition in granular systems. *Phys. Rev. Lett.*, 98:058001, Jan 2007.

[4] M. E. Cates, J. P. Wittmer, J.-P. Bouchaud, and P. Claudin. Jamming, force chains, and fragile matter. *Phys. Rev. Lett.*, 81:1841–1844, Aug 1998.

[5] Claus Heussinger and Erwin Frey. Floppy modes and nonaffine deformations in random fiber networks. *Phys. Rev. Lett.*, 97:105501, Sep 2006.

[6] Michelle M. Driscoll, Bryan Gin-ge Chen, Thomas H. Beuman, Stephan Ulrich, Sidney R. Nagel, and Vincenzo Vitelli. The role of rigidity in controlling material failure. *Proceedings of the National Academy of Sciences*, 113(39):10813–10817, 2016.

[7] William Henry Bragg and William Lawrence Bragg. The reflection of x-rays by crystals. *Proceedings of the Royal Society of London. Series A, Containing Papers of a Mathematical and Physical Character*, 88(605):428–438, 1913.

[8] Lord Rayleigh F.R.S. Xxxiv. on the transmission of light through an atmosphere containing small particles in suspension, and on the origin of the blue of the sky. *The London, Edinburgh, and Dublin Philosophical Magazine and Journal of Science*, 47(287):375–384, 1899.

[9] Siméon Denis Poisson. *Sur la propagation du mouvement dans les milieux elastiques*. 1831.

[10] James D Watson, Francis HC Crick, et al. Molecular structure of nucleic acids. *Nature*, 171(4356):737–738, 1953.

[11] Linus Pauling, Robert B Corey, and Herman R Branson. The structure of proteins: two hydrogen-bonded helical configurations of the polypeptide chain. *Proceedings of the National Academy of Sciences*, 37(4):205–211, 1951.

[12] Pol Grasland-Mongrain, Ali Zorgani, Shoma Nakagawa, Simon Bernard, Lia Gomes Paim, Greg Fitzharris, Stefan Catheline, and Guy Cloutier. Ultrafast imaging of cell elasticity with optical microelastography. *Proceedings of the National Academy of Sciences*, 115(5):861–866, 2018.

[13] P. Grasland-Mongrain, R. Souchon, F. Cartellier, A. Zorgani, J. Y. Chapelon, C. Lafon, and S. Catheline. Imaging of shear waves induced by lorentz force in soft tissues. *Phys. Rev. Lett.*, 113:038101, Jul 2014.

[14] Ivo Buttinoni, Jinwoong Cha, Wei-Hsun Lin, Stéphane Job, Chiara Daraio, and Lucio Isa. Direct observation of impact propagation and absorption in dense colloidal monolayers. *Proceedings of the National Academy of Sciences*, 114(46):12150–12155, 2017.

[15] Douglas R Daum and Kullervo Hynynen. A 256-element ultrasonic phased array system for the treatment of large volumes of deep seated tissue. *IEEE transactions on ultrasonics, ferroelectrics, and frequency control*, 46(5):1254–1268, 1999.

[16] Dirk LJ Vossen, Astrid van der Horst, Marileen Dogterom, and Alfons van Blaaderen. Optical tweezers and confocal microscopy for simultaneous three-dimensional manipulation and imaging in concentrated colloidal dispersions. *Review of Scientific Instruments*, 75(9):2960–2970, 2004.

[17] Ivan R Perch-Nielsen, Peter John Rodrigo, and Jesper Glückstad. Real-time interactive 3d manipulation of particles viewed in two orthogonal observation planes. *Optics express*, 13(8):2852–2857, 2005.

[18] Anita Jannasch, Ahmet F Demirörs, Peter DJ Van Oostrum, Alfons Van Blaaderen, and Erik Schäffer. Nanonewton optical force trap employing anti-reflection coated, high-refractive-index titania microspheres. *Nature Photonics*, 6(7):469, 2012.

[19] John C Crocker, Megan T Valentine, Eric R Weeks, Thomas Gisler, Peter D Kaplan, Arjun G Yodh, and David A Weitz. Two-point microrheology of inhomogeneous soft materials. *Physical Review Letters*, 85(4):888, 2000.

[20] Francesco Varrato, Lorenzo Di Michele, Maxim Belushkin, Nicolas Dorsaz, Simon H Nathan, Erika Eiser, and Giuseppe Foffi. Arrested demixing opens route to bigels. *Proceedings of the National Academy of Sciences*, 109(47):19155–19160, 2012.

[21] Himabindu Nandivada, Xuwei Jiang, and Joerg Lahann. Click chemistry: versatility and control in the hands of materials scientists. *Advanced Materials*, 19(17):2197–2208, 2007.

[22] Lorenzo Di Michele, D Fiocco, F Varrato, Srikanth Sastry, Erika Eiser, and Giuseppe Foffi. Aggregation dynamics, structure, and mechanical properties of bigels. *Soft matter*, 10(20):3633–3648, 2014.

[23] Jiří Šponer, Judit E Šponer, Arnošt Mládek, Petr Jurečka, Pavel Banáš, and Michal Otyepka. Nature and magnitude of aromatic base stacking in dna and rna: Quantum chemistry, molecular mechanics, and experiment. *Biopolymers*, 99(12):978–988, 2013.

[24] G Felsenfeld and H T Miles. The physical and chemical properties of nucleic acids. *Annual Review of Biochemistry*, 36(1):407–448, 1967. PMID: 18257727.

[25] Wolf H. Rombouts, Marcel Giesbers, Jan van Lent, Frits A. de Wolf, and Jasper van der Gucht. Synergistic stiffening in double-fiber networks. *Biomacromolecules*, 15(4):1233–1239, 2014. PMID: 24580533.

[26] Wei-Chun Lin, Alba Marcellan, Dominique Hourdet, and Costantino Creton. Effect of polymer–particle interaction on the fracture toughness of silica filled hydrogels. *Soft Matter*, 7(14):6578–6582, 2011.

[27] Rien Van De Weygaert. The cosmic foam: Stochastic geometry and spatial clustering across the universe. In *Statistical Challenges in Astronomy*, pages 175–196. Springer, 2003.

[28] Jens Eggers and Emmanuel Villermaux. Physics of liquid jets. *Reports on progress in physics*, 71(3):036601, 2008.

[29] Stefan Münster, Louise M Jawerth, Beverly A Leslie, Jeffrey I Weitz, Ben Fabry, and David A Weitz. Strain history dependence of the nonlinear stress response of fibrin and collagen networks. *Proceedings of the National Academy of Sciences*, 110(30):12197–12202, 2013.

[30] P. Walstra. *The Syneresis of Curd*, page 141–191. Springer US, Boston, MA, 1993.

[31] Manfred Kroger. Quality of yogurt. *Journal of Dairy Science*, 59(2):344–350, 1976.

[32] Gastón Ares, Ana Giménez, and Adriana Gámbaro. Understanding consumers' perception of conventional and functional yogurts using word association and hard laddering. *Food Quality and Preference*, 19(7):636–643, 2008.

[33] Inae Lee, Sanghoon Lee, Nara Lee, and Sanghoon Ko. Reduced-fat mayonnaise formulated with gelatinized rice starch and xanthan gum. *Cereal Chemistry*, 90(1):29–34, 2013.

[34] P. Hébraud, F. Lequeux, J. P. Munch, and D. J. Pine. Yielding and rearrangements in disordered emulsions. *Phys. Rev. Lett.*, 78:4657–4660, Jun 1997.

[35] M Laurati, SU Egelhaaf, and G Petekidis. Plastic rearrangements in colloidal gels investigated by laos and ls-echo. *Journal of Rheology*, 58(5):1395–1417, 2014.

[36] DJ Pine, DA Weitz, JX Zhu, and E Herbolzheimer. Diffusing-wave spectroscopy: dynamic light scattering in the multiple scattering limit. *Journal de Physique*, 51(18):2101–2127, 1990.

[37] Thomas E Kodger, Rodrigo E Guerra, and Joris Sprakel. Precise colloids with tunable interactions for confocal microscopy. *Scientific reports*, 5:14635, 2015.

[38] Myung Han Lee and Eric M. Furst. Response of a colloidal gel to a microscopic oscillatory strain. *Phys. Rev. E*, 77:041408, Apr 2008.

[39] Ryohei Seto, Romain Mari, Jeffrey F. Morris, and Morton M. Denn. Discontinuous shear thickening of frictional hard-sphere suspensions. *Phys. Rev. Lett.*, 111:218301, Nov 2013.

[40] Chiao-Peng Hsu, Shivaprakash N Ramakrishna, Michele Zanini, Nicholas D Spencer, and Lucio Isa. Roughness-dependent tribology effects on discontinuous shear thickening. *Proceedings of the National Academy of Sciences*, 115(20):5117–5122, 2018.

[41] Abdoulaye Fall, Anaël Lemaître, Fran çois Bertrand, Daniel Bonn, and Guillaume Ovarlez. Shear thickening and migration in granular suspensions. *Phys. Rev. Lett.*, 105:268303, Dec 2010.

[42] Martin Trulsson, Bruno Andreotti, and Philippe Claudin. Transition from the viscous to inertial regime in dense suspensions. *Phys. Rev. Lett.*, 109:118305, Sep 2012.

[43] Francesco Picano, Wim-Paul Breugem, Dhrubaditya Mitra, and Luca Brandt. Shear thickening in non-brownian suspensions: An excluded volume effect. *Phys. Rev. Lett.*, 111:098302, Aug 2013.

[44] M. Wyart and M. E. Cates. Discontinuous shear thickening without inertia in dense non-brownian suspensions. *Phys. Rev. Lett.*, 112:098302, Mar 2014.

[45] Jaroslaw Drelich, Garth W Tormoen, and Elvin R Beach. Determination of solid surface tension from particle–substrate pull-off forces measured with the atomic force microscope. *Journal of Colloid and Interface Science*, 280(2):484–497, 2004.

[46] E Meyer, H Heinzelmann, P Grütter, Th Jung, H-R Hidber, H Rudin, and H-J Güntherodt. Atomic force microscopy for the study of tribology and adhesion. *Thin Solid Films*, 181(1-2):527–544, 1989.

[47] Erik Schäffer, Simon F Nørrelykke, and Jonathon Howard. Surface forces and drag coefficients of microspheres near a plane surface measured with optical tweezers. *Langmuir*, 23(7):3654–3665, 2007.

Summary

Material mechanics play a crucial role in a wide variety of scenarios and applications. Here we focused on two central material properties: stiffness and strength. Whereas stiffness characterizes the resistance to deformation for small strains, where the response remains linear, strength describes the resilience of a material to larger deformations and mechanical damage. For conventional materials strength and stiffness are readily described by established mechanical theories. However, many materials in Nature, or engineering materials during processing, live in a state where stiffness and/or strength becomes so weak that classical mechanical theories no longer apply. This has been the focal point of this thesis.

The exploration of such ultrasoft and/or ultraweak solids faces many challenges, some of which have been addressed in this thesis, including their structure-property relationships and the question how one characterizes these fragile materials where conventional mechanical methods are no longer viable.

In **chapter 2** we address the challenge of characterizing the mechanical response of solids at the verge of a mechanical instability, where classical approaches fail. We present a new method based on the propagation of infrasonic waves. These waves propagate at low Reynolds numbers, where dissipation is strong. We have not only shown an experimental approach to evaluate wave propagation properties, but also established a theoretical framework to interpret these data and extract quantitative mechanical properties with a unique resolution. In **chapter 3** we detail the technical challenges associated with these measurements, performed with the help of optical tweezers to create travelling mechanical waves.

When marginal networks are combined with secondary elastic matrices remarkable stiffening is observed. In **chapter 4** we present a theoreti-

cal model to study the effect of bending rigidity to the mechanics in hybrid materials with simulations. We show how different mechanical regimes arise depending on the bending stiffness and the stiffness of the secondary network. Each of these regimes have different mechanisms that lead to mechanical enhancement of the composite network. Experimental access to these mechanisms is extremely challenging. In **chapter 5** we take the first steps to studying these mechanisms experimentally. Here we propose a a simple click-chemistry based surface modification method that can help to achieve the complex inter-particle interactions required for establishing hybrid colloidal networks.

The second part of this thesis covers hyperweak solids and irreversible deformation. Chapters 6 to 8 deal with colloidal gels that are prototypical examples of hyper weak solids. In **chapter 6** we address the structure to dynamics part of the structure-property relation in colloidal gels. We experimentally establish the connection between the intermittent dynamics of individual particles and their local connectivity. We interpret our experimental results with a model that describes single-particle dynamics based on highly cooperative thermal debonding. Our model is in quantitative agreement with experiments and provides a microscopic picture for the structural origin of dynamical heterogeneity and provides a new perspective of the link between structure and the complex mechanics of these heterogeneous solids.

Chapter 7 focuses on the dynamics to mechanics part of the structure-property relation by studying fatigue in colloidal gels. Here we combine experiments and computer simulations to show how mechanical loading leads to irreversible strand stretching, which builds slack into the network that softens the solid at small strains and causes strain hardening at larger deformations. We thus find that microscopic plasticity governs fatigue at much larger scales. This sheds new light on fatigue in soft thermal solids and calls for new theoretical descriptions of soft gel mechanics in which local plasticity is taken into account.

In chapter 8 we take first steps in investigating the overlooked role of inter-particle friction in colloidal gels. We present a colloidal system with a thermo-responsive trigger for systematically studying the effect of surface properties, grafting density and chain length, on the particle dynamics within colloidal gels. Microscopically, for colloids with a lower grafting density, we observe an increase in the thermal bond angle fluctuations of aggregated colloids. Macroscopically, we observe a clear increase of the linear elastic modulus for gels with increased grafting density and longer chain lengths. These effects are inversely proportional to the magnitude of local bond angle fluctuations. Our model system will allow for further study of the microscopic origins of the complex macroscopic mechanical behavior of hyperweak solids that include bending modes within the network.

Fracture and mechanical failure are highly stochastic processes and predicting fracture is highly challenging with conventional theories but crucial to assessing the lifetimes of e.g. buildings, bridges and implants. In **chapter 9** we explore new opportunities for predicting fracture in marginal fiber networks. Fracture is the ultimate form of irreversible deformation and, especially in soft materials, characterized with highly non-linear mechanics preempting the moment of failure. We show how machine learning methods can by employed to predict the critical fracture stress solely based on structural and topological input parameters. We show that neural networks, despite their black box behavior, can be used to study the physical mechanisms underlying fracture. By varying the input parameters for our fracture stress predictions we found three parameters for which we can achieve the same prediction quality as for all tested input parameters combined.

In the last chapter, the **general discussion**, we discuss how our results relate to each other and how they fit in a broader context. Furthermore we suggest and describe experiments that can help advance our knowledge of hypersoft and hyperweak materials in the future.

List of Publications

THIS DISSERTATION:

- J.M. van Doorn, J.E. Verweij, J. Sprakel and J. van der Gucht: **Strand plasticity governs fatigue in colloidal gels** *Physical Review Letters*, 120, 208005 (2018) (Chapter 7)
- J.M. van Doorn, J. Bronkhorst, R. Higler, T. van de Laar and J. Sprakel: **Linking Particle Dynamics to Local Connectivity in Colloidal Gels** *Physical Review Letters*, 118, 188001 (2017) (Chapter 6)
- J.M. van Doorn, J. Sprakel and T.E. Kodger: **Temperature-triggered colloidal gelation through well-defined grafted polymeric surfaces** *Gels*, 3, 21 (2017) (Chapter 8)
- J.M. van Doorn, L. Lageschaar, J. Sprakel and J. van der Gucht: **Criticality and mechanical enhancement in composite fiber networks** *Physical Review E*, 95, 042503 (2017) (Chapter 4)
- J.M. van Doorn, R. Higler, R. Fokkink, R. Wegh, A. Zaccone, J. Sprakel and J. van der Gucht: **Infrasonic wave propagation in ultrasoft solids at low Reynolds numbers** Submitted
- J.M. van Doorn, R. Higler, R. Fokkink, R. Wegh, J. Sprakel and J. van der Gucht:: **Calibration of deflected AOD intensity field for optical tweezers** manuscript in preparation
- J.M. van Doorn, P.Hage, T. van de Laar, I.Voets and J. Sprakel: **Simple one-step synthesis of azide functionalized polymer colloids** manuscript in preparation
- J.M. van Doorn, S. Dussi and J van der Gucht: **Learn to Break: Predicting mechanical failure in dilute fiber networks with machine learning** manuscript in preparation

OTHER WORK:

- T. van de Laar, H. Schuurman, P. van der Scheer, J.M. van Doorn, J. van der Gucht and J. Sprakel: **Light from Within; Sensing Weak Strains and femtoNewton Forces in Single Molecules** *Chem*, 4(2), 269-284 (2018)
- S. Stuij, J.M. van Doorn, T.E. Kodger, J. Sprakel, C. Coulais, P. Schall: **Buckling of self-assembled colloidal structures** submitted

Acknowledgements

Dit proefschrift is tot stand gekomen dankzij fantastische samenwerkingen. In dit deel wil ik graag iedereen bedanken die iets heeft bijgedragen aan dit werk, te beginnen met Jasper en Joris. Jasper, bedankt voor de laagdrempelige begeleiding en de kans om dit werk uit te mogen voeren. Ik bewonder hoe je, ondanks alle drukte op het lab, je deur altijd open weet te houden voor prangende vragen. Je wil altijd een stap verder gaan en ik denk dat dit proefschrift daardoor een stuk beter is geworden. Joris, jij hebt mijn enthousiasme voor soft matter aangewakkerd sinds ik eind 2012 het Advanced Soft Matter practicum binnenstapte. Je bent nooit bang om duidelijk te zeggen als dingen beter kunnen en dat heb ik altijd zeer gewaardeerd. Daarnaast weet je een fantastische werksfeer te creëren waardoor het altijd weer een plezier was om naar het lab te gaan. Ik heb veel van jullie geleerd en denk dat zonder jullie begeleiding dit proefschrift er heel anders uit had gezien.

Ik wil mijn studenten, Luuk Lageschaar en Jochem Bronkhorst bedanken. Ik vond het erg leuk om jullie te mogen begeleiden en samen problemen op te lossen. Jullie inzet heeft geleid tot prachtige resultaten welke een belangrijk onderdeel zijn geworden van dit proefschrift.

Thanks to all the collegues from PCC for creating a wonderful atmosphere in the lab. I look back on great labtrips, PhD trips, SinterFysko's, Veluwe lopen, boardgame night's and coffee breaks. I believe this atmosphere is an essential contribution to this thesis. In het bijzonder wil ik de mensen van de H.E.G. bedanken, we hebben erg veel lol gehad en ik denk dat dat een van de dingen is die ik het meest ga missen.

Verder wil ik een aantal mensen specifiek bedanken waarmee ik veel heb samengewerkt. Ronald en Remco, heel erg bedankt voor alle hulp bij het bouwen en programmeren van de optical tweezers. Ik denk dat er uiteindelijk een erg mooie opstelling is gerealiseerd. Joanne, ik heb erg prettig met

je samengewerkt. Toen ik er niet uitkwam met mijn experimenten heb jij met je grondige en gestructureerde simulaties ervoor gezorgd dat het plaatje rond kwam. Tom, I want to thank you for endless discussions about colloidal gels and colloid synthesis. I think we had a great collaboration from which I learned a lot. Simone, thank you for working together with me on the last chapter in this thesis. It was great to be able to discuss our approach to use machine learning for fracture problems. Ruben, heel erg bedankt voor alle programmeer tips en je introductie tot HOOMD-blue. Patrick, dankjewel dat je het aandurfde met met mij azide modificaties uit te voeren. Het was misschien niet de best georganiseerde synthese maar ik denk dat we een erg mooi resultaat hebben bereikt. Ties, heel erg bedankt voor je tips en ondersteuning, specifiek in de laatste fase van mijn promotietraject. Ik ben erg blij dat je mij als paranimf ter zijde wil staan.

Naast collega's wil ik ook nog mijn vrienden en familie bedanken. Ik begin met de kliertjes uit Ugchelen. Ik denk dat ik de meesten van jullie al langer ken dan dat ik jullie niet ken en toch is het nooit saai. Ik hoop dat ik nog vaak voor jullie mag blijven koken. Jiska, we hebben elkaar niet heel veel gezien de afgelopen jaren maar heb desondanks van onze discussies genoten. Ik ben erg onder de indruk van je maatschappelijke en wetenschappelijke avonturen en hoop dat we elkaar nog lang blijven zien. Maxime, bedankt voor je interesse en steun bij mijn project, ik vond het erg leuk om je een paar keer op te zoeken in Lund en ben erg blij dat je naast me op het podium wil staan als paranimf. Ik wil mijn familie bedanken voor alle interesse de afgelopen 4 jaar. In het bijzonder wil ik mijn vader en moeder bedanken voor alle steun, advies en zorg. Frederik, onze wijntrips en wandelvakanties waren altijd een welkome ontspanning en ik hoop dat we dat nog lang de verkeerde flessen zullen open maken. Saide, bedankt voor je voortdurende ondersteuning. Ondanks dat we elkaar relatief kort kennen hebben we samen al behoorlijk wat meegemaakt. Ik heb het idee dat we de afgelopen tijd persoonlijk enorm gegroeid zijn en hoop dat we samen nog verder zullen groeien.

About the author

Jan Maarten Hendrik van Doorn was born on the 16th of june 1991 in Ughelen, the Netherlands. He obtained his gymnasium diploma with majors in Nature & Technology and Nature & Health in 2009 from the Chistelijk Lyceum Apeldoorn in Apeldoorn.

In September 2009 he started with a bachelor in molecular life sciences at Wageningen University with a minor in innovation & entrepreneurship. During his bachelor thesis he worked on plant hormone receptor proteins in arabidopsis thaliana. In fall 2012 he started his master in molecular life sciences at Wageningen University with a specialization in physical chemistry. After is his master thesis on microrheology in jammed microgel suspensions Jan Maarten went to Lund University in Sweden to work on an internship on milk fouling in UHT plants. In fall 2014 he went back to the laboratory of physcical chemistry and colloid science in Wageningen to work as a research technician and later, from summer 2015, as a PhD student. This thesis, entitled 'On the verge: Mechanics in the limmit of vanishing strength and stiffness' is the result of that project.

As from July 2019 Jan Maarten has taken up a position as data scientist at Alliander N.V. where he works on predicting electricity consumption and production as part of the energy transition in the Netherlands.

Overview of completed training activities

Discipline specific activities

Han sur Lesse winter school, Belgium (WUR, 2015)

Jülich Soft Matter Meeting, Germany (Jülich, 2015)*

Soft Matter Meeting, Italy, Croatia (2017-2018)*

CHAINS, The Netherlands (NWO, 2016-2017)*

Physics@Veldhoven, Netherlands (FOM, 2017-2018)*

Advanced Soft Matter, Netherlands (WUR, 2017)

*poster or oral presentation

General courses

VLAG PhD week, The Netherlands (VLAG, 2015)

Taking charge of your phd, The Netherlands (FOM, 2015)

The art of presenting science, The Netherlands (FOM, 2017)

Scientific integrity, The Netherlands (WUR, 2017)

Journal Club, The Netherlands (2015-2019)

Optionals

Group meetings & colloquia (2015-2019)

Preparation of research proposal (2015)

PhD trip UK (2014)

The research described in this thesis is part of the Industrial Partnership Program Hybrid Soft Materials that is carried out under an agreement between Unilever Research and Development B.V. and the Netherlands Organization for Scientific Research (NWO)
Printed by Proefschriftmaken.nl in 150 copies